



## Coordinate Metrology by Traceable Computed Tomography

Müller, Pavel

*Publication date:*  
2013

*Document Version*  
Publisher's PDF, also known as Version of record

[Link back to DTU Orbit](#)

*Citation (APA):*  
Müller, P. (2013). *Coordinate Metrology by Traceable Computed Tomography*. Technical University of Denmark.

---

### General rights

Copyright and moral rights for the publications made accessible in the public portal are retained by the authors and/or other copyright owners and it is a condition of accessing publications that users recognise and abide by the legal requirements associated with these rights.

- Users may download and print one copy of any publication from the public portal for the purpose of private study or research.
- You may not further distribute the material or use it for any profit-making activity or commercial gain
- You may freely distribute the URL identifying the publication in the public portal

If you believe that this document breaches copyright please contact us providing details, and we will remove access to the work immediately and investigate your claim.

Coordinate Metrology  
by  
Traceable Computed Tomography

by

Pavel Müller

For fulfilment of the degree

Philosophiæ Doctor

Department of Mechanical Engineering

Technical University of Denmark

December 2012



# Preface

This thesis has been prepared as one of the requirements of the Ph.D. degree.

This Ph.D. thesis was funded by the Technical University of Denmark and the Danish project CIA-CT: Centre for Industrial Application of CT scanning. The thesis was carried out from January 2010 to December 2012 at the Department of Mechanical Engineering (MEK), Section of Manufacturing Engineering, Technical University of Denmark (DTU) under the supervision of Professor Leonardo De Chiffre, Professor Hans Nørgaard Hansen and Dr. Angela Cantatore. Two months, May and June 2012, were spent at the Physikalisch-Technische Bundesanstalt (PTB), Braunschweig, Germany under the supervision of Dr. Markus Bartscher.

First of all, I would like to thank all my supervisors. Mainly to Prof. Leonardo De Chiffre and Prof. Hans Nørgaard Hansen for giving me the opportunity to carry out this Ph.D. project at DTU MEK. I am grateful to Prof. Leonardo De Chiffre for his inspiration to my work, support and discussions on metrology related topics during the three years. Dr. Angela Cantatore is acknowledged for her advices in the project. A special thanks belong to Dr. Jochen Hiller. Discussions with Dr. Hiller on topics about computed tomography belong to the greatest contributions of this work. I am grateful to Dr. Hiller for showing me the way to successfully finish this work.

Furthermore, I would like to express my gratitude to the staff of department 5.34 Multisensor-Koordinatenmesstechnik at PTB, especially to Dr. Markus Bartscher, Dr. Ulrich Neuschaefer-Rube and Dr.-Ing. Frank Härtig, for their hospitality and inspiration to my research activities at PTB. Experimental work carried out at the PTB belongs to a valuable part of this Ph.D. thesis. Discussions with Dr. Bartscher are highly appreciated.

Then, I want to thank the staff at DTU MEK, namely to Mr. Jakob Rasmussen, Mr. Erik Larsen and Mr. René Sobiecki in connection with all kinds of dimensional measurements and for valuable discussions on metrology topics. My colleagues at the MEK department, Chris Valentin Nielsen, Ermanno Ceron, Alessandro Godi, Jais Andreas Breusch Angel and Peter Søe Nielsen, are also acknowledged for creating a nice and friendly atmosphere.

I would like to thank all the Consortium partners of the CIA-CT project, mainly to Novo Nordisk A/S and Danish Technological Institute (DTI) in connection with the use of their CT equipment. Namely, to Dr. Jan Lassen Andreasen and B.Sc. Yongying Dai from Novo Nordisk A/S and Mr. Peder



Pedersen and Ph.D. Maria Holmberg from DTI for helping me with CT measurements. Moreover, chapter of this thesis with a title: "Application of the substitution method using calibrated workpieces for uncertainty estimation of dimensional and geometrical measurements" has been carried out in collaboration with Novo Nordisk A/S. Many thanks belong to B.Sc. Dai for performing all the CT scans.

I want to thank a company Volume Graphics GmbH, Heidelberg, Germany for providing me for free for couple of months software VG Studio Max enabling me to carry out analysis of CT data.

I would like to thank my former supervisor for M.Sc. project Prof. Miroslav Píška from Brno University of Technology in Czech Republic for supporting me in going to study at DTU, and carrying out a master project under the supervision of Prof. Leonardo De Chiffre. My memories will always go back to year 2006 when I first came to Denmark.

Last but not least I would like to thank my girlfriend Malwina and my family for their support throughout the work at DTU.

Kgs. Lyngby, December 2012  
Pavel Müller

# Abstract

X-ray computed tomography (CT) is a measuring technique which has become an important technology in the production environment over the last years. Due to a number of advantages of CT compared to, e.g., coordinate measuring machines (CMMs), CT has been recently spread in the field of manufacturing metrology and coordinate metrology and is currently becoming more and more important measuring technique for dimensional measurements. This is mainly due to the fact that with CT, a complete three-dimensional model of the scanned part is in a relatively short time visualized using a computer, and measurements of outer as well as inner geometries can be performed with a micrometer accuracy.

The result of every dimensional CT measurement, as of every other measuring instrument, has to be accompanied with a statement about measurement uncertainty. The knowledge about measurement uncertainty is an important factor for decision making about manufactured parts. However, due to many influences in CT, estimation of the uncertainty is a challenge, also because standardized procedures and guidelines are not available yet.

In this thesis, several methods for uncertainty estimation were applied in connection with a number of industrial components as well as calibrated workpieces. Measurement uncertainty was often used as a parameter for quantification of a selected influence quantity. Uncertainty estimation using the substitution method appeared to be well applicable to CT measurements in production environment. By performing repeated measurements of the calibrated workpiece, characterization of a CT system under study for a specific task part was achieved. The task-specific measurement uncertainty from repeated measurements was then transferred to other uncalibrated workpieces. It was documented in the thesis that CT is a well-established technique for tolerance verification of manufactured parts.

Two reference objects for performance characterization of industrial CT systems were developed within the scope of the Ph.D. thesis. Namely, CT ball plate and CT tree, which were further used for identification, characterization and correction of measurement errors in the CT volume. Their application appeared to be suitable for this task. Because the two objects consist of ruby spheres and carbon fibre, CT scans did not produce image artifacts, and evaluation of sphere-to-sphere distances was robust.

Several methods for scale error correction were implemented to correct original reconstructed volume data sets. This was done using the CT ball plate, the CT tree, the calibrated features measured by

CMM and the "data base" approach considering a previous characterization of the CT system with a number of CT measurements using a calibrated ball bar. As, for example, methods using the two reference objects consisting of spheres, is a classical way for correction of the voxel size, when the distance between centres of spheres measured by CT is compared to calibrated measures, the application of calibrated features was documented on a metallic as well as on a plastic part and resulted in comparable observations. The last mentioned method using the "data base" approach seemed to work well, but its applicability shall be further validated.

# Resume

Røntgen computer tomografi (CT) er en måleteknik som er blevet en vigtig teknologi i produktionsmiljøer gennem de seneste år. På grund af et antal fordele ved CT, eksempelvis sammenlignet med koordinatmålemaskiner (CMM'er), er CT på det seneste blevet udbredt indenfor produktions- og koordinatmåleteknik og er aktuelt ved at blive en mere og mere vigtig måleteknik til dimensionsmålinger. Dette er primært på grund af at man med CT relativt hurtigt kan visualisere en komplet tredimensionel model af et scannet emne på en computer, og målinger af såvel ydre som indre geometrier kan foretages med mikrometernøjagtighed.

Resultatet af hver dimensionelle CT-måling skal, som ved alle andre måleinstrumenter, følges af en angivelse af måleusikkerheden. Kendskabet til måleusikkerhed er en vigtig faktor i stillingstagen i forbindelse med fremstillede emner. Grundet mange indvirkninger i CT er det imidlertid en udfordring at estimere usikkerheden, også fordi der endnu ikke er tilgængelige standardiserede procedurer og retningslinjer.

I nærværende afhandling er anvendt adskillige metoder til estimering af måleusikkerhed i forbindelse med en række industrielle komponenter og kalibrerede emner. Måleusikkerhed blev ofte brugt som en parameter til kvantificering af en udvalgt influensstørrelse. Estimering af usikkerhed ved brug af substitutionsmetoden forekommer passende til CT-målinger i produktionsmiljø. Ved udførelse af gentagne målinger af det kalibrerede emne kan karakterisering af et CT-system for en specifik opgave opnås. Den opgavespecifikke måleusikkerhed fra gentagne målinger kan herefter nemt overføres til andre ukalibrerede emner. Det er dokumenteret i afhandlingen at CT er en veletableret teknik til toleranceverifikation af fremstillede dele.

To referenceobjekter til karakterisering af industrielle CT-systemers performance er udviklet indenfor afgrænsningen af denne Ph.D.-afhandling. Disse er CT-kugleplade og CT-træ som yderligere er brugt til identificering, karakterisering og korrektion af målefejl i CT-volumenet. Deres anvendelse forekommer at være velegnet til denne opgave. Da de to objekter består af rubinkugler og kulfiber danner CT-scanninger ikke billedartefakter, og evaluering af kugle-til-kugle afstande er robust.

Adskillige metoder til korrektion af skalafejl er implementeret til at korrigere originale, rekonstruerede volumendatasæt. Dette er gjort ved brug af CT-kuglepladen, CT-træet, de kalibrerede egenskaber målt ved brug af CMM og "database"-fremgangsmåden ved betragtning af tidligere karakterisering af CT-systemet med et antal CT-målinger med en kalibreret kuglestang. Eksempelvis er metoderne med de

to referenceobjekter indeholdende kugler klassiske måder at korrigere størrelsen af volumenelementet (voxel), når afstanden mellem centrene af kuglerne målt med CT sammenlignes med kalibrerede mål. Brugen af kalibrerede egenskaber er dokumenteret for både metal- og plastikemner med resulterende sammenlignelige observationer. Den sidstnævnte metode ser ud til at virke godt ved brug af ”database”-fremgangsmåden, men dens anvendelighed skal valideres yderligere.

# Contents

|   |            |
|---|------------|
| <b>Preface</b>  | <b>i</b>   |
| <b>Abstract</b>   | <b>iii</b> |
| <b>Resume</b>   | <b>v</b>   |
| <b>1 Introduction</b>   | <b>1</b>   |
| 1.1 Brief introduction of computed tomography . . . . .                         | 1          |
| 1.2 Centre for Industrial Application of CT scanning (CIA-CT project) . . . . . | 4          |
| 1.3 Problem identification . . . . .  | 4          |
| 1.4 Project structure . . . . .   | 4          |
| <b>2 Dimensional measurement with CT</b>  | <b>7</b>   |
| 2.1 Industrial computed tomography . . . . .                                    | 7          |
| 2.2 Basic theory about X-ray physics . . . . .                                  | 8          |
| 2.2.1 Production of X-rays . . . . .  | 8          |
| 2.2.2 Interaction of X-rays with matter . . . . .                               | 9          |
| 2.3 Principle of computed tomography . . . . .                                  | 10         |
| 2.3.1 Acquisition of projection images . . . . .                                | 11         |
| 2.3.2 Reconstruction . . . . .  | 12         |
| 2.3.3 Segmentation and surface determination . . . . .                          | 12         |
| 2.3.4 Volume and surface model . . . . .  | 13         |
| 2.3.5 Dimensional measurement . . . . .   | 13         |
| 2.4 Advantages and disadvantages of industrial CT systems . . . . .             | 14         |
| <b>3 Traceability of CT</b>   | <b>23</b>  |
| 3.1 Introduction of measurement traceability in CT metrology . . . . .          | 23         |
| 3.2 Standards and guidelines for CT . . . . .                                   | 24         |
| 3.3 Influence factors . . . . .   | 26         |
| 3.3.1 Scale errors . . . . .  | 26         |
| 3.3.2 Beam hardening . . . . .  | 28         |
| 3.4 Measurement uncertainty . . . . .   | 31         |
| 3.5 Reference objects . . . . .   | 36         |
| <b>4 Development of reference objects at DTU</b>                                | <b>41</b>  |
| 4.1 CT ball plate . . . . .   | 41         |
| 4.1.1 Use . . . . .   | 42         |

|          |  |           |
|----------|--|-----------|
| 4.1.2    | Manufacture . . . . .  | 42        |
| 4.1.3    | Calibration . . . . .  | 42        |
| 4.1.4    | Procedure for surface determination . . . . .  | 51        |
| 4.1.5    | Procedure for definition of evaluation parameters . . . . .  | 52        |
| 4.1.6    | Procedure for scale error correction . . . . .   | 54        |
| 4.2      | CT tree . . . . .  | 55        |
| 4.2.1    | Use . . . . .  | 55        |
| 4.2.2    | Manufacture . . . . .  | 56        |
| 4.2.3    | Design considerations . . . . .  | 57        |
| 4.2.4    | Calibration . . . . .  | 58        |
| 4.2.5    | Procedure for surface determination . . . . .  | 59        |
| 4.2.6    | Procedure for definition of evaluation parameters . . . . .  | 59        |
| 4.2.7    | Procedure for scale error correction . . . . .   | 60        |
| 4.3      | Component of a dose engine . . . . .   | 60        |
| 4.3.1    | Calibration . . . . .  | 61        |
| <b>5</b> | <b>Performance characterization of CT systems using newly developed reference objects</b>                                    | <b>65</b> |
| 5.1      | Performance characterization of CT systems using the CT ball plate . . . . .   | 65        |
| 5.1.1    | Measurement procedure . . . . .  | 65        |
| 5.1.2    | Results . . . . .  | 67        |
| 5.1.3    | Conclusion . . . . .   | 69        |
| 5.2      | Characterization and quantification of measurement errors of a CT system using the CT ball plate . . . . .                   | 69        |
| 5.2.1    | Current approach . . . . .   | 69        |
| 5.2.2    | Measurement setup . . . . .  | 71        |
| 5.2.3    | Data evaluation . . . . .  | 72        |
| 5.2.4    | Results and discussion . . . . .   | 72        |
| 5.2.5    | Experimental validation of the proposed method . . . . .   | 76        |
| 5.2.6    | Conclusion . . . . .   | 79        |
| 5.3      | Characterization of measurement errors of a CT system in the direction of the magnification axis using the CT tree . . . . . | 80        |
| 5.3.1    | Measurement setup . . . . .  | 80        |
| 5.3.2    | Data evaluation . . . . .  | 82        |
| 5.3.3    | Results and discussion . . . . .   | 82        |
| 5.3.4    | Conclusion . . . . .   | 85        |
| 5.4      | Characterization of measurement errors of a CT system in the vertical direction using the CT tree . . . . .                  | 86        |
| 5.4.1    | Measurement setup . . . . .  | 86        |
| 5.4.2    | Data evaluation . . . . .  | 87        |
| 5.4.3    | Results and discussion . . . . .   | 87        |
| 5.4.4    | Conclusion . . . . .   | 88        |
| <b>6</b> | <b>Experimental study</b>  | <b>91</b> |
| 6.1      | Investigation on the relationship between scanning time and dimensional measurements of an industrial part . . . . .         | 92        |
| 6.1.1    | Design of experiment . . . . .   | 92        |
| 6.1.2    | Experimental setup . . . . .   | 93        |

|          |   |            |
|----------|---|------------|
| 6.1.3    | Data evaluation . . . . .   | 94         |
| 6.1.4    | Results and discussion . . . . .  | 95         |
| 6.1.5    | Conclusion . . . . .  | 98         |
| 6.2      | Investigation on the influence of scale error correction . . . . .  | 101        |
| 6.2.1    | Calibration of the Lego brick . . . . .   | 101        |
| 6.2.2    | Experimental setup . . . . .  | 102        |
| 6.2.3    | Data evaluation . . . . .   | 103        |
| 6.2.4    | Results and discussion . . . . .  | 105        |
| 6.2.5    | Conclusion . . . . .  | 109        |
| 6.2.6    | Outlook . . . . .   | 109        |
| 6.3      | A study on evaluation strategies by estimation of measurement uncertainty . . . . .   | 110        |
| 6.3.1    | Case description . . . . .  | 110        |
| 6.3.2    | Measurement setup . . . . .   | 111        |
| 6.3.3    | Process chain for data evaluation and definition of measuring strategies for CT measurements . . . . .  | 113        |
| 6.3.4    | Uncertainty estimation . . . . .  | 116        |
| 6.3.5    | Results and discussion . . . . .  | 117        |
| 6.3.6    | Conclusion . . . . .  | 122        |
| 6.3.7    | Outlook . . . . .   | 123        |
| 6.4      | Tolerance verification of industrial parts . . . . .  | 124        |
| 6.4.1    | Case description . . . . .  | 124        |
| 6.4.2    | Measurement setup . . . . .   | 125        |
| 6.4.3    | Process chain for data evaluation and definition of measuring strategies . . .  | 126        |
| 6.4.4    | Uncertainty assessment . . . . .  | 128        |
| 6.4.5    | Results and discussion . . . . .  | 129        |
| 6.4.6    | Conclusion . . . . .  | 131        |
| 6.4.7    | Outlook . . . . .   | 132        |
| 6.5      | Application of the substitution method using calibrated workpieces for uncertainty estimation of dimensional and geometrical measurements . . . . . | 133        |
| 6.5.1    | Measurement setup . . . . .   | 133        |
| 6.5.2    | Data evaluation . . . . .   | 135        |
| 6.5.3    | Test plan . . . . .   | 138        |
| 6.5.4    | Uncertainty estimation . . . . .  | 139        |
| 6.5.5    | Results and discussion . . . . .  | 141        |
| 6.5.6    | Conclusion . . . . .  | 146        |
| 6.5.7    | Outlook . . . . .   | 148        |
| <b>7</b> | <b>Conclusion</b>   | <b>151</b> |
| 7.1      | Summary . . . . .   | 151        |
| 7.2      | Outlook . . . . .   | 154        |
|          | <b>References</b>   | <b>158</b> |
|          | <b>Own references</b>   | <b>171</b> |
|          | <b>Appendix</b>   | <b>173</b> |





# Chapter 1

## Introduction

This chapter provides a brief introduction of Computed Tomography (CT), an imaging technique becoming widely used in the manufacturing metrology and coordinate metrology. Further, a short introduction of a CIA-CT project is given, and then problem identification and project structure are presented.

### 1.1 Brief introduction of computed tomography

In today's industrial world, the focus on precision in production engineering is of the main importance. Industrial components are more and more complex and the demands for quality control and quality assurance increase. Therefore, new technologies are being developed in order to fulfil the customer's needs and requirements. Computed tomography (CT), known for its broad use in the medical world since more than 30 years, has been recently rapidly developed also for industrial use. CT can be considered as the third generation of measuring techniques in coordinate metrology, together with coordinate measuring machines (CMMs) and optical systems. Using CT, a complete three-dimensional model of the scanned part can be produced in a relatively short time, which is achieved by penetrating the X-ray beam through the object and projecting it on a detector. This is one of the reasons why the interest for the industrial applications of CT is non-destructive testing (NDT), i.e., non-destructive analysis of faults (e.g., cracks or shrink holes) and material composition inside the scanned part. The main applications of CT can be found in automotive and aerospace industry for inspection and quality control of big castings and mechanical samples. These parts contain complex internal structures, and cutting the parts into sections is often expensive and may change the part's geometry. Other current applications of CT are measurements of components containing hard-to-access internal micro structures, like components produced by additive manufacturing or  $\mu$ -injection moulding processes, as well as measurements of assemblies. Thanks to the improved technology in terms of hardware and software, industrial CT is now being developed towards a quantitative inspection technique. Thus, current CT systems, shown in figure 1.1, are not only able to detect defects, but can also make statements about the size and the distribution of these defects [1]. A summary of CT applications for NDT and metrology is presented in table 1.1 and some examples are shown in figure 1.2. Industrial applications of CT are described, e.g., in [2, 3]. Since CT data contain complete volumetric information about the measured part, it is possible, after the reconstruction of the two-dimensional projection images, by generating surfaces on the scanned volume, to determine coordinates of the measured body. This means that CT can be used to perform dimensional measurements like, e.g., CMM. Due to the ability of X-rays to penetrate the inspected

object, CT is capable to measure external and internal structures and provide accurate dimensional and geometrical information with micrometer accuracy. This is also why CT offers new possibilities compared to traditional measuring techniques like CMMs and optical measurement systems. Since some years CT is increasingly used in industry for dimensional measurements. Measuring tasks are focused here on the absolute determination of geometrical features like wall thickness or on the comparison of the measured geometry with reference data sets [4]. A very popular method for determining whether a manufactured part is within the specifications is to use so called actual/nominal comparison, where the actual scanned geometry is compared either with a CAD model or reference measurements performed on the part by means of a more accurate or traceable measuring instrument.

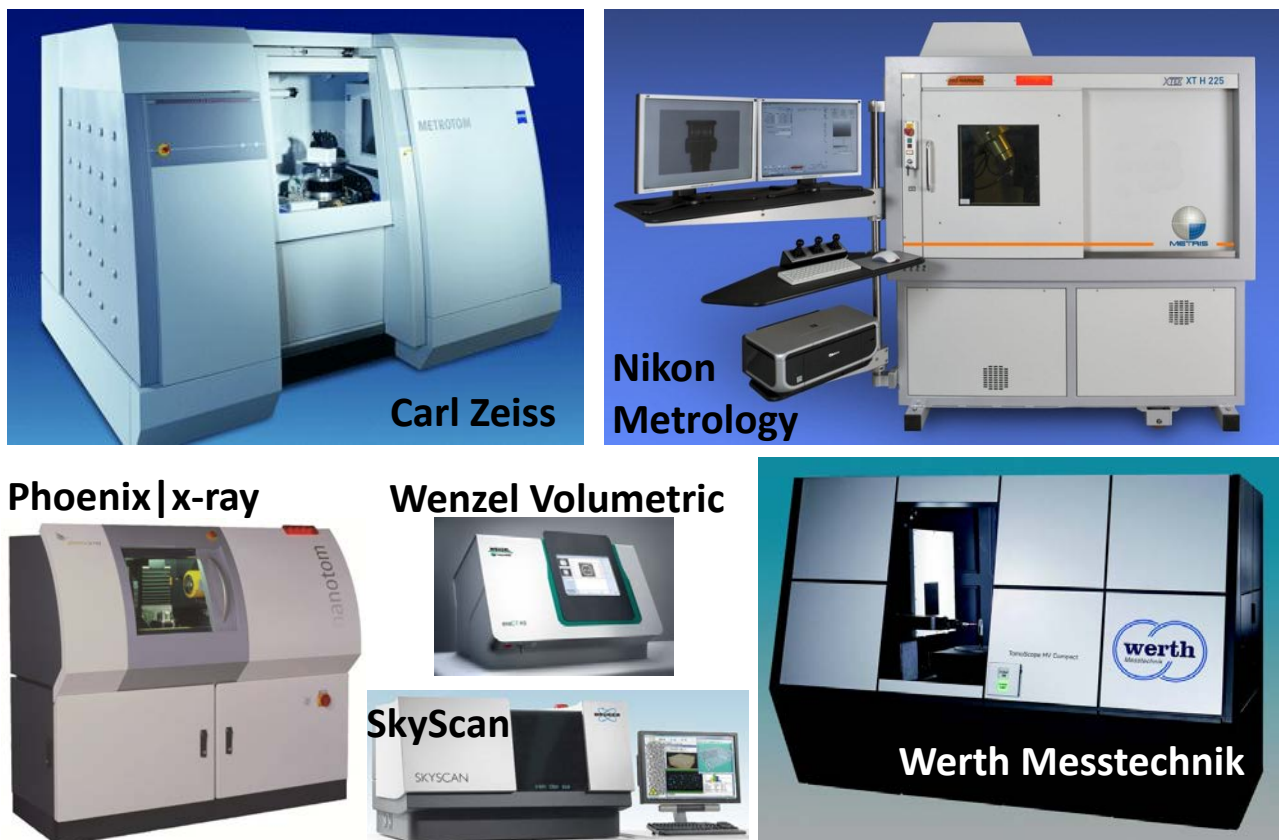


**Figure 1.1:** Example of industrial CT scanners.

**Table 1.1:** CT applications.

| NDT   | Metrology                             |
|---|---------------------------------------|
| Defect/Failure Analysis                       | CAD Comparison                        |
| Crack Detection and Measurement               | Non-destructive Internal Measurements |
| Porosity and Void Detection and Analysis      | Reverse Engineering                   |
| Density Discrimination - Material Composition | 3D Volume Analysis                    |
| Assembly Inspection                           | First-Article Inspection (FAI)        |

Because CT has been spread into the field of manufacturing metrology and coordinate metrology, an important parameter for quality control and reliability of the measurement process is an estimation of measurement uncertainty. Measurement uncertainty is also an important parameter for comparability and acceptance of CT systems as a measuring instrument. Because CT systems are quite new in their applications as coordinate measuring systems (CMSs), and, in general, due to the fact that there are many influence quantities in CT, standardized procedures and guidelines dealing with their testing are not available yet [1]. Thus, the assessment of the task-specific uncertainty becomes a challenge for all researchers. In this case, measurement traceability cannot be fully ensured. One possible way for achieving traceability in CT is the application of reference objects, as it is done in classical coordinate metrology [1]. Moreover, measurement capability in CT is reduced due to measurement errors (so called image artifacts). These artifacts appear in the reconstructed volume of the scanned part and cause, for example, problems in surface determination, and thus the measurement result is inaccurate and not traceable. Understanding of error sources, in general, their quantification and impact on a measurand is a current topic in dimensional CT metrology.

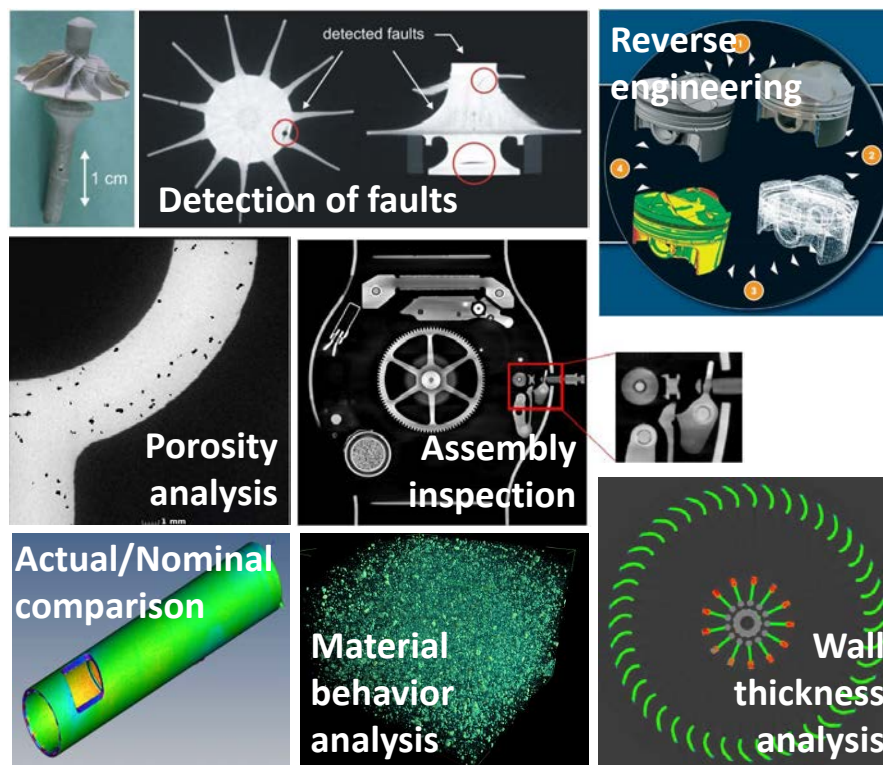


**Figure 1.2:** Examples of CT applications. From top left to right bottom: Detection of faults inside of a micro turbine [4], reverse engineering in automotive industry [5], porosity analysis of a mini cylinder head [6], assembly inspection for watch [3], actual/nominal comparison of housing of an insulin pen [7], material behaviour analysis (distribution of PTFE additive in POM) [8] and wall thickness analysis of a car inlet fan [3].

## **1.2 Centre for Industrial Application of CT scanning (CIA-CT project)**

This Ph.D. project was part of the CIA-CT project (Centre for Industrial Application of CT scanning) (<http://www.cia-ct.mek.dtu.dk>). The project started in September 2009 and will finish in August 2013, and consists of five main research projects. The main partner of the Ph.D. project was Novo Nordisk A/S, a company specialized in development and production of insulin pens. A network around the project has been created and has been expanding throughout the project. New companies (e.g., LEGO System A/S) and international institutions (e.g., Physikalisch-Technische Bundesanstalt) as well as universities (e.g., University of Padova, University of Leuven) are part of the network. The main activities of the project rely upon the industrial applications of CT as advanced 3D scanning measurement, quality assurance and product development. The project aims, among others, to help the participating companies and Danish industry with the introduction of CT as a measuring equipment and help with research at the international level. The project initiated new activities in the field of dimensional CT metrology at DTU and in Denmark in general.

## **1.3 Problem identification**

CT is a relatively new measuring technique in the field of coordinate metrology, featuring great advantages compared to conventional measuring systems, however, bringing numerous challenges, too. This is due to the fact that CT systems are multi-purpose measuring devices, influence factors and their impact on the measurand are in many cases unknown, standardized procedures and guidelines are not fully established and are still under development, and estimation of measurement uncertainty is rather a difficult task. Moreover, uncertainties vary with the task being performed and the users are not able to provide a correct statement of CT measurement uncertainties. Therefore, traceability of CT cannot be fully ensured, and thus CT cannot be yet considered to be a recognized measuring technique. The need is to develop reference objects for identification and compensation of errors, as it is done in classical coordinate metrology, in order to be able to provide a link to traceable measurements. As the title of this Ph.D. thesis suggests, the thesis deals with achieving traceability of dimensional CT measurements in coordinate metrology. The research work includes the following four main tasks defining a metrological approach:

1. Identification of all relevant influence factors and potential error sources.
2. Quantitative description of the impact of influence factors on measurands.
3. Development and testing of measurement procedures and development of uncertainty budgets.
4. Development and testing of reference objects and calibration workpieces.

## **1.4 Project structure**

The structure of the Ph.D. thesis basically reflects the above mentioned tasks. These will be discussed in the following chapters of the thesis:

- Chapter 2 describes dimensional measurement with CT as a tool for coordinate metrology. In this chapter a basic theory about X-ray physics is presented, too. Furthermore, advantages and disadvantages of CT with respect to coordinate measuring machines (CMMs) and optical scanning methods are discussed.
- Chapter 3 discusses traceability of CT. Influence factors in CT are identified and divided into groups. Two most relevant influence quantities selected by the author, scale errors and beam hardening effect, are described in more details. Available standards and guidelines for CT are presented and their relevance to CT applications is discussed. Also, a state-of-the-art of current methods for uncertainty estimation in CT as well as state-of-the-art of reference objects in CT used for identification, characterization and correction of measuring errors is presented.
- Chapter 4 presents two reference objects and one calibration workpiece developed within the scope of the Ph.D. project. In particular, a CT ball plate and a CT tree, two objects for performance characterization of industrial CT systems. Use, manufacture and calibration of the objects are addressed in the chapter. Another object is a calibrated workpiece - component of a dose engine from an insulin pen - used in connection with uncertainty estimation of dimensional CT measurements using calibrated workpieces.
- Chapter 5 discusses procedures for characterization of CT systems and measurement errors in the measuring volume using the two reference objects - CT ball plate and the CT tree.
- Chapter 6 presents a comprehensive experimental study. This chapter is divided into sections, where each section discusses a specific case study. In particular, investigations on image-related influence factors, scale error correction methods, measurements on volume and surface data, measuring strategy, suitability of CT for tolerance verification and application of a substitution method for uncertainty estimation are presented in the chapter.
- Chapter 7 summarizes findings and achievements of this work. Suggestions for future work based on this Ph.D. project and in the field of CT in general are provided, too.



# Chapter 2

## Dimensional measurement with CT

This chapter describes dimensional measurement with computed tomography as a tool for coordinate metrology. In particular, introduction to industrial CT is given first, followed by a basic theory about X-ray physics. After that, general principle of CT, process chain for dimensional measurement with CT and considerations which need to be taken into account prior to tomography are presented. Finally, advantages and disadvantages of CT with respect to other measuring techniques are presented.

### 2.1 Industrial computed tomography

A typical industrial CT scanner generally consists of four hardware subsystems: X-ray source, rotary table, X-ray detector, and data processing unit.

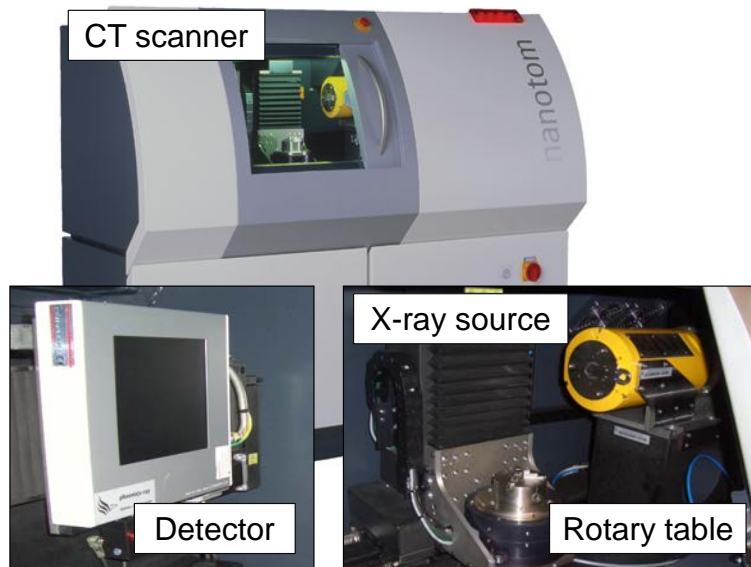


**Figure 2.1:** The main hardware subsystems of a typical industrial cone beam CT scanner: X-ray source, rotary table, X-ray detector. The data processing unit is not shown. As an example, Nanotom cone beam CT scanner from GE Phoenix|x-ray is shown.

There are two main types of CT systems: 2D-CT (fan beam CT) and 3D-CT (cone beam CT with



circular trajectory). 2D-CT systems shown in figure 2.2(a) have a fan beam source and a line detector which enable the acquisition of a slice of an object by coupling a translation and rotation movement of the object. This sequence of rotation and translation is repeated depending on number of slices which have to be reconstructed. The main drawback of these systems is long scanning times (especially when working with big parts). This problem is overcome by 3D-CT systems shown in figure 2.2(b). The systems consist of a flat area detector and a cone beam source, enabling acquisition of a slice of the object only with one revolution of the rotary table. No linear translation of the rotary table is needed. This solution allows significant improvement in acquisition time but other problems arise due to, e.g., the cone beam source. Scattered radiation and reconstruction artifacts can affect the quality of the reconstructed geometry when the object is scanned at the borders with the detector. In particular, because of geometrical reasons, scanning quality deteriorates from the center to the borders of the detector [9]. Moreover, loss of spatial resolution in the direction of the rotation axis can lead to image artifacts (so called Feldkamp artifacts [10]). These artifacts increase with the increase of the cone beam angle [11]. The most recent evolution of 3D-CT is represented by systems exploiting a helical scan geometry shown in figure 2.2(c), where rotation of the object is simultaneously performed with a translational movement along the rotation axis [9, 12]. The advantages of this solution are two: first, there are no restrictions on the sample length (along the rotation axis direction); the helical trajectory can be prolonged for object bigger than detector dimension and theoretically object of unlimited length can be reconstructed, and second, with an appropriate shift of the part, a bigger number of slices of the object can be projected in the middle part of the detector, leading to a more complete acquisition, and so, to a constant resolution along the rotation axis. In this way, also top and bottom areas will be scanned with the same resolution as the central one.

## 2.2 Basic theory about X-ray physics

### 2.2.1 Production of X-rays

X-rays are electromagnetic waves with a wavelength smaller than 10 nm. A smaller wavelength corresponds to a higher energy according to equation 2.1. The energy of each photon  $E$  is proportional to its frequency  $f$  and is described as follows:

$$E = h \cdot f = \frac{h \cdot c}{\lambda} \quad (2.1)$$

where  $h$  is Planck's constant ( $h = 6.63 \cdot 10^{-34} \text{Js}$ ),  $c$  is a speed of light ( $c = 3 \cdot 10^8 \text{ms}^{-1}$ ), and  $\lambda$  is a wavelength of the X-ray. Therefore, X-ray photons with longer wavelengths have lower energies than the photons with shorter wavelengths. The X-ray energy is usually expressed in eV ( $1 \text{eV} = 1.602 \cdot 10^{-19} \text{J}$ ).

One of the main parts of the CT system is an X-ray source, which, among other parameters, determines the final image quality. Its main components are shown in figure 2.3. The X-ray tube, as the X-ray source is also called, consists of two electrodes, a negatively charged cathode and positively charged anode, containing a metal target. When the cathode filament (the filament is in most cases a tungsten wire) is heated, electrons are ejected from its surface. An electrical potential between the cathode and the anode forces the electrons to accelerate towards the anode. At the anode, X-rays are produced as the accelerated electrons penetrate a few tens of micrometers into the metal target and

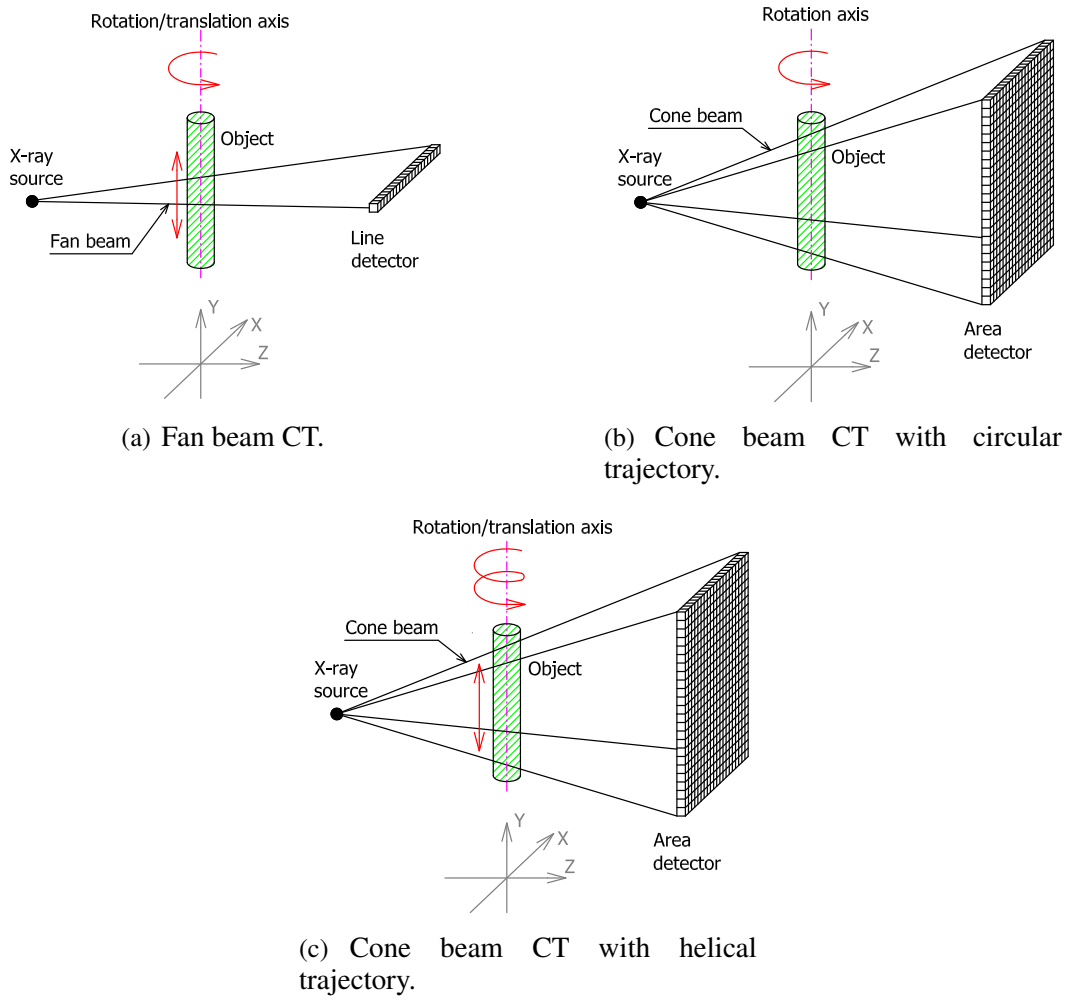


**Figure 2.2:** CT scan geometries.

lose their kinetic energy. Since energy must be conserved, the energy loss results in the release of X-rays photons of energy equal to the energy loss. The emitted X-rays consist of two components: The first is called continuous radiation (Brehmsstrahlung, where "Bremse" is a German name for slowing down), since the incoming electrons release X-rays as they slow down in the target. An incoming electron may also collide with an inner-shell electron in the target, "kicking out" an electron and leaving a vacancy in one of the atom's electron shells. Another electron may fill the vacancy and in doing so release an X-ray photon of a specific energy (a Characteristic radiation). The characteristic radiation results in a discrete X-ray spectrum of characteristic peaks (the X-ray spectrum is generally characterized by two peaks, corresponding to  $K_\alpha$  X-ray and  $K_\beta$  X-ray, depending which electron is displaced by the incoming electron), the bremsstrahlung provides a continuous spectrum, which has a maximum at approximately one-third of the maximum photon energy. Both radiation types are shown in figure 2.4. The X-ray energy spectrum, defining the penetrative ability of the X-rays, as well as their expected relative attenuation as they pass through materials of different densities, is affected by: tube current, tube voltage, filtration and target material. These are described in the following.

#### (a) X-ray tube current and voltage

The X-ray tube current and voltage are variables that can be chosen by the operator within a

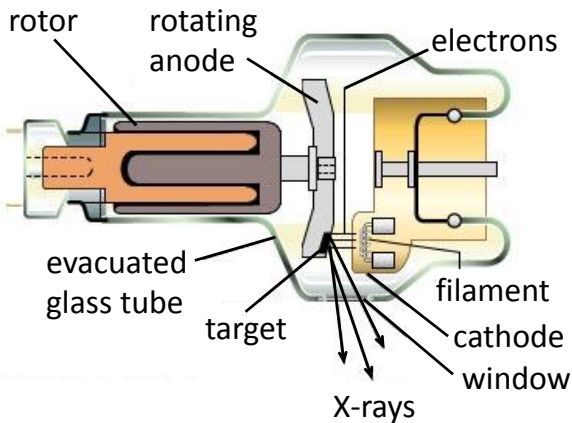


**Figure 2.3:** X-ray source and its components  
[Source: Merriam-Webster 2006].

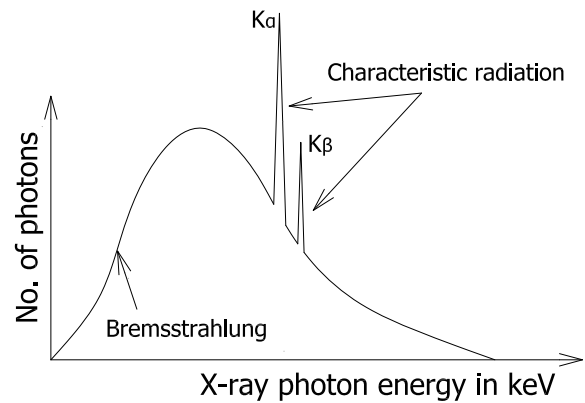


**Figure 2.4:** Continuous (Brehmsstrahlung) and Characteristic radiation.

machine specific range. While the current affects only the intensity (amount of radiation) without modifying the quality (penetration) of the energy spectrum, tube voltage has an influence on both. Change of tube current causes a change in the amplitude of X-ray spectrum at all energy levels but the curve shape is preserved (see figure 2.5(a)). On the other hand an increase of tube voltage causes both an increase in amplitude and a shift of the curve towards high energy levels [13].

#### (b) Filtration

The physical filters are the most popular method for reducing an effect called beam hardening [14] (discussed later in section 3.3.2). These filters are made of different materials (e.g., aluminium, copper, brass, etc.) and are used to harden the X-ray spectrum generated by the X-ray tube (filters provide a cleaner image). By using such filters low energy photons are filtered out. The emission spectrum is not modified but increases the average energy of the X-ray beam with an increase of quality and a reduction of quantity (in terms of total energy) (see figure 2.5(b)). Thus, the amplitude becomes smaller and the spectrum is shifted to the right (higher energy levels). This method has, however, one disadvantage: when the low energy photons are filtered out, the amount of X-rays is decreased resulting in decrease of the image signal-to-noise ratio (SNR).

#### (c) Target material

X-rays with higher energy penetrate more effectively than lower energy ones. High atomic number elements like tungsten ( $Z=74$ ) enable to reach higher penetration (because the spectrum is shifted towards high energy levels), enhancing the efficiency of X-ray generation (both quantity and quality of X-rays) and energy of Characteristic and Brehmsstrahlung X-rays [13].

### 2.2.2 Interaction of X-rays with matter

As the X-rays pass through the object, the intensity of the rays decreases due to absorption and scattering. The mechanisms responsible for the two contributions to the attenuation are Photoelectric effect and Compton (scatter) effect. Both of them are energy dependent. The intensity loss is described by Lambert-Beer's law. The law states that each layer of equal thickness absorbs an equal fraction of the radiation that traverses it [15]. This can be expressed as follows:

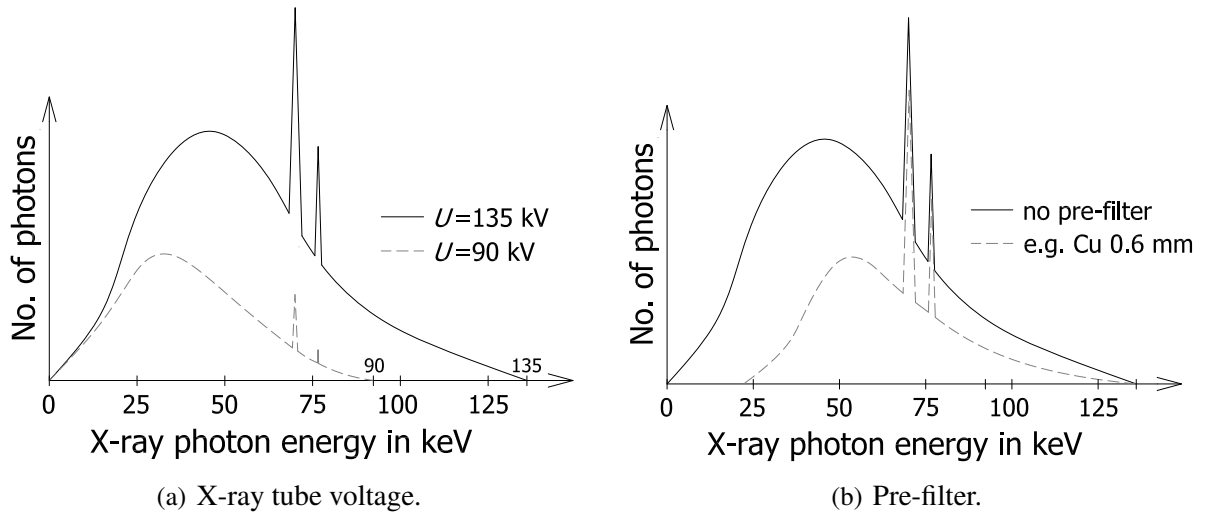


**Figure 2.5:** Factors affecting size and relative position of X-ray spectrum.

$$\frac{dI}{I} = -\mu ds \quad (2.2)$$

where  $I$  is intensity of the incident radiation,  $dI/I$  is fraction of radiation removed from the beam as it traverses a small thickness  $ds$  of material and  $\mu$  is linear attenuation coefficient. When equation 2.2 is integrated, the following is obtained:

$$I = I_0 e^{-\mu ds} \quad (2.3)$$

where  $I_0$  and  $I$  are initial (unattenuated) and final (transmitted through the material of thickness  $s$ ) X-ray intensities. If the X-rays are travelling through an inhomogeneous material, equation 2.3 must be rewritten in a more general form:

$$I = I_0 e^{-\int \mu(s) ds} \quad (2.4)$$

The line integral is taken along the direction of propagation and  $\mu(s)$  is the linear attenuation coefficient at each point on the ray path. The linear attenuation coefficient is a measure of the attenuation per unit distance. It is specific for the used X-ray energy and for the type of absorber. Consequently, equation 2.4 has to be adapted for inhomogeneous materials and polychromatic X-rays:

$$I = \int I_0(E) e^{-\int \mu(s,E) ds} dE \quad (2.5)$$

A value of linear attenuation coefficient accounts generally for number of atoms in a cubic cm volume of material and the probability of a photon being absorbed or scattered from a nucleus or an electron of one of these atoms. The number of photons transmitted through a material depends on the thickness, density and atomic number of the material and the energy of the individual photons, and generally reduces exponentially while travelling through the matter which can be seen in figure 2.6.

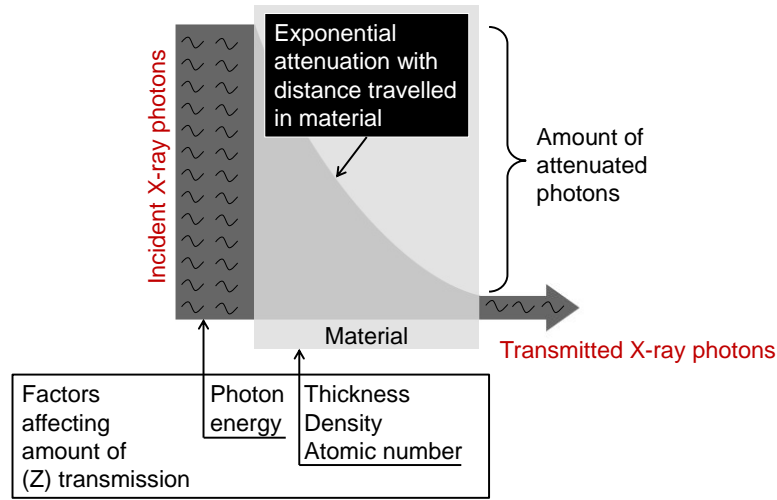


**Figure 2.6:** Emitted and transmitted photons dependence. Adapted from [16].

In theory, an interaction of the X-rays with the matter can result in only one of three possible outcomes [15]: the incident X-ray can be completely absorbed and cease to exist; the incident X-ray can scatter elastically; or the incident X-ray can scatter inelastically. The photon-matter interactions of primary importance to radiography are the ones which dominate observable phenomenon: photoelectric effect, Compton scattering (also called incoherent scattering), and pair production. Of the other possible interactions is Rayleigh scattering (also called coherent scattering) which is small but non-negligible. Thus, the linear attenuation coefficient can be written as:

$$\mu = \mu_{\text{ph}} + \mu_{\text{incoh}} + \mu_{\text{coh}} + \mu_{\text{pp}} \quad (2.6)$$

However, only the photoelectric absorption and the Compton effect are important in the energy ranges used in X-ray  $\mu$ CT [17].

## 2.3 Principle of computed tomography

By generating, emitting and finally projecting a beam composed of photons through a plane of an object, projection images are recorded. Here, the rotary table is used to precisely move the object relative to the source and detector, and to rotate the object at specified angular positions. As the X-rays pass through the object, some are absorbed, some are scattered and some are transmitted. The process of X-ray intensity reduction, corresponding to those X-rays that are scattered or absorbed, is called *attenuation*. The X-rays which are attenuated due to the interactions with the object will not reach the X-ray detector. The amount of attenuation is determined by the object, i.e., by the length the X-rays need to penetrate the object, by the material composition, its density and energy of the X-rays determined by the X-ray power (see figure 2.6). The photons transmitted through the object are captured by the detector, composed of detection elements such as scintillating crystals and photo diodes, in terms of 2D gray images, collected at each angle. Such data are then visualized by a computer cluster creating a complete reconstruction of the scanned object. The reconstructed 3D object is composed of voxels, **volumetric pixels**, where each single voxel represents a local attenuation of the object. A schematic presentation of the CT process chain, including the actual scanning of the object, acquisition of the projection images, their reconstruction and final visualization of the

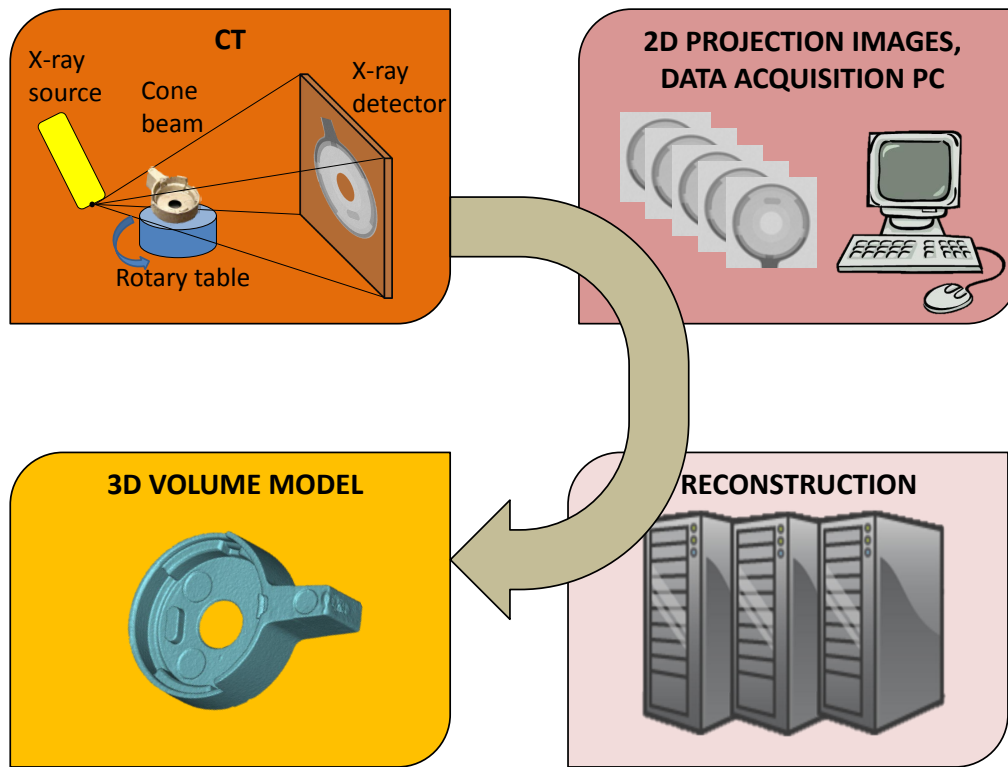


**Figure 2.7:** A typical CT process chain: From scanning of the object through acquisition of the projection images at defined angular positions, their reconstruction using a reconstruction cluster to a visualization of the 3D volume model.

volumetric model, is shown in figure 2.7.

A flow chart of a typical dimensional CT measurement process, that is the way a measurement result is obtained, is presented in figure 2.8 and described in the following.

Some considerations have to be taken into account prior to the actual scanning of the object: Several parameters (e.g., energy of the source determined by the tube voltage and current, orientation of the object in the measuring volume, detector integration time, number of images being averaged, number of projection images, etc.) have to be carefully chosen to obtain a high resolution CT scan, yielding the best possible accuracy. These depends also on the part's size, geometry complexity, material composition, CT system's properties, etc. The accuracy of the CT scan finally depends on the geometrical magnification determined by the position of the object with respect to the source and detector. The closer to the source the object is positioned, the higher magnification and thus smaller voxel size is obtained, resulting in a higher resolution CT scan. The resolution is also affected by the size of the focal spot (blurring), the quality of the rotary axis (tilt), and other characteristics of the machine components [18]. The size of the focus spot is a function of voltage (X-ray power) and current, and thus is also a function of material. In general, the smaller the focal spot is and the closer the object is positioned to the focus, the bigger is the geometrical magnification in the detector. For cone beam CT, the highest accuracy is achieved in the beam which is perpendicular to the rotary axis and is at the focus spot of the X-rays. All other slices than those in the central plane are affected by beam artifacts, which are pronounced at the borders of the object with the detector. The geometrical

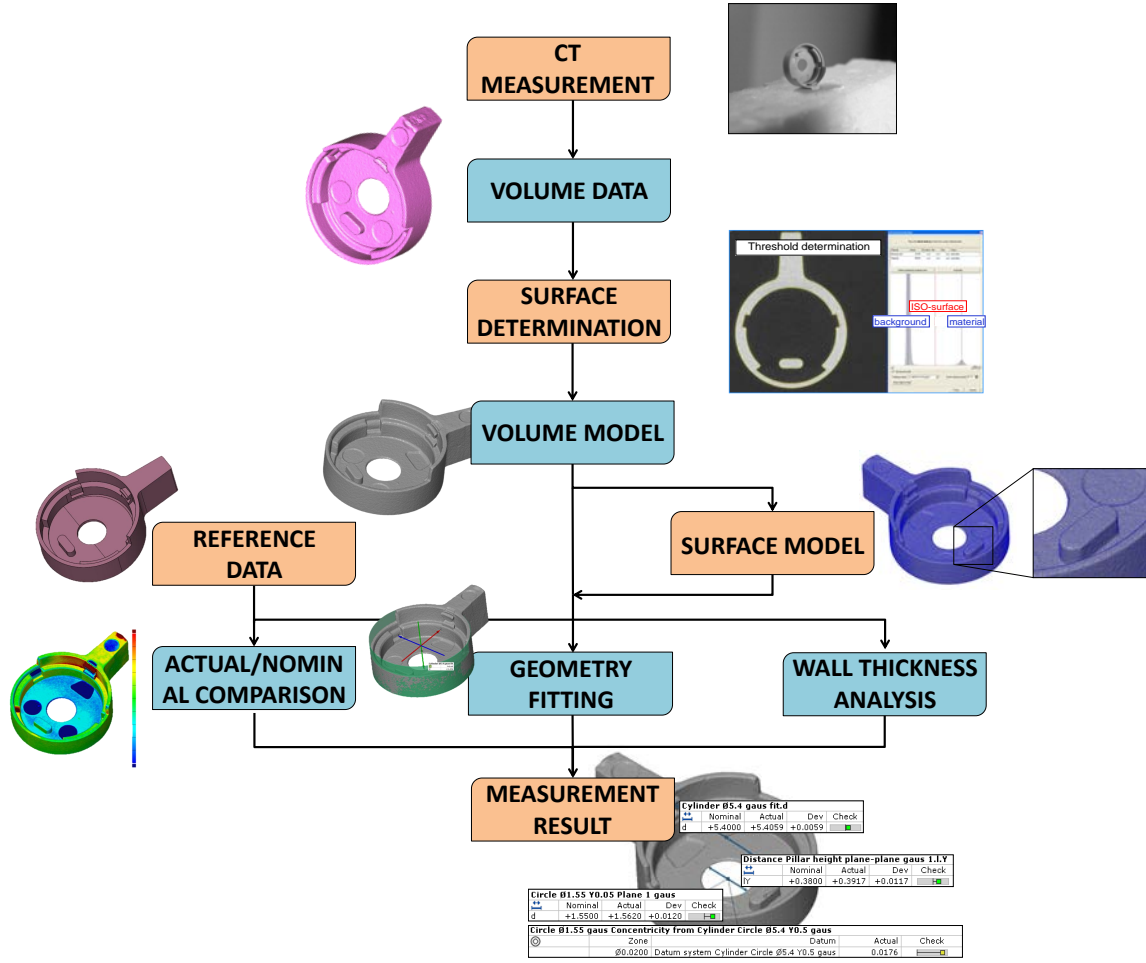


**Figure 2.8:** A flow chart of a typical dimensional CT measurement process.

magnification then determines the opening cone beam angle, and at high magnifications, the angle increases and so the measurement errors. Geometrical magnification  $m$  is given as a ratio between a source-detector distance  $SDD$  and a source-object distance  $SOD$  according to equation 2.7. The size of a voxel  $s$  is then determined by the detector pixel size  $p$  according to equation 2.8.

$$m = \frac{SDD}{SOD} \quad (2.7)$$

$$s = \frac{p}{m} \quad (2.8)$$

In order to make an accurate reconstruction of the volumetric data, the entire sample must remain within the field of view and the cone beam during the rotation. The maximum magnification is limited by the ratio of the effective detector width  $D$  and the sample diameter  $d$ , and can be expressed according to equation 2.9. The whole geometry of CT is presented in figure 2.9.

$$m = \frac{D}{d} \quad (2.9)$$

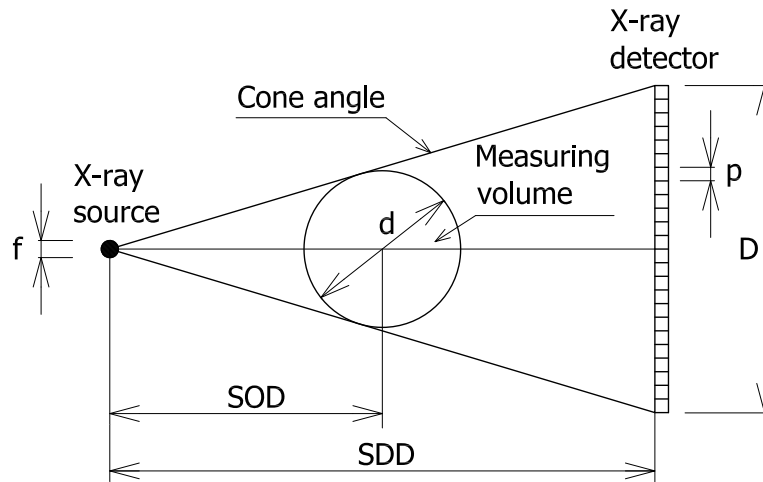


**Figure 2.9:** Typical geometry of CT (top view). Geometrical magnification is determined by the source-object distance  $SOD$  and source-detector distance  $SDD$ , as well as the effective detector width  $D$  and the measuring volume  $d$ . Further,  $f$  is the focus size and  $p$  is the detector pixel size.

Measurement accuracy can be improved by scanning a selected region of interest (ROI), when the object is moved closer to the source. Choosing to select the ROI happens also in case when small features in large parts are to be measured to increase the resolution [19]. By restricting the analysis to relevant component areas, the influence of scanning irrelevant areas, e.g. those yielding artifacts, can be disregarded.

### 2.3.1 Acquisition of projection images

Projection images are acquired at every rotational step of the object, defined by the operator. The gray level of each image depends on the attenuation of the X-rays travelling through the object. The amount of projection images then determines the quality of the resulting volumetric model, as well as needed measurement time. By averaging the projection images at each specified angular position, noise for a single projection can be reduced to enhance the quality of the resulting data set. Figure 2.10 shows a projection image of a toggle, a hearing aid component.

### 2.3.2 Reconstruction

After scanning and obtaining a set of 2D projection images, the volume is reconstructed by a computer cluster connected to the CT system. The most popular approximate reconstruction scheme for cone-beam projections is the algorithm according to Feldkamp, Davis and Kress [10]. It is often referred to as FDK method. This algorithm is used by many research groups and commercial vendors for cone-beam CT with 2D area detectors. To increase image quality and thus the quality of the resulting volumetric model, the projections are filtered prior to the reconstruction. That is why this reconstruction method is called "filtered back projection". The volume is modelled as a 3D matrix of voxels. Here, some correction techniques can be applied on the 2D projection images in order to minimize some of the physical effects, e.g., scattered radiation and beam hardening. Figure 2.11 shows a reconstruction image of the toggle as an example.



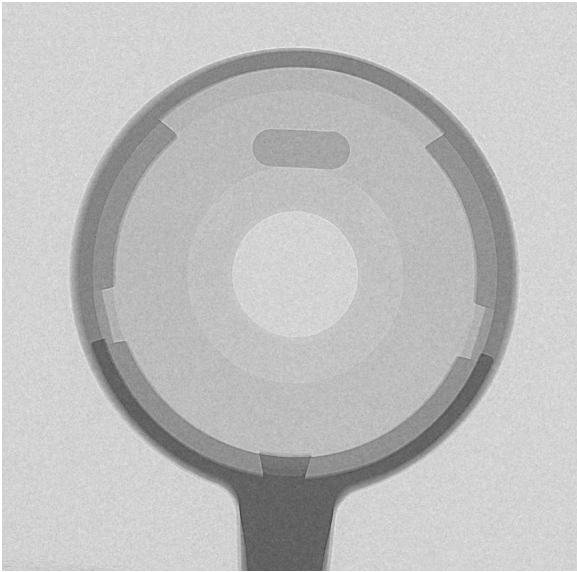


**Figure 2.10:** 2D projection image of a plastic component (toggle). Different levels of gray values on the picture can be recognized showing actual intensity of the X-rays passing through the part.

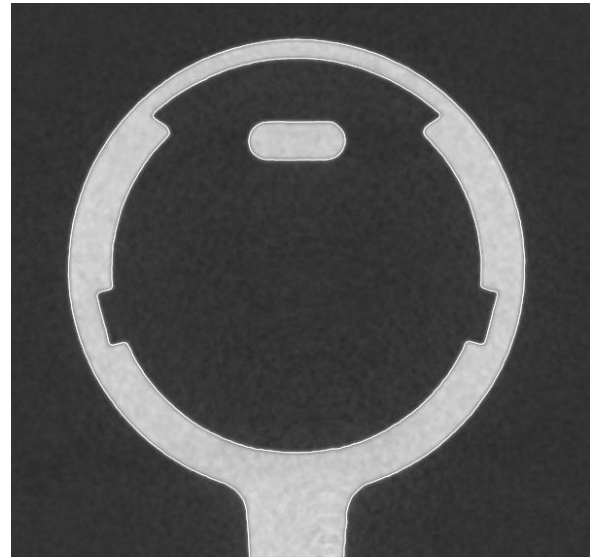


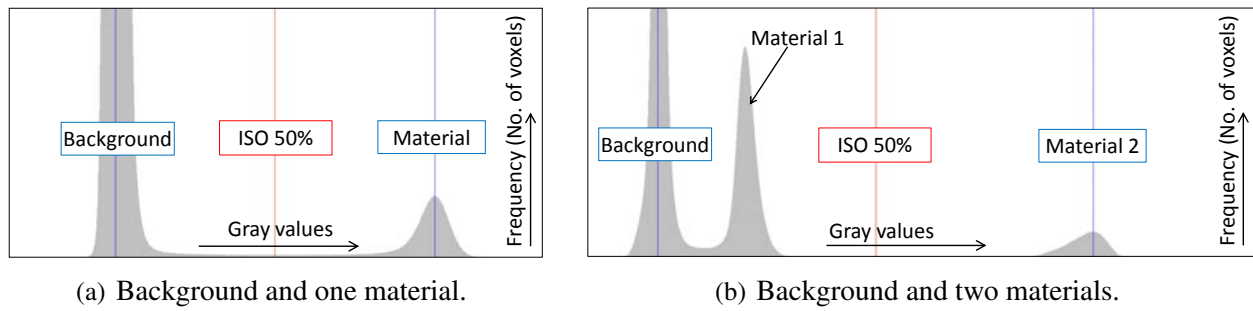
**Figure 2.11:** 2D reconstruction image of a plastic component (toggle).

### 2.3.3 Segmentation and surface determination

To be able to perform dimensional measurements of a part, a threshold value has to be carefully determined, as it is a critical parameter for accurate image segmentation and surface data determination, and therefore, has a great influence on the final scan geometry [20]. A typical way is to use an iso-50% value [21], determined as a ratio between the air (background) and the material (object), where 50% is assigned to the air and 50% to the material (see figure 2.12(a)). This is generally illustrated by a histogram showing a gray value distribution of the scanning volume, i.e., frequency (number of voxels) on y-axis and gray values on x-axis. Figure 2.12(b) shows a situation of scanning multi-material object (in this case two materials within one object, highlighted by the two distinctive peaks). Here, the iso-50% is determined between background and material 2.

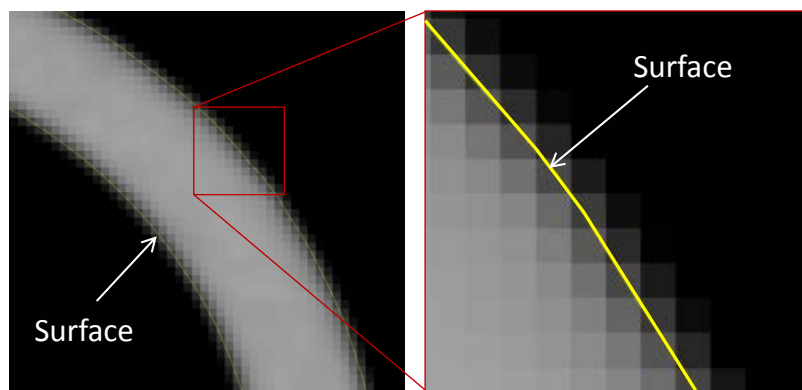
In the ideal case, i.e., when scanning a homogeneous object (only one material) and assuming no artifacts in the reconstructed volume, this method, also called global method (see figure 2.13), would work just fine. However, this is not the case for real CT scans, where occurrence of image artifacts, caused by, e.g., beam hardening, scattered radiation or artefacts created by insufficient penetration of the object [22], is common. Thus, iso-50% method can only be applied as a first estimate for surface determination. For a more accurate surface determination, resulting in a more precise and accurate coordinate measurement, a local adaptive threshold method shall be applied, where the surface is determined in each voxel locally. In principle, this method is based on searching of a sharp edge in gray level perpendicularly to the originally defined surface through global method within a pre-defined (by user) search distance at both sides of the original surface. It is mentioned in [22] that this method is able to determine an edge with an uncertainty of less than 1/10th of a voxel.

Figure 2.14 presents diameter measurements of a ball bar, where global and local threshold methods



**Figure 2.12:**  
surface. In cas

% threshold



**Figure 2.13:** Determination of the object's surface by applying iso-50% threshold method.

were applied for segmentation of background (air) and material (spheres made of ruby). The influence of the method applied is evident, difference of approximately  $10 \mu\text{m}$  was experienced for 31 CT measurements characterized by a big variation of scanning parameters. However, this applies only to diameter measurements, which are threshold sensitive. We will experience in this thesis, that even though measurement of diameter is threshold sensitive, this does not apply to measurements of a distance between spheres centres, as the threshold method has nearly no influence and is very robust.

### 2.3.4 Volume and surface model

After the threshold value is determined, a volume model consisting of voxels (three-dimensional pixels) is generated. Since generally such a volume is big in size and memory, and can only be handled by specific designated software tools, a surface model (STL) is generated preferably, which is characterized by a polygonal mesh in the shape of triangles (see figure 2.15). Such data can be easily handled by other software tools, not only those designated to CT measurements. However, additional errors are encountered when performing the evaluation on the STL model [7, 23]. Generally speaking, STL data is very sensitive regarding image noise. When a polygonal mesh is created on the volume model with noise, this noise becomes a part of the mesh. Difference between volume and surface models is shown in figure 2.16, represented as a variance map (also called color map). Here, maximum deviations occur where the radiographic lengths are big.

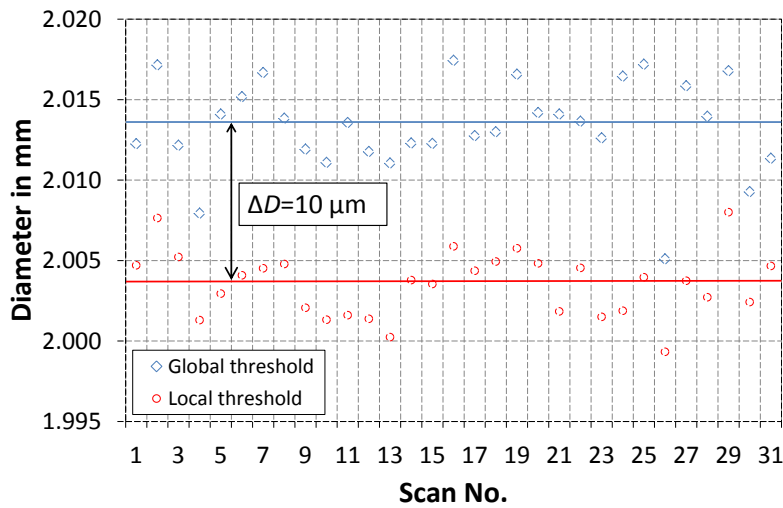


**Figure 2.14:** Global and local threshold methods influencing measurement of diameter of one of the balls of a ball bar. Difference of approximately  $10\ \mu\text{m}$  was experienced for 31 CT measurements of the ball bar with a big variation of scanning parameters.

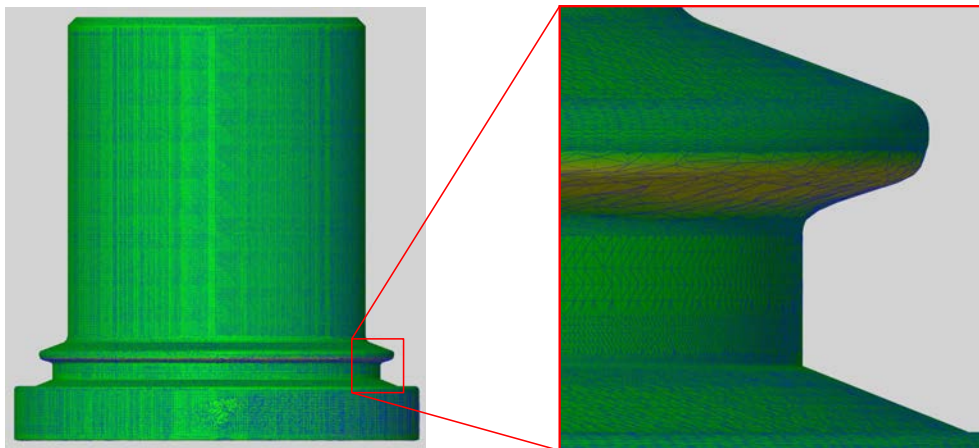


**Figure 2.15:** A polygonal mesh (STL) created on the voxel model of the pipe connector.

### 2.3.5 Dimensional measurement

Dimensional measurements (e.g. actual/nominal comparison (figure 2.17), fitting of geometrical primitives (figure 2.18) and wall thickness analysis) can be performed on either of the earlier mentioned data sets (volume or surface).

- The first mentioned - actual/nominal comparison - is a common means of quality assurance for newly manufactured parts. Here, the actual measurement of the geometry by CT is compared with reference data. Reference data can be obtained from measurements using a more precise measuring instrument (e.g. tactile CMM) or, as it is sometimes the case, a CAD model of the inspected part. As a result, detailed deviations of the product are visualised. However, the comparison of CT and CMM measurements is not trivial, due to the intrinsic differences of the two types of measurement, and requires a special care. One example is, e.g., the number of acquired points and their sampling by the two measuring systems, which is evidently different.

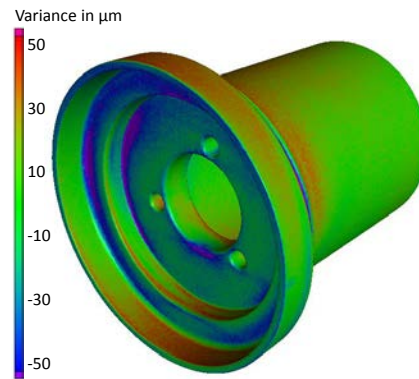


**Figure 2.16:** A variance map showing difference between volume and STL models [7]. Pipe connector is shown as an example.

By CT a big amount of points can be acquired on a feature, while the same amount of points may represent a large data quantity for a tactile CMM. Moreover, it is mentioned in [24], that a problem with comparisons between CAD data and CT data is that it is not known whether the deviations are associated with inaccuracies in the manufacturing process or with the CT scan itself. Therefore, calibration of the parts using a traceable measuring instrument is necessary. One has to keep in mind that the tactile probing of the surface of the inspected part performs a morphological filtering of the surface profile by the probe tip and so does not consider the real surface [25]. Among other critical points regarding the two different measuring instruments belong, e.g., measuring strategy, measurement of freeforms, filtering of data points, etc. [26, 27].

- By fitting geometrical primitives (e.g. spheres, cylinders, circles) on voxel data or surface data, and applying a relevant fitting method (e.g. Gaussian or Chebyshev), dimensional (e.g. length, diameter) and geometrical (e.g. form error, position) measurements can be performed. Definition of the measurand (in this case a measured feature) with respect to the coordinate system needs to be precise, i.e., information regarding number of fitted points, fitting method, use of filters etc. has to be provided.
- Wall thickness analysis enables to examine thickness of whole part or selected ROIs on the part. By aligning the scanned model with a CAD model, a detailed color-coded map of deviations is created providing information on minimum and maximum deviations.

## 2.4 Advantages and disadvantages of industrial CT systems

As discussed earlier, CT has recently become an accepted inspection tool for a large number of industrial applications. In particular, CT has become an important player in the field of coordinate metrology. This is due to the fact that using CT, a complete three-dimensional volume model of the scanned part can be obtained in a relatively short time. Compared to other measuring techniques, e.g. tactile measuring techniques, parts scanned by CT yield high information density. One of the greatest advantages of CT is to measure and examine internal structures of products without destroying them. This makes the CT technology unique and in many cases preferable to commonly used tactile or

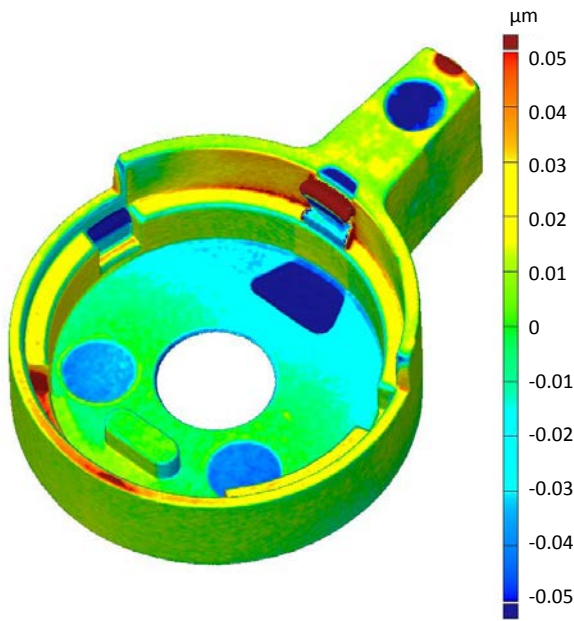


**Figure 2.17:** Actual/nominal comparison (variance map) showing difference between the scanned voxel model and a CAD model. Toggle is shown as an example.

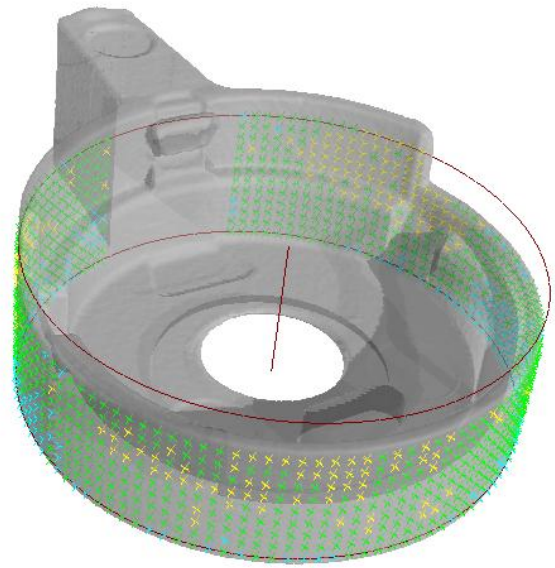




**Figure 2.18:** Fitting of geometrical primitives. In this case a cylinder is fit on the outer surface of the part. Local deviations (in color) can be observed. Toggle is shown as an example.

optical CMMs. Measurement of parts which are flexible or small is difficult by means of CMMs due to the problems related to object deflection and probing limitations [28], but is not a problem for CT, as no forces are developed on the part during CT scanning. Non-contact optical methods have certain limitations in terms of accuracy for the measurements of 3D features [29]. Another advantage is measurement of high aspect ratios, which is, e.g., not possible by means of optical instruments. A common means of quality assurance for newly manufactured parts is a 3D geometry comparison (a so-called actual/nominal comparison), where the actual measurement of geometry by CT is compared with reference data and/or CAD data. As a result, detailed deviations of the product are visualised.

Due to a large number of influence quantities occurring in the whole CT process, and the fact that CT systems are multi-purpose measuring devices, measuring uncertainties are in many cases unknown, and thus the measurement traceability cannot be assured. Issues concerning CT traceability will be discussed in chapter 3. When using CT, measurement capability is reduced due to measurement errors, e.g., image artifacts. According to [15] an artifact is a "discrepancy between the actual value of some physical property of an object and the map of that property generated by a CT imaging process". In other words, artifact is something in an image that does not correspond to a physical feature in the test object. Problem concerning image artifacts is one of the recent topics in CT metrology. Several studies document that artifacts in CT images have a great influence on dimensional measurements [24, 30]. Among artifacts which mostly occur in CT images belong beam hardening, scatter radiation, ring artifacts, being the physical effects in CT. These appear in the reconstructed volume and cause, e.g., problems in surface determination, and thus measurement errors. Methods dealing with corrections of these unwanted effects are being developed. An overview of image artifacts along with correction techniques is given in [2].

Advantages and disadvantages of using CT for dimensional metrology are summarized in figure 2.19.

|    |    |
|---|--|
| <ul style="list-style-type: none"><li>○ non-destructive</li><li>○ determination of inner and outer geometry</li><li>○ high information density</li><li>○ possibility to scan any surface, shape, color or material up to a certain density and thickness penetrable by X-rays</li></ul> | <ul style="list-style-type: none"><li>○ complex and numerous influence quantities</li><li>○ no accepted test procedures and standards</li><li>○ reduced measurement capability due to measurement errors (artifacts)</li><li>○ measurement uncertainty often unknown → results not traceable</li><li>○ problems with scanning multi-material objects</li></ul> |

**Figure 2.19:** Advantages and disadvantages of CT.



# Chapter 3

## Traceability of CT

In this chapter, first, a brief introduction of measurement traceability in CT metrology is given, followed by discussion on available standards and guidelines for CT. Then, identification and classification of influence factors is presented. Two influence factors - scale errors and beam hardening effect - are described in more details. Different methods for uncertainty estimation in CT are also presented. Lastly, an overview of reference objects for identification, characterization and compensation of errors is shown.

### 3.1 Introduction of measurement traceability in CT metrology

Measurement traceability is a requirement of ISO 9001 [31], ISO 17025 [32] and ISO 14253-1 [33]. According to VIM [34], traceability is defined as: "the property of the result of a measurement or the value of a standard whereby it can be related to stated references, usually national or international standards, through an unbroken chain of comparisons, all having stated uncertainties." This means that to make CT systems traceable measuring instruments, the measurement results obtained by CT have to be traceable to the SI units through chains of calibrations. In CT, due to a large number of influence quantities occurring in the whole CT process chain, and the fact that CT systems are multi-purpose measuring devices, measurement uncertainties are in many cases unknown. This is also because standards and procedures for CT use are still under development [1]. The attempt is to develop reference objects, similar to those used in classical coordinate metrology, for identification of error sources and their subsequent correction.

In coordinate metrology, and for any Coordinate Measuring System (CMS), e.g., CMMs and CT systems, basically two steps are needed for checking the accuracy of the CMS and for obtaining measurement traceability: (i) metrological performance verification and testing, and (ii) assessment of a task-specific measurement uncertainty [35]. Regarding the first mentioned, such a test for comparability of results is described in a German guideline VDI/VDE 2617-13 [36], which is intended for tactile and optical CMMs, but can also be applied for verification of CT systems. In close reliance on ISO 10360-2, the guideline defines procedures for acceptance testing and for the monitoring of length measurement error  $E$  and probing errors (probing error size  $PS$  and probing error form  $PF$ ) when using CT. Regarding the second mentioned, determination of the task-specific uncertainty according to the Guide to the Expression of Uncertainty in Measurement (GUM) [37] requires a model that covers all variables influencing the value of the measurand and that describes the effect on the measurand of any changes in the influencing variables. Measurement uncertainty analysis for CT



measurements must, therefore, contain a clear definition of the measurand to be determined [38].

Measurement traceability in CT can, in general, be achieved following these few steps:

- Development of reference objects (e.g., for correction parameter assessment, task-specific measurement uncertainty assessment, etc.)
- Understanding of influence factors
- Assessing methods for measurement uncertainty

### 3.2 Standards and guidelines for CT

Norms and standards are used in the field of metrology to define criteria assessing the accuracy of measurement results. They mainly provide information whether a measuring instrument is suitable for a specific measurement task. Additionally, they specify accuracy which can be reached by a given measuring system [39].

Standardized procedures and guidelines exist and are well internationally recognized in tactile and optical coordinate metrology. In CT, these procedures and guidelines for testing of CT systems and quantification of error sources are still under development. This is mainly due to the fact, that CT systems still belong to the new generation of measuring systems, CT systems are multi-purpose measuring devices, and as such, yield numerous influence quantities. For this reason, and until the procedures will not be accepted, the traceability of CT measurements cannot be ensured. Therefore, CT users are typically not able to provide appropriate statements of CT measurement uncertainties [40]. It is discussed in [1], that the idea is to use the knowledge from classical coordinate metrology and apply to CT. Thus, e.g., the performance characteristics, such as probing error form  $PF$  (equation 3.1), probing error size  $PS$  (equation 3.2) and length measuring errors  $E$ , defined in ISO 10360-2 [41], shall be defined to characterize properties of the CT system. This idea is also supported in [42], where the authors suggest that the standards for CT should be closely related to the principles of this ISO standard, because of two main reasons: (i) large acceptance of this standard and (ii) because CT systems must give results comparable to measurements from tactile probes. The above mentioned characteristics are described by formulas in the following.

$$PF = R_{\max} - R_{\min} \quad (3.1)$$

where  $PF$  is the span of the radial deviations of the measurement points from the calculated regression sphere. This corresponds to the difference between the maximum  $R_{\max}$  and minimum  $R_{\min}$  distances from the probing points to the centre of the regression sphere. The regression sphere is determined using the least-squares method. The  $PS$  is calculated as the difference between the measured diameter  $D_a$  and the calibrated diameter  $D_r$  of the sphere as follows:

$$PS = D_a - D_r \quad (3.2)$$

For determination of the length measurement error using ball bars or ball plates, the centres of the two probed spheres shall be calculated for each test length from the probing points through regression analysis. The distance between the two sphere centres is the displayed value  $L_{ka}$  of the test length. In

analogy with VDI/VDE 2634-2 [43], the difference between the displayed value  $L_{ka}$  (test length) and the conventional true value (calibrated sphere distance)  $L_{kr}$  is the sphere distance error  $SD$ , expressed in equation 3.3. This parameter will be used in most of the cases throughout this thesis. In addition to  $SD$  parameter, diameter error  $PS$  and the probing error form  $PF$  are added for expression of  $E$  according to rules described in the standard.

$$SD = L_{ka} - L_{kr} \quad (3.3)$$

The currently available international standards for the use of CT are summarized in table 3.1. These generally cover terminology and theory of CT. Moreover, the VDI/VDE Society for Metrology and Automation Engineering (GMA) is working on defining guidelines describing the state of the art in the field of dimensional measurement using CT in industrial environments. The purpose is to establish outline conditions and methods that ensure comparability and traceability of measurements. The following VDI/VDE 2630 series have been published:

- Part 1.1: Basics and definitions [44]
- Part 1.2: Influencing variables on measurement results and recommendations for computed tomography dimensional measurements [38]
- Part 1.3: Guideline for the application of DIN EN ISO 10360 for coordinate measuring machines with CT-sensors [36]
- Part 1.4: Measurement procedure and comparability [45]
- Part 2.1: Determination of measurement uncertainties in measurements using CT systems (in preparation)

Additionally to the tests performed to specify the accuracy of CT systems, described in a German guide VDI/VDE 2630-1.3 [36], or previously developed guidelines VDI/VDE 2617-6.1 [56] and VDI/VDE 2617-6.2 [57], by evaluating the length measurement errors and probing errors, tests concerning structural resolution shall be carried out and the statement shall be specified together with the accuracy specifications. According to VDI/VDE 2630-1.3, the structural resolution describes the size of the smallest structure that can still be measured dimensionally. Additionally, the structural resolution for dimensional measurements  $D_g$  is specified as the diameter (limit diameter) of the smallest sphere for which the measurement system is able to determine a diameter. The error relative to the calibrated value is stated by the manufacturer. A test method for determining the structural resolution is described in the guideline. Other tests concerning investigation on the structural resolution have been recently published [58, 59]. In [58], the authors found that results of edge radii, a measure for the metrological structural resolution, are in a good correlation with geometrical resolution (unsharpness estimates, discussed also in section 5.2) for CT scans carried out at different magnification levels.

Since CT measurement data in dimensional measurements always undergo a threshold value process to obtain the relevant geometrical information, the structural resolution for dimensional measurements must in principle be distinguished from the structural resolution in the grey scale range of the voxels, as this does not encompass the complete dimensional measurement chain.

**Table 3.1:** International standards for CT.

| International Standard | Reference | Title   |
|------------------------|-----------|---|
| ISO 15708-1            | [46]      | Non-destructive testing – Radiation methods – Computed tomography – Part 1: Principles (2002)   |
| ISO 15708-2            | [47]      | Non-destructive testing – Radiation methods – Computed tomography – Part 2: Examination practices (2002)  |
| EN 16016-1             | [48]      | Non destructive testing - Radiation method - Computed tomography - Part 1: Terminology (2011)   |
| EN 16016-2             | [49]      | Non destructive testing - Radiation method - Computed tomography - Part 2: Principle, equipment and samples (2011)                                  |
| EN 16016-3             | [50]      | Non destructive testing - Radiation method - Computed tomography - Part 3: Operation and interpretation (2011)                                      |
| EN 16016-4             | [51]      | Non destructive testing - Radiation method - Computed tomography - Part 4: Qualification (2011)   |
| ISO/WD 10360-11        | [52]      | Geometrical product specifications (GPS) - Acceptance and reverification tests for coordinate measuring machines (CMM) - Computed tomography (2011) |
| ASTM E 1695-95         | [53]      | Standard test method for measurement of computed tomography (CT) system performance (2006)  |
| ASTM E 1441-11         | [15]      | Standard guide for computed tomography (CT) imaging (2011)  |
| ASTM E 1570-11         | [54]      | Standard practice for computed tomographic (CT) examination (2011)  |
| ASTM E 1672-12         | [55]      | Standard guide for computed tomographic (CT) system selection (2012)  |

### 3.3 Influence factors

One of the reasons why it is difficult to achieve traceability of CT is the big number of factors which influence the overall performance of CT. Studies concerning quantification of influence factors have been carried out by a number of authors [1, 2, 20, 23, 27, 60–62]. The author found it useful to categorize the influence factors into five groups: factors connected with the hardware (X-ray source, rotary table, X-ray detector), software and data processing (3D reconstruction, threshold determination and surface generation, data correction), environment (temperature, humidity), measured object (geometry, material) and operator settings (scanning parameters) (see figure 3.1). The German guideline VDI/VDE 2630-1.2 [38] offers a complete overview of all the influencing factors in CT. In this thesis, only two, the most relevant influence factors selected by the author, will be discussed in more details. These are factors which nearly each user has to deal with when performing dimensional measurements. In particular, scale errors and errors caused by beam hardening effect will be discussed in section 3.3.1 and 3.3.2 respectively.

#### 3.3.1 Scale errors

Determination of scale errors is, in general, an important factor in dimensional metrology. In CT, the correction of scale errors relies in correction of the original voxel size by the use of reference objects, e.g. ball bars or other objects featuring spherical (or cylindrical) shapes, independent of

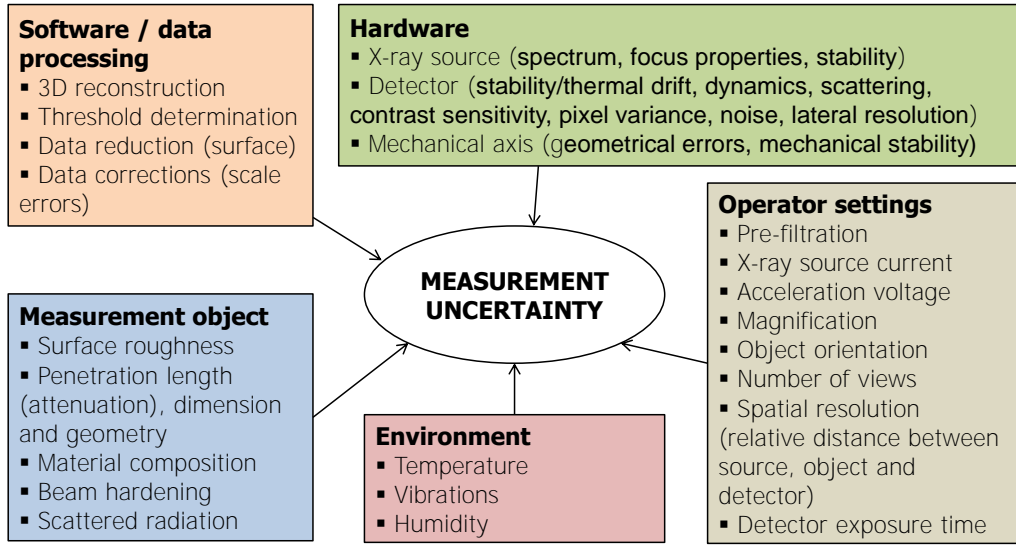


**Figure 3.1:** An overview of influence factors in CT.

threshold. In principle, the correction is done by measuring distance between ball centres. Simply, distance measured by CT is compared to the calibrated distance by, e.g., tactile CMM. The use of these reference objects has specific advantages: the distance between the balls is easily measurable on CT data points as the distance between two fitted spheres. Furthermore, the distance between sphere centres measured using CT systems is nearly independent from the threshold applied during the surface determination. This makes the evaluation of scaling errors very robust. Scale error correction can be done by calculating a correction factor  $s_{\text{vox}}$  as follows:

$$s_{\text{vox}} = \frac{L_{\text{REF}}}{L_{\text{CT}}} \quad (3.4)$$

where  $L_{\text{REF}}$  is reference length measured by, e.g., tactile CMM and  $L_{\text{CT}}$  is actual length measured by CT. The rescaled voxel size  $s_{\text{cor}}$  is obtained by multiplying the calculated  $s_{\text{vox}}$  by the original uncorrected voxel size  $s_{\text{uncor}}$  as follows:

$$s_{\text{cor}} = s_{\text{vox}} \cdot s_{\text{uncor}} \quad (3.5)$$

It was, however, mentioned in [63] that it is possible to perform the correction of the voxel size with known diameter of a feature, in that case of a core hole of a micro gear (assessed by tactile micro CMM measurements). In this thesis, such an approach for correction of the original volume CT data set will be applied, too, to investigate the applicability of this method.

Another important point is that scaling errors occur only in the CT systems where the scales (manipulator system) are not precise, or in other words in the systems which are not corrected for this error. Furthermore, special calibration procedures are required for compensation of this error. It is discussed throughout the thesis, that some of the scanned parts were scale corrected and some not, depending on the system under study.

A schematic illustration of the influence of the correction of the original CT data set for scale errors on

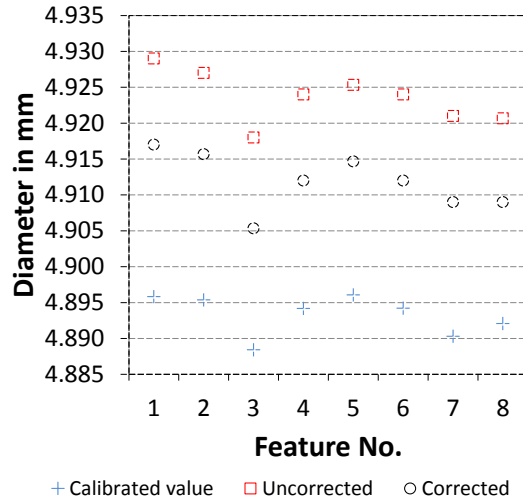


**Figure 3.2:** A schematic illustration of the influence of scale error correction method on diameter measurements. An example of diameter measurements of eight knobs of a Lego brick is shown. A reduction of an error in diameter measurement by approximately  $12\ \mu\text{m}$  can be observed. Still, some unknown residual errors are present.

diameter measurements of a plastic part (Lego brick) is shown in figure 3.2. A reduction of the error (difference between corrected CT data and calibrated values) by approximately  $12\ \mu\text{m}$  was achieved. Still, some unknown residual errors can be observed.

It was investigated in [4] that scaling errors up to 1.01 were observed on different CT systems as relative length measurement errors, i.e., a sample of 100 mm length was measured with a measurement deviation of up to 1 mm. Another observation was realized on an industrial 450 kV 2D-CT system. Scaling errors were found to change over a period of time. This was due to changes in the system geometry. The authors therefore recommended to scan the reference object simultaneously together with the object under study and so to evaluate and correct for scaling errors. A similar observation was made on 50 CT scans of a conventional ball bar (with calibrated distance between sphere centres of 14.7437 mm and nominal sphere diameters of  $\varnothing 2\ \text{mm}$ ), see figure 3.3. Correction factor greater than 1 can be noticed for most of the CT scans carried out at magnification level smaller than 4.8. The correction factor increases nearly linearly with decrease of magnification level, as at smaller magnification levels the  $SOD$  parameter (source-object distance) becomes bigger which gives rise to  $s_{\text{vox}}$ , and the distance between sphere centres is measured shorter (bigger voxel size). A reasonably good fit of values ( $R^2=0.818$ ) was obtained for all the 50 scans, taking into account a great variability of scanning setting parameters (e.g. current, voltage, integration time, number of image averaging, etc.). Taking this information into consideration, a magnification level of approximately 4.8 can be found for  $s_{\text{vox}}=1$ . Thus, in principle, and with the CT system under consideration, if all the CT scans were performed at this magnification level, there would be no further need for scale error correction for CT measurements.

### 3.3.2 Beam hardening

X-ray beam traversing the matter consists of X-rays with a spectrum of different energies. Polychromatic X-ray beams with the lowest energies are preferentially absorbed, as the linear

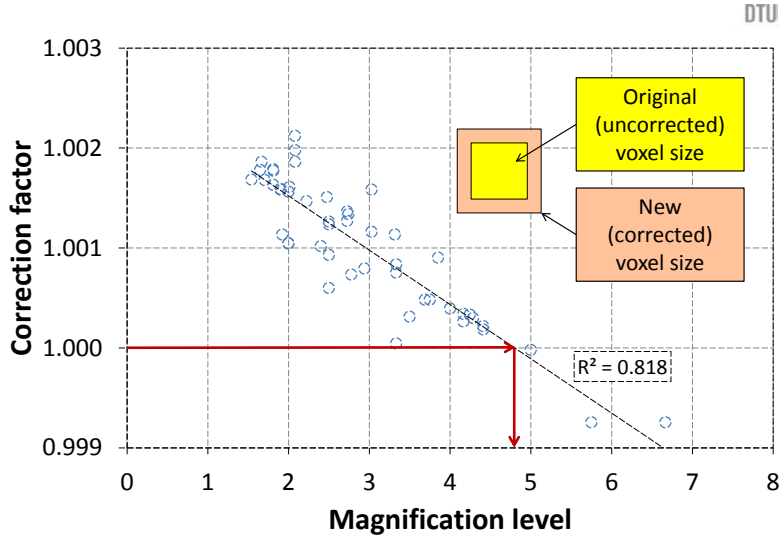


**Figure 3.3:** Correction factor calculated for 50 independent CT measurements of a ball bar with calibrated length of 14.7437 mm. The factor increases nearly linearly with decrease of magnification level.

attenuation coefficient generally decreases with increasing energy. As a consequence, only X-rays with higher energies remain in the beam when passing the matter. These X-rays are less likely to be attenuated. Also, the longer the X-ray paths through the object, the more low energy photons are absorbed, resulting in a more penetrating beam (because the mean energy is increased). In other words, the beam becomes harder, which explains why this is called *beam hardening*. Hence, for polychromatic radiation, the total attenuation is no longer a linear function of object's thickness. If this non-linear beam hardening effect is not compensated, the reconstructed images in X-ray CT will be corrupted by artifacts, e.g. edge artifacts, streaks, etc. Beam hardening makes it difficult to interpret the measured data quantitatively because it changes the attenuation. This complicates the threshold determination (workpiece surface) and measurements of density and resolution. Consequently, higher measurement errors are expected if no beam hardening correction is applied.

Artifacts caused by beam hardening can be reduced, or even completely eliminated. The reduction of beam hardening effect can be done in following ways:

- Pre-hardening of the beam using physical filters (aluminium, copper, brass, etc.) (see section 2.2.1).
- Correction before and during image reconstruction.

Beam hardening can be overcome by using smaller samples or samples of lower absorption (e.g. plastics). To avoid the beam hardening effect totally, monochromatic radiation is used [64, 65]. Such radiation is provided by synchrotron and is sometimes called *synchrotron radiation*. Typical characteristic curves for monochromatic and polychromatic radiation can be seen in figure 3.4. It can be noticed that the intensity change is linear for monochromatic radiation (see equation 2.3) while the curve is non-linear for polychromatic radiation (see equation 2.5). The importance of the problem of correcting of beam hardening effect in CT is reported in many research publications, e.g. [9, 13, 19, 24, 65–68].

Two most used methods for correction of beam hardening effect based on a linearisation technique are described in the following:

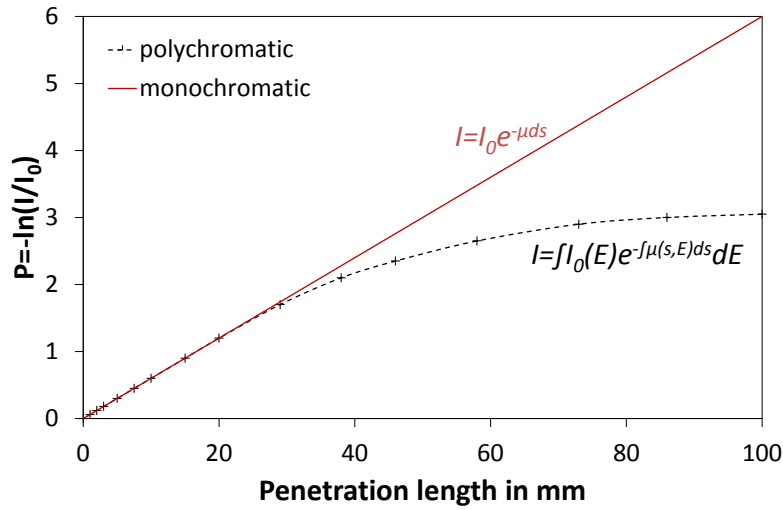


**Figure 3.4:** Mono- and polychromatic radiation curves.  $P$  is a projection value obtained by normalizing equation 2.4 by  $I_0$  and subsequent computation of logarithm of the resulting fraction. Adapted from [69].

- **Based on a reference object [70–72]**

The technique is based on the estimation of the relation between the propagated path length within the specimen and the corresponding measured weakened intensity. The resulting characteristic line is used to compute beam hardening corrected intensity values which allow the reconstruction of an artifact-free CT image. The characteristic line can be determined by the use of a reference object - a step wedge [69]. The step wedge has to be composed of the same material as the specimen. The application of this method has also been investigated at DTU and is presented in the following.

- **Software based**

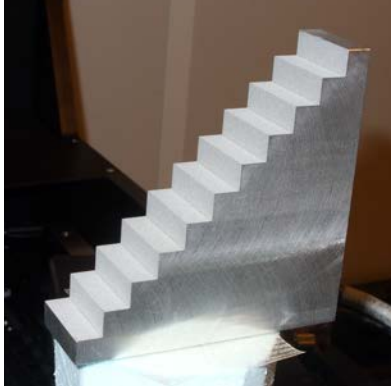
This method is called Iterative Artifact Reduction (IAR) method. It is an iterative process where several post-processing steps are applied to the reconstructed volume in order to calculate a beam hardening correction independently of any reference object. The IAR process includes a model for estimating scattering called Length Based Scattering Approximation (LBSA). The IAR method requires projection data and currently works only for homogeneous specimens. This method was realized in [24].

### **Application of the linearisation technique using a reference object - step wedge - at DTU**

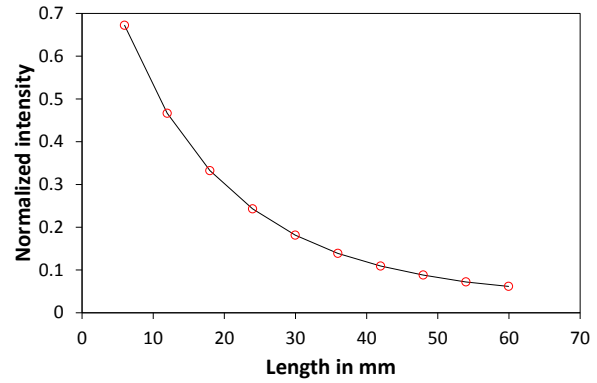
A Matlab (version 7.11.0 R2010b) GUI was developed at DTU for beam hardening correction (BHC) using a step wedge [73]. The step wedge (see figure 3.5(a)) is made of aluminium and features 11 steps with thickness of steps in range from 6 mm to 66 mm. The thickness (penetration length in fact) of individual steps was calibrated using a tactile CMM. The GUI works in the following way:

1. A projection image of the step wedge is acquired in the CT scanner (figure 3.5(b)) with the same scanning settings as the real object, with the steps facing the X-ray source.
2. This image is loaded in the Matlab GUI.
3. Calibration values of the steps are loaded.

4. By selecting a ROI at each step of the projection image of the step wedge in the GUI, a corresponding intensity is measured and saved.
5. A correction curve (figure 3.5(c)) is calculated from the calibrated values of individual steps and corresponding measured intensity.
6. Using the curve and applying it on the uncorrected projection images of the object with the same material results in correct



(a) Step wedge.



(c) Correction curve.

**Figure 3.5:** Principle of beam hardening correction method using a reference object - step wedge.

A screenshot of the GUI is shown in figure 3.6. After all the raw (uncorrected) projection images are corrected applying the correction curve, new projection images are saved and a new reconstruction is required to be done for obtaining new voxel data.

The application of the BHC method using the step wedge was tested on a step cylinder. The object was scanned using Nikon Metrology XT H 225 ST CT scanner at PTB. Figure 3.7 shows uncorrected and corrected (using the GUI) projection images of the step cylinder. A great improvement (correction) for beam hardening effect can be observed. This is also documented on the reconstruction slices, taken in the middle height of the step of the highest penetration length (see figure 3.8).

### 3.4 Measurement uncertainty

Every measurement result should be accompanied by a statement about the measurement uncertainty. In this way, measurement traceability to the SI unit (in our case unit of length - meter) will be ensured. According to the (GUM) [37], measurement uncertainty is "a parameter associated with the result of a measurement, that characterizes the dispersion of the values that could reasonably be attributed to the measurand". A complete statement of a measurement result, following ISO 14253-1 [33], can be then expressed as specified in equation 3.6. Moreover, a dimensional (CT) measurement has to include a correct statement of the task specific uncertainty [35]. Determination of task-specific uncertainty of measurement requires a model that covers all variables influencing the value of the measurand and that describes the effect on the measurand of any changes in the influencing variables [38].



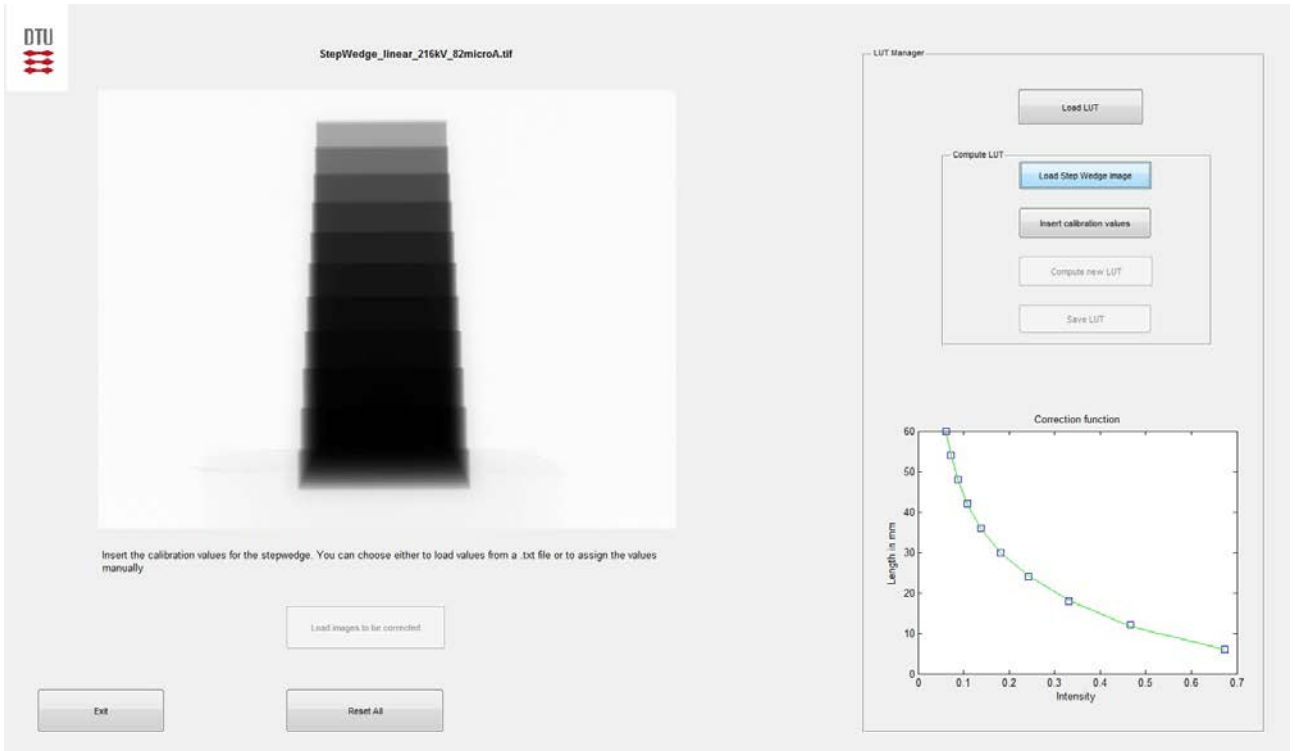
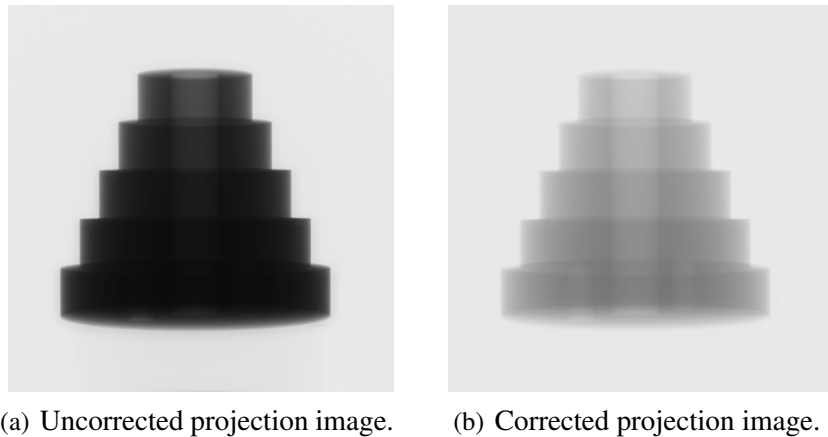


**Figure 3.6:** Matlab GUI for beam hardening correction developed at DTU.



(a) Uncorrected projection image. (b) Corrected projection image.

**Figure 3.7:** Raw (uncorrected) and corrected projection images of an aluminium step cylinder using the developed Matlab GUI.

$$Y = y \pm U \quad (3.6)$$

where  $y$  is a result of measurement and  $U$  is an expanded uncertainty of measurement.

No accepted standards and guidelines for the evaluation of the measurement uncertainty exist up to now [63]. One of the main reasons, already discussed in sections 3.2 and 3.3, is the large amount of influencing factors. Therefore, the statement about the measurement uncertainty cannot be appropriate. The Technical Committee VDI/VDE-GMA 3.33 has been working on uncertainty

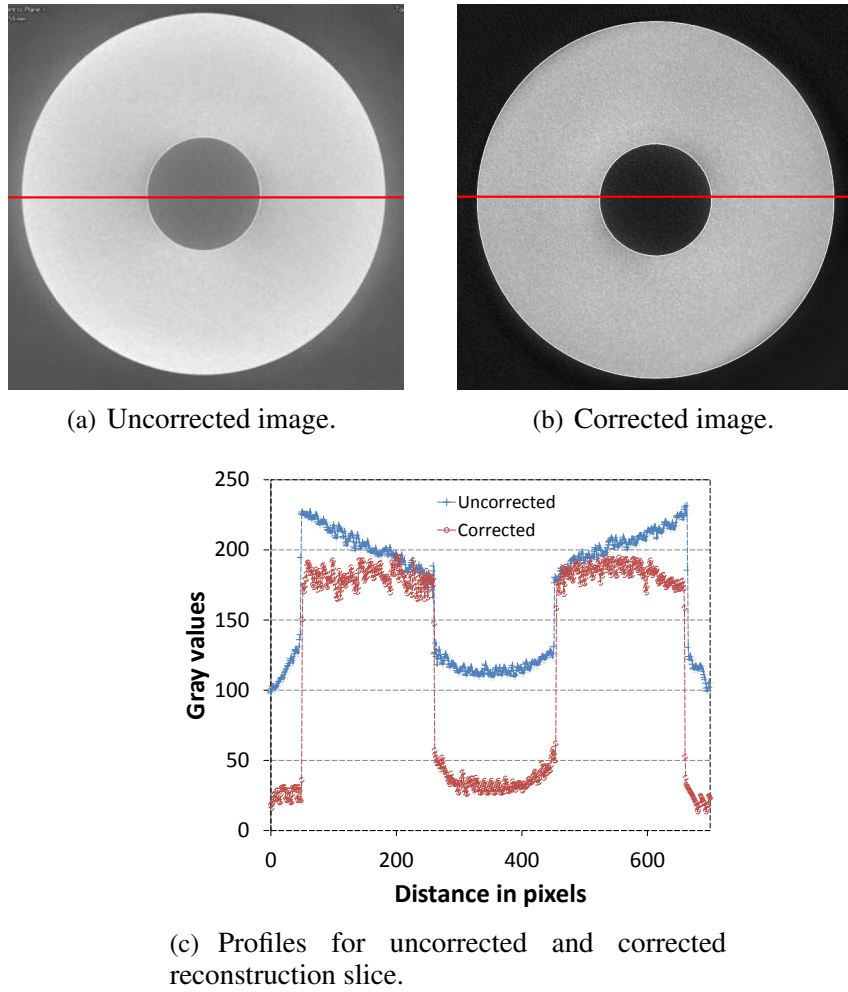


**Figure 3.8:** Reconstruction images of the step cylinder at the highest penetration length. The original uncorrected images are corrected using the step wedge approach in the developed GUI for correction of beam hardening effect. The corrected images become more homogeneous.

evaluation methods for CT measurement data (VDI/VDE 2630-2.1 draft). Anyhow, a few possible methods for the evaluation of measurement uncertainty in CT are listed below:

- Assessment of a model equation - GUM method (JCGM 100:2008) [37], Simplified uncertainty budget ISO/TS 14253-2 (PUMA method) [74].
- Empirical methods - Use of calibrated workpieces or standards ISO 15530-3 [75], Use of multiple measurement strategies in calibration artefacts ISO/DTS 15530-2 [76].
- Computer simulation - Suppl. 1 to GUM (JCGM 101:2008) [77], VDI/VDE 2617-7 [78] and ISO/TS 15530-4 [79].
- Combination of mentioned methods.

In the following, the above mentioned methods for uncertainty evaluation are described.

The general method for estimation of measurement uncertainty is outlined in the GUM. However, due to many complex influence quantities in CT, establishment of an equation for uncertainty estimation according to the GUM requires knowledge of all the uncertainty sources and thus is a challenging task. The individual uncertainty components are then combined in a model function. The estimation of measurement uncertainties is divided into two types:

- **Type A uncertainty:** is estimated by statistical analysis of observations (usually from repeated readings).
- **Type B uncertainty:** is calculated for an estimate which has not been obtained from repeated observations, but from assigned probability distributions, from previous measurement data, from experience with or general knowledge of the behaviour and properties of relevant materials and instruments, from manufacturer's specifications, from data provided in calibration and other certificates, from uncertainties assigned to reference data taken from handbooks

The overall uncertainty may be evaluated through the substitution method, adapting the approach described in ISO 15530-3. Since the substitution method is based on the use of calibrated workpieces, traceability of CT measurements can be established by comparison with (calibration) results obtained from a more accurate measuring system (e.g. tactile CMM) [20], where measurements carried out on the CMM are set as reference [80] (few points on the comparison of measurements using CMM and CT were discussed in section 2.3.5). This approach requires performing a series of repetitive measurements (20 measurements are recommended by the standard) under the same or similar conditions which are used in the production. Therefore, such a reference object has to be as close as possible in size, geometry and material with respect to the real workpiece [81]. The application of the substitution approach was used, e.g., in [1, 61, 82–84]. In practice, such a procedure is time consuming and might be very costly. Therefore, it is suggested in [61] to use a safety factor which is based on a Student-*t* distribution (with higher number of repeated measurements this factor becomes smaller). So, by multiplying the empirically obtained standard deviation with this factor, we ensure that the measurement uncertainty is not underestimated. The application of the substitution method is also presented in this thesis (see section 6.5). As discussed by many researchers, a critical point when applying the substitution method for uncertainty estimation is how to correctly treat the systematic effects. The GUM suggests to correct the measurement results for any systematic effects. Recently, there has been a change in the assessment of the uncertainty calculation. In particular, in ISO/TS 15530-3:2009 [85] the bias contribution *b* was considered, being squared under the square root together with other uncertainty contributors (an example of this application is used in section 6.3). However, in the latest version of the ISO 15530-3:2011 [75] the formula describing the assessment of measurement uncertainty is rewritten according to equation 3.7. Here, the bias is assessed separately (as shown in equation 3.8) and only a residual bias contribution  $u_b$  is stated.

$$U = k \sqrt{u_{\text{cal}}^2 + u_p^2 + u_b^2 + u_w^2} \quad (3.7)$$

where *k* is coverage factor (*k*=2 for an approximated coverage probability of 95%,  $u_{\text{cal}}$  is standard uncertainty associated with the uncertainty of the calibration of the calibrated workpiece stated in the calibration certificate,  $u_p$  is standard uncertainty associated with the measurement procedure,  $u_b$  is standard uncertainty associated with the systematic error of the measurement process evaluated using the calibrated workpiece,  $u_w$  is standard uncertainty associated with material and manufacturing variations.

In cases where the correction of systematic effects is not feasible, or one wants to point out the quantity of the systematic error, the measurement result can be expressed as:

$$Y = y - b \pm U \quad (3.8)$$

where  $b$  is the systematic error (called also *bias*), expressed in the following way:

$$b = \bar{y} - x_{\text{cal}} \quad (3.9)$$

where  $\bar{y}$  is the actual value obtained by, e.g., CT and  $x_{\text{cal}}$  is the calibrated value obtained by, e.g., CMM. Furthermore, figure 3.9 schematically highlights the situation presented in the equation. It can be seen that accuracy and precision are two key quantities which form the complete statement of the measurement result. Precision is the spread of the distribution of repeated measures on a single part, called *precision* (repeatability, reproducibility). Accuracy is the difference between the mean value  $\bar{y}$ , called *accuracy* (Bias,  $b$ ), and the calibrated value  $x_{\text{cal}}$ , considered as a reference value. A more precise and accurate measurement result is one that is closer to the reference value and has a smaller spread.

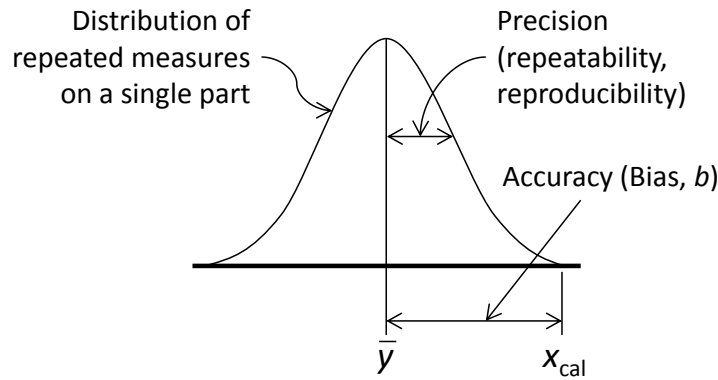


**Figure 3.9:** Precision and accuracy. Random and systematic errors.

PUMA method (Procedure for Uncertainty Management) is based on the concepts of the GUM. The basis of PUMA is to decide on the target uncertainty from experience or investigations. The target uncertainty is the largest acceptable measurement uncertainty based on an economical evaluation of manufacturing and measuring costs. PUMA gives an instruction on how to assess the model equation, taking into account different sources of uncertainty. PUMA is an iterative process for uncertainty estimation - it rates the uncertainty contributors from the most influencing to the least important. This approach may be sometimes time consuming and costly. The general problem of the application of the PUMA method for CT measurements is the fact, that knowledge of the standard uncertainties of all the influencing factors is required [63]. In case of CT, this is sometimes not possible, as it is difficult to provide a complete list of all the influencing factors and to assess their impact on the measurand.

ISO/DTS 15530-2 describes a procedure for estimation of the task specific measurement uncertainty from multiple measurements of the object positioned in different orientations and locations within the measuring volume. The results of CT measurements are, however, strongly dependent on the object's orientation and location in the measuring volume. By positioning the object in different orientations, the properties of the X-ray absorption change. This can be, however, overcome by a

skilled operator, who can position the object in such a way, so that the results of CT measurement will be minimized for effects having negative influence on the measurement result. Thus, only changes within reasonable limits should be applied to orientation and location of the workpiece when performing CT measurements.

Simulation is another method used for the estimation of the measurement uncertainty. Here, as for the GUM, knowledge of all the influencing factors is needed, along with a type of distribution of each factor. Widely used simulation method is Monte Carlo simulation [35]. Examples of the application of this method to estimate measurement uncertainty for dimensional measurements can be found in [24, 60, 61, 81, 86].

A comparison of CT systems - *CT audit* - was carried out and organized by the University of Padova (UNIPD), Italy. The aim was to investigate the metrological performance of 15 industrial CT systems from Europe, America and Asia and to investigate the current practice of dealing with measurement traceability in CT. The specific project objectives were: to deepen the knowledge on CT dimensional metrology, to spread information on available standards and procedures for testing CT systems, to compare different CT measuring systems, to evaluate and compare the participants' measurement and uncertainty evaluation methods, to identify causes of measurement errors and to establish an international network of laboratories using CT systems for dimensional metrology. Four reference objects (CT tetrahedron, Pan flute gauge, 3D calotte cube and QFM cylinder), further described in the following section 3.5, were used in this international project. The results of the intercomparison were published in a number of publications (e.g. [40, 87, 88]). One of the main result of this intercomparison was that participants had problems to properly evaluate the measurement uncertainty. Figure 3.10 presents results from the project, showing methods for uncertainty estimation used by different participants. It can be noticed that there is not only one method for uncertainty estimation of CT measurements. Moreover, almost half of measurement results have  $E_n > 1$ , which revealed an invalid evaluation of the uncertainty associated with the measurement result [89].

Relevant description of existing methods for expression of measurement uncertainty along with discussions related to measurement traceability in CT is, for example, given in [2, 59, 61, 63, 81].

### 3.5 Reference objects

One of the main issues in CT is reduction and correction of systematic errors, which, according to the GUM, have to be always carried out. This is done through the use of calibrated reference objects, similar to those used in classical coordinate metrology. By correcting such errors (e.g. threshold or scale errors), measurement traceability can be partially achieved. Figure 3.11 presents an overview of reference objects which have been developed for these purposes in connection with CT. Their particular use in CT metrology is different, however, some of them are used for the same or similar applications [2, 90]. In the following, different types of reference objects are described, grouped according to their design and use in connection with correction of error sources in CT.

As discussed in section 3.4, one of the currently valid approaches for uncertainty estimation is the application of the ISO 15530-3, a substitution method using reference objects which are similar in size, shape and material composition to the real parts. Such a reference object - a miniaturized single cylinder head [6, 80, 82] (figure 3.11(c)) was developed by Physikalisch-Technische Bundesanstalt

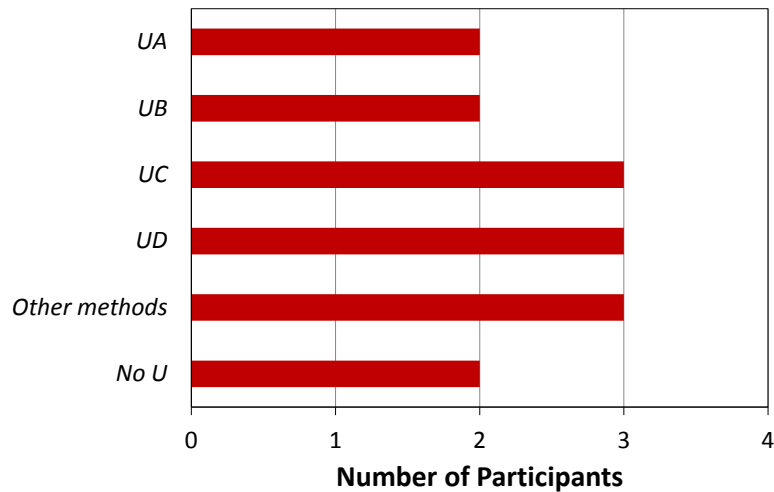


**Figure 3.10:** Evaluation methods for uncertainty estimation used by the participants during the CT Audit project [89]. The symbols in the figure have the following meaning: *UA* is uncertainty budget through analytical calculation of uncertainty contributors, *UB* is evaluation based on the use of similar calibrated items and substitution method, *UC* is evaluation based on the experience of the Participant on similar measurement tasks, *UD* is evaluation based on measuring performance specification stated by the CT system manufacturer, *No U* is that the participant did not state the measurement uncertainties.

(PTB), Germany and Bundesanstalt für Materialforschung und prüfung (BAM), Germany, to check the entire measurement process of industrial CT measurements. This piece is fully dismountable into four segments, each featuring reference points (reference spheres) glued on carbon fibre rods which are accessible for tactile measurements, providing measurement traceability. An example of other object is a sandblasted aluminium cube (figure 3.11(k)) used in [61] to investigate several influence quantities in relation with calculation of the measurement uncertainty.

Step-cylinders with or without a central hole [1] (figure 3.11(a) and figure 3.11(g) respectively) are suited for optimization of a threshold value. This method is based on simultaneous measurement of the inner and outer geometries which are then compared to calibrated measures. These objects are used to analyse material-specific absorption and for adjusting measurement parameters. It allows detecting of the maximum possible material thickness which can be penetrated by a given CT system. The application of step cylinders is described in [36] and suggests several accuracy characteristics to allow for performance verification of CT systems. Step cylinders without inner hole as well as step wedges (linear (figure 3.11(h)) or exponential [69]) can be further used for beam hardening correction. Aluminium hollow cylinders [1] (figure 3.11(b)) developed by PTB, Pan flute gauge (consisting of five calibrated glass tubes of different lengths and supported by a carbon fibre frame) [87] (figure 3.11(e)) and Fibre gauge (includes 12 fibres and 12 holes with their nominal diameters of 125  $\mu\text{m}$ , and fibres having different lengths varied from 350  $\mu\text{m}$  to 700  $\mu\text{m}$ ) [42] (figure 3.11(n)), both developed by UNIPD, can also be used for a precise determination of threshold values.

Commonly used reference objects are those consisting of spheres made of different materials (preferably ruby, alumina, zirconia and steel) allowing point-to-point distance measurements. In most of the cases these objects are glued on or other way attached to carbon fibre rods. Reference objects like Invar 27-sphere gauge (consisting of 27 ruby spheres on carbon fibre rods) [39] (figure 3.11(f))

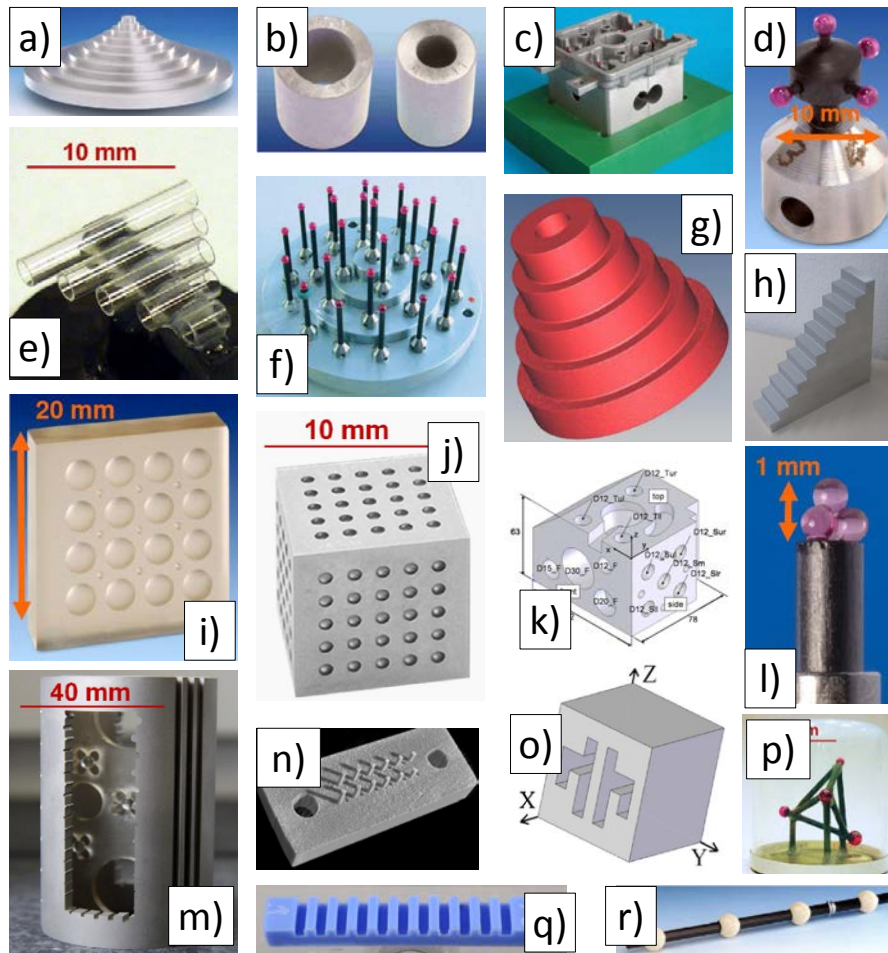


**Figure 3.11:** An overview of existing reference objects in CT.

being a property of Zeiss, Germany, CT tetrahedron (consisting of four ruby spheres of different diameters, on a carbon fibre frame) [87] (figure 3.11(p)) manufactured by UNIPD, Micro tetrahedron (consisting of four ruby spheres of 0.5 mm in diameter) [91] (figure 3.11(l)), Mini probe [92] (figure 3.11(d)) and ball bar [1] (figure 3.11(r)), last three manufactured by PTB, are all used for scale factor corrections in the CT volume. They are independent of the threshold, since only the centres of spheres are taken into consideration for evaluation of distance measurements. Some of these can also be used for verification of CT system accuracy, i.e., assessment of the Maximum Permissible Error of length measurements ( $MPE_E$ ), as well as for monitoring of errors in the CT volume.

Another, similar reference objects to objects featuring spheres, are those with manufactured spherical calottes. These are calotte plate (consisting of a regular 4 x 4 array of calottes, made of zerodur) [1, 93] (figure 3.11(i)) and 3D calotte cube (consisting of a regular 5 x 5 array of calottes arranged on three planar faces of the cube, made of titanium) [93, 94] (figure 3.11(j)), both objects developed by PTB. These objects can be used for scale error correction and for mapping of 2D ([95]) and 3D anisotropies of the measuring volume.

Other commonly used reference objects are those having plane-parallel surfaces like aluminium

cactus step gauge (with machined internal grooves) [96] manufactured by University of Leuven (KU Leuven), Belgium (figure 3.11(o)) and replica step gauge [97, 98] (figure 3.11(q)) developed by DTU. Both reference objects have internal and external surfaces allowing edge detection (determination of threshold value). Measurement accuracy of both of the reference objects can be assessed uni- and bidirectionally, measuring point-to-point or face-to-face length errors. The cactus step gauge can also easily be manufactured from different materials. The replica step gauge, initially developed for optical scanner verification, can be used for performance verification of CT systems [99]. DTU has manufactured new series of step gauges from PEEK and PPS materials yielding better accuracy as well as stability [100].

The last reference object mentioned here is a QFM cylinder (consisting of a titanium cylinder with several geometrical features and a ball plate with five sapphire balls) [87] (figure 3.11(m)), developed by University Erlangen-Nuremberg (FAU), Germany. This object was among other objects (CT tetrahedron, Pan flute gauge and 3D calotte cube) which were used during the first international intercomparison of CT systems for dimensional metrology [40] organized by the UNIPD, mentioned in the previous section.





# Chapter 4

## Development of reference objects at DTU

As described in chapter 3, the use of the reference objects serves, in general, to correct measurement results for systematic effects, such as scale errors, threshold determination, beam hardening, etc. In this chapter, three reference objects are introduced: *CT ball plate* and *CT tree*, both developed by the author at the laboratories of DTU. The general concept of the two reference objects is similar, however, the application of one of the objects may be more suitable for one problem and vice versa. Their use is presented in chapter 5 and their practical application in chapter 6. The third reference object is an object from a production - *component of a dose engine from an insulin pen* - provided by Novo Nordisk A/S, a company specialized in development of insulin pens. In this chapter, an introduction of the object is given. The object is used in connection with the application of ISO 15530-3 for uncertainty determination of dimensional CT measurements, presented in section 6.5.

### 4.1 CT ball plate

The CT ball plate (figure 4.1) [101] is the first reference object developed by the author at DTU in connection with the metrological performance characterization of CT systems. The object features a regular 5 x 5 array of ruby spheres, which are glued on a carbon fibre plate. The general concept of the CT ball plate is similar to the conventional ball plates [102] and hole plates [103, 104] used in classical coordinate metrology. In our case, the spheres are smaller in size and are made of ruby material compared to ceramic or steel spheres used for the ball plates. Moreover, the spheres are supported by carbon fibre material compared to a firm steel construction used to position the ceramic/steel spheres.



**Figure 4.1:** CT ball plate.

### 4.1.1 Use

The 2 mm thick carbon fibre plate supporting the spheres is a widely used material in CT applications due to its high penetrability to X-rays. Moreover, as a multi-material object, the carbon fibre does not produce any image artifacts in the reconstructed volume. The CT ball plate can be considered as a multi-purpose reference object enabling to measure 300 sphere-to-sphere distances at the same time (5 x 5 array of 25 spheres). The main applications of the object are:

- Performance characterization of industrial CT scanners.
- Determination of measuring errors in the CT volume.
- Geometrical correction of CT data, e.g., scale errors.

### 4.1.2 Manufacture

The object features a regular 5 x 5 array of ruby spheres with a nominal diameter of  $\varnothing 5$  mm and a very low form error (sphericity of 0.0006 mm). The spheres are glued on a 2 mm carbon fibre plate using a two-component epoxy resin, ensuring long-term stability of the position of the balls. Since the balls are glued manually, conical holes were cut in the plate to achieve a more precise distribution of the balls on the plate. The nominal pitch between sphere centres is 10 mm. It shall be noted that it is not necessary to achieve a perfect distribution of the spheres on the plate as the center coordinates of the spheres are calibrated using a tactile CMM. An aluminium plate is glued in the corner of the plate for identification of sphere 1 (see figure 4.1).

### 4.1.3 Calibration

The calibration of the CT ball plate was carried out using two tactile CMMs: a Zeiss OMC 850 (further only OMC) and a Zeiss UPMC 850 CARAT (further only CARAT) at the laboratory of DTU. The two CMMs feature different accuracy and thus, differences in the calibration, including both the measurands and associated uncertainties, are expected. In the following, calibration procedure, results of the calibration and comparison between the two CMMs are described.

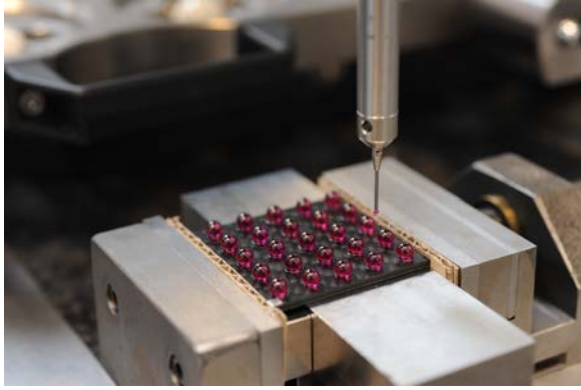
#### **CT BALL PLATE CALIBRATION USING OMC TACTILE CMM**

The maximum permissible error (MPE) of the OMC is  $MPE=(3+L/250) \mu\text{m}$  ( $L$  in mm). A static probe head and a probe of diameter  $\varnothing 1.5$  mm with 21 mm long stylus were used. Temperature was measured throughout the whole calibration process to be  $19.5 \pm 0.8^\circ\text{C}$ . Due to the coefficient of thermal expansion (CTE) of the carbon fibre plate to be  $0 \text{ K}^{-1}$ , no compensation of the results for temperature changes had to be done. The measurement setup on the OMC is shown in figure 4.2.

#### **Definition of the coordinate system**

The coordinate system is defined as follows:

- X axis: direction of X axis is given by the line that goes from centre of sphere no. 1 to centre of sphere no. 5. The direction from the origin to sphere no. 5 defines the positive X-axis direction.
- Y axis: plane XY is given by the plane that goes through three centres of sphere no. 1, 5 and 21. As a result, Y axis is located in the XY plane, it is perpendicular to the X axis and its positive direction is from sphere no. 1 to sphere no. 21.



(a) Clamping of the CT ball plate in a vice.



(b) CT ball plate during the traceability transfer.

**Figure 4.2:** Measurement setup for calibration of the CT ball plate using the OMC tactile CMM.

- Z axis: results from X and Y axes, so that the final X-Y-Z reference system is a right-handed Cartesian Coordinate System (CCS).

As a result of the definition given above, coordinates X, Y and Z of sphere no. 1 are set to zero (see figure 4.3).

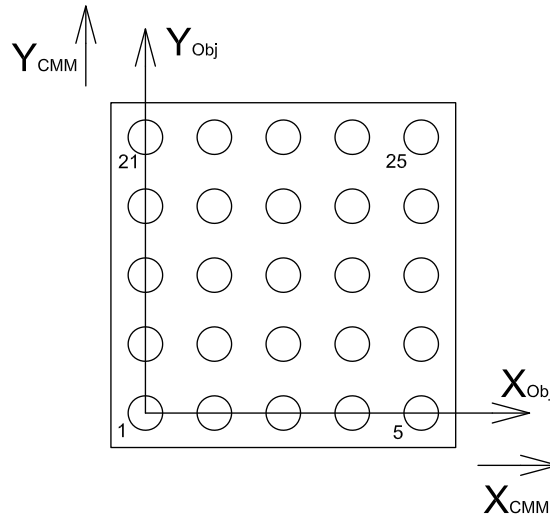


**Figure 4.3:** Alignment of the CT ball plate. Alignment of the object is done with spheres no. 1, 5 and 21 following principles of a Plane-Line-Point (also called 3-2-1) alignment.

The calibration procedure is a slightly modified reversal method, a standard method for DKD calibrations of ball and hole plates, explained in, e.g., [102]. According to [105] (renamed EA-10/05), the *reversal method* is: "A method utilising the measurement of a component and subsequent re-measurement of the component in a different orientation which is designed to cancel out errors associated with the measurement system and reveal errors associated with the component." The method consists of two steps: step 1 is the actual reversal method and step 2 is traceability establishment with the use of a reference object. In step 1 of the procedure, the plate is measured in four different positions in the working space (determined by rotating the plate). By averaging

the center coordinates of the spheres/holes, elimination of the CMM errors can be done, or at least minimized.

The adapted calibration procedure of the CT ball plate is done in the following two steps:

Due to the fact that a full DKD calibration could not be used, as the CT ball plate cannot be flipped in all four positions, the object is measured in two positions in step 1 of the procedure: D0 and D180 (figure 4.4), defined by turning of the plate on the CMM table by 180°. In both positions, three repeated measurements are realized. All 25 spheres are measured in the two positions, centres of the spheres, their diameters and form errors are recorded. By averaging the coordinates of all sphere centres in the workpiece coordinate system, and by performing repeated measurements, some errors of the CMM can be eliminated, or at least minimized. In each of the two positions, two measurements are performed: First, measurement in counter-clockwise (spiral-in) and second, measurement in clockwise (spiral-out) spiral sequence measurement strategy is followed, see figure 4.5. By averaging the results of the spiral-in and spiral-out measurements, thermal drift and hysteresis effects can be identified and eliminated. 25 points are probed on each sphere of the CT ball plate, following procedure described in [57] (see figure 4.6). The points are approximately equally distributed over a top hemisphere of the sphere. The decision for the application of the 25-point measuring strategy is to acquire a reasonable amount of points using CMM, as in CT a big amount of points (e.g. 1000 points) is generally considered for evaluation.

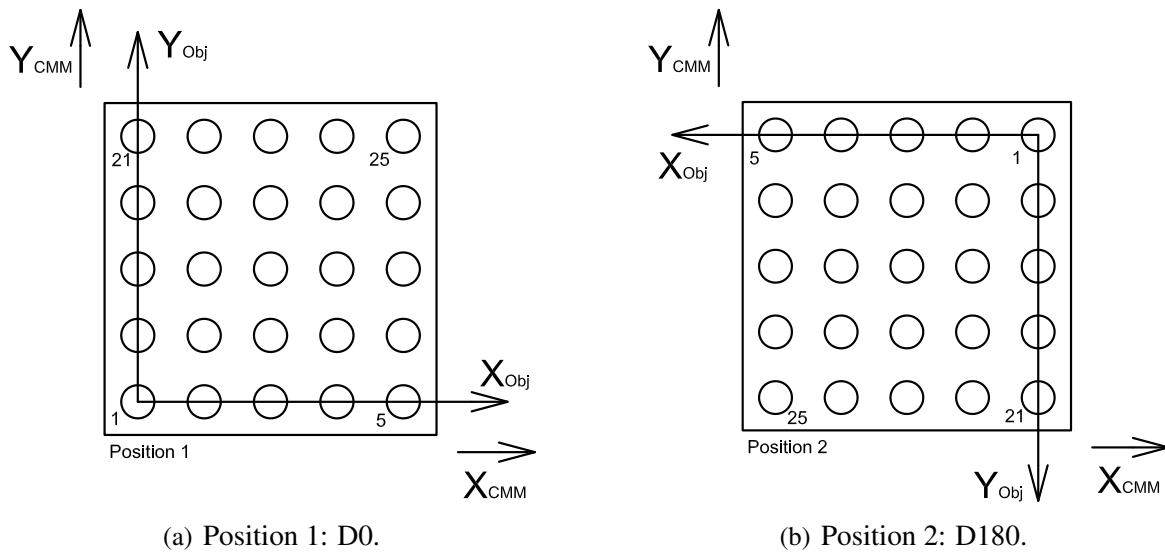


**Figure 4.4:** Two positions of the CT ball plate in step 1 of the calibration procedure.

Step 2 of the calibration procedure is determination of the scale errors. This is done to establish the traceability of the measurement by measuring spheres of the CT ball plate in X and Y directions of the workpiece coordinate system. Re-measurement of the CT ball plate is done after step 1 of the calibration procedure, when the CT ball plate is placed close to a reference object which is used for the traceability transfer (in our case a standard ball plate). Spheres no. 11 and no. 15 of the CT ball plate in one direction (D0) and spheres no. 3 and no. 23 in the second direction (D90, when the object is turned by 90° in counter-clockwise direction) are measured together with two spheres of the

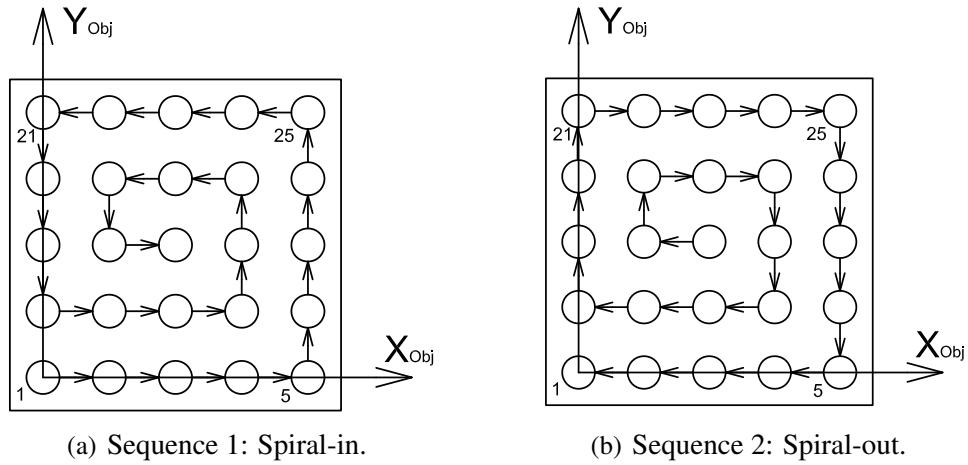


**Figure 4.5:** Measurement sequence spiral-in and spiral-out in each plate position in step 1 of the calibration procedure.

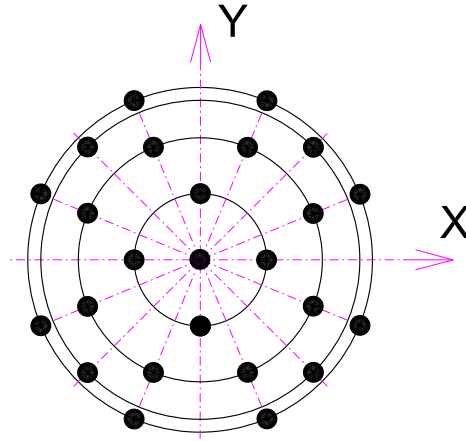


**Figure 4.6:** 25-point probing strategy during step 1 and step 2 of the calibration procedure using OMC applied on all the 25 spheres of the CT ball plate (top view).

ball plate in only one direction of the CMM coordinate system (figure 4.7). By comparing the two measured distances (i.e., measurements of the CT ball plate and the ball plate), scale errors can be corrected. Spheres A and B in figure 4.7 represent two neighbouring spheres (sphere no. 11 and no. 12) of the ball plate with a nominal distance between sphere centres of 83 mm. The step 2 of the calibration procedure was run in the following five sequence runs:

- Sequence 1: Length of the ball plate ( $L_{REF}$ , sphere 11-12) - Length of the CT ball plate ( $L_{CT}$ , sphere 11-15)
- Sequence 2: Length of the CT ball plate ( $L_{CT}$ , sphere 15-11) - Length of the ball plate ( $L_{REF}$ , sphere )
- ...

Probing strategy in step 2 of the calibration procedure applied on the ball plate is in accordance with the DKD procedures described in [106], and relies in taking 13 points on the sphere (see figure 4.8).

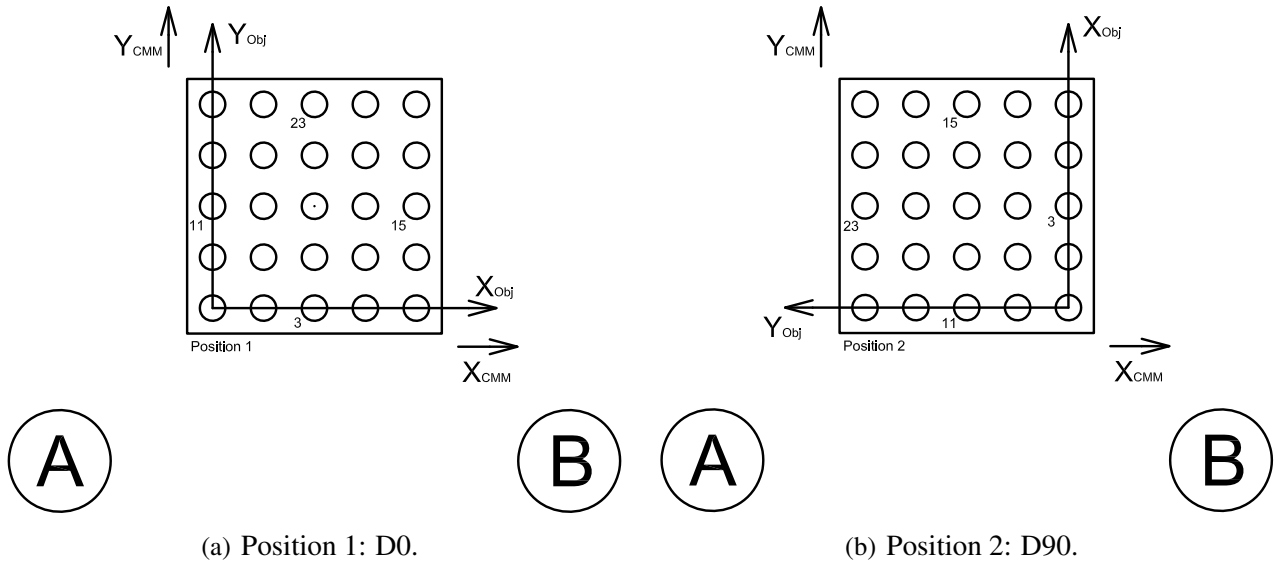


**Figure 4.7:** Length transfer during step 2 of the calibration procedure of the CT ball plate using two spheres (A and B) of the ball plate as a reference length. During step 2 of the procedure the CT ball plate is measured in two positions (D0 and D90), while the ball plate remains in the same position.

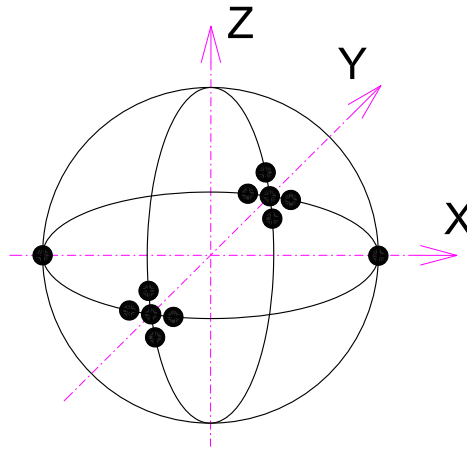


**Figure 4.8:** 13-point probing strategy during step 2 of the calibration procedure applied on two spheres of the ball plate.

Calibration was reproduced in three days. Reproducibility was assessed by measurements in different days and by re-positioning of the plate in the fixture.

#### **Estimation of calibration uncertainty**

Calibration uncertainty was estimated for five selected measurands: diameter and form of the spheres and X-, Y- and Z-coordinates of sphere centres, according to equation 4.1.

$$U_{\text{cal,OMC}} = k \sqrt{u_{\text{cert}}^2 + u_{\text{tran}}^2 + u_{\text{repeat}}^2} \quad (4.1)$$

where  $k$  is coverage factor ( $k=2$  for a confidence level of 95%),  $u_{\text{cert}}$  is standard uncertainty from the calibration certificate of the ball plate, calculated as  $u_{\text{cert}}=U_{\text{cert}}/k$ ,  $u_{\text{tran}}$  is standard uncertainty

during the traceability transfer (during step 2 of the calibration procedure) measured in two positions (D0 and D90), calculated as a maximum standard uncertainty for measurements in three days:  $u_{\text{tran}} = \text{MAX}(u_{\text{tran},i})$  for  $i=1,2,3$ , calculated for each of the two positions,  $u_{\text{tran},i} = s / \sqrt{n}$  where  $s$  is standard deviation of three repeated measurements (the five sequence runs are averaged) and  $n$  is number of measurements,  $u_{\text{repeat}}$  is standard uncertainty of measurement repeatability in two positions (D0 and D180), calculated according to equation 4.2.

$$u_{\text{repeat}} = \sqrt{u_{\text{D0}}^2 + u_{\text{D180}}^2} \quad (4.2)$$

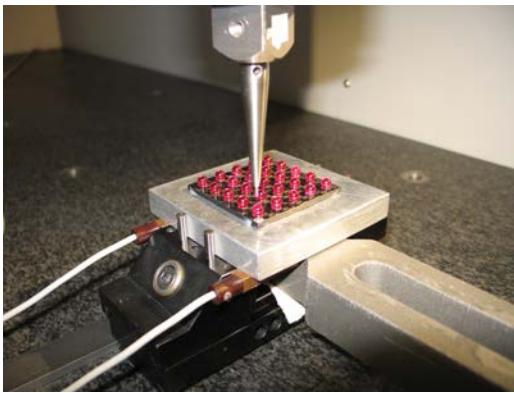
where  $u_{\text{D0}}$  and  $u_{\text{D180}}$  are calculated according to equation 4.3, considering measurements of all 25 spheres.

$$u_{\text{D0}} = u_{\text{D180}} = \sqrt{\sum_{i=1}^m \frac{s^2}{n}} \quad (4.3)$$

where  $m$  is number of spheres of the CT ball plate ( $m=25$ ),  $s$  is standard deviation of reproduced measurements (standard deviation of average values obtained from three repeated measurements carried out in each day of calibration in positions D0 and D180 respectively) and  $n$  is number of measurements ( $n=3$  representing three days of calibration).

### **CT BALL PLATE CALIBRATION USING CARAT TACTILE CMM**

The maximum permissible error (MPE) of the CARAT is  $\text{MPE} = (0.4 + L/900) \mu\text{m}$  ( $L$  in mm). A dynamic probe head, a probe of diameter  $\varnothing 2$  mm and a conical 55 mm long stylus were used. A probing force of 0.05 N was applied. Temperature of the environment was measured throughout the whole calibration process to be  $20 \pm 0.5^\circ\text{C}$ . Due to the CTE of the carbon fibre plate to be  $0 \text{ K}^{-1}$ , no compensation of the results for temperature changes had to be done. The measurement setup on the CARAT is shown in figure 4.9. The object was glued in its four corners to an aluminium plate which was clamped in a fixture, ensuring high stability during the calibration. As can be seen in the figure, the fixture is guided along the X-axis eliminating deviations in the axis.



(a) Positioning of the CT ball plate on an aluminium plate.



(b) CT ball plate during the traceability transfer.

**Figure 4.9:** Measurement setup for calibration of the CT ball plate using the CARAT tactile CMM.



Definition of the coordinate system was the same as for calibration on the OMC. Alignment of the object was done in two steps: first, a rough alignment and then fine alignment were performed.

Calibration procedure was carried out in two steps, as already described in the case of OMC, however, the following points of the calibration procedure were modified:

- Measurements of the CT ball plate in position D0 was performed five times and measurements in position D180 was performed three times (because of high repeatability of the CARAT).
- Probing strategy in step 1 of the calibration procedure is in accordance with DKD procedures described in [106], and relies in taking five points on the sphere (four at the equator and one at the pole) as indicated in figure 4.10. Only five points are taken on the sphere due to the fact that the spheres feature very small form errors, and because of the high accuracy CMM employed.
- During the step 2 of the calibration procedure (traceability transfer), sphere no. 4 and 5 of the ball plate were measured.
- Six sequence runs on the ball plate and six sequence runs on the CT ball plate were carried out during the step 2 of the calibration procedure (traceability transfer). This procedure was repeated three times.
  - Sequence 1 (ball plate):  $L_{REF}$ , sphere 4 -  $L_{REF}$ , sphere 5
  - Sequence 2 (ball plate):  $L_{REF}$ , sphere 5 -  $L_{REF}$ , sphere 4
  - ...
  - Sequence 1 (CT ball plate):  $L_{CT}$ , sphere 11 -  $L_{CT}$ , sphere 15
  - Sequence 2 (CT ball plate):  $L_{CT}$ , sphere 15 -  $L_{CT}$ , sphere 11
  - ...

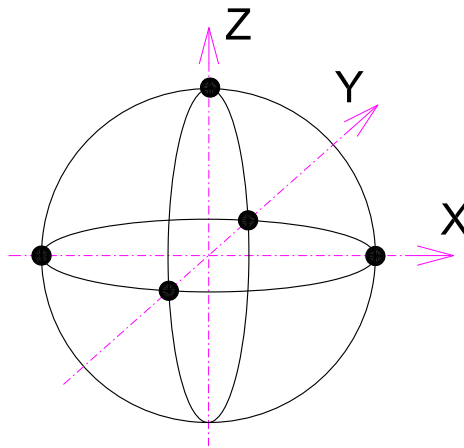


**Figure 4.10:** 5-point probing strategy during step 2 of the calibration procedure using CARAT applied on all the 25 spheres of the CT ball plate.

Due to the fact that the calibration procedure for measurements on the CARAT was slightly different, also the estimation of the calibration uncertainty differs and is presented in the following.

### Estimation of calibration uncertainty

Calibration uncertainty for measurements on the CARAT was estimated for the same five selected measurands as for measurement carried out on the OMC according to equation 4.4.

$$U_{\text{cal,CARAT}} = k \sqrt{u_{\text{cert}}^2 + u_{\text{tran}}^2 + u_{\text{repeat}}^2} \quad (4.4)$$

where  $k$  is coverage factor ( $k=2$  for a confidence level of 95%),  $u_{\text{cert}}$  is standard uncertainty from the calibration certificate of the ball plate, calculated as  $u_{\text{cert}}=U_{\text{cert}}/k$ ,  $u_{\text{tran}}$  is standard uncertainty during the traceability transfer (during step 2 of the calibration procedure) measured in two positions (D0 and D90) and calculated for each of the two positions,  $u_{\text{tran}} = s/\sqrt{n}$  where  $s$  is standard deviation of repeated measurements (the six sequence runs are averaged) and  $n$  is number of measurements ( $n=3$ ),  $u_{\text{repeat}}$  is standard uncertainty from measurement repeatability in two positions (D0 and D180) and calculated according to equation 4.5.

$$u_{\text{repeat}} = \sqrt{u_{\text{D0}}^2 + u_{\text{D180}}^2} \quad (4.5)$$

where  $u_{\text{D0}}$  and  $u_{\text{D180}}$  are calculated according to equation 4.6, considering measurements of all 25 spheres.

$$u_{\text{D0}} = u_{\text{D180}} = \sqrt{\sum_{i=1}^m \frac{s^2}{n}} \quad (4.6)$$

where  $m$  is number of spheres of the CT ball plate ( $m=25$ ),  $s$  is standard deviation of repeated measurements and  $n$  is number of measurements ( $n=5$  in position D0 and  $n=3$  in position D180).

Table 4.1 presents an overview of those uncertainty contributors taken into account for the uncertainty estimation (equation 4.1 and equation 4.4) of each measurand (marked with symbol "x"). One can notice that not all the uncertainty contributors were considered for the assessment of the calibration uncertainty of each measurand. For example, calibration of the ball plate ( $u_{\text{cert}}$ ) does not include measurements of diameter and form of the spheres and that is why there is no "x" for  $u_{\text{cert}}$  for diameter and form measurements. Also, due to the fact that traceability was not transferred for measurements of diameter, form and Z-coordinates, the standard uncertainty  $u_{\text{tran}}$  was not taken into account for the uncertainty estimation of these three measurands. A special case is for  $u_{\text{cert}}$  for measurements of the Z-coordinate, as Z-coordinates of the ball plate are not calibrated (i.e., they are not part of the calibration certificate). They are, however, estimated by an expert.

**Table 4.1:** An overview of uncertainty contributors taken into account for the estimation of the calibration uncertainty for selected measurands of the CT ball plate.

| Uncertainty contributor | Diameter | Form | X-coord. | Y-coord. | Z-coord. |
|-------------------------|----------|------|----------|----------|----------|
| $u_{\text{cert}}$       |          |      | X        | X        | X        |
| $u_{\text{tran}}$       |          |      | X        | X        |          |
| $u_{\text{repeat}}$     | X        | X    | X        | X        | X        |

Measurement uncertainties were assessed at 95% confidence level for each measurand, taking into account measurement of all 25 spheres. The results of the estimation of the calibration

uncertainties are summarized in table 4.2. It can be seen from the table that the biggest uncertainty contributor is due to the measurement repeatability ( $u_{\text{repeat}}$ ). Measurement uncertainties obtained from measurements using CARAT are smaller compared to OMC by a factor of two at least. This is mainly due to a higher measuring precision (and repeatability) of the CARAT. The application of the probing force may play a big role, too. As mentioned earlier, OMC uses a static probing force, estimated to be approximately 1 N, while CARAT uses a dynamic probing force, which can be varied (in our case a probing force of 0.05 N was used). The application of the probing force for both CMMs is most likely causing lower measuring repeatability (higher standard uncertainty) of Z-coordinate, resulting in standard uncertainty approximately two times greater compared to measurements of X- and Y-coordinates. The application of the measuring force induced on the spheres could possibly lead to a deflection of the carbon fibre plate during the calibration. Another critical point here is, that the actual fixturing of the object was a challenge, too.

**Table 4.2:** Calibration uncertainties from calibration of the CT ball plate, estimated at a 95% confidence interval ( $k=2$ ).  $D$ ,  $F$ ,  $X$ ,  $Y$  and  $Z$  correspond to diameter, form and X-, Y- and Z-coordinates respectively. All values are in  $\mu\text{m}$ .

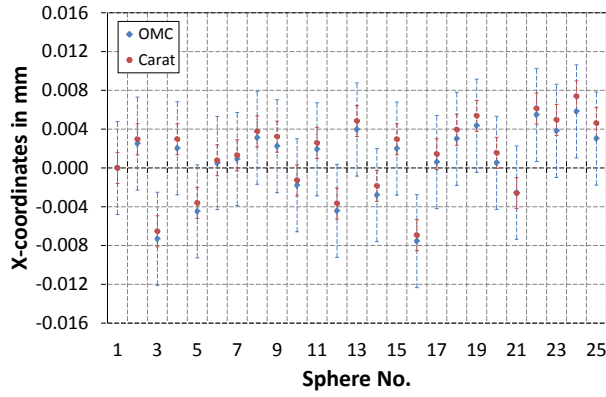
| Uncertainty contributors       | OMC        |            |            |            |            | CARAT      |            |            |            |            |
|--------------------------------|------------|------------|------------|------------|------------|------------|------------|------------|------------|------------|
|                                | $D$        | $F$        | $X$        | $Y$        | $Z$        | $D$        | $F$        | $X$        | $Y$        | $Z$        |
| $u_{\text{cert}}$              |            |            | 0.3        | 0.3        | 0.3        |            |            | 0.3        | 0.3        | 0.3        |
| $u_{\text{tran}}$              |            |            | 0.1        | 0.1        |            |            |            | 0.0        | 0.0        |            |
| $u_{\text{repeat}}$            | 0.4        | 0.5        | 2.4        | 2.1        | 3.9        | 1.2        | 0.7        | 0.7        | 0.6        | 1.5        |
| Expanded uncertainty ( $k=2$ ) | <b>0.7</b> | <b>1.0</b> | <b>4.8</b> | <b>4.2</b> | <b>7.8</b> | <b>2.5</b> | <b>1.4</b> | <b>1.6</b> | <b>1.4</b> | <b>3.1</b> |

Comparison of calibration results from the two CMMs (OMC and CARAT) is shown in figure 4.11. The results of the X-,Y- and Z-coordinates are normalized with respect to their nominal values (in order to fit coordinates of all spheres in a reasonably small range). Average measured values are shown in the figure. A good agreement between the two measuring instruments can be observed, taking into account the estimated calibration uncertainties. The comparability of the results was checked by calculating  $E_n$  values (equation 4.7) of X-,Y-,Z-coordinates for individual spheres. Calculation of  $E_n$  values was done according to [107]. In all cases  $E_n$  value was calculated smaller than 1, showing a very good agreement between the result of calibration by the two CMMs, as well as the stability of the object. Calibration using CARAT was carried out approximately 5 months after using OMC.

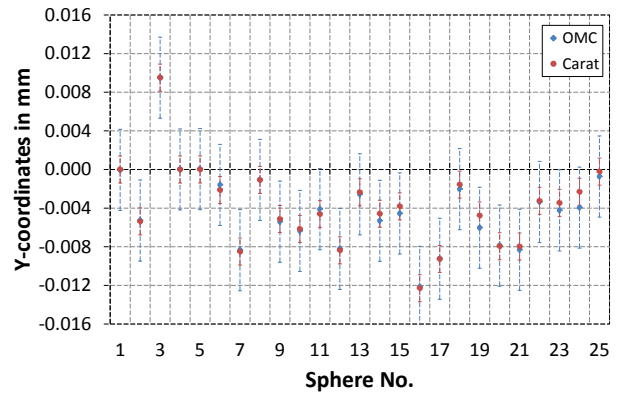
$$E_n = \frac{y_{\text{OMC}} - y_{\text{CARAT}}}{\sqrt{U_{\text{cal,OMC}}^2 + U_{\text{cal,CARAT}}^2}} \quad (4.7)$$

where  $y_{\text{cal,OMC}}$  and  $y_{\text{cal,CARAT}}$  are measurement results from calibration using OMC and CARAT, respectively, and  $U_{\text{OMC}}$  and  $U_{\text{CARAT}}$  are the corresponding expanded uncertainties (calculated according to equation 4.1 and equation 4.4, respectively).

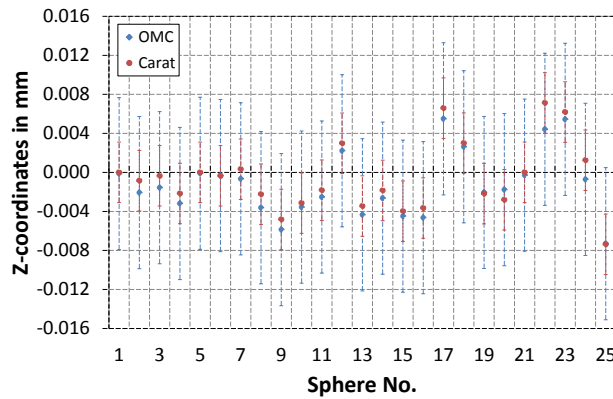
Calibration certificate of the CT ball plate, including the average measured values for diameter, form and X, Y and Z coordinates is attached in the appendix 7.2.



(a) X-coordinate.



(b) Y-coordinate.



(c) Z-coordinate.

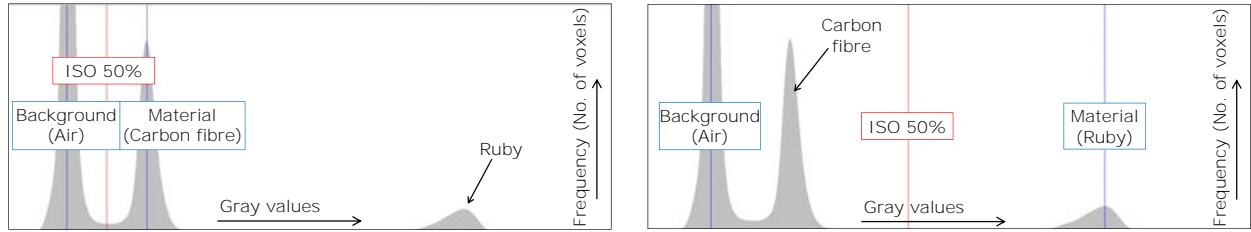
**Figure 4.11:** Comparison of calibration results from two CMMs: OMC and CARAT. The results of the X-, Y- and Z-coordinates are normalized with respect to the nominal values. Average measured values are shown. Error bars represent expanded calibration uncertainties calculated according to equation 4.1 and equation 4.4, summarized in table 4.2.

#### 4.1.4 Procedure for surface determination

Determination of the surface was for all investigations using the CT ball plate in this thesis carried out using inspection software VG Studio Max 2.2 from Volume Graphics, and is done in two steps. Figure 4.12 presents a gray value distribution of the reconstructed volume during individual steps of the procedure for surface determination and data evaluation.

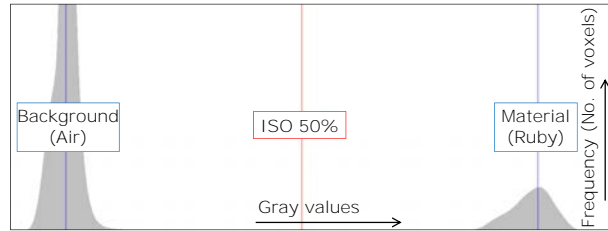
1. Three peaks in figure 4.12(a) correspond to air, carbon fibre plate and ruby spheres. Since the automatic iso-50% (global) method for surface determination did not segment the air and ruby spheres (which are needed for data evaluation), but air and carbon fibre plate, the segmentation was done by manually selecting the ruby spheres on the reconstruction images from different views in the software. In this way, the vertical blue line moves to the peak with ruby material, and iso-50% threshold is automatically determined (iso-50% threshold was discussed in section 2.3.3). Afterwards, an advanced surface method is applied (figure 4.12(b)) for better estimation of the surface. Here, the vertical red line represents a starting value for threshold in adaptive (local) surface determination.
2. Figure 4.12(c) then shows two peaks (gray values) for air and ruby spheres after a selection of a

ROI on upper hemi-spherical surfaces of the balls, as specified in the following section 4.1.5 for data evaluation. In this situation, the peak corresponding to the carbon fibre plate is no longer



(a) Initial situation when gl applied on the reconstructe determined between the air :

1 of the ruby spheres on the ie threshold is determined by spheres.



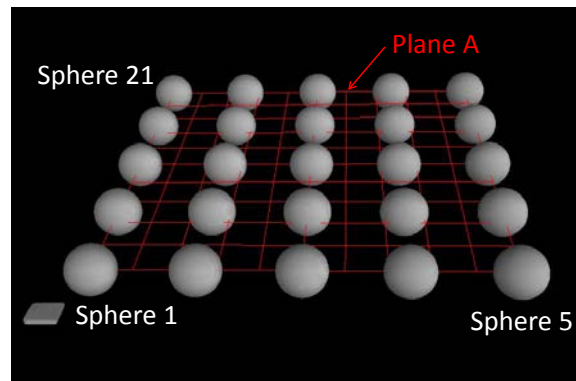
(c) Finally, after the selection of the ROI on the upper-spherical surfaces of the balls, the volume is represented by only two peaks.

**Figure 4.12:** Histogram of gray value distribution of the reconstructed volume of the CT ball plate and determination of threshold value.

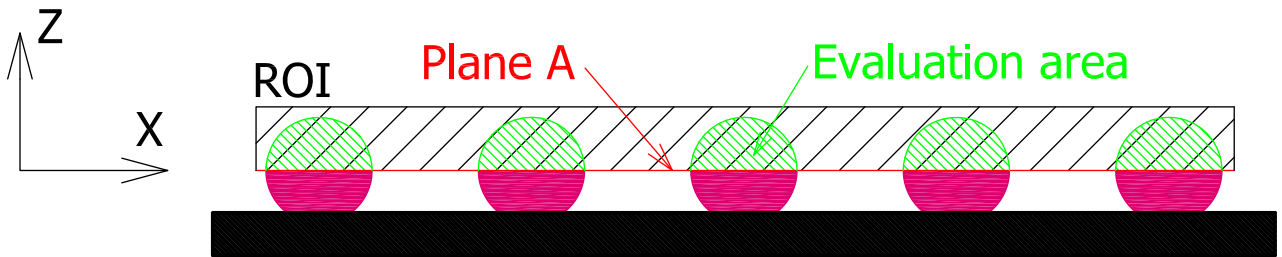
#### 4.1.5 Procedure for definition of evaluation parameters

After the reconstruction of the volume model and determination of the object's surface (see figure 4.13(a)), measuring (fit) points need to be carefully defined on the surface of the spheres. These data (fit) points are those on the upper-spherical surfaces of the ruby balls, defined by selecting a ROI on the original volume model (see the black-hatched marked hemi-spherical surface in figure 4.13(b)), leaving out the part of spheres glued to the plate, which could lead to inaccuracies in measurements. The ROI is determined by Plane A, equivalent to Plane XY of the coordinate system from figure 4.3, and defines the evaluation area (green-hatched color) on the spheres. Figure 4.13(c) shows the result of the selected data set, with only the upper-spherical surfaces considered in the final evaluation. Local point deviations (form errors) are shown in the figure, too.

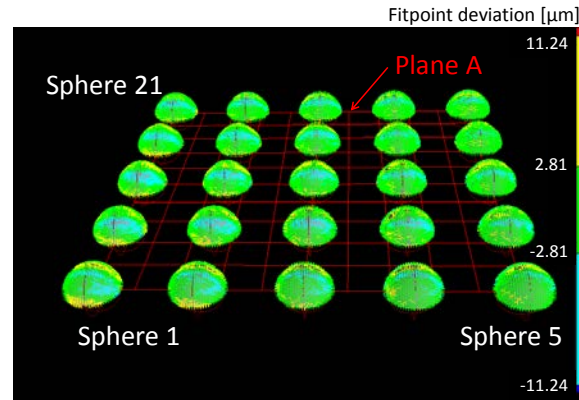
Before selecting the ROI, a rough alignment of the object is carried out according to figure 4.3. Using projection views in the software, the ROI from figure 4.13(b) can be selected quite precisely. After obtaining volume with only upper-spheres shown in figure 4.13(c), a new (final) alignment is made in the same way as described earlier.



(a) Reconstructed volume model of the CT ball plate. A metallic plate in the left bottom corner is used for identification of Sphere 1.



(b) Schematic representation of selection of the ROI (black hatched color) determined by Plane A. The selected ROI and Plane A further



(c) Selected data (fit) points on the upper hemispherical surfaces of the balls after the application of the ROI. The color map shows local form deviations.

**Figure 4.13:** Procedure for correct selection of data (fit) points of the upper-spherical surfaces of the balls by selecting a ROI defined by Plane A (equivalent to Plane XY of the coordinate system from figure 4.3).

Approximately 1000 points are fit to define geometrical primitives ("half" spheres in our case). In this case, the fit points are equally distributed on the sphere surface.

For form measurement, in case of high form deviations, it is recommended to filter the data, which might be due to dust or other ball imperfections. In this case, only 95% ( $P95\%$  value) of all the fit

points are considered, the 5% of the biggest deviations is removed for evaluation.

25 ideal half-spheres are associated with the 25 sets of extracted fit points, which correspond to the 25 hemi-spherical surfaces of the balls. This association is following the least squares method ("Gaussian fitting").

#### 4.1.6 Procedure for scale error correction

The method for correction of the scale errors using the CT ball plate is realized by applying linear regression. By fitting a linear line through the whole data set of 300 length deviations with its intersection in point [0,0], a linear regression coefficient  $a$  is obtained (this coefficient corresponds to the slope of the linear fit line for CT systems). A correction factor  $s_{\text{vox}}$  is calculated according to equation 4.8. This method was first introduced in [95]. The resulting corrected voxel size of the CT data set (voxel model)  $s_{\text{cor}}$  is given by multiplying the correction factor  $s_{\text{vox}}$  and the original voxel size  $s_{\text{uncor}}$ , as it is expressed in equation 3.5 in section 3.3.1.

$$s_{\text{vox}} = \frac{1}{a + 1} \quad (4.8)$$

Figure 4.14 presents an example of uncorrected and corrected data sets after the application of the correction method using the CT ball plate. This is done for  $SD$  parameter, calculated in the uncorrected state according to equation 4.9 (equivalent with equation 3.3). By applying the regression linear coefficient  $a$ , the corrected  $SD$  parameter can be expressed according to equation 4.10.

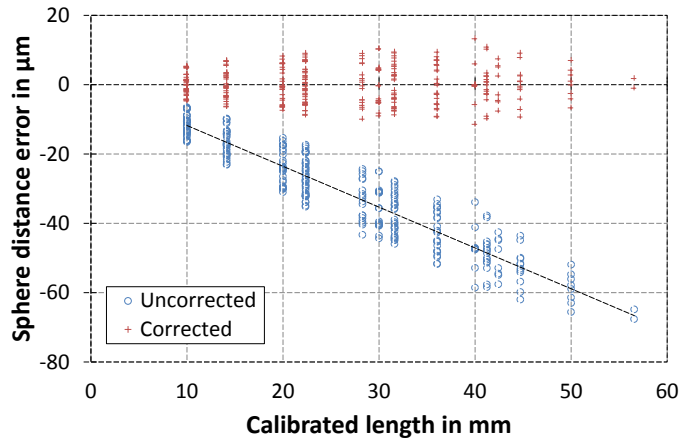


**Figure 4.14:** Scale error correction of voxel data set for calculation of the sphere distance error ( $SD$ ) using the CT ball plate by applying linear regression. The data set before the correction (Uncorrected) and after the correction (Corrected) are shown.

$$SD_{\text{uncor}} = L_{\text{CT}} - L_{\text{CMM}} \quad (4.9)$$

where  $L_{\text{CT}}$  is distance between sphere centres measured by CT and  $L_{\text{CMM}}$  is distance measured by CMM.

$$SD_{\text{cor}} = SD_{\text{uncor}} + a \cdot L_{\text{CMM}} \quad (4.10)$$

## 4.2 CT tree

The CT tree shown in figure 4.15 is another new reference object for performance characterization of CT systems, developed by the author at DTU. The overall concept of this object is basically identical to the above described CT ball plate. The decision for development of this object is argued in section 4.2.1. The object consists of five ball bars (pair of spheres belonging to one rod) of different lengths, nominally ranging from 16 to 40 mm. The designation of the ball bars and associated spheres is shown in figure 4.16. Table 4.3 further

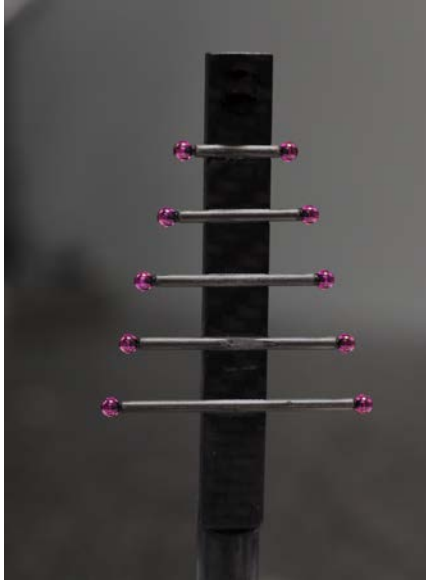


**Figure 4.15:** CT tree.

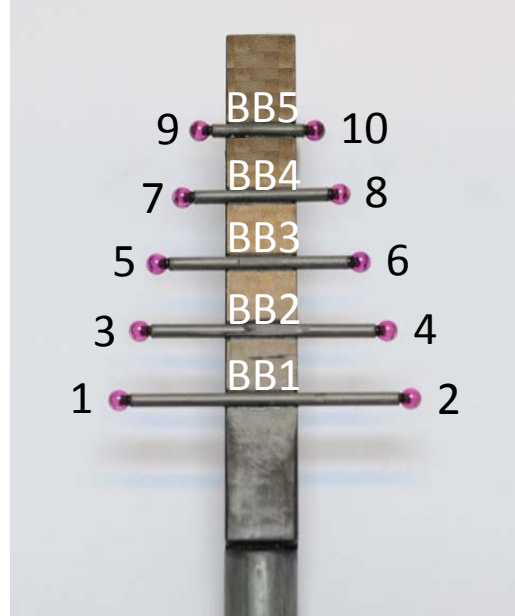


**Figure 4.16:** Designation of the ball bars with associated spheres of the CT tree.

**Table 4.3:** Designation of the ball bars with associated spheres and calibration lengths of the CT tree.

| Ball bar No. | Symbol | Calibration length in mm | Sphere couple No. |
|--------------|--------|--------------------------|-------------------|
| 1            | BB1    | 40.1213                  | 1-2               |
| 2            | BB2    | 34.3547                  | 3-4               |
| 3            | BB3    | 28.4855                  | 5-6               |
| 4            | BB4    | 22.2395                  | 7-8               |
| 5            | BB5    | 16.4010                  | 9-10              |

### 4.2.1 Use

Using the CT tree, a total of 45 lengths (sphere-to-sphere lengths) can be evaluated. The general use of the CT tree is in fact similar to the CT ball plate:

- Performance characterization of industrial CT scanners.
- Determination of measuring errors in the CT volume.



- Geometrical correction of CT data, e.g., scale errors, tilt of the rotational axis.

There were several reasons for development of this object. These are argued in the following:

- First of all, as the design of the CT tree suggests it is a simplified version of the CT ball plate.
- The CT tree is calibrated so that both the ball bar lengths and the center coordinates of all the spheres can be used for evaluation (see section 4.2.4).
- Five distinctive ball bar lengths give better (more robust) estimation of a fit for correcting the scaling errors compared to a conventional ball bars featuring two spheres only.
- Any of the ball bar length of the CT tree can be used for voxel size correction, depending on the size of the measuring volume (corresponding to the size of an object under study).
- By vertically spacing the ball bars on the tree trunk of the CT tree gives a possibility to study measuring anisotropies in vertical direction.

#### 4.2.2

All the ba  
di-oxide)  
mm circu  
rectangula  
vertical di  
too. The r

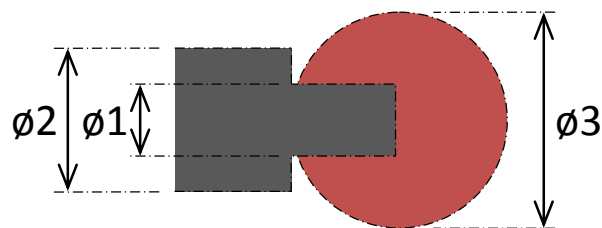
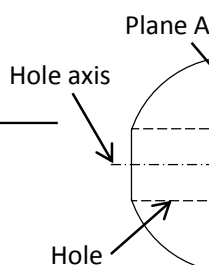


**Figure 4.17:** Schematic picture of a connection of the ruby ball with the carbon fibre rod.

**Table 4.4:** Material characteristics of the CT tree assembly.

| Part name           | Material   | Density                     | Thermal expansion coefficient |
|---------------------|--|-----------------------------|-------------------------------|
|                     |  | $\rho$ in g/cm <sup>3</sup> | CTE in K <sup>-1</sup>        |
| Spheres             | Synthetic ruby monocrystal (Al <sub>2</sub> O <sub>3</sub> ) | 3.99                        | $(5.4 \pm 0.5) \cdot 10^{-6}$ |
| Rods                | Carbon fibre   | 1.5                         | $(0.0 \pm 0.5) \cdot 10^{-6}$ |
| Rectangular bar     | Carbon fibre   | 1.5                         | $(0.0 \pm 0.5) \cdot 10^{-6}$ |
| Cylindrical support | Carbon fibre   | 1.5                         | $(0.0 \pm 0.5) \cdot 10^{-6}$ |



### 4.2.3 Design considerations

Figure 4.18 shows projection images of the CT tree taken at two angular positions, enabling measurement of the minimum and maximum absorption of individual parts of the CT tree. It can be noticed that the absorption measured on the ruby spheres belonging to individual ball bars at the highest penetration lengths, i.e., when the spheres overlap with the carbon fibre material (figure 4.18(a)), is approximately the same, being in the range from 26000 to 29000 gray values. Thus, as the design of the CT tree may seem to be critical due to the extended cylindrical part at the lower end of the object, this can now be excluded. Although the absorption of the spheres at the position overlapping with the carbon fibre material is higher compared to the position of the spheres without any overlap (40000 gray values, see figure 4.18(b)), such a difference in gray values for the few angular positions at which the spheres overlap with the carbon fibre material during scanning will not influence the quality of the final scan, and so the accuracy of dimensional measurements. In a position (orientation) of the CT tree rotated by  $90^\circ$  with respect to figure 4.18(b), the absorption of the BB3 where the two spheres fully overlap (i.e., in the center of the spheres) is approximately 17000 gray values. This situation occurs only for a very few angular positions. The acquisition of the projection images shown here was taken for selected scanning parameters presented in table 4.5.

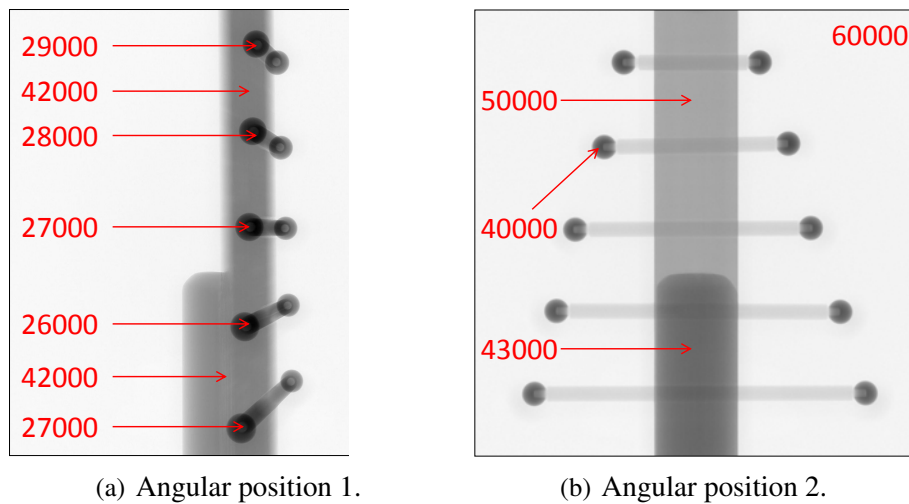


**Figure 4.18:** Absorption (16 bit gray values) of individual parts of the CT tree assembly read from the projection images at two angular positions of the object during CT scanning.

**Table 4.5:** Scanning parameters set for measuring of absorption of the CT tree at different angular positions. The selection of scanning parameters was based on obtaining high contrast CT images.

| Voltage      | Power       | Integration time | No.of image averagings | No.of views | Magnification factor | Uncorrected voxel size  |
|--------------|-------------|------------------|------------------------|-------------|----------------------|-------------------------|
| $U$<br>in kV | $P$<br>in W | $t$<br>in s      | $i_{\text{avg}}$       | $V$         | $m$                  | $s$<br>in $\mu\text{m}$ |
| 110          | 10.65       | 1.415            | 2                      | 1000        | 7.5                  | 26.7                    |

#### 4.2.4 Calibration

The object was calibrated at the ISM3D laboratory in Gijon using a Zeiss Prismo Navigator CMM, according to the procedure T2-04 "Calibration de of 3D Ball Artefacts" of ISM3D.

##### **Definition of the coordinate system**

The coordinate system is defined as follows:

- $u$ -axis: direction of  $u$ -axis is given by the line that goes from centre of sphere no. 1 to centre of sphere no. 2. The direction from the origin to sphere no. 2 defines the positive  $u$ -axis direction.
- $v$ -axis: plane  $uv$  is given by the plane that goes through three centres of sphere no. 1, 2 and 9. As a result,  $v$ -axis is located in the  $uv$  plane, it is perpendicular to the  $u$ -axis and its positive direction is from sphere no. 1 to sphere no. 9.
- $w$ -axis: results from  $u$ - and  $v$ -axes, so that the final  $u$ - $v$ - $w$  reference system is a right-handed CCS.

As a result of the definition given above, coordinates  $u$ ,  $v$  and  $w$  of sphere no. 1 are set to zero (see figure 4.19).

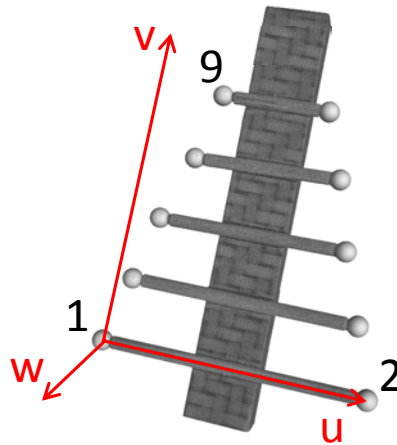


**Figure 4.19:** Definition of the coordinate system.

The calibration procedure consists of a total of 12 measurements performed in three positions with four orientations each within the measuring volume of the CMM (see the setup during the calibration of the CT tree on the CMM in figure 4.20). The multi-orientation measurements are used to average out CMM errors. Average scale factor of the CMM was calibrated by traceable reference objects (gage blocks) in multiple positions and orientations on the CMM. Each sphere of the object was measured by scanning (scanning mode of the tactile probe) more than 1000 points, defined as two circles being off-set from the sphere center in  $u$ -direction of the coordinate system by 0.75 mm.

As a result of the calibration, the coordinates of all sphere centres, the sphere-to-sphere distances (pairs of spheres belonging to one rod), and the form errors of all spheres are obtained.

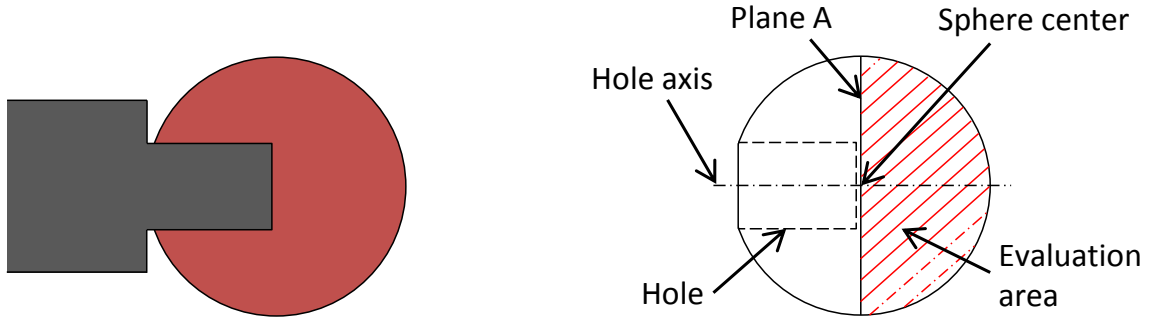


**Figure 4.21:** Schematic representation of the points extracted on the hemi-spherical surface of the ball identified by the red hatched area.

The expanded calibration uncertainty  $U_{\text{cal}}$  ( $k=2$ ) of the calibrated  $u$ -,  $v$ - and  $w$ -coordinates is  $1.2 \mu\text{m}$ . This uncertainty results from the calibration of the CMM, the uncertainty resulting from the repeatability of the measurements, taking into account the number of repetitions, and from the probing process which includes deflections of the object. The uncertainty for the lengths in  $u$ -direction is  $1.0 \mu\text{m}$ , and the uncertainty of form errors is  $0.8 \mu\text{m}$ , being the form error as obtained from a measurement of a reference sphere with very small form error, using a similar strategy as applied for the calibration of the object.

#### 4.2.5 Procedure for surface determination

The determination of the surface is carried out using inspection software VG Studio Max from Volume Graphics, and is done in two steps, identical with the procedure for surface extraction of the CT ball plate introduced in the previous section 4.1.4. This is also due to the fact, that both reference objects comprise of the same two materials (ruby and carbon fibre). Thus, the procedure is not explained for the CT tree.

#### 4.2.6 Procedure for definition of evaluation parameters

A schematic representation of the points extracted on the CT tree can be seen in figure 4.21. These are the points on the hemi-spherical surfaces identified by the red hatched area ("Evaluation area"). It can be seen in the figure that the extracted points on the surface exclude the hole (for connection with the carbon fibre rods), and are determined by Plane A. Plane A is perpendicular to the hole axis and passes approximately through the sphere center (exact definition of the plane in the center of all the spheres of the CT tree is difficult with the software used). The fit points on the surface are selected manually; each fit point attributes another approximately 30 points. Thus, the fit points on the surface are not distributed homogeneously, rather randomly. Approximately 1000 points are fit to define geometrical primitives (half spheres in our case).

For form measurements, only 95% ( $P95\%$  value) of all the fit points are considered, the 5% of the biggest deviations is removed (filtered out) for the evaluation.

10 ideal half-spheres are associated with the 25 sets of extracted fit points, which correspond to the 10 hemi-spherical surfaces of the balls. This association is following the least squares method ("Gaussian fitting").

#### 4.2.7 Procedure for scale error correction

The method for correction of the scale errors using the CT tree is realized by applying linear regression, done exactly in the same way as for the CT ball plate (see section 4.1.6). Here, a line is fitted through the data set of 45 length deviations with its intersection in point [0,0]. The correction factor  $s_{\text{vox}}$  is calculated according to equation 4.8.

### 4.3 Component of a dose engine

Another reference object is a calibrated workpiece - *a component of a dose engine from an insulin pen*, shown in figure 4.22. This component is manufactured by a company Novo Nordisk A/S. For purposes of this thesis, this part is considered as a master piece, on which, the application of the ISO 15530-3 standard is presented in section 6.5. This object is made of brass and is coated with  $5\ \mu\text{m}$  of Ni. There are several reasons for choosing this particular item as the master piece:

- It is a metal part and as such is more challenging for CT scanning due to, e.g., selection of "correct" scanning parameters and related occurrence of image artifacts in the reconstruction volume.
- The component is asymmetric and provides couple of interesting geometrical features, especially at one end of the object.
- The object can show limitations of a CT system under study and perhaps can suggest clues for scanning optimization.
- This object is a part from a production, manufactured by a company involved in the CIA-CT project.



**Figure 4.22:** Master piece: Component of a dose engine from an insulin pen.

### 4.3.1 Calibration

Calibration of the item was carried out using a Zeiss OMC 850 tactile CMM at the laboratory of DTU. The maximum permissible error (MPE) of the CMM is  $MPE=(3+L/250) \mu\text{m}$  ( $L$  in mm). The probe configuration consisted of three probes, one vertical (probe diameter of  $\varnothing 2.0$  mm and stylus length of 45 mm) and two horizontal (probe diameters of  $\varnothing 0.8$  mm and styli lengths of 20 mm). Temperature was measured throughout the whole calibration process. The measurement setup on the CMM is shown in figure 4.23. The object was clamped vertically in a vice. For measurements of the total length, the object was measured in another setup (horizontally, parallel to the CMM table), enabling probing from both sides of the object.

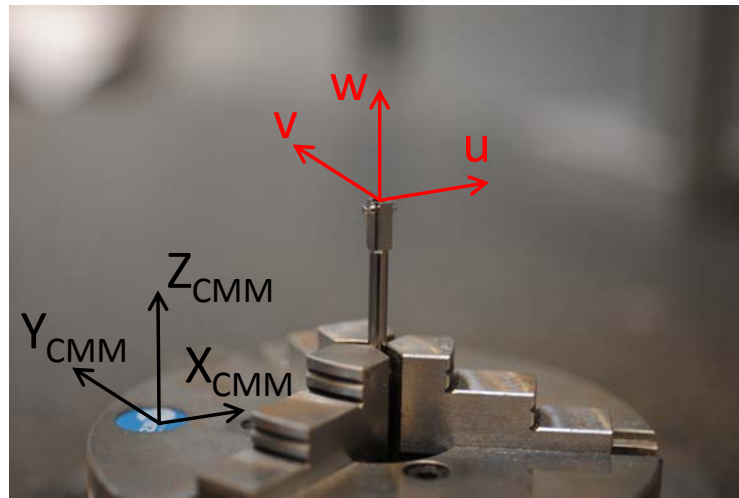


**Figure 4.23:** Measurement setup for calibration of the item on the CMM and definition of the coordinate system.

#### **Definition of the coordinate system**

The coordinate system is defined as follows:

- Primary datum reference (spatial alignment): is determined by a cylinder, defined by two circles at two levels inside the bore of the object (at height 5 mm and 10 mm in negative direction of the  $w$ -axis) (see the coordinate system shown in figure 4.23).
- Secondary datum reference (plane alignment): is determined by a line that goes from centre of circle 1 to centre of circle 2. Circle 1 and circle 2 respectively are defined on two cylindrical pins of the object approximately 1 mm from their ends. The direction from circle 1 to circle 2 defines the positive  $u$ -axis direction. Circle 1 is the one on the left hand side of the operator of the CMM.
- Origin datum reference: the origin is defined in the intersection of the cylinder in the bore and a plane at the top flat surface of the object which defines the positive  $w$ -axis direction.

$v$ -axis results from  $w$ - and  $u$ -axes, so that the final  $u$ - $v$ - $w$  reference system is a right-handed Cartesian Coordinate System (CCS).

### Definition of measurands

Figure 4.24 shows measurands defined on the item. In particular, dimensional and geometrical measure : between two par: rance. In the follc

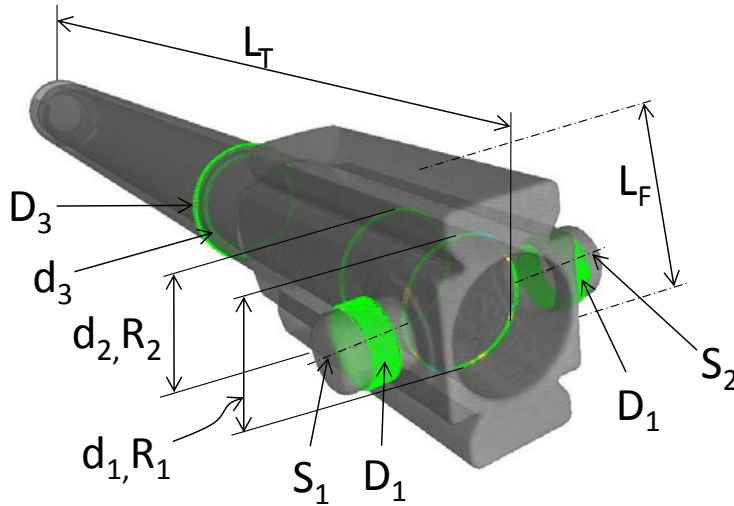


**Figure 4.24:** Definition of measurands.

- 3 x Diameter  $\varnothing 3.4$  mm ( $d_{1,2,3}$ ) and 2 x Roundness ( $R_{1,2}$ ): Three diameters and two roundness measurands are defined by creating Circle features by probing 16 equally distributed points around the hole circumference. Diameters are measured at heights 2 mm, 5 mm and 15 mm in the negative direction of the  $w$ -axis, roundness is measured at heights 2 mm and 5 mm only. Both diameters and roundness are measured using the vertical probe.
- 2 x Diameter  $\varnothing 1.9$  mm ( $D_{1,2}$ ): Two diameters are defined by creating a Circle feature by probing 16 equally distributed points around the hole circumference at a distance of 5.5 mm from the origin in both directions of  $u$ -axis. These are measured using two horizontal probes, each pin is measured by one probe, depending on the setup.
- Diameter  $\varnothing 4.12$  mm ( $D_3$ ): Diameter is defined by creating Circle feature by probing 16 equally distributed points around the hole circumference at height 15 mm in the negative direction of the  $w$ -axis. Diameter is measured using both horizontal probes, each measuring half of the circle. Diameter is then calculated as an average of the two half-circles.
- Length 6.3 mm ( $L_F$ ): Length is defined as a distance between two parallel planes created on the flat surfaces by taking 12 points approximately equally distributed on the surface. The length is measured in the direction of  $v$ -axis. The length is measured using the vertical probe.
- Length 46.4 mm ( $L_T$ ): The total length of the object was measured in another setup, when the object was positioned horizontally in the  $X$ -direction of the CMM coordinate system. Length is defined as a distance between two parallel planes created on both sides of the object, by taking 24 points equally distributed on a flat surface at one end (the cylindrical end of the object), and 8 points approximately equally distributed on the other flat surface of the part (end of the object).

with the two pins). Length is measured in the direction of  $u$ -axis (in the new setup), equivalent with the  $X$ -axis of the CMM coordinate system. And since the alignment of the object is on the outer surface, length is measured in the direction parallel to the cylinder axis. Length is measured using the vertical probe.

- 2 x Symmetry (S): Symmetry axes of the two pins (diameter  $\varnothing 1.9$  mm) is measured with respect to the symmetry plane defined between the two parallel surfaces, where  $L_F$  is measured. Symmetry tolerance is measured using all the three probes.

*Note:* All the features are defined following Least Square Method.

### **Estimation of the calibration uncertainties**

It is discussed in [105] that any CMS shall be calibrated for individual measurement tasks, where both the measurement strategy and measurement conditions are well specified. This is called a task-specific calibration, i.e., measurement uncertainties are estimated for a specific task (measuring strategy, measured feature) individually. A valid approach for the estimation of the task-specific uncertainty is the application of ISO 15530-3, use of calibrated workpieces. The task-specific measurement uncertainties for tactile measurements  $U_{cal}$  of the item were estimated according to ISO 15530-3 [75], as described in equation 4.11.

$$U_{cal} = k \sqrt{u_{ref}^2 + u_p^2 + u_w^2 + u_b^2} \quad (4.11)$$

where

- $k$  is coverage factor ( $k=2$  for a confidence level of 95%)
- $u_{ref}$  is standard calibration uncertainty from the calibration certificate, calculated as  $u_{ref}=U_{ref}/k$ , where  $U_{ref}$  is expanded uncertainty of the reference object stated in the calibration certificate
- $u_p$  is standard uncertainty of the measuring procedure carried out on the calibrated workpiece (working standard, e.g. ring, gauge block), taking into account five repeated measurements
- $u_w$  is standard uncertainty from the manufacturing process consisting of two contributors, (i) temperature-related uncertainty calculated for a deviation of  $\pm 0.5^\circ\text{C}$  and uncertainty of the thermal expansion coefficient (CTE) of the uncalibrated workpiece (component of a dose engine) evaluated from the range of expansion coefficient delivered by the material supplier, and (ii) standard uncertainty associated with the calibration of the part, on which five repeated measurements were carried out (this procedure was repeated three times)
- $u_b$  is standard uncertainty of the residual bias contribution consisting of two contributors, (i) standard uncertainty associated with the difference between a value stated in the calibration certificate and an average measured (calibrated) value, and (ii) the effect of the uncertainty in the CTE value for the calibrated workpiece specified by the manufacturer

Due to the application of the task-specific measurement uncertainty, the accuracy of the CMM was verified individually for different measurands by measuring specific calibrated workpieces (working standards). The following working standards were measured:

- Reference ring diameter  $\varnothing 8$  mm: for verification of measurements of diameter  $\varnothing 3.4$  mm ( $d_1$  and  $d_2$ ) and roundness ( $R_1$  and  $R_2$ )



- Reference sphere diameter  $\varnothing 2.5$  mm: for verification of measurements of diameter  $\varnothing 1.9$  mm ( $D_1$  and  $D_2$ ) and symmetry tolerance ( $S_1$  and  $S_2$ )
- Gauge blocks length 6.3 mm and 50 mm: for verification of measurements of length 6.3 mm ( $L_F$ ) and 46.4 mm ( $L_T$ ) respectively

Calibrated workpieces were, naturally, measured using the same CMM and the same probe configuration as the item. Measuring strategy (e.g. number of probing points, probing direction and orientation) applied on the calibrated workpieces was as close possible to the calibration of the item, as it is also suggested by the standard. Moreover, the same probes were used for measurement of a specific feature during the calibration of the item and for the verification of the CMM using the calibrated workpieces. In other words, if hole diameter  $\varnothing 3.4$  was measured with the vertical probe, the same probe was then used for measurement of the reference ring. The accuracy verification using the calibrated workpieces is straight forward: the difference between the measured dimension and the dimension stated in the calibration certificate is added/subtracted from the measurement result of that particular feature for which the CMM is verified. Verification of the CMM for symmetry measurement was a little bit a challenge - symmetry was measured using the calibrated sphere as follows: symmetry tolerance of the item is assessed by axes of two cylindrical pins with respect to the symmetry plane, defined between two parallel surfaces. Each of the pins is measured using two horizontal probes of diameter  $\varnothing 0.8$  mm (probes in +X and -X direction of the CMM coordinate system). The two parallel surfaces are probed using vertical probe of diameter  $\varnothing 2.0$  mm. Thus, the calibrated sphere was first measured using  $\varnothing 2.0$  mm probe, X, Y and Z coordinates of the sphere were set to [0,0,0] and then the sphere was measured using the two horizontal probes. Deviation of the sphere center measured by the two probes in Y direction was considered for the verification of the symmetry tolerance, as this is the direction for the assessment of symmetry tolerance of the item.

Every measurement result of the item was first corrected for a temperature change from the reference temperature of 20°, and for systematic error calculated according to equation 3.9, i.e., difference between a measured value and a value stated in the calibration certificate. Uncertainty budget for the calibration of the item, including all the calibrated features, is presented in table 4.6.

**Table 4.6:** Uncertainty budget for the calibration of the item following ISO 15530-3:2011. All values are in  $\mu\text{m}$ .

| Uncertainty component | $d_1$ | $d_2$ | $d_3$ | $D_1$ | $D_2$ | $D_3$ | $L_F$ | $L_T$ | $R_1$ | $R_2$ | $S_1$ | $S_2$ |
|-----------------------|-------|-------|-------|-------|-------|-------|-------|-------|-------|-------|-------|-------|
| $u_{\text{ref}}$      | 0.81  | 0.81  | 0.81  | 0.15  | 0.15  | 0.15  | 0.04  | 0.05  | 0.43  | 0.43  | 0.50  | 0.50  |
| $u_p$                 | 0.14  | 0.14  | 0.14  | 1.04  | 0.42  | 0.30  | 1.24  | 0.67  | 0.25  | 0.25  | 0.88  | 0.82  |
| $u_w$                 | 0.37  | 0.26  | 0.28  | 0.25  | 0.19  | 0.23  | 0.33  | 0.58  | 0.38  | 0.33  | 1.18  | 1.07  |
| $u_b$                 | 0.05  | 0.05  | 0.05  | 0.33  | 0.13  | 0.10  | 0.40  | 0.21  | 0.08  | 0.08  | 0.28  | 0.26  |
| $U_{\text{cal}}(k=2)$ | 1.8   | 1.7   | 1.7   | 2.3   | 1.0   | 0.8   | 2.7   | 1.8   | 1.3   | 1.2   | 3.2   | 2.9   |

# Chapter 5

## Performance characterization of CT systems using newly developed reference objects

In this chapter, procedures for characterization of CT systems using the two newly developed reference objects - CT ball plate and CT tree - are presented. The CT ball plate was used in connection with performance characterization of three industrial CT scanners according to a procedure described in a VDI guideline. The CT ball plate as well as the CT tree were then used in connection with characterization of errors in a measuring volume of a CT system.

### 5.1 Performance characterization of CT systems using the CT ball plate

In general, acceptance tests serve to determine whether a coordinate measuring machine with CT sensors meets the limits for the characteristics as specified by the manufacturer. Such tests related to CT are described in a German guideline VDI/VDE 2630-1.3 [36]. In this section the suitability of the CT ball plate for performance characterization of industrial CT systems is demonstrated. By scanning the CT ball plate, it is possible, by evaluating probing errors and length measurement errors, to determine and characterize measuring errors of the CT system. It is, however, not possible to test material- and geometry-dependent effects (determination of the task-specific measurement uncertainty) on measurements performed with the CT system, since, in general, the required similarity with real measurement tasks is not achieved.

#### 5.1.1 Measurement procedure

The following CT systems were employed: Nikon Metrology XT H 225 ST (at PTB), Zeiss Metrotom 1500 (at Danish Technological Institute) and Nanotom from GE Phoenix|x-ray (at Novo Nordisk A/S). The VDI guideline suggests to carry out CT measurements at two distinctive magnification levels in the scanning volume and at two orientations. Figure 5.1 presents a schematic picture of the setup of the object in the scanner. Scanning parameters are presented in table 5.1. Different scanning parameters are naturally selected due to different possibilities and characteristics of individual CT systems, carefully chosen by the operators. *SOD* and *SDD* parameters provide an indication about the position of the CT ball plate in the scanner and a measuring range of the scanner, respectively. The angle  $\alpha$  is defined by the position of the object (*SOD*) in the measuring volume of the scanner.

Before the test, the object was in all cases placed inside of the scanner for a certain period of time to reach the temperature of the scanner. Due to a relatively big size of the CT ball plate and a relatively small size of the measuring volume of Nanotom CT scanner, the CT ball plate was scanned only at two positions, position 1 and position 3.

It shall be emphasized that it is not an intention to compare the tested CT systems but to evaluate the suitability of the reference object - CT ball plate - for this task.

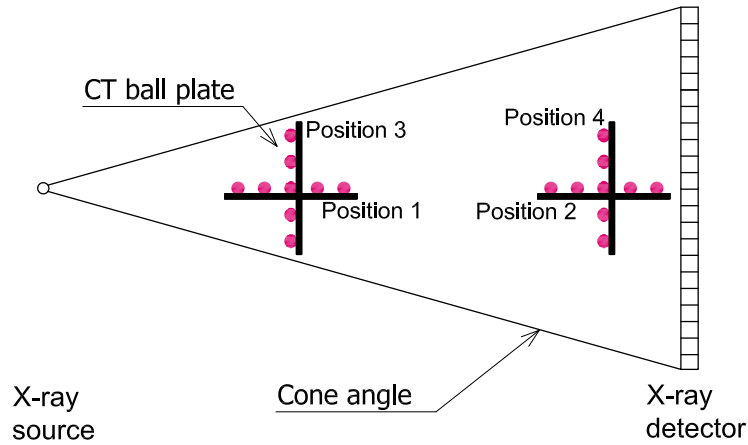


**Figure 5.1:** Four positions of the CT ball plate in the CT volume (side view) defined according to VDI/VDE 2630-1.3.

**Table 5.1:** An overview of scanning parameters for characterization of the three CT systems using the CT ball plate.

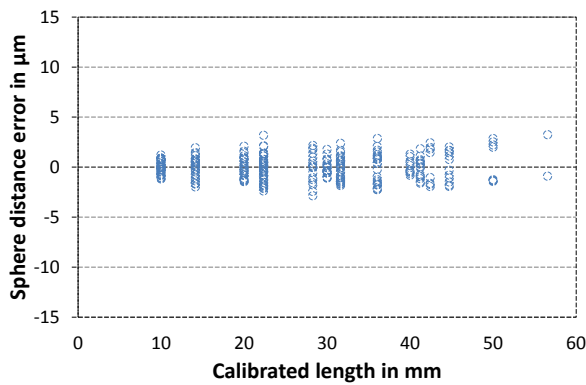
| Parameter                                | Unit          | XT H 225 ST |      | Metrotom 1500 |      | Nanotom |
|--|---------------|-------------|------|---------------|------|---------|
|  |               | 1(3)        | 2(4) | 1(3)          | 2(4) | 1(3)    |
| Voltage, $U$                             | kV            | 78          | 81   | 180           | 180  | 90      |
| Current, $I$                             | $\mu\text{A}$ | 100         | 96   | 250           | 250  | 100     |
| Power, $P$                               | W             | 7.8         | 7.8  | 45            | 45   | 9       |
| Focus spot size, $f$                     | $\mu\text{m}$ | 7           | 7    | 45            | 45   | 8       |
| Detector pixel size, $p$                 | $\mu\text{m}$ | 200         | 200  | 400           | 400  | 100     |
| Integration time, $t$                    | ms            | 708         | 708  | 1000          | 1000 | 750     |
| No. of views, $V$                        |               | 1200        | 1200 | 1080          | 1080 | 1000    |
| No. of image averaging, $i_{\text{avg}}$ |               | 1           | 1    | 1             | 1    | 3       |
| Source to detector distance, $SDD$       | mm            | 1112        | 1112 | 1500          | 1500 | 500     |
| Source to object distance, $SOD$         | mm            | 316         | 473  | 256           | 510  | 300     |
| Magnification factor, $m$                |               | 3.52        | 2.35 | 5.86          | 2.94 | 1.67    |
| Uncorrected voxel size, $s$              | $\mu\text{m}$ | 57          | 85   | 68            | 136  | 60      |
| Opening cone beam angle, $\alpha$        | $^\circ$      | (8)         | (5)  | (10)          | (5)  | (9)     |

Note: Numbers 1(3) and 2(4) stand for position of the object in the scanner according to figure 5.1. Numbers in the bracket correspond to position 3 and 4 respectively.

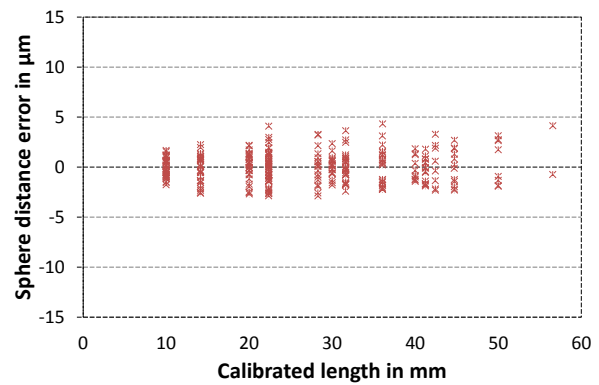
For simplification reasons,  $SD$  parameter, calculated according to equation 4.10, will be the only parameter considered.

## 5.1.2 Results

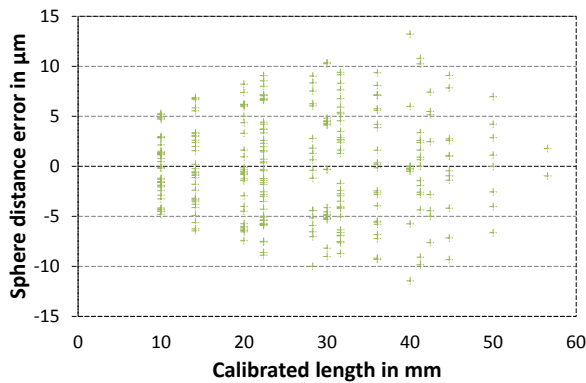
Figure 5.2 presents results of corrected  $SD$  errors which occur at the four positions. Results from scanning of the object using XT H 225 ST CT scanner are shown as an example. Results of the  $SD$  parameter from other systems are then summarized in table 5.2. Maximum absolute errors are displayed only, since the general shape (tendency) of errors at each tested position is similar for all the CT systems. The results were corrected for scale errors applying linear regression function.



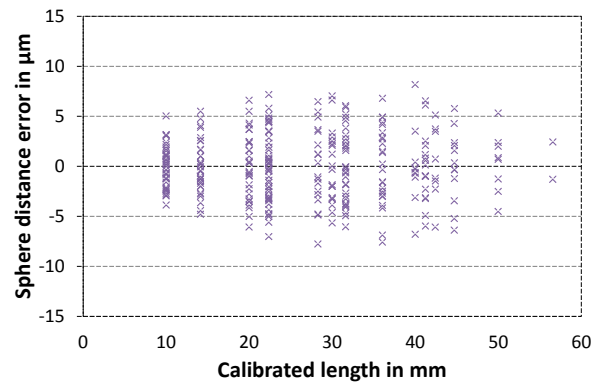
(a) Position 1.



(b) Position 2.



(c) Position 3.



(d) Position 4.

**Figure 5.2:** Results of performance characterization of Nikon Metrology CT scanner using the CT ball plate.

Errors found at different positions and orientations of the object in the CT volume are result of anisotropies in the measuring volume of the CT system. A clear difference in the magnitude of the errors can be observed between the two positions not only from figure 5.2 but also from table 5.2. Errors at positions 1 and 2 are, in general, comparable, as well as errors at positions 3 and 4. This indicates that the voxel size, determined by the position of the object in the measuring volume, has no significant effect on the evaluated parameter  $SD$ . However, errors at positions 1 and 2 are approximately two times smaller compared to errors at positions 3 and 4. This is most likely caused by the fact that the object at these positions is scanned closer to the borders with the detector, where

**Table 5.2:** Maximum absolute *SD* error obtained for the CT ball plate scanned at four positions in a specific CT system. The four positions are schematically shown in figure 5.1.

|               | Position |     |      |     |
|---------------|----------|-----|------|-----|
|               | 1        | 2   | 3    | 4   |
| XT H 225 ST   | 3.2      | 4.3 | 13.2 | 8.2 |
| Metrotom 1500 | 2.2      | 3.3 | 8.4  | 4.0 |
| Nanotom       | 2.2      | 5.2 |      |     |

**Table 5.3:** Summary of a linear regression coefficient  $a$  obtained for the CT ball plate scanned at four positions in a specific CT system. This coefficient characterizes the slope of the linear fit line through a data set of 300 length deviations. The four positions are schematically shown in figure 5.1. Values before correction are presented.

|               | Position x $10^4$ |        |        |        |
|---------------|-------------------|--------|--------|--------|
|               | 1                 | 2      | 3      | 4      |
| XT H 225 ST   | -11.99            | -13.46 | -11.78 | -13.97 |
| Metrotom 1500 | -0.23             | 0.28   | 0.30   | 0.33   |
| Nanotom       | -10.86            | -14.29 |        |        |

errors due to Feldkamp effect are pronounced. This can already be observed by looking at positions 3 and 4, where the object is scanned under different opening angles (see also  $\alpha$  in table 5.1). Due to this fact, greater measurement errors may be expected by positioning the object even closer to the source providing greater geometrical magnification. The difference in the opening angle is not that big at positions 1 and 2.

The advantage of the use of the CT ball plate is that when it is scanned at positions 1 and 2 (i.e., horizontally placed) it does not cause beam hardening problems, as could be perhaps expected, even though the overall penetration length through the balls is quite big. This is due to the fact that the material (ruby) from which the spheres are produced is low absorbent material.

As mentioned above, the results in figure 5.2 are corrected for scaling errors using linear regression. A linear regression coefficient  $a$  obtained by fitting a linear line through the data set of all 300 length deviations is for all the systems presented in table 5.3. This coefficient basically represents the linear dependence of *SD* errors on measured length in uncorrected state. The bigger is the slope the bigger errors are present in the system for bigger measured lengths. Differences in the coefficient are clear from the table. It can be noticed that XT H 225 ST and Nanotom CT scanners behave in a similar way, i.e., the errors in the uncorrected state are of the same magnitude. This is not the case for Metrotom 1500, for which the slope  $a$  is nearly zero. It shall be noted that Metrotom 1500 CT scanner features a high precision positioning system which ensures the positioning of the workpiece in the beam path during an X-ray down to the micrometer [108] and the correction for scaling errors is integrated in the system. Therefore, the errors are nearly zero. Some residual errors, in terms of a slope  $a$ , are still measured. These can be caused, for example, by an uncertainty from the calibration of the sphere center coordinates of the CT ball plate.

### 5.1.3 Conclusion

Procedure for characterization of industrial CT systems using the CT ball plate has been presented. By scanning the object at two magnifications and two orientations, as suggested by the VDI guideline,  $SD$  errors up to  $\pm 13.2 \mu\text{m}$  were observed. This was, however, different for each particular tested CT system. In [109] Metrotom 1500 was tested using several reference objects (sphere gauge, ball bar, calotte ball plate and ball plate) under different measuring conditions. Based on the results obtained,  $MPE_E$  was assessed to be  $MPE_E = (9 + L/50) \mu\text{m}$  ( $L$  in mm). This was, in principle, also achieved in our case using the CT ball plate, even though only  $SD$  parameter was evaluated. By scanning the CT ball plate repeatedly, the  $MPE$  parameter could be assessed also for the other tested CT systems. The CT ball plate should be scanned over time to determine its long-term stability and to document its suitability for this task.

## 5.2 Characterization and quantification of measurement errors of a CT system using the CT ball plate

One way to analyse the influence of several factors and their interaction at the same time is an application of so called design of experiment (DOE). This is a systematic approach to experimentation, when all the factors, defined at different levels, and their interactions, are considered simultaneously. As an output of the experiment, the influence of individual factors and their interactions on a response variable, which can be, for example, measurand (diameter, length, etc.) or calculation of measurement uncertainty, is quantified. The motivation of this investigation is to design an experimental plan in order to be able to predict and optimize scanning parameters based on the results of dimensional measurements of a reference object and to characterize and quantify measuring errors occurring in the system.

### 5.2.1 Current approach

In this investigation, an alternative approach of experimental design in CT is introduced. The approach is based on defining factors through combination of scanning parameters (X-ray source current, integration time, image averaging, scanning geometry, etc.) and derived quantities in connection with the physical-technical characteristics of the X-ray tube (focus spot) and the detector system (resolution) as the two main system components. The two selected factors, spatial resolution and pixel noise, are well-known key characteristics describing the quality of CT images [110].

Spatial resolution in a volumetric CT image,  $U_{TOT}$ , is mainly influenced by the focus size, focus drift during scanning, contrast transmission of the detector system, reconstruction algorithm, and scanning geometry [110]. For simplification reasons, the focus size, the detector system, and the scanner geometry were taken into account only. The estimated spatial resolution is then defined as [110]:

$$U_{TOT} = \sqrt{U_F^2 + U_D^2} \quad (5.1)$$

where  $U_F$  is geometrical unsharpness associated with focus size and  $U_D$  is geometrical unsharpness associated with the contrast transmission of the detector. Both can be described as follows [111, 112]:

$$U_F = \frac{m-1}{m} \cdot W_F \quad (5.2)$$

$$U_D = \frac{W_D}{m} \quad (5.3)$$

where  $m$  is geometrical magnification, defined according to equation 2.7.  $W_F$  is size of the focus spot which is linked to the X-ray tube power [112, 113] and  $W_D$  is detector image unsharpness which is assumed to be double the pixel size [114]. Only two geometrical unsharpness parameters  $U_F$  and  $U_D$  were considered, also because they are the most dominant geometrical unsharpness sources.

The symbol of spatial resolution  $U_{TOT}$  should not be confused with measurement uncertainty which has typically the same symbol  $U$ .

Pixel noise,  $\sigma_{pn}$ , is expressed in the form of standard deviation evaluated in 2D reconstruction images as follows [46, 111]:

$$\sigma_{pn} = \frac{k \cdot \pi}{s \cdot \sqrt{V}} \cdot \frac{1}{\sqrt{I \cdot t \cdot i_{avg}}} \quad (5.4)$$

where  $k$  is constant depending on a back-projection filter type (in our case  $k=0.23$  was chosen),  $s$  is pixel size in a 2D slice in  $\text{mm}^2$ ,  $V$  is number of views (projections),  $I$  is X-ray source current in mA,  $t$  is integration time of the detector in s and  $i_{avg}$  is number of image averaging.

The pixel noise should not be confused with the noise in the projection images.

With the increase of X-ray source current and integration time, more photons are detected by the detector system. An increased number of photons and image averaging improve the detector image statistics, which follows a Poisson distribution, leading to an improved signal-to-noise ratio (SNR). The influence of individual factors affecting the pixel (image) noise is for instance discussed in [115].

Based on the formulas described above (equation 5.1 and equation 5.4), a  $3^2$  full factorial DOE was assessed and is shown in table 5.4. The two factors, spatial resolution and pixel noise, are defined theoretically by the assessment of scanning parameters at three levels, approximately equally distributed. The DOE was created in statistical software Minitab Release 14.1. This software is used to create a design to examine the relationship between factors. The design is fully randomized which helps to ensure that the model meets certain statistical assumptions. Column Run Order in the table indicates the order in which the data are collected.

The individual positions of the object in the CT volume, i.e., positions of the object with respect to the X-ray source in the direction of the magnification axis, are shown in figure 5.3. Explanation of the full cone angle  $\alpha$  from table 5.4 is also shown in the figure. The angle is defined by the position of the object (*SOD*) in the measuring volume of the scanner. The system under study has a fixed *SDD*.

In order to minimize the influence of the focus spot size, this was nominally kept constant by using constant X-ray power. The focal spot size was assumed to be approximately  $1 \mu\text{m}$  per Watt tube power [113]. Since all the nine experimental runs yield different contrast, the corresponding X-ray

**Table 5.4:** Experimental plan with calculated factors  $U_{TOT}$  and  $\sigma_{pn}$  from equation 5.1 and equation 5.4.

| Run Order | Voltage      | Current      | Int. time   | No.of image avg. | No.of views | Magnif. factor | Uncor. voxel size | Full cone angle         | Spatial res.       | Pixel noise   |
|-----------|--------------|--------------|-------------|------------------|-------------|----------------|-------------------|-------------------------|--------------------|---|
|           | $U$<br>in kV | $I$<br>in mA | $t$<br>in s | $i_{avg}$        | $V$         | $m$            | $s$<br>in $\mu m$ | $\alpha$<br>in $^\circ$ | $U_{TOT}$<br>in mm | $\sigma_{pn}$ in<br>$mm^{-2} \cdot (mA \cdot s)^{-1/2}$ |
| 1         | 70           | 0.112        | 1.415       | 2                | 1200        | 3.52           | 57                | 8.2                     | 0.114              | 0.65  |
| 2         | 70           | 0.112        | 2.829       | 4                | 1200        | 7.04           | 28                | 16.2                    | 0.057              | 0.65  |
| 3         | 81           | 0.096        | 0.708       | 1                | 1200        | 2.35           | 85                | 5.4                     | 0.170              | 0.94  |
| 4         | 78           | 0.100        | 0.708       | 1                | 1200        | 3.52           | 57                | 8.2                     | 0.114              | 1.38  |
| 5         | 87           | 0.090        | 0.354       | 1                | 1200        | 2.35           | 85                | 5.4                     | 0.170              | 1.37  |
| 6         | 78           | 0.101        | 2.829       | 1                | 1200        | 7.04           | 28                | 16.2                    | 0.057              | 1.37  |
| 7         | 78           | 0.100        | 1.415       | 1                | 1200        | 2.35           | 85                | 5.4                     | 0.170              | 0.65  |
| 8         | 72           | 0.109        | 1.415       | 4                | 1200        | 7.04           | 28                | 16.2                    | 0.057              | 0.93  |
| 9         | 72           | 0.108        | 0.708       | 2                | 1200        | 3.52           | 57                | 8.2                     | 0.114              | 0.94  |

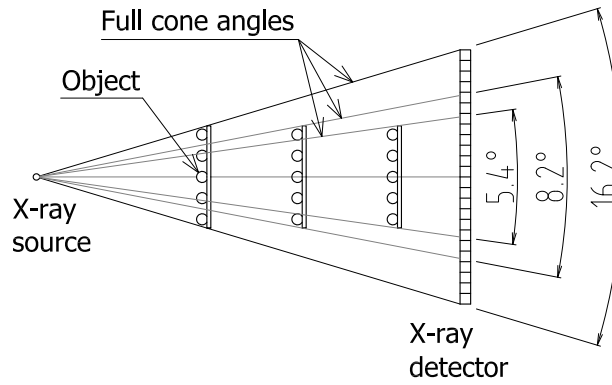


**Figure 5.3:** Three positions of the object (CT ball plate) (side view) in the CT volume according to the DOE plan presented in table 5.4. The full cone angle at individual positions is specified.

tube power (X-ray tube current and acceleration voltage) were adjusted so, that the focus spot size was approximately  $7 \mu m$ .

## 5.2.2 Measurement setup

The experiment was carried out using a Nikon Metrology XT H 225 ST CT scanner at PTB. FDK based reconstruction was done using software CT Pro V2.2 SP2 provided by Nikon Metrology, too. The object - CT ball plate (figure 5.4), introduced in section 4.1 was used in this study. The CT ball plate was positioned vertically, and was not repositioned during individual runs of the experiment. The position of the object in Z direction (Z axis points from X-ray tube to the detector, see figure 5.5) of the CT scanner's coordinate system was in accordance with table 5.4.



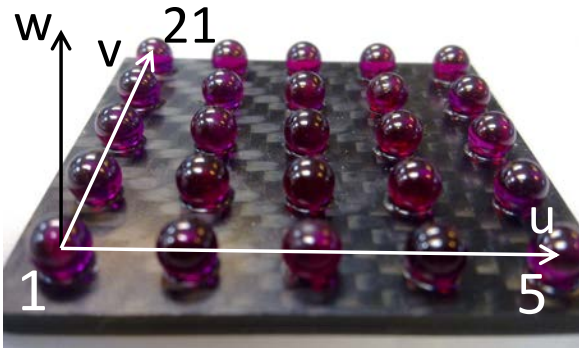


**Figure 5.4:** CT ball plate used for quantification of measurement errors in the CT volume and workpiece coordinate system.

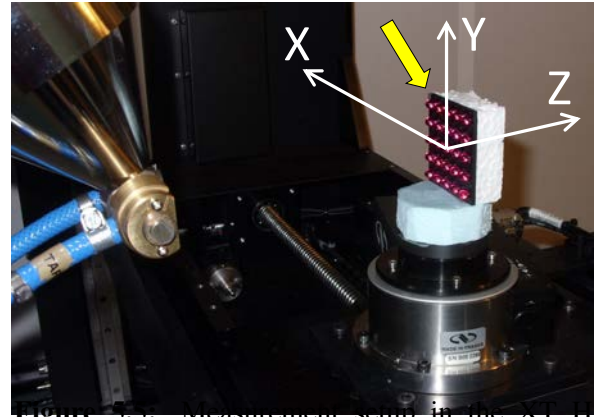


**Figure 5.5:** Measurement setup in the X11 225 ST CT scanner at PTB. The CT ball plate was scanned in vertical position. The coordinate system of the CT scanner and the position of a thin metal plate (yellow arrow), indicating origin of the object, are also shown.

### 5.2.3 Data evaluation

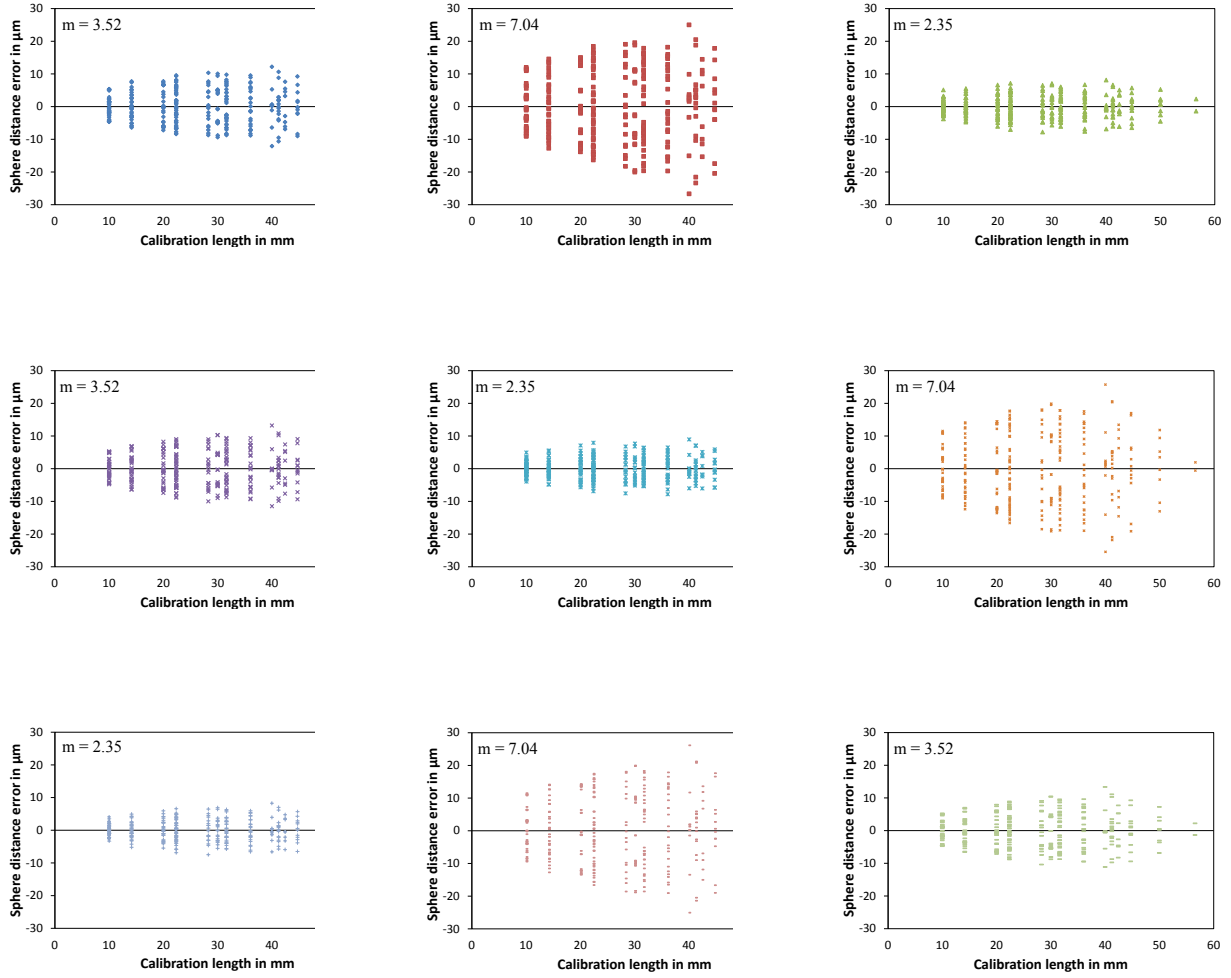
For determination of the surface, inspection software VG Studio Max 2.2 is used. The method for surface determination was described in section 4.1.4.

As evaluation parameters, sphere distance error  $SD$  and probing errors  $PS$  and  $PF$  were selected according to VDI/VDE 2630-1.3.  $SD$  is a robust parameter independent of errors due to a threshold determination, and it is a parameter used for correction of scaling errors. The evaluation parameters were evaluated in accordance with a procedure described in section 4.1.5.

The CT scans were corrected for scale errors by applying linear regression, following procedure described in section 4.1.6.

### 5.2.4 Results and discussion

Results of sphere distance errors (figure 5.6) show that the errors in the present study are bigger at high geometrical magnification (=high resolution), approximately  $\pm 30 \mu\text{m}$ , and smaller at low magnification (=low resolution), approximately  $\pm 10 \mu\text{m}$ . This can be due to three reasons: Feldkamp effect [95], focus drift or rotary axis misalignment in X and Y directions [116] (for orientation see figure 5.5). It is known that Feldkamp effect is most pronounced when an object is scanned at large opening angles. Table 5.4, among others, show that a cone angle at high magnification ( $\alpha = 16.2^\circ$ ) is approximately three times bigger than at low magnification ( $\alpha = 5.4^\circ$ ). Image artifacts, most likely caused by the Feldkamp effect, were observed on reconstruction images for CT scans at high resolution (see figure 5.7). The potential impact of the focus drift rotary axis drift is also most pronounced at high magnifications [117]. At high magnifications, the difference between the focus drift and the misalignment of axis of the rotary table is small. Therefore, it is difficult to separate the three effects - Feldkamp, focus drift and rotary axis drift. Due to experience of the author in general and with the CT system under study it is assumed for the series of measurements performed here that the Feldkamp effect is the most dominant of the three error types.



(g) Run 7 ( $U_{TOT}=0.170$  mm;  $\sigma_{pn}=0.65\text{mm}^{-2} \cdot (\text{mA} \cdot \text{s})^{-1/2}$ ); (h) Run 8 ( $U_{TOT}=0.057$  mm;  $\sigma_{pn}=0.94\text{mm}^{-2} \cdot (\text{mA} \cdot \text{s})^{-1/2}$ ); (i) Run 9 ( $U_{TOT}=0.114$  mm;  $\sigma_{pn}=0.94\text{mm}^{-2} \cdot (\text{mA} \cdot \text{s})^{-1/2}$ )

**Figure 5.6:** Results of sphere distance error for all the nine runs of the experiment, as specified in table 5.4.  $U_{TOT}$  and  $\sigma_{pn}$ , specified in the brackets, are the calculated spatial resolution and the calculated pixel noise, respectively.  $m$  is magnification. The original voxel data set is corrected for scale errors using linear regression, explained in section 4.1.6.

Figure 5.7 shows an example of a reconstructed image corresponding to Run 2 of the experiment, i.e., CT scan at high spatial resolution. Here, image artifacts at the upper and lower borders of the image can be recognized. The occurrence of the Feldkamp effect is more clear here. Image in this figure was taken in the XY plane of the CT scanner's coordinate system.

Plot in figure 5.8 shows results of one-factor effects, so called main effects, calculated in Minitab DOE software. In particular, the figure shows the influence of spatial resolution and pixel noise on data scatter of  $SD$  parameter, expressed as  $2 \cdot$  standard deviation of this parameter. Individual points in the graph represent a mean of all runs using individual level of either of the factors, i.e., in case of  $3^2$  DOE each data point corresponds to a mean value of three runs. One can observe, that the influence of spatial resolution on data scatter is clearly significant (steep nearly linear trend), compared to pixel

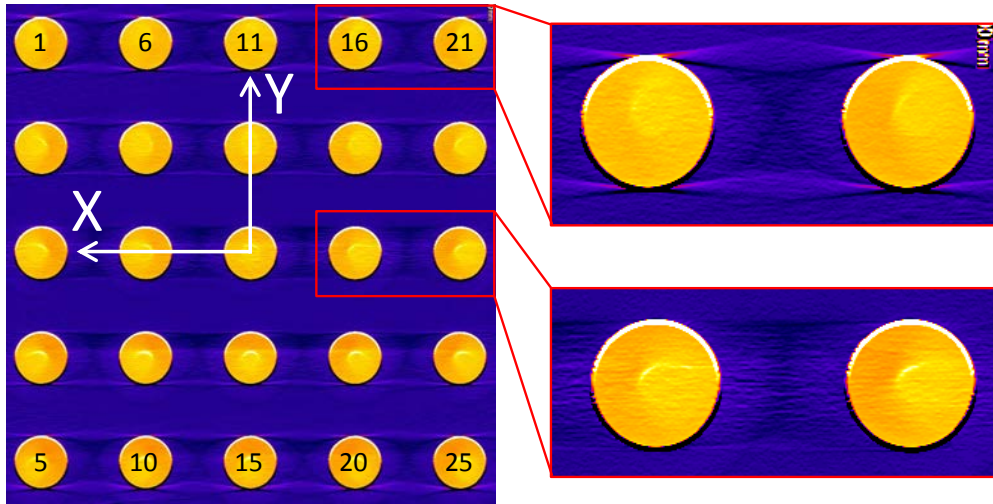


**Figure 5.7:** A reconstructed image for Run 2 of the experiment with high resolution ( $U_{TOT}=0.057$  mm;  $\alpha = 16.2^\circ$ ), taken in the XY plane of the CT scanner's coordinate system. Image artifacts can be recognized on the spheres at the upper and lower borders of the image, where Feldkamp effect is most pronounced. The orientation of this image is equivalent to position of the object in figure 5.5.

noise, where this factor seems not to be significant (horizontal linear trend - providing approximately the same pixel noise value at all three levels). The figure confirms the problem of scanning at high resolution, during which big data scatter concerning measured  $SD$  values occurs.

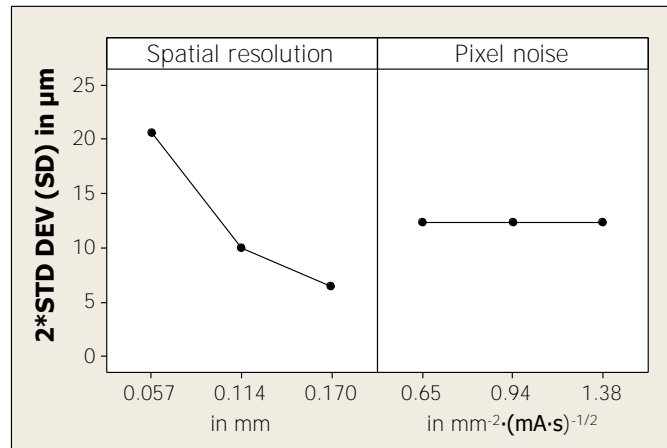


**Figure 5.8:** DOE results showing influence of the calculated spatial resolution (equation 5.1) and the calculated pixel noise (equation 5.4) on data scatter for calculation of the sphere distance error ( $SD$ ), expressed as 2-standard deviation (STD DEV) of this parameter.

Results of probing error size ( $PS$ ) are shown in figure 5.9. Three nearly linear trends of errors at high magnification for each five spheres of the object in Y-direction (for orientation see figure 5.5) can be observed. The trend starts with spheres no. 1, 6, 11, 16 and 21 and goes in negative direction of the  $PS$  error towards spheres no. 5, 10, 15, 20 and 25 respectively (the designation of sphere numbers is shown in figure 5.7). Such a "top-bottom oscillation" of values is caused due to the orientation of the object in the CT scanner, whose spheres, mentioned above, are close to the detector borders

(see figure 5.7), where image artifacts, most likely caused by the Feldkamp effect, were observed. This oscillation basically repeats for all three triple combinations of spatial resolution, however, is most pronounced at high resolution. However, this can also be caused due to the rotary axis tilt. This would explain why  $PS$  errors for spheres at the upper border with the detector are positive and  $PS$  errors for spheres at the lower border with the detector are negative, which is then connected with the magnification and voxel size. Looking at the average  $PS$  values at all three spatial resolution levels, the  $PS$  becomes greater (negative) at lower magnification levels. In particular, calculating the average  $PS$  at high resolution ( $U_{TOT}=0.057$  mm for runs no. 2, 6 and 8) results in  $PS=0.3 \mu\text{m}$  and at low resolution ( $U_{TOT}=0.170$  mm for runs no. 3, 5 and 7) results in  $PS=-6.5 \mu\text{m}$ . These values correspond to average values for all 25 spheres and three pixel noise levels. The smallest  $PS$  error is therefore at the highest spatial resolution for spheres at position  $Y=0$ . This off-set of the average  $PS$  errors at the three spatial resolution levels can possibly be caused by increased interpolation error within a voxel ("sub-voxel") connected with fitting of a sphere for diameter measurements, i.e., finding the edge between the air and material in the voxel.

Results of probing error form ( $PF$ ) are shown in figure 5.10.  $PF$  errors are mainly influenced by the spatial resolution, too. Here, again, three distinctive triples of spatial resolution combinations can be observed (except of run 2 which is for unknown reasons an outlier in this case). As for the  $PS$  errors, the average  $PF$  errors are the smallest at high spatial resolution ( $PF=7 \mu\text{m}$ ) and the greatest at low spatial resolution ( $PF=13 \mu\text{m}$ ). These values correspond to average values for all 25 spheres and three pixel noise levels. A trend corresponding to measurements of the spheres at the borders of the detector can be slightly recognized, too.

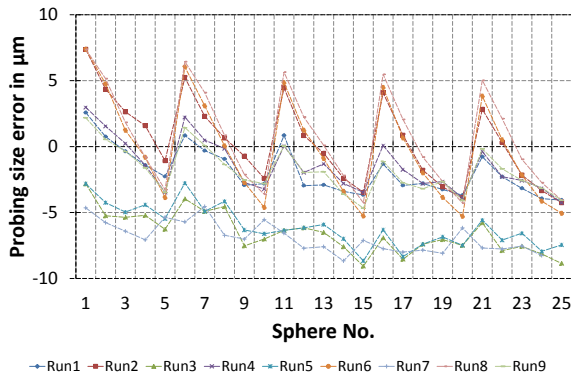


**Figure 5.9:** Results of probing error size ( $PS$ ) for all the runs of the designed experiment.

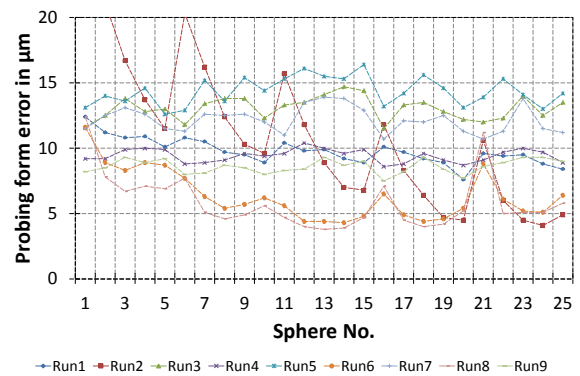


**Figure 5.10:** Results of probing error form ( $PF$ ) for all the runs of the designed experiment.

DOE results (main effect plots) showing the influence of spatial resolution and pixel noise on  $PS$  and  $PF$  are presented in figure 5.11 and figure 5.12 respectively. The same observation, as realized for the evaluation of the  $SD$  parameter, was made for  $PS$  and  $PF$  parameters, i.e., the influence of the spatial resolution is significant, which is in contrast with the pixel noise, which, again, seems not to be significant. Moreover, the DOE results are in a good agreement with the plots in figure 5.9 and figure 5.10, where the curves belonging to different levels of pixel noise provide nearly the same trend, and so, the trend of the line for pixel noise in figure 5.11 and figure 5.12 is nearly horizontal.

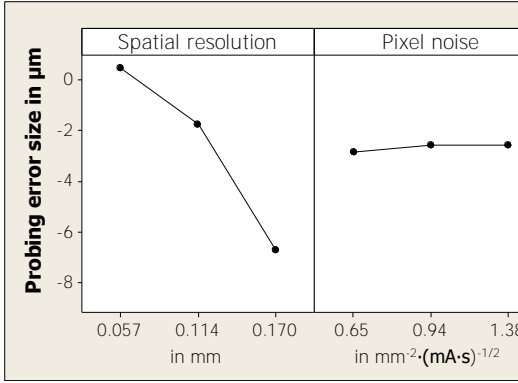


**Figure 5.11:** DOE results showing influence of the calculated spatial resolution (equation 5.1) and the calculated pixel noise (equation 5.4) on probing error size ( $PS$ ).

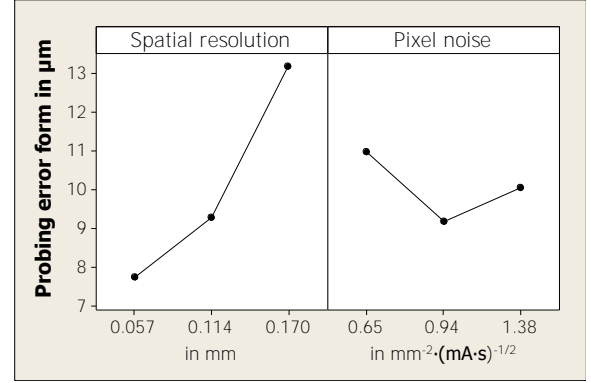


**Figure 5.12:** DOE results showing influence of the calculated spatial resolution (equation 5.1) and the calculated pixel noise (equation 5.4) on probing error size ( $PF$ ).

### 5.2.5 Experimental validation of the proposed method

From the results of the DOE analysis it appears that spatial resolution is a dominant factor having a great influence on dimensional measurements. In contrast, pixel noise seems not to have a visible influence for the selected scanning parameters and the selected measurand  $SD$ . Therefore, in the following, reconstruction images were analysed for image quality.

It is known that, in general, CT scans produced at higher spatial resolution lead to an increased noise [118]. This was also confirmed in this case - low SNR was measured on reconstructed images for CT scans at high resolution (see figure 5.13). SNR was measured in the XZ plane of the CT scanner's coordinate system on a middle sphere, by selecting a region of interest (ROI) positioned in the center of the sphere (see figure 5.14). The same ROI was applied to measure the SNR values for all the runs of the experiment. SNR is determined as a ratio between average gray values (signal) in the ROI,  $\mu$ , and associated standard deviation of the gray values (noise),  $\sigma$ , according to equation 5.5.

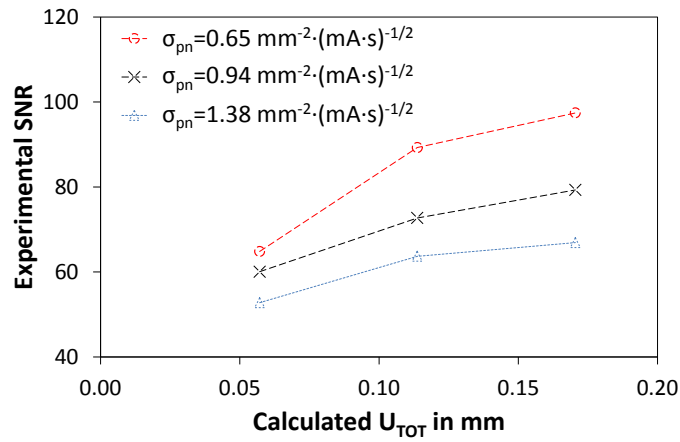


**Figure 5.13:** Signal-to-noise ratio (SNR) measured on reconstruction images, showing low SNR for high resolution CT scans and vice versa.

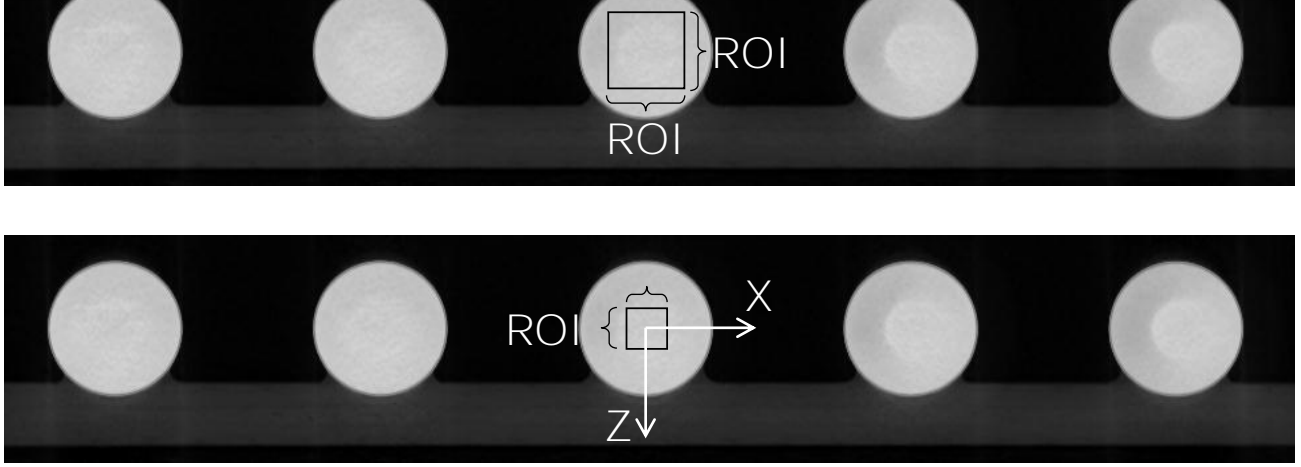


**Figure 5.14:** Selection of the ROI for measurements of the SNR. The reconstruction image was taken in the XZ plane of the CT scanner's coordinate system.

<sup>1</sup> P. Müller, PhD student, DTU Mechanical Engineering

Novo Nordisk 26/04/2012

$$SNR = \frac{\mu}{\sigma} \quad (5.5)$$

As three levels of pixel noise were theoretically specified according to equation 5.4, three levels of SNR were expected to be measured. This was validated in the experiment and can be seen in figure 5.13, where, clearly three levels of SNR are plotted at three associated levels of spatial resolution. The results are in a good agreement with the theory, i.e., the experimentally obtained values of SNR increase when pixel noise decreases. It can also be observed that the range of SNR values is bigger at lower spatial resolution and vice versa. It is believed that the levels for pixel noise should have been selected in a wider range, where the influence of the pixel noise is bigger (see results of pixel noise variation in figure 5.8). It should also be noted that each data point in the figure has an attributed uncertainty derived from the assessment of the SNR values, which might be influenced, e.g., by the size and position of the ROI.

For further validation of pixel noise formula, three additional CT scans were carried out at three increased noise levels for selected levels of spatial resolution (the same levels as in the original DOE). Scanning parameters for these scans, shown in table 5.5, were selected based on Run 5 of the original DOE (table 5.4), the one yielding high noise ( $\sigma_{pn}=1.37\text{mm}^{-2} \cdot (\text{mA} \cdot \text{s})^{-1/2}$ ), determined mainly with a low integration time of 0.354 s. The three high noise levels are determined by selecting number of image averaging  $i_{avg}=1$  (this means that each acquired projection image is used for the reconstruction, without any averaging of other images), low integration time  $t=0.354$  s, while keeping the number of views constant ( $V=1200$ ), in order not to create any additional influences.

**Table 5.5:** Experimental plan for validation of the pixel noise formula with increased noise. Three CT scans are based on Run 5 of the original DOE from table 5.4 with calculated factors  $U_{TOT}$  and  $\sigma_{pn}$  from equation 5.1 and equation 5.4.

| Run Order | Voltage      | Current      | Int. time   | No.of image avg. | No.of views | Magnif. factor | Uncor. voxel size       | Full cone angle         | Spatial res.       | Pixel noise  |
|-----------|--------------|--------------|-------------|------------------|-------------|----------------|-------------------------|-------------------------|--------------------|--|
|           | $U$<br>in kV | $I$<br>in mA | $t$<br>in s | $i_{avg}$        | $V$         | $m$            | $s$<br>in $\mu\text{m}$ | $\alpha$<br>in $^\circ$ | $U_{TOT}$<br>in mm | $\sigma_{pn}$ in<br>$\text{mm}^{-2} \cdot (\text{mA} \cdot \text{s})^{-1/2}$ |
| 1         | 87           | 0.090        | 0.354       | 1                | 1200        | 2.35           | 85                      | 5.4                     | 0.170              | 1.37   |
| 2         | 87           | 0.090        | 0.354       | 1                | 1200        | 3.52           | 57                      | 8.2                     | 0.114              | 2.06   |
| 3         | 87           | 0.090        | 0.354       | 1                | 1200        | 7.04           | 28                      | 16.2                    | 0.057              | 4.11   |



Experimental validation of the test including both, the original DOE (only three values of pixel noise for Runs 6, 9 and 7 respectively presented in table 5.4) and the additional test with increased noise levels (presented in table 5.5) is highlighted in figure 5.15. Here, the experimentally obtained values of SNR (in particular its inverse) are fitted against the calculated pixel noise. A linear fit of values ( $R^2=0.999$ ) for the two independent tests can be observed, supporting the validation of the formulation of pixel noise. Due to the linearly increasing trend, a coefficient  $C$ , characterizing the slope, has to be added to the pixel noise formula. Thus, the final expression of the pixel noise formula is given in equation 5.6. Due to the linearity of the fit, this expression can be used in connection with the estimation of  $\sigma_{pn}$  for different test conditions.

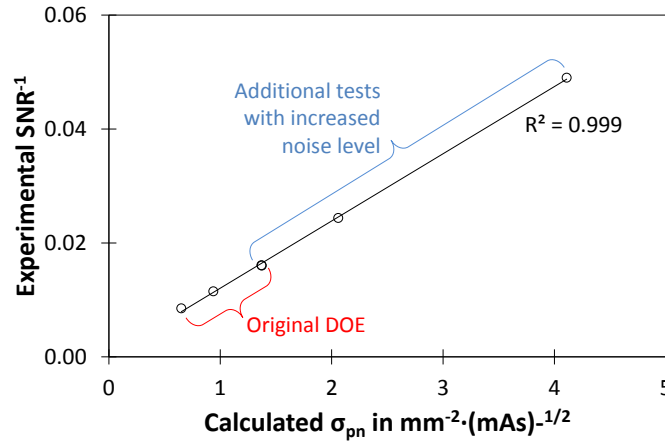


**Figure 5.15:** Experimental inverse values of SNR fitted against the theoretically calculated pixel noise  $\sigma_{pn}$  showing a linear fit of values for two independent tests (the original DOE and the additional three CT scans with increased pixel noise levels).

$$\sigma_{pn} = C \cdot \frac{k \cdot \pi}{s \cdot \sqrt{V}} \cdot \frac{1}{\sqrt{I \cdot t \cdot i_{avg}}} \approx \frac{1}{SNR_{exp}} \quad (5.6)$$

Since big errors were attributed to a position of the object close to the X-ray source (=high magnification) yielding big cone angle, further validation of the results was done, in order to exclude some of the error sources and to be able to make more general statements and conclusion about the proposed method. In particular, the question is, whether the errors come from the opening angle (Feldkamp effect) or any drift effect (rotary axis tilt). For this reason, the CT ball plate was scanned at low magnification ( $m=2.35$ , identical with the position of the plate during the DOE experiment) and, at the same time, at the upper or lower position at large opening angle, see figure 5.16. As can be seen from the sketch, these two positions were determined so that the opening cone beam angle is the same as at high geometrical magnification ( $m=7.5$ ).

Results presented in figure 5.17 show nearly symmetrical behaviour for the selected parameter  $SD$ . This is a clear indication of the rotary axis tilt. Positive  $SD$  errors are found at the upper detector regions and negative errors at the lower detector regions. Moreover, the magnitude of the errors is approximately equivalent with the results of the original DOE test (figure 5.6) at high geometrical magnification ( $m=7.5$ ), i.e., errors up to 40  $\mu m$  are observed. Thus, the Feldkamp effect cannot be neglected, as in both cases (upper and lower regions of the detector and low magnification, and high

magnification of  $m=7.5$  of the original DOE test) the object was scanned at the same opening cone beam angle.

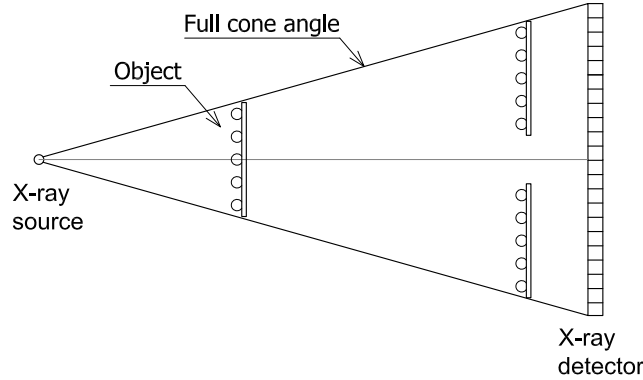


**Figure 5.16:** A sketch of the setup of the CT ball plate at upper and lower detector regions (side view).

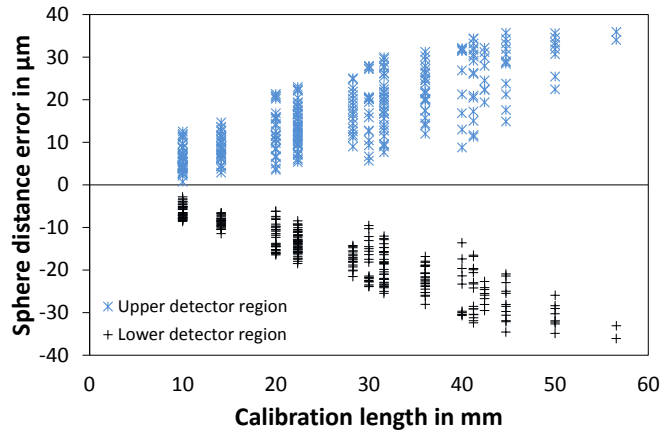


**Figure 5.17:** Scanning of the CT ball plate at upper and lower detector regions.

## 5.2.6 Conclusion

This investigation described a method allowing systematic analysis of measurement errors which occur in the volume of the CT system. The method is based on defining factors through combination of scanning parameters. A CT ball plate was used to investigate the influence of image quality on dimensional CT measurements. Image quality was assessed in terms of spatial resolution and pixel noise. Both factors were determined theoretically. Measurement accuracy was determined by the analysis of sphere distance errors  $SD$  and probing errors  $PS$  and  $PF$ . In the following, several conclusions are drawn:

- Results of the  $SD$  parameter have shown that by selecting proper combination of scanning parameters, minimization of these errors down to  $10\ \mu\text{m}$ , compared to the worst case being approximately  $30\ \mu\text{m}$ , can be achieved. Greater errors were found for CT scans at high resolution, i.e., for a position of the object close to the X-ray source where spheres are imaged at large opening angle. At this position, image artifacts, probably caused by the Feldkamp effect were pronounced.



- Analysis of the source of the errors was enhanced by additionally scanning the object at the upper and lower regions of the detector. The results indicated the tilt of the rotary axis. Thus, the errors for the case presented were caused by both the tilt and the Feldkamp effect.
- The DOE analysis has shown the spatial resolution being dominant factor and thus, having a big influence on dimensional measurements. In contrast, the pixel noise appeared not to be significant. However, this was only investigated for three selected parameters  $SD$ ,  $PS$  and  $PF$  and a limited number of runs of DOE under study.
- The theoretical formulation of pixel noise was experimentally validated by analysing images obtained from a reconstruction volume. As three levels of pixel noise were theoretically defined, three levels (values) of SNR were expected. These were found in a well-specified ROI and thus, it can be concluded that the experiment is in a good agreement with theory. Moreover, with decreased pixel noise, increase of SNR values was observed. The three levels of SNR were more distinctive for CT scans at low resolution. Moreover, the pixel noise formula was experimentally validated by additional tests characterized with increased noise levels.

### 5.3 Characterization of measurement errors of a CT system in the direction of the magnification axis using the CT tree

The nature of measurement errors in CT systems is in many cases unknown. Therefore, procedures for characterization and quantification of these errors are needed. In this section, such a procedure using the newly developed reference object - CT tree - is described, enabling quantification of the errors in the direction of the magnification axis.

#### 5.3.1 Measurement setup

The assessment of the errors in the direction of the magnification axis is carried out by scanning the object at five magnification levels, shown in figure 5.18. The figure, in fact, shows projection images of the CT tree. The object was scanned in a vertical orientation with a ball bar BB3 (for identification of ball bars see figure 4.16) in the central beam, highlighted by the red dashed horizontal line. Magnification range was selected to provide a maximum possible magnification (small voxel size) on one side, and on the other side magnification which results in a voxel size being approximately double.

Scanning parameters were selected to yield high contrast between background (air) and material (ruby spheres), and are summarized in table 5.6. Scanning parameters were kept constant for all the CT scans. The only variable in this test was the position of the object in the direction of the magnification axis.

The decision for selecting 1000 projection views was to achieve reasonably low scanning time and sufficient quality of the scan. Moreover, the quality of the scan was improved by choosing image averaging 2 (which increases SNR). However, choosing only 1000 projections results in undersampling of the volume data set. The condition for CT data set being undersampled is characterized by the angular increments  $s_{ang}$  between individual projections and the maximum scanning volume determined in XZ plane of the CT scanner's coordinate system (for orientation

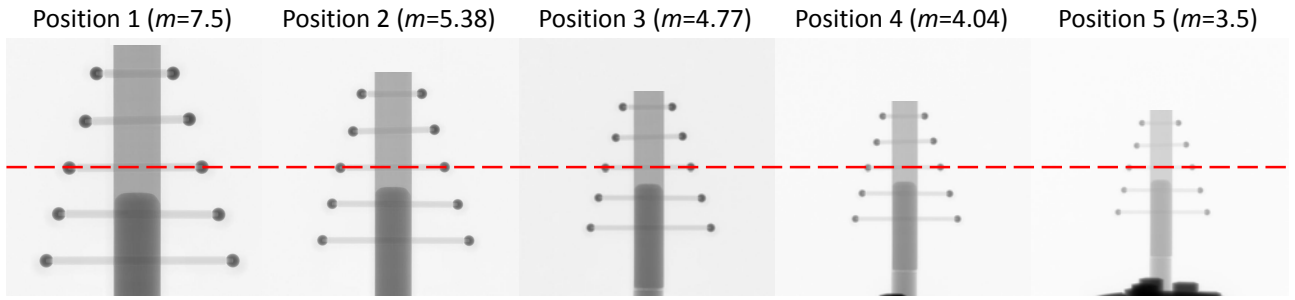


**Figure 5.18:** Measurement setup of the CT tree at five positions (magnification levels) in the measuring volume. The red dashed horizontal line shows the position of ball bar BB3 being in the central beam at all five positions.

**Table 5.6:** An overview of scanning parameters. Variables changed at individual positions are highlighted in bold.

| Parameter              | Unit          | Position 1  | Position 2  | Position 3  | Position 4  | Position 5  |
|------------------------|---------------|-------------|-------------|-------------|-------------|-------------|
| Voltage                | kV            | 110         | 110         | 110         | 110         | 110         |
| Power                  | W             | 12.65       | 12.65       | 12.65       | 12.65       | 12.65       |
| Detector matrix        | pixel         | 2000 x 2000 | 2000 x 2000 | 2000 x 2000 | 2000 x 2000 | 2000 x 2000 |
| Detector pixel size    | $\mu\text{m}$ | 200         | 200         | 200         | 200         | 200         |
| Integration time       | ms            | 1000        | 1000        | 1000        | 1000        | 1000        |
| No. of views           |               | 1000        | 1000        | 1000        | 1000        | 1000        |
| No. of image averaging |               | 2           | 2           | 2           | 2           | 2           |
| Vertical position      | mm            | 194.4       | 194.4       | 194.4       | 194.4       | 194.4       |
| Magnification factor   |               | <b>7.5</b>  | <b>5.83</b> | <b>4.77</b> | <b>4.04</b> | <b>3.5</b>  |
| Uncorrected voxel size | $\mu\text{m}$ | <b>26.7</b> | <b>34.3</b> | <b>41.9</b> | <b>49.5</b> | <b>57.2</b> |

see figure 5.19), and the size of a voxel  $s$ . Voxel data is undersampled if the ratio between the two is greater than 1, expressed as follows:

$$\frac{s_{\text{ang}}}{s} > 1 \quad (5.7)$$

where  $s_{\text{ang}}$  is expressed as:

$$s_{\text{ang}} = R \cdot \alpha \cdot \frac{\pi}{180} \quad (5.8)$$

where  $R$  is radius of the measuring volume in XZ plane of the CT system and  $\alpha$  is an angle between two neighbouring projections. In practise,  $R$  corresponds to half of the size (length) of a scanned object.

For our case, undersampling was present for some of the ball bars of the CT tree at some of the positions. The author believes that the undersampling problem in case of an ideal object like a ball bar featuring spheres will not influence the results of sphere center coordinate estimation, since the geometry of the spheres is well defined and the sampling is robust.

Nikon Metrology XT H 225 ST CT scanner at PTB was used for this study. FDK based reconstruction was done using software CT Pro V2.2 SP2 provided by Nikon Metrology, too. The images used for

the reconstruction were 16-bit TIFF images. The gray values of the images are scaled to fully use the 16-bit target area (65000 gray values).

The coordinate system of the measuring volume along with the setup of the CT tree is shown in figure 5.19. Here, the  $Z$  coordinate defines the geometrical magnification of the scanned part.

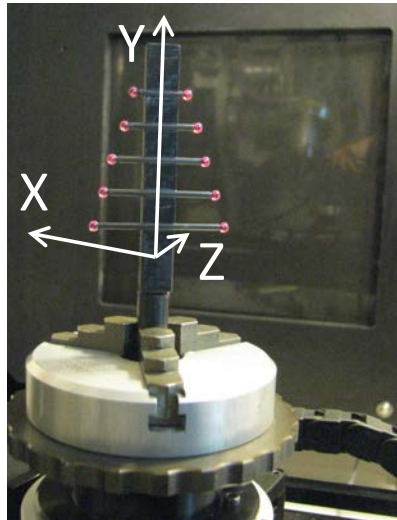


**Figure 5.19:** Definition of the coordinate system in the measuring volume.

### 5.3.2 Data evaluation

#### Surface determination

For determination of the surface, inspection software VG Studio Max 2.1 was used. For more details about the procedure for surface determination of the CT tree see section 4.2.5.

#### Evaluation parameters

After the reconstruction of the 3D voxel model and determination of the surface, evaluation of CT data was carried out. Sphere distance error  $SD$  and probing form error  $PF$  were selected for the evaluation. The assessment of the data points for the evaluation of the two characteristics is schematically shown in figure 4.21, presented in section 4.2.6.

#### Scale error correction

The correction of the CT data for scaling errors was done in accordance with procedure described in section 4.2.7.

### 5.3.3 Results and discussion

After correcting the CT data for scaling errors,  $SD$  errors of  $\pm 22 \mu\text{m}$  were observed for the object at position 1, i.e., at high spatial resolution. The errors decreased with decrease of the magnification level (= decrease of spatial resolution), and errors of  $\pm 10 \mu\text{m}$  were observed for the object at position 5. Similar results were obtained in [119]. It was discussed in [119] that this can be due to three reasons: Feldkamp effect, focus or rotary axis drifts in X and Y directions (for orientation see figure 5.19). The impact of the focus drift is most pronounced at high magnifications.

Assuming a conventional value of  $5\text{ }\mu\text{m}$  for focus drift, the geometry of the CT system under study and the detector properties, will cause an error  $\Delta d$  of approximately 0.2 pixels at a magnification level of 7.5. The relationship between the error  $\Delta d$ , focus spot size  $\Delta f$  and magnification  $m$  is given in equation 5.9. In principal, the magnitude of the drift is the same at all magnification levels, nevertheless, the impact of the drift on determination of sphere center is smaller at smaller magnification levels. Therefore, the drift effect may be neglected in our case.

$$\Delta d = \Delta f \cdot (m - 1) \quad (5.9)$$

This error  $\Delta d$  is in fact a shift of the center coordinate of the sphere in the projection, leading to an increased unsharpness in the reconstruction. When it comes to geometrical measurements, such unsharpness has a further effect on an increased form error.

Figure 5.20 shows measurement results of the relative *SD* parameter (normalized with respect to the length of a corresponding ball bar), where individual points in the graph represent length deviations determined for the five ball bars only (length deviations between spheres belonging to one rod), providing five measures at each position of the object. From the graph, several observations can be noticed. Firstly, the *SD* parameter increases in the direction from the central beam, i.e., for ball bars farther from the center. Thus, the best accuracy is achieved for measurements of the ball bar being in the central beam (i.e., BB3). A very good fit ( $R^2 = 0.99$ ) of five ball bar length deviations was calculated for measurements of the CT tree at all five magnification levels. The relative *SD* error is nearly symmetrical to a position of the BB3 being imaged in the central beam. Moreover, the positive and negative errors indicate a tilt of the rotary table axis, as it was experienced in the previous section. The orientation of the tilt of the rotary axis is schematically shown in figure 5.21. This can be explained as follows: at smaller magnification levels the source-object distance becomes bigger and lengths measured by CT are shorter, resulting in bigger voxel size, and thus the *SD* error is negative. A similar investigation was carried out and discussed in [120], where the authors attributed the error to a geometrical distortion of a detector image occurring in the plane of the detector array (the problem was observed on a similar detector type PaxScan 2520V with CsI scintillator, the detector at PTB is PerkinElmer 1620 with CsI scintillator). Furthermore, it is claimed that this is mainly caused by grains of the scintillator's layer which are not perfectly perpendicular to the panel. Thus, these may introduce local-dependent shift of the incident intensity. The authors developed a special distortion map which helped to eliminate the error.

It can be noticed from figure 5.20 that the relative *SD* error decreases at smaller magnification levels. This is due to the fact that at smaller magnification levels the impact of the rotary axis tilt becomes smaller, even though the tilt is the same.

Figure 5.22 shows three possible scenarios of a trend of errors when using the CT tree. First, in the ideal case (left figure) with no influences of the CT system (i.e., no Feldkamp effect or rotary axis tilt), there would be no error of the *SD* parameter for any of the measured lengths of the CT tree. In the case when the errors are caused by cone-beam angle in Y direction (Feldkamp effect) the errors yield the trend depicted in the middle figure. Due to the tilt of rotary axis, the different length of the ball bars of the CT tree does not cause additional errors. An indication of the trend of the errors caused by the tilt of the rotary table is shown in the figure on the right. It is assumed that there is a significant image unsharpness correlated with the Y-height due to the Feldkamp effect. An increased unsharpness may then lead to an underestimation of the ball's diameter but the sphere-to-sphere distance is quite robust

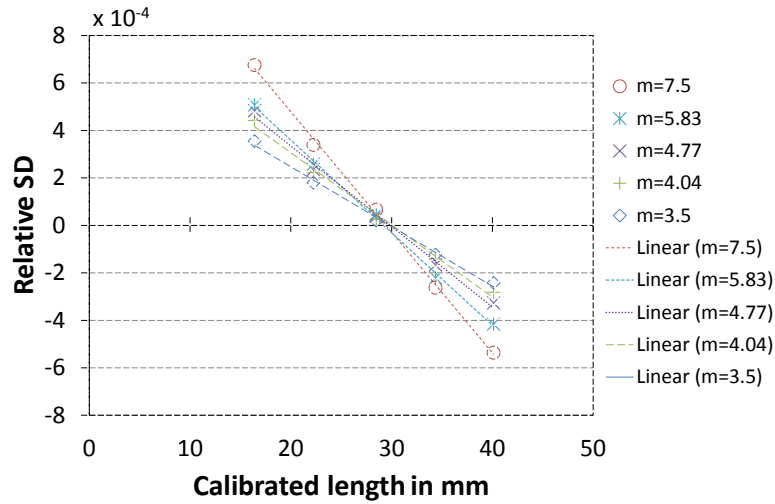


**Figure 5.20:** Measurement results of relative  $SD$  parameter (normalized with respect to the ball bar length) evaluated for individual ball bar measurements (horizontal lengths only) at five magnification levels.

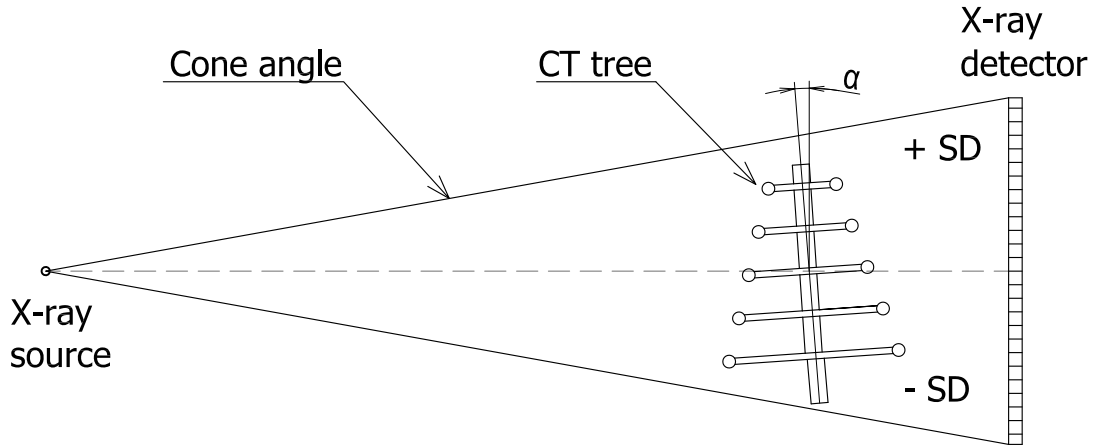


**Figure 5.21:** Orientation of the tilt of the rotary axis.

regarding threshold errors. Therefore, a symmetric behaviour is assumed.

The influence of the tilt is predominate in our case, because, in general, at high magnification levels the balls of the CT tree (considering only e.g. BB1 and BB5, bottom and upper ball bars respectively) are CT scanned under bigger opening angle compared to balls at low magnification level. Thus, it is expected that the form error of balls under bigger opening angle is bigger and vice versa. Figure 5.23 shows that this is not the case -  $PF$  errors are smaller at higher magnification and increases with decrease of magnification level.

Taking into account the magnitude of errors and calculating the relative error at the five magnification levels (normalized with respect to the voxel size), this was found to be always smaller than size of one voxel (considering, e.g., the biggest errors of  $22 \mu\text{m}$  at magnification of  $m=7.5$ , corresponding to a voxel size of  $26.7 \mu\text{m}$ , the relative error equals to  $22/26.7=0.82$  voxel, which is smaller than 1 voxel size. The relative error at other magnification levels is smaller than 0.82, as the absolute error is smaller and the voxel size is bigger.

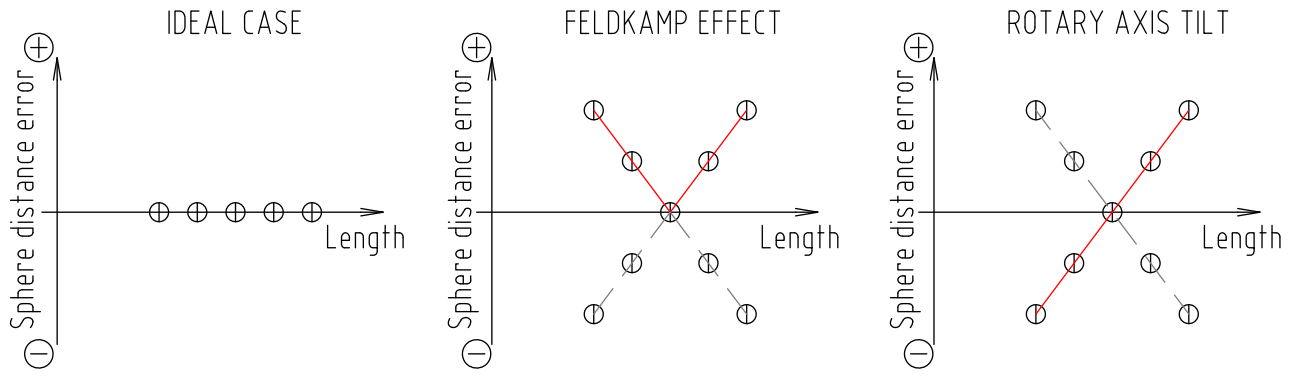


**Figure 5.22:** Scenarios explaining the general trend of errors. The error caused by one of the effects is either the one with full red line or dashed gray line.

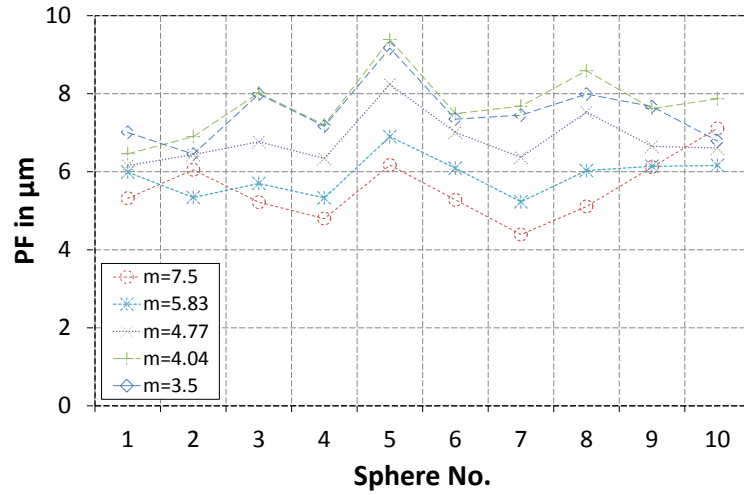


**Figure 5.23:** Measurement results of relative *PF* parameter (normalized with respect to the voxel size) at five magnification levels.

The error caused by the axis tilt will, in general, have an effect on: sharpness, resolution and accuracy. In particular, the tilt of the rotary axis causes (i) detrimental effects on the reconstruction images in X and Y directions exhibiting positional uncertainty of X-ray data in the reconstruction, provoking, e.g., occurrence of image artifacts and (ii) degradation of data in spatial resolution (Z direction), influencing the correction for scaling errors. These then lead to inaccurate dimensional measurements.

### 5.3.4 Conclusion

A procedure for the assessment of measurement errors in the measuring volume using the CT tree has been presented. By scanning the object at different magnification levels, quantification of errors occurring during CT acquisition was possible. The errors were assessed by calculating the *SD* parameter. Based on the results obtained, explanation for the nature of the sources was discussed. The errors were mainly due to the tilt of the rotary axis and Feldkamp effect.

## 5.4 Characterization of measurement errors of a CT system in the vertical direction using the CT tree

In this section, a procedure for characterization and quantification of errors in the vertical direction in the measuring volume using the CT tree is described.

### 5.4.1 Measurement setup

The assessment of the errors in the vertical direction is carried out by scanning of the object at five vertical levels (heights), shown in figure 5.24. The object was scanned in a vertical orientation so that each time one of the ball bars of the CT tree of a different length was placed in the central beam, highlighted by the red dashed horizontal line. The object was scanned at the highest possible

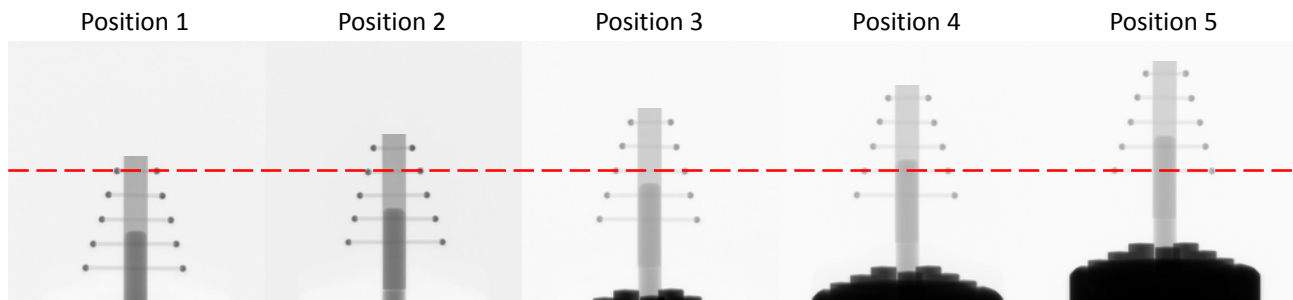


**Figure 5.24:** Measurement setup of the CT tree at five vertical positions in the measuring volume. At each position, a ball bar of a different length is positioned in the central beam, highlighted by the red dashed horizontal line.

Scanning parameters are summarized in table 5.7. The scanning parameters as well as positions of the object in X and Z direction were kept constant for all the CT scans, except of the vertical position (Y direction), in which the object was moved as mentioned earlier (for orientation see figure 5.19).

**Table 5.7:** An overview of scanning parameters. Variables changed at individual positions are highlighted in bold.

| Parameter              | Unit          | Position 1   | Position 2   | Position 3   | Position 4   | Position 5   |
|------------------------|---------------|--------------|--------------|--------------|--------------|--------------|
| Voltage                | kV            | 105          | 105          | 105          | 105          | 105          |
| Power                  | W             | 11.6         | 11.6         | 11.6         | 11.6         | 11.6         |
| Detector matrix        | pixel         | 2000 x 2000  | 2000 x 2000  | 2000 x 2000  | 2000 x 2000  | 2000 x 2000  |
| Detector pixel size    | $\mu\text{m}$ | 200          | 200          | 200          | 200          | 200          |
| Integration time       | ms            | 1415         | 1415         | 1415         | 1415         | 1415         |
| No. of views           |               | 1000         | 1000         | 1000         | 1000         | 1000         |
| No. of image averaging |               | 1            | 1            | 1            | 1            | 1            |
| Vertical position      | mm            | <b>174.5</b> | <b>184.3</b> | <b>194.6</b> | <b>204.6</b> | <b>214.7</b> |
| Magnification factor   |               | 3.7          | 3.7          | 3.7          | 3.7          | 3.7          |
| Uncorrected voxel size | $\mu\text{m}$ | 54.1         | 54.1         | 54.1         | 54.1         | 54.1         |

### 5.4.2 Data evaluation

Because of the similarity of the method for surface determination, alignment of the object and definition of evaluation parameters, described in section 5.3, these will not be described here.

#### Scale error correction

All the CT scans were corrected for scaling errors by applying linear regression (a linear trend line is fit through the data set and intersects in a coordinate [0,0], as presented in section 4.2.7. The linear regression coefficient  $a$  was obtained by fitting a linear line through the data set of all five positions. Using the CT tree, a total of 45 measuring lengths can be evaluated at the same time. This means, that the whole data set includes a total number of  $5 \times 45 = 225$  measured lengths ( $5 = 5$  vertical positions).

### 5.4.3 Results and discussion

Maximum errors of the  $SD$  parameter of approximately  $\pm 30 \mu\text{m}$  were observed. This was, however, different at each position of the object. Bigger errors were associated with measurements of the CT tree at the borders with the detector, under bigger opening angles. Figure 5.25 presents results of the corrected data sets - length deviations of the CT tree measured at all the five vertical positions. In particular, results of the relative  $SD$  error (normalized with respect to the ball bar length) are shown. Linear trend of the errors at different heights of the object in the measuring volume is very similar to the previous case, i.e., when the CT tree was scanned at different magnification levels. Moreover, the range of the relative  $SD$  parameter is dependent on the position at which the object was scanned. This means that positive  $SD$  errors are found for positions of the object in the upper region and vice versa, i.e., the positive errors are measured for ball bars imaged up from the central plane and negative errors for ball bars imaged down from the central plane. Source of the errors are basically the same as in the previous case, i.e., the main influence factor is the tilt of the rotary table and then it is the Feldkamp effect.

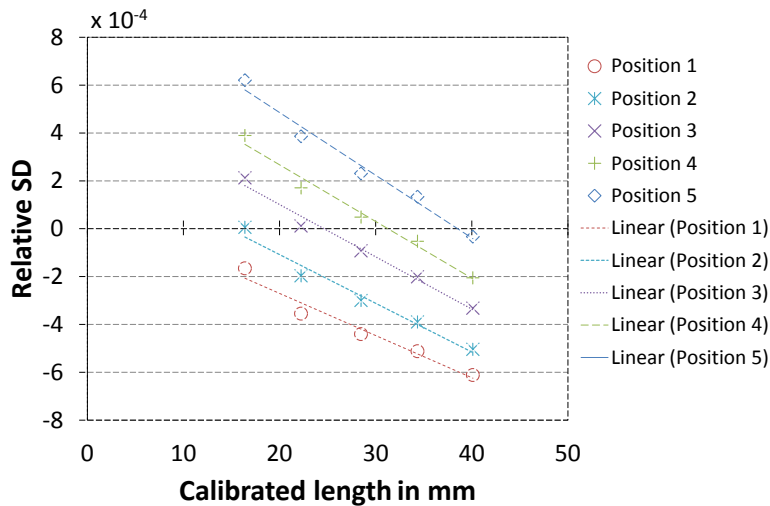
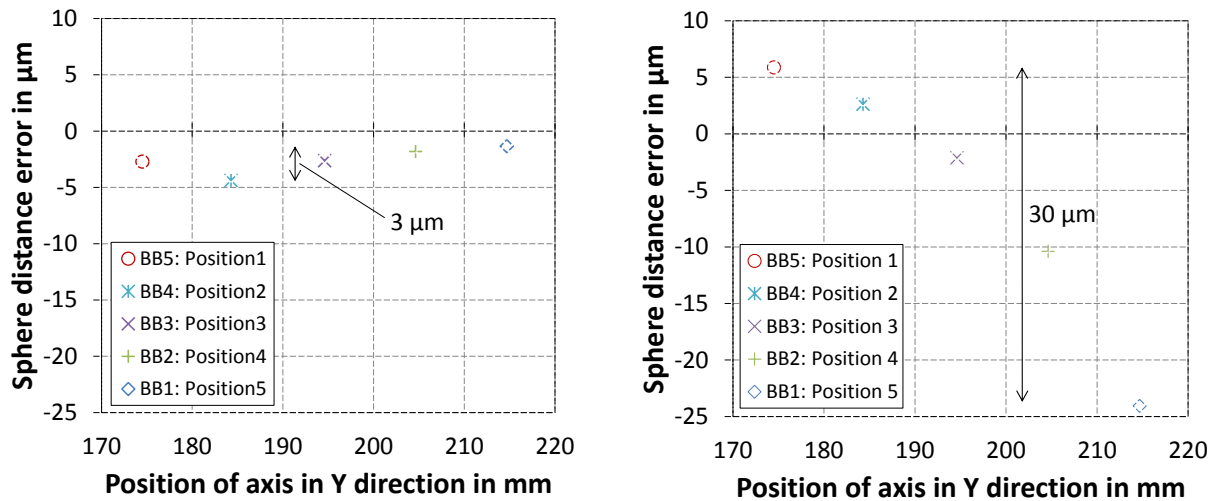


**Figure 5.25:** Measurement results of relative  $SD$  parameter (normalized with respect to the ball bar length) evaluated for individual ball bar measurements (horizontal lengths only) at five vertical positions. The correction of the CT data for scaling errors was done for data sets with all 225 length deviations (i.e., all five data sets are corrected simultaneously).



Figure 5.26 presents results of relative *SD* parameter, considering measurements of ball bars in the central beam only at all five positions. This implies that measurement of BB5 at position 1, BB4 at position 2, etc. (see figure 5.24) was taken into account for the evaluation. Figure 5.26(a) shows situation when a data set of all the 225 length deviations (5 positions x 45 lengths) was considered simultaneously for correction of scaling errors. Correction of the data set for scaling errors in figure 5.26(b) was done for only 45 length deviations, i.e., the correction was done at each position of the CT tree individually. Measurement errors of 3  $\mu\text{m}$  and 30  $\mu\text{m}$ , respectively, can be observed for the two scale error correction approaches. This confirms the fact that measurements performed in the central beam, i.e., in the direction of the X-ray beam perpendicular to the detector, yield the highest accuracy. This error of the *SD* parameter is obviously caused by the tilt error as well as Feldkamp effect. The conclusion is that if the CT tree was not moved in the magnification axis (Z direction), but only along the vertical axis (Y direction), the scale error correction shall be done for all five positions at the same time, otherwise errors due to the positioning of the object in the CT volume occur (unless errors due to the tilt or Feldkamp effect can be excluded).



(a) Scale error correction for data sets at all five positions considered together (5 x 45 = 225 length deviations).

(b) Scale error correction for data sets at each of the five positions considered separately (45 length deviations).

**Figure 5.26:** Measurement results of *SD* parameter evaluated only for measurements of the ball bars being in the central beam.

#### 5.4.4 Conclusion

A procedure for the assessment of measurement errors in the measuring volume using the CT tree has been presented. By scanning the object at different different vertical heights, quantification of errors occurring during CT acquisition was possible. The errors were assessed by calculating the *SD* parameter. Based on the results obtained, explanation for the nature of the sources was discussed. The errors were mainly due to the tilt of the rotary axis and Feldkamp effect. It was also discussed that if errors due to, e.g., tilt or Feldkamp are present in the measuring volume, it is important to correct the voxel model for scaling errors by scanning the reference object in the central beam, otherwise measurement results will be affected by these effects.

Previous experimental results from other researchers [117, 121] have shown that there is no noticeable change in measurement dimensions when an object is mounted at different orientations in the measuring volume of the CT scanner. This implies that the object can be positioned anywhere and at any orientation within the scanning volume as long as it remains within the field of view of the detector at all projection angles. However, this is true only for a case where there is no error in geometrical parameters (e.g. rotary axis tilt). This is also based on another premise that there are no cone-beam artifacts.



# Chapter 6

## Experimental study

This chapter discusses an experimental work carried out at the Technical University of Denmark (DTU), as well as at institutes (Physikalisch-Technische Bundesanstalt (PTB) and Danish Technological Institute (DTI)) and companies (Novo Nordisk A/S) closely related to the CIA-CT project. Investigations on image-related influence factors (integration time, number of image averaging and number of projection views), scale error correction methods, measurements on voxel and surface data, evaluation strategies, suitability of CT for tolerance verification and application of a substitution method for uncertainty estimation of dimensional CT measurements are presented in the chapter. This chapter is divided into the following sections:

- Investigation on the relationship between scanning time and dimensional measurements of an industrial part (section 6.1)
- Investigation on the influence of scale error correction (section 6.2)
- A study on evaluation strategies by estimation of measurement uncertainty (section 6.3)
- Tolerance verification of industrial parts (section 6.4)
- Application of the substitution method using calibrated workpieces for uncertainty estimation of dimensional and geometrical measurements (section 6.5)

## 6.1 Investigation on the relationship between scanning time and dimensional measurements of an industrial part

It was shown in section 5.2 that minimization of errors down to  $10\text{ }\mu\text{m}$  can be systematically achieved by optimizing scanning parameters. This was, however, investigated for a specific "ideal" reference object and applying an alternative design of experiment (DOE). In this case study, the intention is to apply a "classical" DOE approach, where individual factors are the scanning parameters.

The objective of this case study is to investigate the relationship between scanning time and dimensional measurements of an industrial part (component of a dose engine, introduced in section 4.3). Because the scanning time, determined by scanning parameters, directly influences image quality - *noise*, the aim is to quantitatively assess its influence on dimensional and geometrical measurements of the industrial object. With this approach, significant reduction of the scanning time may be achieved, depending on fulfilling part's specifications (tolerance limits).

### 6.1.1 Design of experiment

A full factorial  $2^3$  design of experiment (DOE) was carried out. The following three factors influencing image quality were chosen: integration time ( $t$ ), number of image averaging ( $i_{\text{avg}}$ ) and number of views ( $V$ ). All the factors were specified at two levels (low (-1) and high (+1)), as presented in table 6.1. The design is randomized which helps to ensure that the model meets certain statistical assumptions. Completely assessed DOE plan is shown in table 6.2, including all scanning parameter set. The DOE was created in statistical software Minitab Release 14.1. Column Run Order in the table indicates the order in which the data are collected. The total scanning time  $T$  in the table is calculated using equation 6.1. We know from section 5.2 that the selected parameters ( $t$ ,  $i_{\text{avg}}$ ,  $V$ ) are function of pixel noise according to equation 5.4. Figure 6.1 shows this relationship - the noise becomes smaller with increase of scanning time.

**Table 6.1:** A full factorial  $2^3$  design of experiment (DOE).

| Factor                                      | Level |      |
|---|-------|------|
|   | -1    | +1   |
| Integration time, $t$ in s                  | 0.708 | 2    |
| Number of image averaging, $i_{\text{avg}}$ | 1     | 4    |
| Number of views, $V$                        | 800   | 1600 |

$$T = \frac{t \cdot i_{\text{avg}} \cdot V}{60} \quad (6.1)$$

Before each of the experimental runs of the DOE and for individual scanning settings as indicated in table 6.2, shading correction of the detector was performed in the acquisition software, providing projection images with high contrast. This is very important to have in mind, since, generally speaking, a change in the integration time of the detector yields different contrast. Therefore, if the shading correction was not done for each parameter set before scanning, projection images for

**Table 6.2:** Experimental plan including scanning parameters, calculated total scanning time and pixel noise.

| Run Order | Voltage<br>$U$<br>in kV | Power<br>$P$<br>in W | Integration time<br>$t$<br>in s | No.of image averaging<br>$i_{\text{avg}}$ | No.of views<br>$V$ | Scanning time<br>$T$<br>in min | Magnification factor<br>$m$ | Uncorrected voxel size<br>$s$<br>in $\mu\text{m}$ | Pixel noise<br>$\sigma_{\text{pn}}$ in<br>$\text{mm}^{-2} \cdot (\text{mA} \cdot \text{s})^{-1/2}$ |
|-----------|-------------------------|----------------------|---------------------------------|---|--------------------|--------------------------------|-----------------------------|---|--|
| 1         | 193                     | 10.8                 | 2                               | 4   | 1600               | 213                            | 7.5                         | 26.7  | 1.01   |
| 2         | 193                     | 10.8                 | 2                               | 4   | 800                | 107                            | 7.5                         | 26.7  | 1.43   |
| 3         | 193                     | 10.8                 | 0.708                           | 4   | 800                | 38                             | 7.5                         | 26.7  | 2.40   |
| 4         | 193                     | 10.8                 | 0.708                           | 1   | 1600               | 19                             | 7.5                         | 26.7  | 3.40   |
| 5         | 193                     | 10.8                 | 0.708                           | 4   | 1600               | 76                             | 7.5                         | 26.7  | 1.70   |
| 6         | 193                     | 10.8                 | 2                               | 1   | 800                | 27                             | 7.5                         | 26.7  | 2.86   |
| 7         | 193                     | 10.8                 | 0.708                           | 1   | 800                | 9                              | 7.5                         | 26.7  | 4.81   |
| 8         | 193                     | 10.8                 | 2                               | 1   | 1600               | 53                             | 7.5                         | 26.7  | 2.02   |

Note: Copper (Cu) pre-filter 0.5 mm was used.

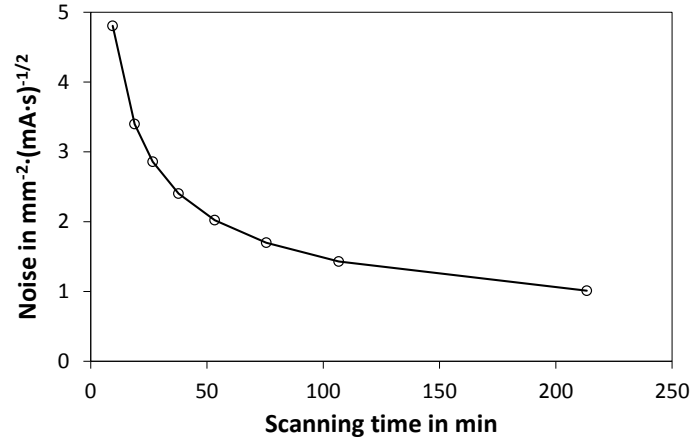


**Figure 6.1:** Relationship between the noise (equation 5.4) and the total scanning time (equation 6.1).

some scanning settings would be too dark or too bright, resulting in no satisfying results and possibly low quality reconstruction model.

### 6.1.2 Experimental setup

The experiment was carried out using a Nikon Metrology XT H 225 ST CT scanner at PTB. FDK based reconstruction was done using software CT Pro V2.2 SP2 provided by Nikon Metrology, too. Beam hardening correction preset value 5 (on a scale between 1 and 6) and noise reduction preset value 2 were used for correction of the projection images. The preset value 5 selected in the reconstruction software reduces beam hardening artifacts which appeared on reconstruction images, as choosing higher preset value will imply a polynomial fit of higher order. It was discussed in [122] that selection of a proper preset value for beam hardening correction can improve the image quality and, in some cases, improve the absolute accuracy.

The object was scanned in a nearly vertical orientation (see figure 6.2), and was freely attached to a fixture made of polystyrene, a material widely used as a fixture in CT applications for its high penetrability. This orientation of the part reduces the occurrence of beam hardening artifacts. The

experiment could not be carried out in a single day due to the time required for CT scanning, as it is indicated in table 6.2. For this reason, a special care was taken on similarity conditions in each day of experiment, including pre-conditioning of the X-ray tube, stabilization of the temperature inside the scanner, normalization of the detector for changed scanning settings (integration time) and positioning the object (the object was in fact not moved at all from the fixture and the rotary table before the end of the experiment).

### 6.1.3 Data evaluation

#### Surface determination

For determination of the surface, inspection software VG Studio Max 2.2 was used. Adaptive (local) surface threshold method was applied for estimation of the surface. A search distance (explained in section 2.3.3) of 0.29 mm was used to cover all the surface of the item, which in some parts exhibited enhanced noise.

#### Definition of measurands

Diameters, lengths and several geometrical tolerances like roundness, flatness, coaxiality and symmetry, were taken into account for the assessment of the influence of scanning parameters on dimensional and geometrical measurements. Measurands are schematically shown in figure 6.3, and their definition is in more details provided in the next section.

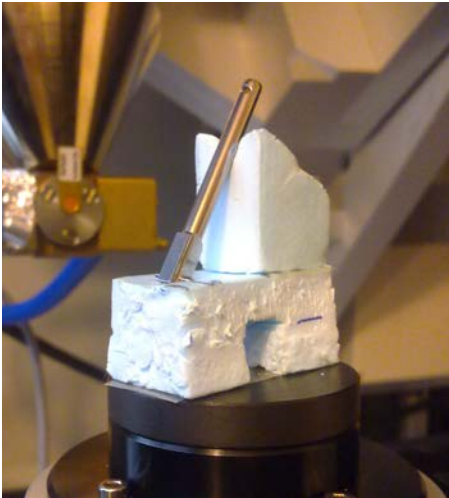


**Figure 6.2:** Measurement setup of the object in the CT scanner.

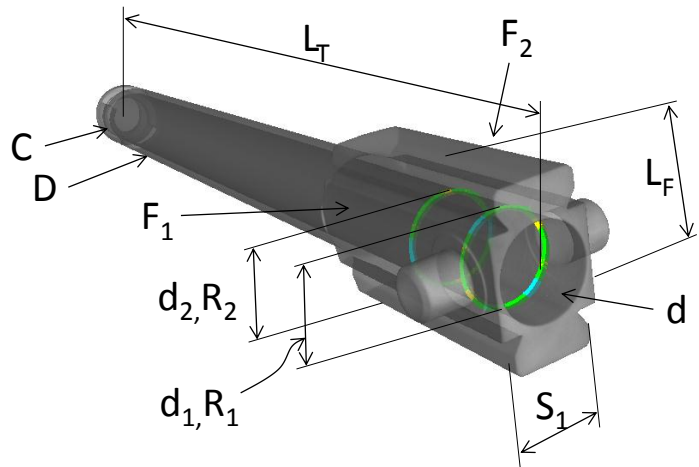


**Figure 6.3:** Definition of measurands.

- 2 x Diameter  $\varnothing 3.4$  mm ( $d_{1,2}$ ) and 2 x Roundness ( $R_{1,2}$ ): Diameter and roundness measurands are defined by creating Circle features and fitting approximately 1000 points, equally distributed around the hole circumference. Both measurands are measured at height 2 mm and 5 mm, from the flat end of the object.
- Length 6.3 mm ( $L_F$ ): Length is defined as a distance between two parallel planes created on the flat surfaces by fitting approximately 1000 points, in a reasonable distance from edges. The length is measured in normal direction to the surface.

- Length 46.4 mm ( $L_T$ ): The total length of the object is defined as a distance between two parallel planes created on both sides of the object, by fitting approximately 1000 points equally distributed on flat surfaces at both ends. Length is measured in the direction parallel with the axis of the inner cylinder  $d$ .
- 2 x Flatness ( $F_{1,2}$ ): Flatness is measured on two parallel surfaces by fitting approximately 1000 points, approximately equally distributed, in a reasonable distance from edges. Flatness is calculated as a difference between maximum and minimum fit points.
- Coaxiality ( $C$ ): Coaxiality of the axis of a cylindrical surface in a vicinity of the thread at one end of the object, defined by creating a cylinder feature by fitting approximately 1000 points, is measured with respect to the axis of another cylindrical surface  $d$  (inner hole of the object) - created as a cylinder feature by fitting approximately 1000 points (the surface at the end of the object is not considered).
- 2 x Symmetry ( $S_{1,2}$ ): Symmetry between two planes, defined by fitting approximately 1000 points on the flat surfaces (edges of the object are not considered) is measured with respect to the axis of a cylindrical surface (outer diameter  $D$ ), defined by fitting approximately 1000 points on the surface.

### Scale error correction

Because the intention of this study was to compare individual image quality factors (integration time, number of image averaging and number of views), and highlight their effect on measurands, it was assumed that the uncorrected CT data (for scaling errors) has no impact on the measurand. This is also due to the fact that real tolerances cannot be delivered due to confidentiality agreement with a company providing the object under study. If we were to carry out the scale correction, we would need an object featuring balls (e.g. ball bar or ball beam) made of a material with higher absorption, e.g., steel balls, or do the correction using calibrated features (as discussed in section 3.3.1).

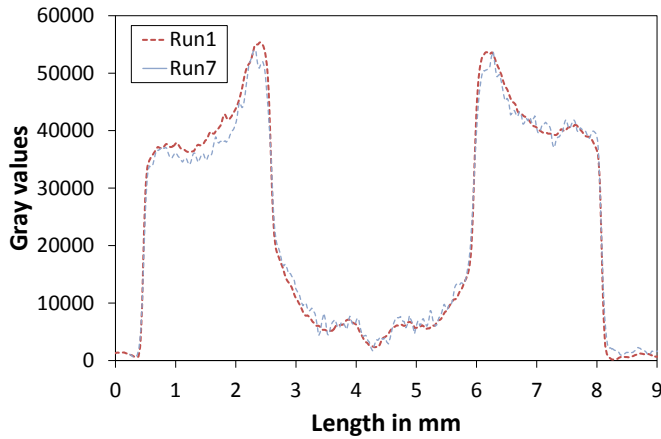
## 6.1.4 Results and discussion

Figure 6.4 shows profiles taken in the area strongly affected by the occurrence of the beam hardening and scattered radiation. In particular, Run 1 and Run 7 of the experiment, i.e., the longest CT scan ( $T=213$  min) and the shortest ( $T=9$  min) scan respectively, are shown. Two important observations from the figure can be noticed:

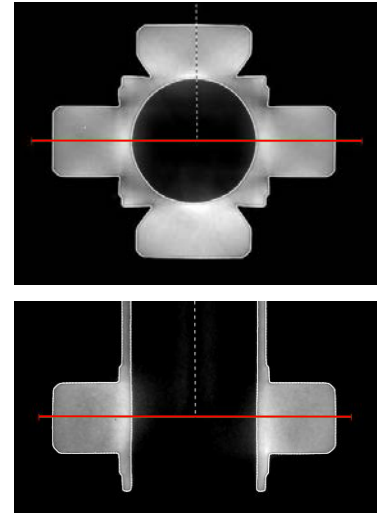
- Strong beam hardening artifacts in the direction towards the bore (the two characteristic peaks - increase of gray values - in the graph). Artifacts in this area are also caused by scattered radiation.
- Differences in the variability of the profiles ("roughness" of the profile lines). This is mainly caused by noise in the CT data. Applying filters in the software for run 7, e.g. Gaussian, could possibly smoothen the profile line.

Volume models of the object for experimental runs 1 and 7 are shown in figure 6.5. The two runs of the experiment are those with the longest ( $T=213$  min) and the shortest ( $T=9$  min) scanning time respectively. Different "pseudo roughness" of the part caused by the noise in the CT data can be clearly noticed, depending on the selection of the scanning parameters. This noise in the CT data





(a) Line profiles.



(b) Indication where the two profiles were measured.

**Figure 6.4:** Profiles taken at a distance of 2 mm from the bottom surface of the object where strong image artifacts due to the beam hardening and scattered radiation occur. The graph shows the best case (Run 1:  $T=213$  min) and worst case (Run 7:  $T=9$  min), respectively.

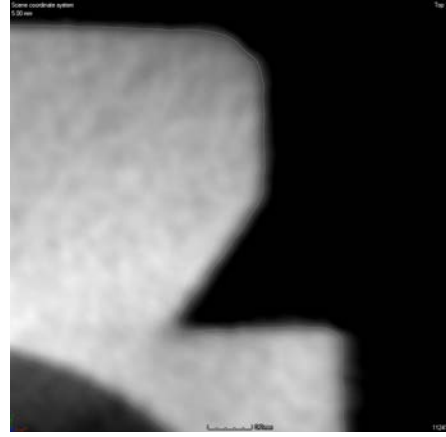
decreased at higher scanning times, and the volume models became smoother. Only by looking at this figure, one can expect differences in dimensional measurements.

Figure 6.6 presents results of the DOE experiment. In particular, a difference between a maximum and a minimum measured dimension ( $\Delta$ ) is shown for each measurand. It can be observed that maximum deviations of approximately  $20 \mu\text{m}$  are obtained for geometrical measurements and deviations up to  $8.6 \mu\text{m}$  for dimensional measurements. This result can be considered not to be significant, when considering the great variety of scanning settings (for orientation see table 6.2). Moreover, no significant effects were observed for these measurements, i.e., no evident relationship between the image quality determined by the scanning parameters (integration time, number of image averaging and number of images) and dimensional measurements have been noticed.

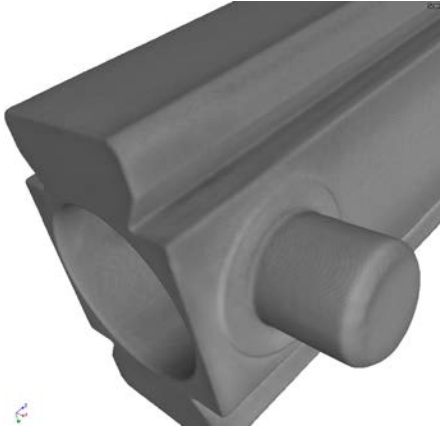
A slightly more distinct agreement between the image quality and geometrical measurements was realized for measurements of roundness  $R_1$  (figure 6.7) (measured in the area where the object exhibits the biggest penetration length in between two pins, for orientation see figure 6.3 and figure 6.4) and flatness  $F_1$  (figure 6.8) measured at one of the flat surfaces of the object). Main effects plots and Pareto charts were employed to represent which parameters have a significant influence on the measurand. Main effects plots for both roundness and flatness show that by selecting the factors (scanning parameters) at their high levels (for orientation see table 6.1), results in smaller roundness and flatness. Still, the range of measured values in both cases is relatively small, considering the excessive increase of the total scanning time by selecting factors at their high level (+1). This is also confirmed with the Pareto plots, which, in principle, should highlight the most influencing factors for a specific measurand. However, the Pareto chart indicates that none of the two factors has a significant effect on the measurand. For example, looking at the chart, all the three factors and their interactions are found too far from being significant at a considered confidence level of 95% (vertical



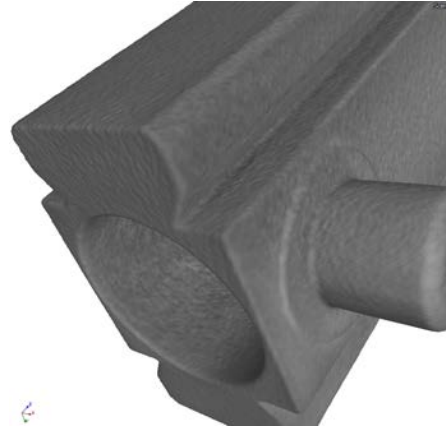
(a) Reconstruction image from Run 1 ( $T=213$  min).



(b) Reconstruction image from Run 7 ( $T=9$  min).



(c) 3D volume from Run 1 ( $T=213$  min).

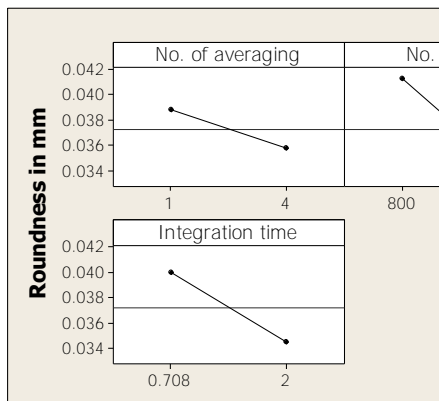
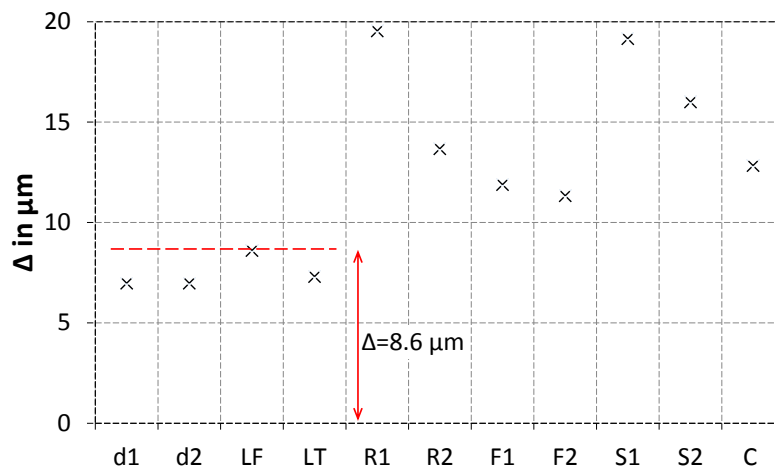


(d) 3D volume from Run 7 ( $T=9$  min).

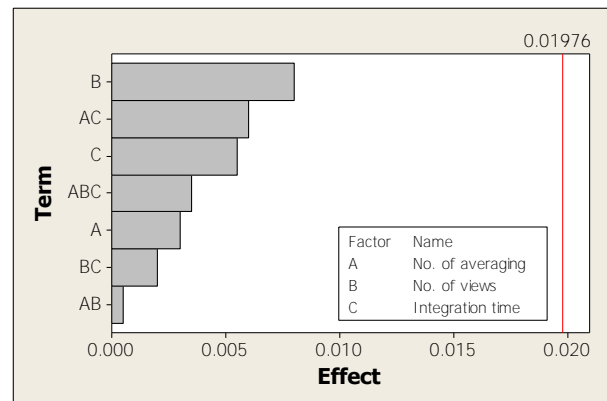
**Figure 6.5:** Comparison of two experimental runs (Run 1:  $T=213$  min and Run 7:  $T=9$  min): Reconstruction images are shown in (a) and (b) and 3D models are shown in (c) and (d). Qualitative differences can be observed on both reconstruction images and 3D models. Higher "pseudo roughness" of Run 7 is evident.

red line). Moreover, the Pareto chart indicates the significance rating of the effect of the factors and their interactions, ordered by the effect magnitude from largest to smallest. One can notice that the rating is more or less random for the two measurands considered.

Influence of the total scanning time  $T$  on flatness measurements ( $F_1$  and  $F_2$ ) is also shown in figure 6.9. It is expected that with increase of the scanning time the surface becomes smoother (smaller roughness) and less distorted, and thus the flatness becomes smaller, too. In our case, good agreement between the scanning time and dimensional measurements of the flatness can be observed in the figure. Flatness decreases nearly linearly ( $R^2$  greater than 0.8 showing reasonably good fit) with increase of the scanning time. Average flatness ( $F_1$  and  $F_2$ ) of approximately  $53 \mu\text{m}$  for a 9 min CT scan and average flatness of approximately  $42 \mu\text{m}$  for a 213 min CT scan are measured. As can be seen, the difference is, however, small, considering the time spent on CT scanning of the part.



(a) Main effects plot.



(b) Pareto chart of the effects.

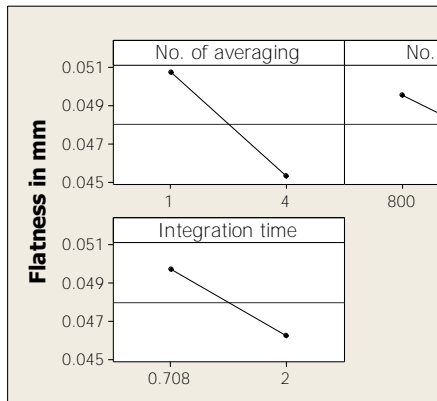
**Figure 6.7:** Statistical results of roundness measurements.

## 6.1.5 Conclusion

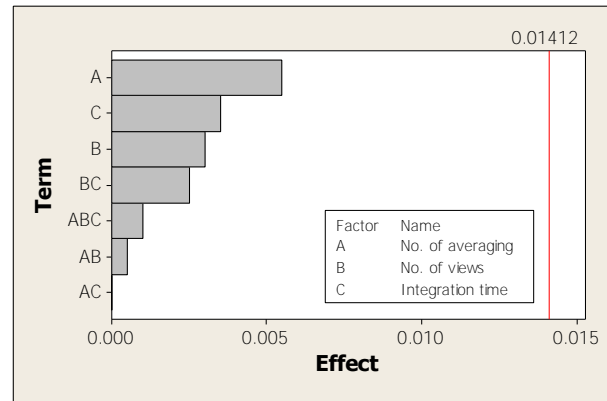
An experimental plan was designed to investigate the influence of image quality - noise - on dimensional measurements carried out on an industrial object (component of a dose engine). Image quality was determined by a combination of scanning parameters which determined the total scanning time.

The following conclusions can be drawn:

- Qualitative inspection of the reconstructed volumes from individual experimental runs of the assessed DOE was performed and indicated image improvement for CT scans performed with scanning settings (factors) at their high levels (+1). Experimental runs at low settings (-1) yielded "rough" pseudo surface and increased noise in the CT data. This "roughness" was improved (visually) with increase of the total scanning time.
- Performing geometrical and dimensional measurements resulted in nearly no significant effects



(a) Main effects plot.



(b) Pareto chart of the effects.

**Figure 6.8:** Statistical results of flatness measurements.

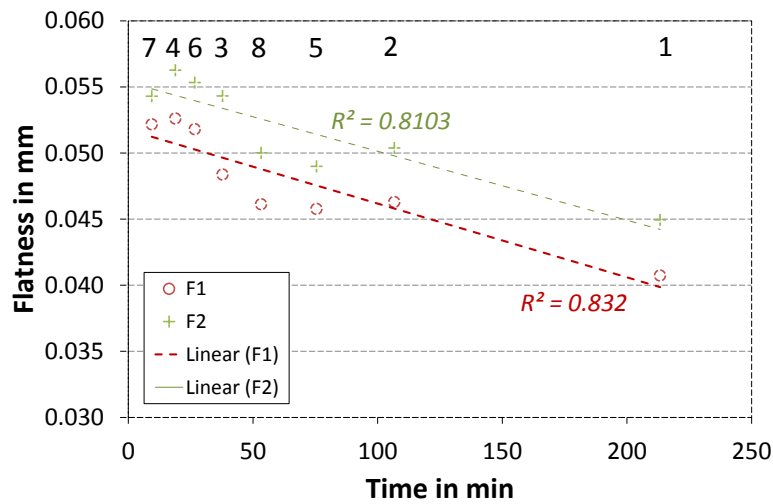


**Figure 6.9:** Measurement of flatness as a function of scanning time. The numbers in the upper part of the graph represent the Run number according to the DOE plan presented in table 6.2.

of any of the selected scanning parameters. Differences of approximately  $20 \mu\text{m}$  for geometrical measurements and differences up to  $8.6 \mu\text{m}$  for dimensional measurements for individual runs of the experiment were obtained, however, without any indication of any of the factors being significant.

- Measurements of flatness and roundness indicated a trend, showing that by selecting factors at their high levels, resulted in smaller measured values. The range of values was, however, not big, being approximately  $6\text{--}8 \mu\text{m}$ . Again, statistical analysis has shown that none of the factors have a significant influence on the measurement result. Moreover, rating (depending on factor significance) of the factors for flatness and roundness measurements indicated random behaviour.
- The overall conclusion is that in the present case study and for the CT system under investigation, the influence of the image quality - noise, determined by the selection of scanning settings, is negligible. Therefore, in principle, there is no need to spend much time for scanning

of the object and to obtain high resolution (in terms of quality) CT scans, as results for scans of 9 minutes and 213 minutes are in a small range. However, since the tolerance limits were confidential, we cannot say with certainty if even such small measured differences between individual runs of the DOE will put the measured result out of tolerance.

## 6.2 Investigation on the influence of scale error correction

The main objective of this study is to quantify the influence of scale error correction procedure on dimensional measurements of a plastic part. The plastic part under study is a standard LEGO brick featuring 2 x 4 knobs, shown in figure 6.10. It was discussed in section 3.3.1 that systems with misalignment errors need to be corrected for scaling errors, as it is done, e.g., in case of CMMs. The correction relies upon correcting (rescaling) the voxel size using a reference object with known (calibrated) length(s). In this study, two reference objects - *CT tree* and *CT tetrahedron* - are used.

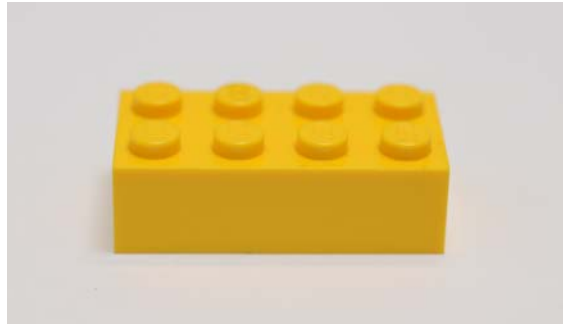


**Figure 6.10:** Lego brick (2 x 4 knobs).

During long acquisition times the stability of the X-ray source may be influenced by a focus drift. This may happen because of temperature changes inside of the X-ray tube and, in particular, dimensional variations of the tube due to the thermal expansion in the presence of heat [123, 124]. So, for long acquisition times, the focus drift may become a critical parameter. Therefore, it is suggested to scan the reference object before and after scanning of the object under study. In this case, the influence from the focus drift or errors due to anisotropy is compensated. The specific aim of this study is to investigate whether scanning of the reference object before and after is necessary and into what extent or if correction done using the reference object being scanned after scanning of the object is sufficient. In this case, reduction of scanning time and cost could be achieved.

### 6.2.1 Calibration of the Lego brick

In order to be able to make reasonable statements on results from CT scanning of the part, first, we need to make a link to measurements from a more accurate and traceable machine, in our case a tactile CMM. The calibration of the Lego brick was carried out using a Zeiss OMC 850 tactile CMM with stated  $MPE_E = (3 + L/250) \mu m$  ( $L$  in mm), in a temperature controlled laboratory. The average measured temperature during the calibration was  $19.6 \pm 0.3^\circ C$ . No temperature correction of the results to  $20^\circ C$  was done. A total of seven measurement series were performed over a period of three weeks to check the stability of the brick. Each measurement series comprised of four repetitions. Two probes of diameter  $\varnothing 0.8$  mm and 20 mm long were employed. The setup for measurement of the Lego brick using CMM, configuration of the probing system and definition of the coordinate system can be seen in figure 6.11. The Lego brick was glued on a steel block which was clamped in a vice. A 2-component epoxy resin was used to attach the brick to the block, ensuring a stable connection. A special attention was paid on measurements of the flatness of the object, as form error of approximately  $20 \mu m$  was measured. The plane on top flat surface of the Lego brick was measured with a high point density (approximately 120 measuring points) to calculate the flatness

form error. The color coded single point deviation can be seen in figure 6.12. Thus, the definition of the measurands (calibrated features) was critical, as it is explained in the following.

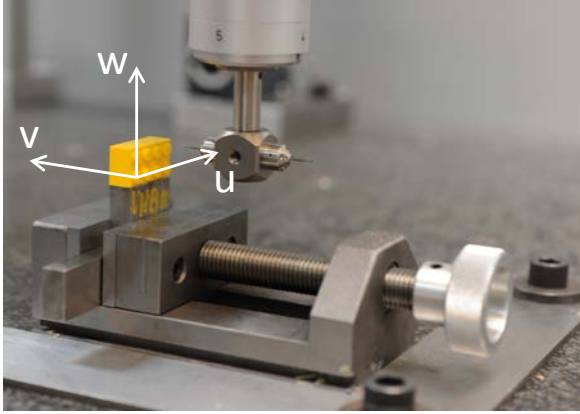


**Figure 6.11:** Measurement setup for Lego brick calibration on the CMM.

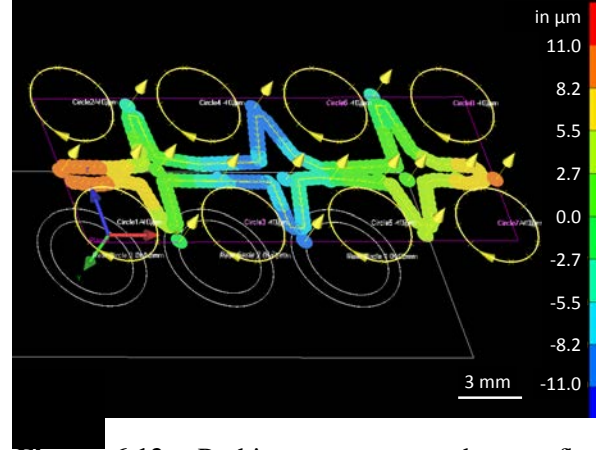


**Figure 6.12:** Probing strategy on the top flat surface of the Lego brick for assessment of flatness form error.

### Definition of measurands (calibrated features)

- **Knob diameter:** Diameter of each knob was measured with a 12-point probing strategy as a circle (points were equally distributed around the circumference of the knob in one level) at a height of 1 mm in negative  $v$ -direction (for orientation see figure 6.11), determined at the top flat surface of the Lego brick. Due to the relatively big flatness ( $20 \mu\text{m}$ ) of this surface, the diameter was also measured at height  $\pm 10 \mu\text{m}$  from  $v=1 \text{ mm}$ . An average value was considered for the evaluation. Circles were fitted following least square method.

Standard uncertainty for measurements of the knobs diameter was calculated to be  $1 \mu\text{m}$  at  $1\sigma$  level. Maximum standard uncertainty of all eight knobs was considered.

- **Distance between knob centres:** Distance between each couple of cylindrical knobs was measured from the center of the circles, previously defined for diameter measurements. In total, 28 distances are measured.

Standard uncertainty for measurements of the distance between individual knobs was calculated to be  $1 \mu\text{m}$  at  $1\sigma$  level. Maximum standard uncertainty of all lengths between knobs was considered.

### 6.2.2 Experimental setup

The experiment was carried out using a Nikon Metrology XT H 225 ST CT scanner at PTB. FDK based reconstruction was done using software CT Pro V2.2 SP2 provided by Nikon Metrology, too.

Two reference objects were used in this study: CT tetrahedron (a well-established reference object developed by PTB, with nominal diameter of spheres  $\varnothing 3 \text{ mm}$  (see figure 6.13(a)) and CT tree (DTU, introduced in section 4.2, see figure 6.13(b)). Positioning and orientation of the Lego brick during CT scanning is shown in figure 6.13(c).



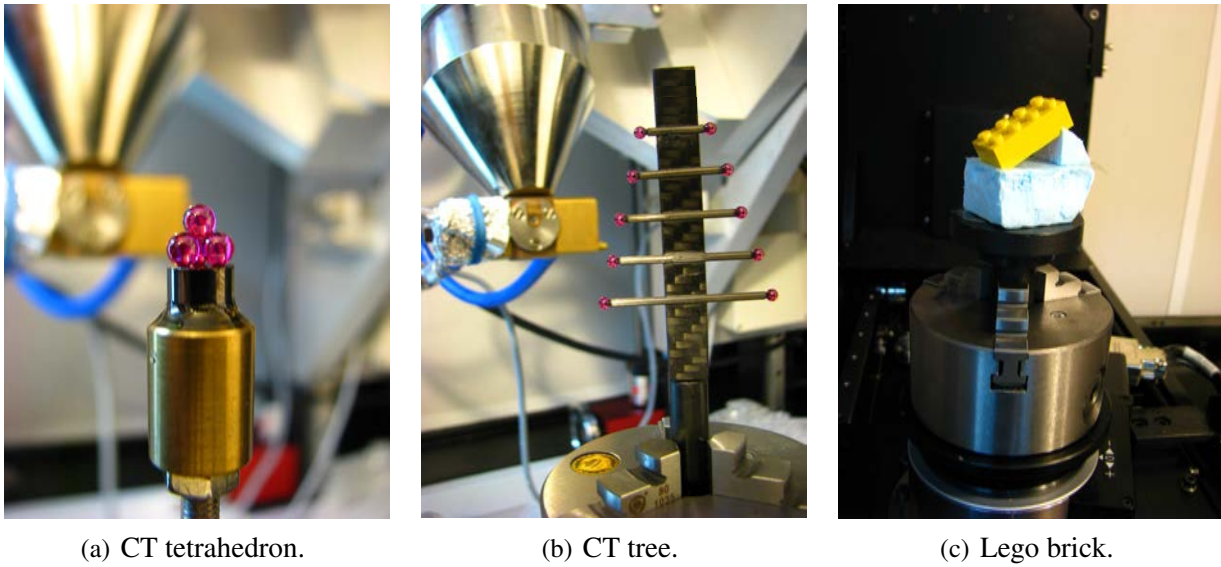


**Figure 6.13:** Measurement setup for CT scanning of the reference objects (a,b) and the Lego brick (c).

Scanning sequence is schematically shown in figure 6.14. First, reference object (CT tetrahedron or CT tree) was scanned, followed by scanning of a real part and reference object again. This measuring

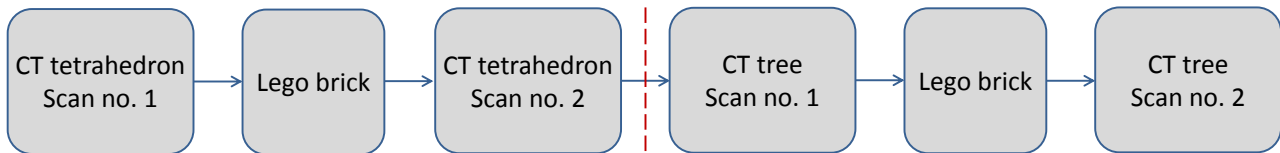


**Figure 6.14:** Scanning sequence: Reference object - Real part - Reference object.

In order to eliminate unwanted errors due to, e.g., misalignment of the rotary axis, there was no movement of the rotary table in between any of the three scans (1. reference object (before), 2. Lego brick, 3. reference object (after)). This means that both objects were positioned manually on the rotary table and adjusted accordingly, based on the projection images, being all approximately in the center of rotation, as shown in figure 6.15.

Scanning parameters selected for the Lego brick and both reference objects are summarized in table 6.3. The same scanning parameters were applied to all the CT scans which is a prerequisite for scale error correction. Highest geometrical magnification of 7.04 was chosen, enabling to acquire volumes of both the reference objects and the Lego brick.

### 6.2.3 Data evaluation

#### Surface determination

For determination of the surface, inspection software VG Studio Max 2.2 was used. For Lego brick and CT tetrahedron, first, automatic (global) surface determination (iso-50%) was used and then an



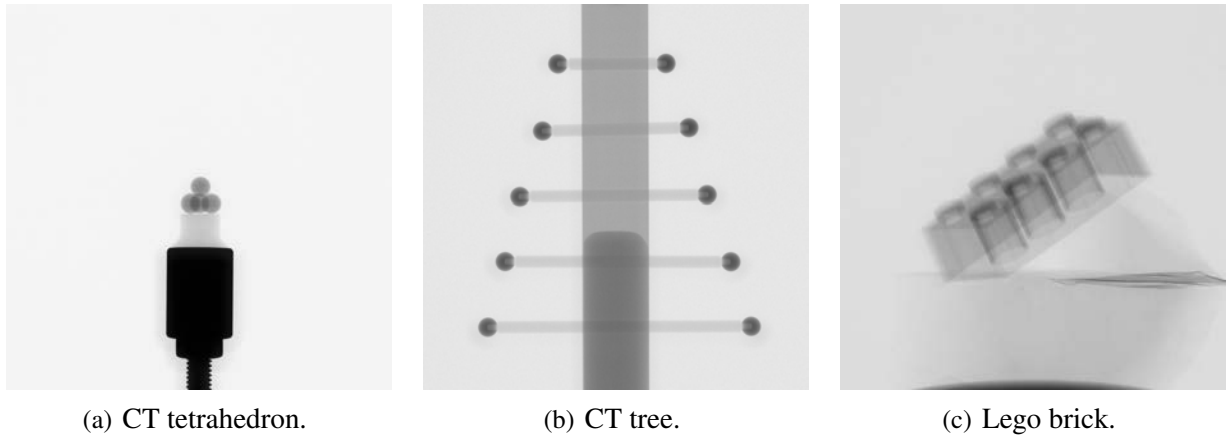


**Figure 6.15:** Projection images of the two reference objects (a,b) and the Lego brick (c). All the items are taken at the same magnification level ( $m=7.04$ ).

**Table 6.3:** Scanning parameters for all the CT scans.

| Voltage      | Power       | Integration<br>time | No.of image<br>averaging | No.of<br>views | Magnification<br>factor | Uncorrected<br>voxel size |
|--------------|-------------|---------------------|--------------------------|----------------|-------------------------|---------------------------|
| $U$<br>in kV | $P$<br>in W | $t$<br>in s         | $i_{\text{avg}}$         | $V$            | $m$                     | $s$<br>in $\mu\text{m}$   |
| 75           | 2.5         | 1.415               | 2                        | 1200           | 7.04                    | 28.4                      |

advanced (local) method was applied for better estimation of the surface. Surface determination for CT tree was done following procedure described in section 4.2.5.

### Measurands

Dimensional measurement of diameters of knobs and distances between knob centres, as already described for the calibration of the object, were performed on the voxel models. Definition of the coordinate system is equivalent for both CMM and CT measurements. Due to the fact that CT works with high point density data, diameters were defined by creating the Circle feature by fitting approximately 1000 points around the knob circumference.

### Scale error correction

The procedure for scale error correction was different for each of the used reference objects and is explained in the following. As discussed in section 3.3.1, in case that reference objects for scale error correction are not available, the correction can be done through measurements of calibrated features (e.g., diameters, distances, lengths) measured by, e.g., tactile CMM. In our case, this correction approach was also applied in order to investigate the robustness of this method for measurement of a plastic part.

- *CT tetrahedron:* This reference object features four ruby spheres of diameter  $\varnothing 3$  mm, glued together and arranged in a tetrahedron shape. In total, six sphere-to-sphere distances between each couple of spheres can be evaluated. The calibration procedure involves measurements of sphere center coordinates, from which the distances are calculated. A correction factor  $s_{\text{vox}}$  is

obtained as a ratio between calibration measurements and CT measurements. An average  $s_{\text{vox}}$  is calculated for all six distances. This value is then used for correction of the original voxel size.

- *CT tree*: The procedure for scale error correction using the CT tree is described in section 4.2.7.
- *Calibrated features measured by CMM*: The calibrated features used for scale error correction are outer and inner diameters of two cylindrical pins from inside of the Lego brick (see figure 6.16). The two diameters are measured at a distance of 2 mm from the bottom plane, and average value (inner and outer diameter, both measured on the two pins) is taken into account. This value is compared with the calibrated measures and correction factor is calculated according to equation 6.2.

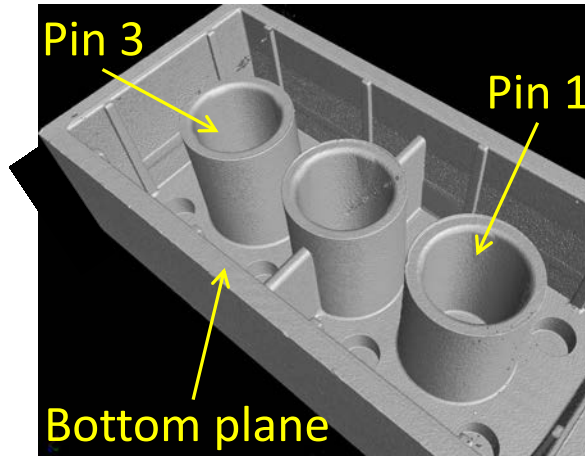


**Figure 6.16:** Indication of two cylindrical pins on which inner and outer diameters are measured as one of the methods for scale error correction (*calibrated features measured by CMM*).

$$s_{\text{vox}} = \frac{\left(\frac{D+d}{2}\right)_{\text{CMM}}}{\left(\frac{D+d}{2}\right)_{\text{CT}}} \quad (6.2)$$

where  $D$  and  $d$  are outer and inner diameters, respectively, measured by CMM (reference values) and CT at the same height. Average diameter values for the two measurements are considered.

When scanning of either of the reference object is performed before & after scanning of the Lego brick, an average  $s_{\text{vox}}$  is taken into account for the correction.

## 6.2.4 Results and discussion

Results of calculation of the correction factor for different correction methods and the corrected voxel sizes are shown in table 6.4. The  $s_{\text{vox}}$  is calculated always smaller than 1, which means that distances between sphere centers for both of the reference objects are measured bigger using CT. Thus, the corrected voxel size is smaller compared to the original voxel size. The difference between the corrected voxel size for CT tetrahedron scans, considering both cases (i.e., scan of the reference object before & after, and after the scan of the Lego brick), is approximately  $0.005 \mu\text{m}$  and for CT

tree the difference is approximately ten times smaller. However, even such a small difference in voxel size may result in bigger measuring deviations for, e.g., diameter or length measurements, which will be discussed later in this section.

**Table 6.4:** Uncorrected voxel size, calculated correction factors and corrected (re-scaled) voxel sizes for the application of different methods for scale error correction.

| Object / correction performed<br>before & after or after CT<br>scanning of the real part | Uncorrected voxel<br>size<br>$s_{\text{uncor}}$ in $\mu\text{m}$ | Calculated<br>correction factor<br>$s_{\text{vox}}$ | Corrected (re-<br>scaled) voxel size<br>$s_{\text{cor}}$ in $\mu\text{m}$ |
|--|--|---|---|
| CT tetrahedron / before & after  | 28.41729   | 0.99828   | 28.36850  |
| CT tetrahedron / after   | 28.41729   | 0.99845   | 28.37314  |
| CT tree / before & after   | 28.41729   | 0.99758   | 28.34840  |
| CT tree / after  | 28.41729   | 0.99757   | 28.34812  |
| Calibrated features (by CMM)   | 28.41729   | 0.99750   | 28.34621  |

Figure 6.17 shows the results of knob diameter measurements, in particular, diameter difference between measurements performed by CT and CMM (calibrated features). First of all, when no correction of scale errors was done, errors of approximately  $30\text{ }\mu\text{m}$  can be observed. After the application of the correction using the reference object, reduction of the errors by approximately  $12\text{ }\mu\text{m}$  (in case of the CT tree) was achieved. Still, deviations from the calibration values of approximately  $17\text{ }\mu\text{m}$  are present. Taking into account the repeatability of the CMM measurements ( $1.9\text{ }\mu\text{m}$ ) and possible thermal effects due to enhanced temperature in the scanner ( $1.5\text{ }\mu\text{m}$ ) (an average temperature measured inside of the scanner was  $24^{\circ}\text{C}$ , thus difference of  $\Delta 4^{\circ}\text{C}$  from reference temperature of  $20^{\circ}\text{C}$ , and considering coefficient of thermal expansion for ABS plastic material of the Lego brick to be  $74 \cdot 10^{-6} (^{\circ}\text{C})^{-1}$ ), still, some residual errors remain. It shall be noted that the results of the CT data were not corrected for temperature of  $20^{\circ}\text{C}$ . Possible contribution could also be the influence of humidity. The humidity in the scanner was approximately  $40\%$  and the humidity in the CMM environment was approximately  $50\%$ .

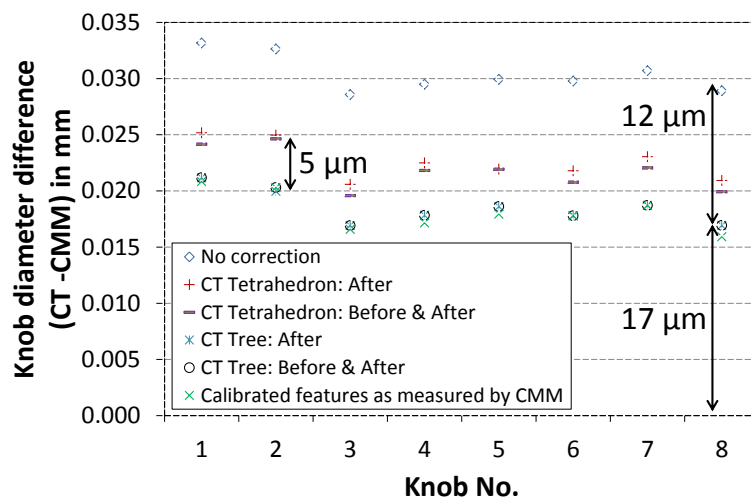


**Figure 6.17:** Results of knob diameter measurements.

Measurement deviations of approximately  $5\ \mu\text{m}$  between the two reference objects used for correction of diameter measurements can be observed in the figure. This can be due to the following reasons:

- The CT tree allows to measure more sphere-to-sphere lengths (45) compared to the CT tetrahedron (6), and thus the statistics and the approximation of the correction method is more robust. Furthermore, the results may be also affected by the tilt of the rotary axis and by the Feldkamp effect, and perhaps also by the anisotropy of the detector. Due to the symmetry configuration of the CT tree, these effects cancel out into some extent.
- By correcting the voxel size using the CT tree, results of the diameter measurements are closer to the reference measurements, compared to the correction done by the CT tetrahedron. This can be explained by the size of the two reference objects, as the CT tree covers bigger measuring (scanning) volume, closer to the volume of the Lego brick (for orientation see projection images of all the three items in figure 6.15). Especially when scanning the CT tree and the real part under bigger opening angles, the tree will compensate for errors caused by the Feldkamp effect. Thus, again, the application of the CT tree for scanning of the Lego brick seems to be more adequate. Taking this information into account, the use of the CT tetrahedron would be preferential for smaller parts, or parts covering smaller volumes.
- The correction of the voxel size using the calibrated features of the Lego brick (inner and outer diameters) measured by tactile CMM works as well. The same residual errors of  $17\ \mu\text{m}$  are found as in the case when using the CT tree. This is a very good result as it indicates that, in principle, there is no need to use reference objects for this task, provided that calibration of inner and outer geometries can be done using an accurate measuring instrument.

The scanning repeatability for measurements of the knob diameters of the Lego brick, calculated for two CT scans of the object, is very high (a maximum deviation of  $0.5\ \mu\text{m}$  was observed on eight knobs), taking into account repositioning of the part in the fixture from the rotary table and scanning of other parts (reference objects scanned with the same scanning parameters) in between measurements (see figure 6.14). This result is very satisfactory as it indicates that the mechanics of the CT system is good and that a correction should be possible and very effective.

The voxel size correction using the CT tree is more repeatable for diameter measurements ( $1\ \mu\text{m}$ ) compared to the CT tetrahedron ( $4\ \mu\text{m}$ ). Here, the repeatability is expressed as a difference between measurements (CT scans) of the reference objects performed before & after, and after scanning of the Lego brick. Even small variations during the scanning of the CT tetrahedron, considering that this part is much smaller compared to the CT tree, may lead to bigger errors. These variations may come from the focus drift, misalignment of the manipulator system or may be caused by the measurements of the lengths between spheres in the evaluation software. The latter was checked and seems not to be the case. Thus, such a deviation between two scans will naturally lead to errors in calculation of the correction factor  $s_{\text{vox}}$  (table 6.4). The influence of the focus drift would be the most reasonable explanation in this case, since the CT scan of the CT tetrahedron was the first scan that day, and thus the temperature of the X-ray source could be not stabilized enough to provide a stable beam. However, the source was pre-conditioned for a maximum voltage of 225 kV and left to stabilize for another 30 minutes. Therefore, the influence of the focus drift should also be excluded.

Evidence of scaling errors, typical for length measuring instruments, is shown in figure 6.18. In this case, uncorrected errors ranging from  $30\ \mu\text{m}$  for the shortest lengths (8 mm) to  $70\ \mu\text{m}$  for the longest

lengths (25 mm) can be observed. The range of scale errors is relatively big compared to, e.g., errors found when scanning the CT ball plate [101], introduced in section 4.1. In case of the CT ball plate, maximum deviations of approximately  $80\text{ }\mu\text{m}$  were found for a maximum measured length of 56 mm in the uncorrected state (i.e., approximately the same errors for double measured length of the Lego brick). This could be due to two reasons: (i) different scanning settings used in connection with scanning of the Lego brick and the CT ball plate, and (ii) more precise length measurement in case of the CT ball plate, as the evaluation of distance between sphere centres is more robust than evaluation of distance between centres of circles, also considering the average roundness of the knobs being approximately  $25\text{ }\mu\text{m}$  (measurement of roundness was done at the same three levels as diameter measurement).

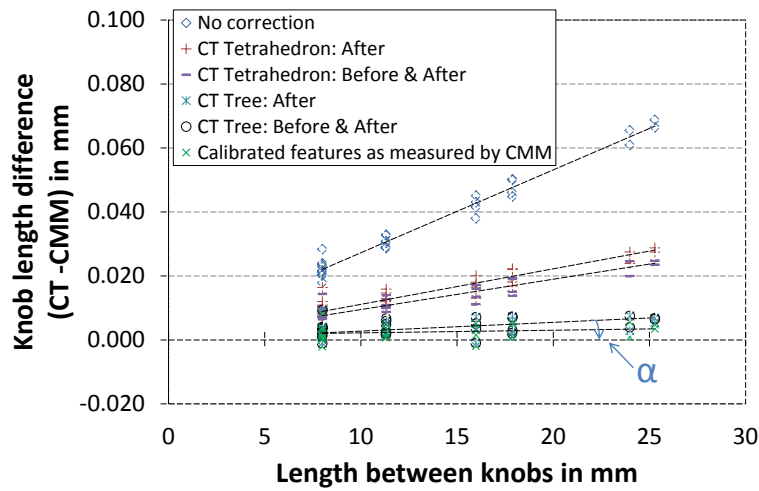


**Figure 6.18:** Results of knob-to-knob length measurements.

The suitability of the application of the reference objects, in particular, of the CT tetrahedron and the CT tree, is evident. By correcting the scale errors using the CT tetrahedron, the correction method does not work perfectly - still, maximum residual errors of  $29\text{ }\mu\text{m}$  can be observed. This can be due to the same reasons as explained earlier in this section, i.e., CT tetrahedron seems not to be applicable for correction of bigger volumes, as the object itself is rather small. By applying the CT tree for correction of scale errors, maximum residual errors of  $8\text{ }\mu\text{m}$  are still present. However, such a residual error of  $8\text{ }\mu\text{m}$  is very small with regards to the voxel size of  $28.41\text{ }\mu\text{m}$ . This is a big improvement of the correction. The residual slope  $\alpha$  of the fit through the data set, shown in the figure, can be a result of the influence of the temperature (for a temperature change of  $\Delta 4^\circ\text{C}$  providing an expansion of the maximum length between knobs of approximately  $7\text{ }\mu\text{m}$ ). Correction of the voxel size using the calibrated features of the Lego brick as measured by CMM (inner and outer diameters) works the best of all the correction methods applied in this study. Some residual errors can be still noticed, however, even smaller with regards to other. Thus, one can conclude that the correction method using the calibrated features works well.

The repeatability of the CT scans of both of the reference objects and their application for correction of the scale errors is the same for length measurement as for diameter measurements, discussed earlier in this section.

### 6.2.5 Conclusion

After the analysis of the results, the following conclusions can be drawn:

- Scale errors were evident for diameter and length measurements performed on the Lego brick. Reduction, and in some cases elimination, of these errors was achieved with the use of reference objects: CT tetrahedron, CT tree and by measuring features of the Lego brick's geometry (inner and outer diameters) using CMM. Measurement of inner and outer diameters of two cylindrical pins was considered for the latter. This correction method worked, in fact, the best of all, i.e., resulting in the smallest deviations from calibration values. Thus, it can be concluded, that for the CT system and the real part considered in this study, only the calibrated features would be appropriate for the correction of scale errors.
- It turned out that the application of the CT tree compared to the well-established CT tetrahedron works very good. This is mainly due to the fact that the size of the CT tree is closer to the size of the real part (Lego brick), covering approximately the same measuring (scanning) volume as the real part. Especially when scanning the CT tree and the real part under bigger opening angles, the tree will compensate for errors caused by the Feldkamp effect. Moreover, due to the statistics - bigger amount of lengths measured within one object, the evaluation of lengths is more robust.
- Correction using the CT tetrahedron appeared to be less repeatable, as even small variations during the scanning may lead to bigger errors. Thus, e.g., the evaluation of the sphere-to-sphere distances is more critical.
- It was investigated that there is no need to scan reference objects before & after scanning of the real part for the correction of measuring errors. Both methods, i.e., scanning before & after, and after the scanning of the real part, resulted in high measuring repeatability. Thus, scanning of the reference object only after scanning of the real part, is enough for the case presented, ensuring a reliable correction. It shall be noted that the scanning settings have not been changed throughout the whole test which minimizes the possible influence of the focus drift.

### 6.2.6 Outlook

Scanning of the reference object for correction of measuring errors could also be done simultaneously with scanning of the real part. The objects should not interfere (overlap) with each other during the scanning acquisition, which could significantly influence the quality of the voxel model and so the accuracy of dimensional measurements. With this approach, reduction of scanning time and related costs could be achieved. Care should be taken for the choice of the material of the reference object with respect to the material of the real part. In the ideal case and for achieving the best accuracy, both objects should be made of the same or at least similar material yielding approximately the same absorption. In the worst case, if the two objects were made of different materials like, e.g., a high density real part with big wall thickness for which high scanning settings (high voltage) shall be applied, and a ball bar made of ruby spheres with diameter  $\varnothing 2$  mm, the reconstruction of the balls (for evaluation of the distance between sphere centres) would yield low quality and high form error, and thus increasing the uncertainty associated with the fitting of geometrical features. This is due to the fact that scanning of the reference object has to be done with the same scanning settings as applied for the real part.

## 6.3 A study on evaluation strategies by estimation of measurement uncertainty

By CT, a complete volumetric 3D model of a scanned part is obtained, both as a volume model or a surface model, defined from the volume model by creating a polygonal mesh. Software tools, devoted to manage either of the models, are used for dimensional measurements and other metrological applications. However, each software tool provides different algorithms for application of measuring strategies to define selected measurands. In the present investigation, three software tools were used. The objective of this case study is to perform dimensional and geometrical measurements on industrial parts using CT and to quantify the influence of the application of different measuring strategies on selected geometrical features by the estimation of measurement uncertainty.

### 6.3.1 Case description

Two industrial parts were selected, each made of different material and of different size. The reason for choosing two such different objects is to point out some of the specific characteristics of CT. The first object is an aluminium alloyed pipe connector. Four measurands (two dimensional and two geometrical) shown in figure 6.19(a) were defined: inner diameter of the hole ( $d_p = 33 \pm 0.02$  mm), distance between two parallel surfaces of the inner flange ( $L_p = 6.4 \pm 0.05$  mm), parallelism between the two surfaces ( $P_p = 0.05$  mm) and cylindricity ( $C_p = 0.03$  mm) of the inner hole. The second part is a polymeric micro component used for a hearing aid applications, a toggle, produced by polymer injection moulding and is made of liquid crystal polymer (LPC) with a part weight of 35 g. Four measurands (three dimensional and one geometrical) shown in figure 6.19(b) were defined according to [125, 126]. These are: outer diameter of the toggle ( $D_T = 5.4 \pm 0.03$  mm), inner diameter of the hole in the middle of the part ( $d_T = 1.55 \pm 0.02$  mm), concentricity defined between the hole in the middle of the part and the outer cylindrical feature ( $C_T = 0.02$  mm), and height ( $H_T = 0.38 \pm 0.03$  mm) of the pillar.

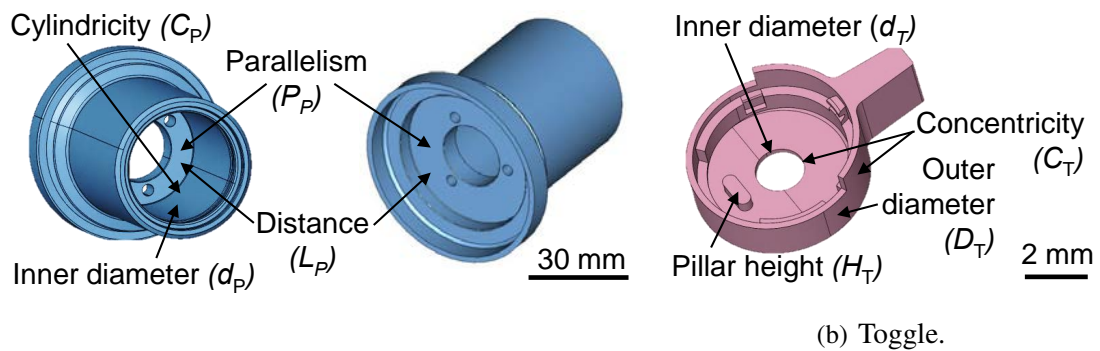


**Figure 6.19:** Definition of measurands for the pipe connector and the toggle.

Dimensional and geometrical measurements were performed both on volume and surface data (polygonal mesh). Three commercial software packages for CT data analysis were used and are summarized in table 6.5. Each of the software offers different algorithms and measuring strategies for fitting geometrical primitives on the 3D models.

**Table 6.5:** An overview of software packages for measurements on volume / surface data.

| Software tool | Data set                  |
|---------------|---------------------------|
| SW1           | Voxel model / volume data |
| SW2           | Voxel model / volume data |
| SW3           | STL model / surface data  |

### 6.3.2 Measurement setup

#### Definition of the coordinate system

The coordinate system for the pipe connector shown in figure 6.20(a) is defined as follows:

- Primary datum reference: is determined by Plane A defined on a flat surface from the bottom side of the object, which assess the negative direction of the  $v$ -axis).
- Secondary datum reference: is determined by a line that goes from centre of Circle 2 to centre of Circle 1. Circle 1 is defined in the middle height of the smaller hole and Circle 2 in the middle height of the bigger hole. The direction from Circle 2 to Circle 1 defines the negative  $w$ -axis direction.
- Origin datum reference: the origin is defined in the intersection of Cylinder A and Plane A.

$u$ -axis results from  $v$ - and  $w$ -axes, so that the final  $u$ - $v$ - $w$  reference system is a right-handed Cartesian Coordinate System (CCS).

The coordinate system for the toggle shown in figure 6.20(b) is defined as follows:

- Primary datum reference: is determined by Plane B defined on a narrow-curved flat surface, which assess the negative direction of the  $v$ -axis).
- Secondary datum reference: is determined by a line that goes from centre of Cylinder B, defined on the outer surface of the object, to an intersection point, defined by Plane B and intersection point of Plane L and Plane R. The direction from Cylinder B to the intersection point defines the positive  $u$ -axis direction.
- Origin datum reference: the origin is defined in Cylinder B.

$w$ -axis results from  $u$ - and  $v$ -axes, so that the final  $u$ - $v$ - $w$  reference system is a right-handed Cartesian Coordinate System (CCS).

Before both parts were measured using CT, they were calibrated using tactile and optical CMMs. These measurements were considered as reference. CT measurements were considered as actual measurements. In this study, the reference and actual measurements were not compared, however, a difference between the two was taken into account for uncertainty estimation.

#### Tactile (CMM) reference measurements

The pipe connector was measured using a Zeiss OMC 850 tactile CMM with stated  $MPE=(3+L/250)\mu m$  ( $L$  in mm). Measurements were performed in a temperature controlled laboratory with temperature



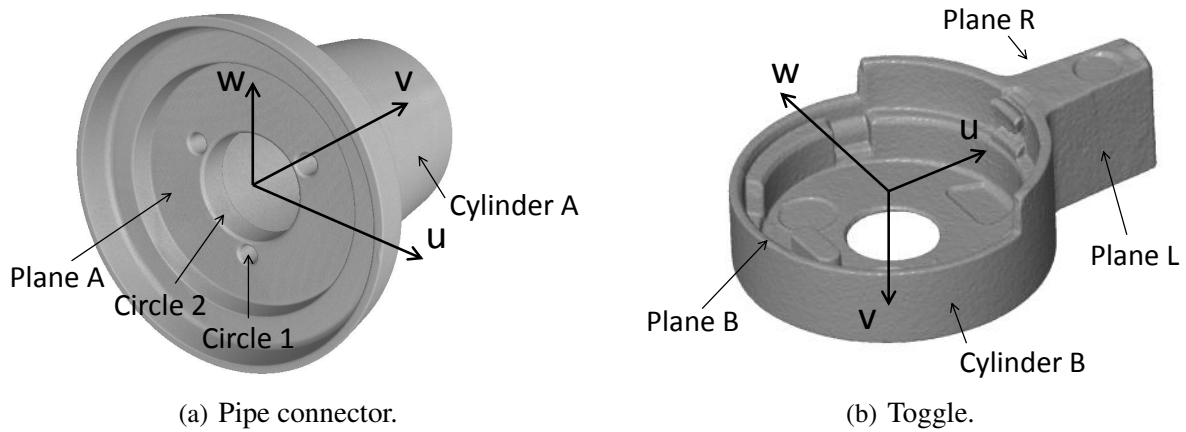


**Figure 6.20:** Definition of the coordinate system.

of  $20 \pm 0.5^\circ\text{C}$ . Measurements carried out using the tactile CMM were realized using three styli with a corresponding number of probes. The nominal dimensions (diameter,  $\varnothing$  and length,  $l$ , of styli) are: 1)  $\varnothing 3.0$  mm,  $l=58$  mm (axial), 2)  $\varnothing 1.5$  mm,  $l=56$  mm (horizontal) and 3)  $\varnothing 5.0$  mm,  $l=53$  mm (horizontal), configured so that measurement in all directions was possible without repositioning of the workpiece. Reference measurements were repeated three times.

### Optical reference measurements

The toggle was calibrated according to procedures described in [125, 126], first using a high accuracy Zeiss tactile CMM with  $\text{MPE} = (0.4 + L/900) \mu\text{m}$  ( $L$  in mm) and secondly by Schut DeMeet 220 optical CMM, yielding accuracy of  $\text{MPE} = (4 + L/150) \mu\text{m}$  ( $L$  in mm) in X and Y direction and  $3.5 \mu\text{m}$  in Z direction. Calibration values from the optical CMM were considered in this study.

### CT measurements

Both parts were then scanned using a Zeiss Metrotom 1500 cone beam CT scanner at the Danish Technological Institute. Measurements performed using the CT scanner were reproduced three times. The reproducibility was assessed by scanning the parts in different days and repositioning of the parts from the fixture. For reliable statistics the number of CT measurements is not appropriate, however, the approach presented is more industrial-like, thus the author found the number of measurements of each part adequate. Both parts were freely placed in a fixture made of polystyrene (PS), however prevented from any movement during the rotation.

Scanning parameters for CT measurements are shown in table 6.6. The choice of different scanning parameters for both parts is due to their different size, material, shape, etc. It can be, for example, noticed that the toggle allows much higher magnification for its smaller size and therefore yields higher resolution in terms of smaller voxel size compared to the pipe connector. In case of the pipe connector, a copper filter 0.25 mm thick was applied to minimize beam hardening effect [30]. Filters are not necessary for scanning of plastic parts. The focus spot size is a result of selected X-ray tube power. It can be noticed that employing higher power (voltage and current) leads to increase of the focus spot size, and thus to increased image blurring. Higher power applied when scanning the aluminium pipe connector is due to higher material density and greater wall thickness. Higher power increases the radiation intensity and the penetration of the X-rays through the object.

**Table 6.6:** An overview of the scanning parameters.

| Parameter              | Unit          | Pipe connector | Toggle      |
|------------------------|---------------|----------------|-------------|
| Voltage                | kV            | 210            | 130         |
| Current                | $\mu\text{A}$ | 500            | 150         |
| Focal spot size        | $\mu\text{m}$ | 105            | 19          |
| X-ray pre-filter       |               | Cu 0.25 mm     |             |
| Detector matrix        | pixel         | 1024 x 1024    | 1024 x 1024 |
| Detector pixel size    | $\mu\text{m}$ | 400            | 400         |
| Integration time       | ms            | 1000           | 1000        |
| No. of views           |               | 720            | 720         |
| Magnification          |               | 3.7            | 20.8        |
| Uncorrected voxel size | $\mu\text{m}$ | 108            | 19          |

CT measurements were performed in a laboratory with temperature of  $21 \pm 0.5^\circ\text{C}$ . The temperature in the CT scanner was measured  $22 \pm 0.5^\circ\text{C}$  in different days during which the parts were scanned.

### 6.3.3 Process chain for data evaluation and definition of measuring strategies for CT measurements

Although the process chain for dimensional measurement in CT is described in section 2.3, some specific considerations had to be taken into account. The process chain for measurements of both parts using three software packages is schematically shown in figure 6.21. The evaluation method for fitting geometrical primitives is least square method (also called Gaussian best fit). After scanning of the parts, 3D reconstruction and surface determination, a 3D volume model is visualized in SW1 and SW2. In SW1, a surface is determined on the reconstructed part using automatically generated "optimal" threshold, whose algorithm for surface determination is unknown. Then, a CAD model with already defined measuring strategies on selected measurands is imported and aligned with the volume model using a best fit method. In SW2, the reconstructed part is visualized, the surface is determined on the part using a local adaptive threshold method and measurements are performed by defining measurands directly on the volume model. A surface model in the form of a triangulated mesh (STL) is generated in SW1 and imported in SW3. Here, measurements are performed by defining measurands on the STL model.

Different measuring strategies for diameter, height, distance, cylindricity and concentricity measurements for both parts under study were applied in each of the software. Table 6.7 presents an overview of measuring strategies for determination of the measurands. It can be noticed that some measuring strategies are common to all software packages and some are different. This is due to various fitting algorithms which individual software packages are equipped with. Moreover, table 6.8 presents a detailed description on number of measuring points in a specific software for both calibration and CT scanning of both objects.

The definition of the measurands is specified in the following:

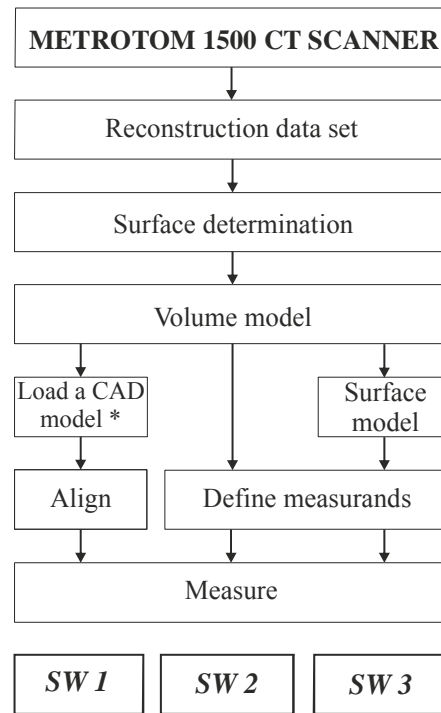


**Figure 6.21:** Measurement procedure for selected software. \*CAD model with already programmed measurement plan.

**Table 6.7:** An overview of evaluation strategies for selected measurands applied in three software packages.

| Measurand                               | SW1                              | SW2                                  | SW3                                  |
|---|----------------------------------|--------------------------------------|--------------------------------------|
| Diameter ( $d_P$ , $D_T$ )              | Circle<br>Spiral<br>Recall       | Circle<br>Feature<br>Cylinder circle | Circle<br>Feature<br>Cylinder circle |
| Diameter ( $d_T$ )                      | Circle                           | Circle                               | Circle                               |
| Distance ( $L_P$ ) and Height ( $H_T$ ) | Feature-Feature<br>Point-Feature | Feature-Feature<br>Point-Feature     | Feature-Feature<br>Point-Feature     |
| Cylindricity ( $C_P$ )                  | Spiral<br>Recall                 | Feature<br>Cylinder circle           | Feature<br>Cylinder circle           |
| Concentricity ( $C_T$ )                 | Circle<br>Spiral<br>Recall       | Circle<br>Feature<br>Cylinder circle | Circle<br>Feature                    |

#### Diameter (Pipe connector and Toggle)

- *Circle*: measurement is performed at different levels with respect to a position of a reference plane in  $v$ -direction by fitting a respective number of circles. Diameter based on a least-square method is then calculated as an average of the respective number of circles.
- *Feature*: by selecting a feature (in our case a cylindrical surface), a least square cylinder is

**Table 6.8:** Number of points to define geometrical features for calibration and CT acquisition of the pipe connector and the toggle using a specific software.

| Software                          |             |                |              |               |              |                 |              |                 |           |
|-----------------------------------|-------------|----------------|--------------|---------------|--------------|-----------------|--------------|-----------------|-----------|
| Calypso(*)/Approve for DeMeet(**) |             |                |              |               |              |                 |              |                 |           |
| Part                              | Measurand   | Strategy       | No.of points | SW1           | No.of points | Strategy        | No.of points | SW2             | SW3       |
| P                                 | $d_P$       | 3xCircle       | 3x8          | 3xCircle      | auto         | 3x1000          | Feature      | 1000            | Feature   |
|                                   |             | auto path      |              | path          |              |                 |              |                 |           |
|                                   |             |                |              | Spiral        | 10000        | 3xCircle        | 3x1000       | 3xCircle        | 3x700     |
|                                   | $L_P$       | Single points  | 2x10         | Recall        | 3000         | Cylinder circle | 1000         | Cylinder circle | 16000     |
|                                   |             |                |              | 2 x Poly-line | 2x700        | Feature-Feature | 1000x1000    | Feature-Feature | 1000x2800 |
| T                                 | $D_T$       | Edge detection |              | Point-Feature | 3x1000       | Point-Feature   | 3x1000       | Point-Feature   | 3x2800    |
|                                   |             |                |              | Feature fit   | 1000         | Feature         | 1000         | Feature         | 43000     |
|                                   |             |                |              | path          |              |                 |              |                 |           |
|                                   | $d_T$       | Edge detection |              | Spiral        | 10000        | 2xCircle        | 2x1000       | 2xCircle        | 2x1500    |
|                                   |             |                |              | Recall        | 2000         | Cylinder circle | 1000         | Cylinder circle | 15000     |
| $H_T$                             | Focus point |                |              | Auto path     | 200          | Feature         | 250          | Circle          | 460       |
|                                   |             |                |              | Single points | 10           | Feature         | 1000         | Feature         | 540       |

Note: (\*)Software for measurement using tactile CMM; (\*\*)Software for optical CMM measurements; P: Pipe connector; T: Toggle.

created on the surface of the respective feature. The diameter is the one of the least square cylinder.

- *Cylinder circle*: by selecting points in circular cross-sections (in  $uw$  planes) at two levels with respect to the position of the reference plane (Plane A in case of the pipe connector and Plane B in case of the toggle), the cylinder is fitted in between these levels. Diameter is then given by the least square fit in the specified range.
- *Spiral*: a spiral is fitted on the cylinder with defined number of revolutions and number of points. Diameter based on a least-square method is then calculated.
- *Recall*: recalls previously created features (in our case - circles). Diameter is then calculated as an average value of both circles.

#### Distance (Pipe connector) and Height (Toggle)

- *Feature-Feature*: by selecting features, best fit planes are fitted on the flat surfaces highlighted in figure 6.19. The distance is then calculated by projecting the center point of the fitted plane on to the other plane in normal direction.
- *Point-Feature*: by selecting three points on one surface and fitting a plane (feature) on the other surface with respect to which the distance/height is to be calculated, the distance/height is calculated by projecting the fitted points on to the plane in normal direction. Then, an average value for three distances/heights is calculated.

Further description of the assessment of measurands is provided in [23].

### 6.3.4 Uncertainty estimation

#### Uncertainty estimation for tactile measurements

Measurement uncertainties for tactile measurements  $U_{\text{cal}}$  of the pipe connector were estimated according to a simplified uncertainty budget - PUMA method (ISO 14253-2) [74], as described in equation 6.3.

$$U_{\text{cal}} = k \sqrt{u_i^2 + u_p^2 + u_w^2} \quad (6.3)$$

where  $k$  is coverage factor ( $k=2$  for a confidence level of 95%),  $u_i$  is standard calibration uncertainty of the measuring instrument, taking into account the MPE of the machine, calculated as  $u_i = \text{MPE}/2$ ,  $u_p$  is standard uncertainty of the measurement procedure, calculated as  $u_p = h \cdot (s/\sqrt{n})$ , where  $h$  is safety factor ( $h=2.3$  for three measurements),  $s$  is standard deviation of three repeated measurements and  $n$  is number of measurements ( $n=3$ ),  $u_w$  is temperature-related standard uncertainty calculated for a deviation of  $\pm 0.5^\circ\text{C}$  and using a coefficient of linear expansion for aluminium of  $23 \cdot 10^{-6}(\text{C})^{-1}$ . As discussed in section 3.4, the safety factor  $h$  is based on a Student- $t$  distribution and ensures that the measurement uncertainty is not underestimated.

#### Uncertainty estimation for optical measurements

Uncertainty assessment of measurements of polymer parts with a high accuracy tactile CMM was based on ISO 15530-3 [127]. Subsequently, the calibration data obtained from tactile measurements is employed to calculate the uncertainty for optical measurements, which are used in our case. A

detailed uncertainty budget is discussed in [126].

A summary of uncertainty estimation from the calibration of the two objects is presented in table 6.9. Lower uncertainties for calibration of the pipe connector could be achieved by calculating task-specific uncertainty. Moreover, using the MPE of the machine for calculation of the uncertainty for geometrical features, like parallelism and cylindricity, is critical.

**Table 6.9:** Expanded uncertainties  $U_{\text{cal}}$  ( $k=2$ ) from the calibration of the pipe connector and the toggle. All values are in  $\mu\text{m}$ .

| Pipe connector |       |       |       |       | Toggle |       |       |
|----------------|-------|-------|-------|-------|--------|-------|-------|
| $d_P$          | $L_P$ | $P_P$ | $C_P$ | $D_T$ | $d_T$  | $H_T$ | $C_T$ |
| 4.6            | 3.4   | 4.0   | 3.8   | 6.9   | 3.7    | 9.9   | 3.3   |

### Uncertainty estimation for CT measurements

Measurement uncertainties  $U_{\text{CT}}$  of both parts measured using the CT scanner were estimated according to ISO 15530-3 [85] as described in equation 6.4.

$$U_{\text{CT}} = k \sqrt{u_{\text{cal}}^2 + u_p^2 + u_w^2 + b^2} \quad (6.4)$$

where  $k$  is coverage factor ( $k=2$  for a confidence interval of 95%),  $u_{\text{cal}}$  is standard uncertainty as previously calculated for tactile and optical measurements ( $u_{\text{cal}}=U_{\text{cal}}/k$ ),  $u_p$  is standard uncertainty of the measurement procedure for each measurand, calculated as  $u_p = h \cdot (s / \sqrt{n})$ , where  $h$  is safety factor ( $h=2.3$  for three measurements),  $s$  is standard deviation of three reproduced measurements and  $n$  is number of measurements ( $n=3$ ),  $u_w$  is temperature-related standard uncertainty calculated for a deviation of  $\pm 0.5^\circ\text{C}$  and using a coefficient of linear expansion for aluminium of  $23 \cdot 10^{-6}(\text{C})^{-1}$  and  $49 \cdot 10^{-6}(\text{C})^{-1}$  for LPC,  $b$  is a systematic error calculated as a difference between measurements performed using CT scanner and tactile CMM and optical CMM respectively (see equation 3.9).

The GUM suggests correcting first all systematic errors (bias) and then to calculate the measurement uncertainty. Due to the fact that in CT many influence factors like scale errors, errors due to the focus drift and other unknown factors have an effect on geometrical measurements, and their quantification is rather a difficult task, these systematic errors are not corrected in this study but on the contrary are part of the estimation of measurement uncertainty (in terms of bias). Bias  $b$  is determined empirically and as such is treated as random errors and therefore has to be added squared under the radical, just like other uncertainty contributors [128]. Assessment of systematic errors is important, showing the actual difference between the two measuring machines.

## 6.3.5 Results and discussion

### Pipe connector

Results of the uncertainty estimation for the pipe connector measurements are presented in figure 6.22. Measurement uncertainties in the figure are estimated according to equation 6.4. Generally, one can observe that bigger uncertainties for selected measurands are associated with measurements carried out using SW3. One of the reasons is the fact that measurements in this software were done on a

polygonal mesh. It is mentioned in [129] that measurements performed on the polygonal mesh result in worsened quality and measurement inaccuracy, which is because the number of triangles on the polygonal mesh has to be optimized so that a software tool is able to handle the mesh. By decimating the number of triangles in the extracted polygonal mesh the number of measured points is reduced. This is further connected with the existence of noise (image artifacts) present at some parts of the volume model. Figure 6.23 shows, for example, artifacts in the reconstructed image, occurring at the top where this part of the object was at the borders of the detector, and at the bottom where this part of the object was at the borders of the detector too and, moreover, where the length of the X-rays travelling through the aluminium matter of the pipe connector was big. Artifacts at the upper detector region are caused by Feldkamp effect and artifacts at the bottom detector region are caused by beam hardening effect and scattered radiation. These are common problems when using CT for scanning metal parts. In order to reduce these unwanted image artifacts, it is advisable to position the workpiece on the rotary table so that the length the X-rays travel through the matter is minimized. The pipe connector was positioned at approximately  $45^\circ$ , however the length of the X-rays travelling across the part was big enough to cause noise (image artifacts). Generally speaking, STL data is very sensitive regarding image noise. So, when a polygonal mesh is created on the volume model with

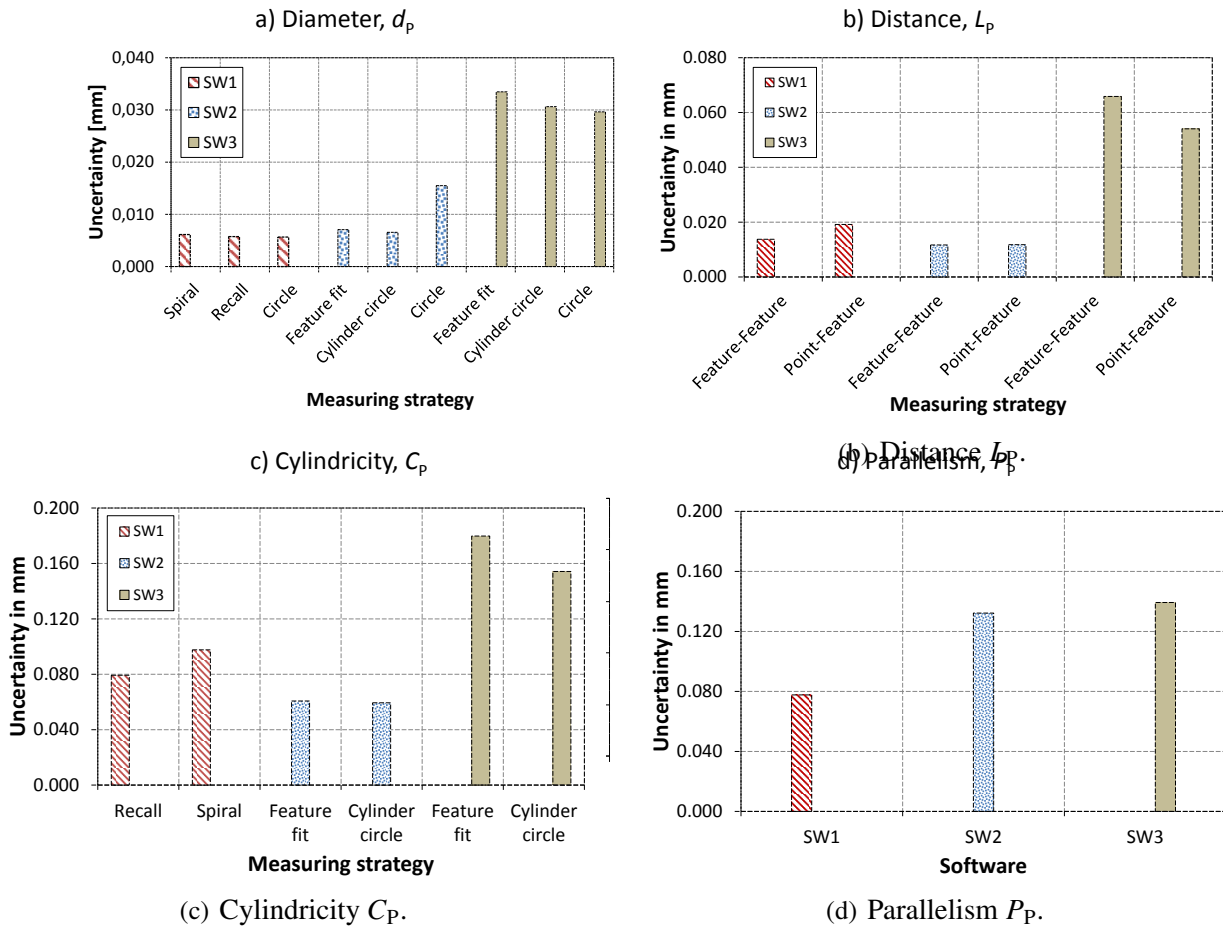


**Figure 6.22:** Expanded uncertainties at 95% confidence level for measurements performed on the pipe connector. Measurement uncertainties are estimated according to equation 6.4.

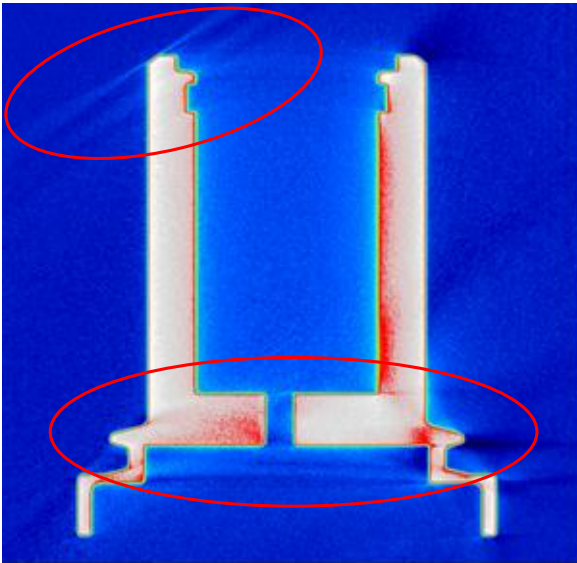


**Figure 6.23:** 2D reconstruction image of the pipe connector showing image artifacts at the top (object at the borders of the detector), and at the bottom (object at the borders of the detector plus big length of the X-rays travelling through the aluminium matter). Feldkamp artifacts at the top and artifacts caused by beam hardening and scattered radiation at the bottom are highlighted.

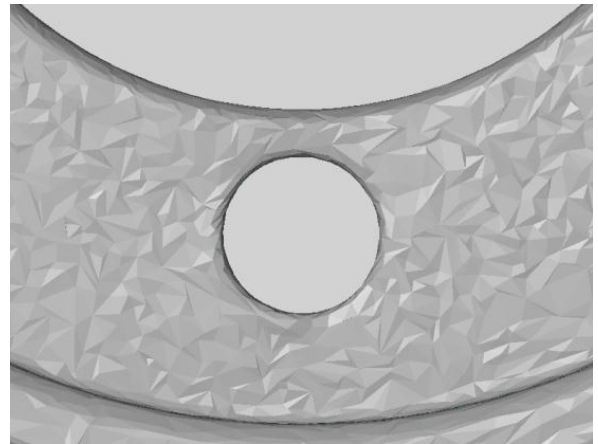


**Figure 6.24:** A polygonal mesh (STL) created on the pipe connector. Pseudo "rough" surface on the inner flange can be observed.

For diameter measurements the uncertainties calculated using SW1 and SW2 are in the same range as uncertainties obtained for reference measurements. This is due to more robust fitting algorithms applied for diameter evaluation (see figure 6.22(a)) rather than for measurements of distance between planes (figure 6.22(b)). That is because bidirectional measurements (distance between two parallel surfaces of the inner flange) are, in our case, greatly influenced by the noise (image artifacts), and moreover, these measurements are threshold sensitive. Uncertainties calculated for measurements of diameter and distance in SW3 are greater than 100% compared to uncertainties calculated for measurements in SW1 and SW2, which confirms the problematic concerning measurements on the polygonal mesh. Considering individual software tools, the selection of measuring strategies for diameter and height measurements seems not to be significant. Small variations among measurement uncertainties calculated for different measuring strategies are naturally due to different fitting algorithms, as explained in section 6.3.3, however, the difference is negligible. For example, values obtained using measuring strategy *Circle* for diameter measurements  $d_p$  in SW2 are double compared to other strategies. Alignment could be a critical point here, since the alignment was defined on a part of the object where image artifacts occurred (i.e., Plane A defined on the inner flange, for orientation see figure 6.20(a)). Therefore, the definition of the circles, and in particular, the position of the circles with respect to the alignment plane, may play a role. Comparing the two software tools for analysis of volume data sets, SW1 and SW2, difference between measurement uncertainties is smaller than  $8 \mu\text{m}$ . Moreover, uncertainties related to diameter and distance measurements are estimated in a reasonable range for CT measurements. Uncertainties related to geometrical tolerances, cylindricity and parallelism (figure 6.22(c) and figure 6.22(d), respectively) are bigger compared to measurements of diameter and distance. This is due to the fact that measurements of geometrical features are more



problematic and lead to bigger errors in CT [40]. Uncertainties related to measurements of cylindricity and parallelism are, again, bigger for measurements on surface data. Uncertainties estimated for parallelism tolerance are approximately  $80\text{ }\mu\text{m}$  and greater, possibly showing that noise in the region, where this feature was measured, was critical.

It was investigated that the bias was dominant uncertainty contributor mostly for measurements on the surface data and for measurements of the geometrical tolerances. Table 6.10 summarizes results of bias contribution to the measurement uncertainty, expressed by a ratio  $|b|/U_{CT}$  ( $b$  is bias and  $U_{CT}$  is expanded measurement uncertainty). Bias is a critical factor and for this reason, it is recommended to carry out reference measurements on the features which can be measured (for example tactilely) and to take this factor into account for calculation of the measurement uncertainty in CT (in case of uncertainty estimation based on ISO 15530-3:2009).

**Table 6.10:** Bias contribution to the measurement uncertainty ( $|b|/U_{CT}$  in %) calculated for the pipe connector.

| Measurand | Measuring strategy | Software tool |     |     |
|-----------|--------------------|---------------|-----|-----|
|           |                    | SW1           | SW2 | SW3 |
| $d_P$     | Circle             | 3             | 47  | 44  |
|           | Feature            |               | 29  | 46  |
|           | Cylinder circle    |               | 31  | 33  |
|           | Spiral             | 17            |     |     |
|           | Recall             | 1             |     |     |
| $L_P$     | Feature-Feature    | 29            | 31  | 41  |
|           | Point-Feature      | 22            | 24  | 46  |
| $P_P$     | Feature-Feature    | 47            | 48  | 50  |
| $C_P$     | Feature            |               | 50  | 49  |
|           | Spiral             | 49            |     |     |
|           | Recall             | 50            |     |     |

### Toggle

Results of the uncertainty estimation for the toggle measurements are presented in figure 6.25. Measurement uncertainties for CT measurements are estimated according to equation 6.4. Generally speaking, bias (its contribution to the expanded uncertainty is summarized in table 6.11), was found to be dominating uncertainty contributor for measurements of inner diameter  $d_T$ , height of the pillar  $H_T$  and concentricity  $C_T$ , being in the range from  $13$  to  $32\text{ }\mu\text{m}$ . This was the same for all three software tools. For measurements of the outer diameter  $D_T$ , a maximum bias value of  $4\text{ }\mu\text{m}$  was obtained for measurements in SW3, in SW1 and SW2 bias was  $1\text{ }\mu\text{m}$ . Low bias values for outer diameter measurements of the toggle are in good agreement with measurements of the pipe connector, and confirms that measurements of diameters, where selection of measured points is well defined, is robust. Uncertainties estimated for measurements of outer diameter using SW1 and SW2 are in agreement with reference measurements. Uncertainties estimated for measurements in SW3 are approximately double.

As bigger measurement uncertainties for most of the measurands of the pipe connector were

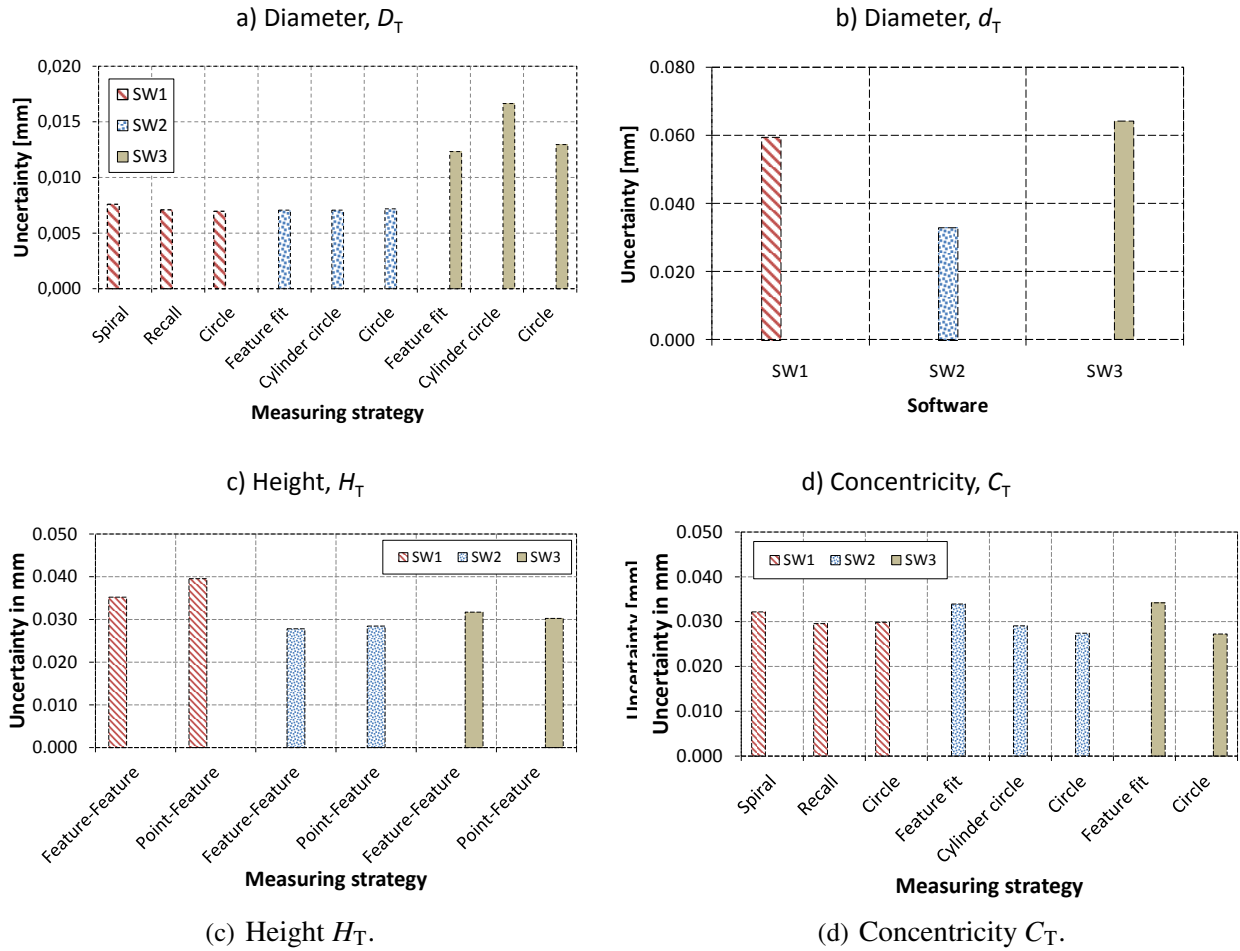


**Figure 6.25:** Expanded uncertainties at 95% confidence level for measurements performed on the toggle. Measurement uncertainties are calculated according to equation 6.4.

connected with measurements in SW3, it was investigated that this was not the case for measurements of the toggle (except for outer diameter measurements). Measurement uncertainties related to height and concentricity were estimated within  $11 \mu\text{m}$  and  $6 \mu\text{m}$ , respectively, when considering all three software tools. This can be explained by the material of the part itself. Low density materials yield high penetration rates (low attenuation of X-rays) and therefore allow more photons to be detected with the detector. Small parts are also preferable, as high resolution CT scans are obtained due to the small voxel sizes, and occurrence of image artifacts is minimized. Uncertainties estimated for measurements of the inner diameter  $d_T$  in SW2 are smaller ( $33 \mu\text{m}$ ) compared to other two software tools (approximately  $60 \mu\text{m}$ ). The reason for this is, again, big contribution of the bias. Measurements of  $d_T$  were complicated due to its rather poor quality of the manufactured edge where the hole has reduced thickness (see figure 6.26), and thus difficulties when measured. Also for this reason, measuring strategy had to be slightly adapted in order to be able to measure this feature. Similar problem was experienced in [130] when measuring the same object and the same feature.

The selection of measuring strategies for all selected measurands in different software packages seems not to be significant, only small variations can be observed. These are again due to different fitting algorithms.

**Table 6.11:** Bias contribution to the measurement uncertainty ( $|b|/U_{CT}$  in %) calculated for the toggle.

| Measurand | Measuring strategy | Software tool |     |     |
|-----------|--------------------|---------------|-----|-----|
|           |                    | SW1           | SW2 | SW3 |
| $D_T$     | Circle             | 5             | 10  | 32  |
|           | Feature            |               | 10  | 30  |
|           | Cylinder circle    |               | 10  | 40  |
|           | Spiral             | 18            |     |     |
|           | Recall             | 0             |     |     |
| $d_T$     | Circle             | 50            | 39  | 50  |
| $H_T$     | Feature-Feature    | 47            | 47  | 47  |
|           | Point-Feature      | 47            | 47  | 47  |
| $C_T$     | Circle             | 50            | 47  | 50  |
|           | Feature            |               | 47  | 47  |
|           | Cylinder circle    |               | 48  |     |

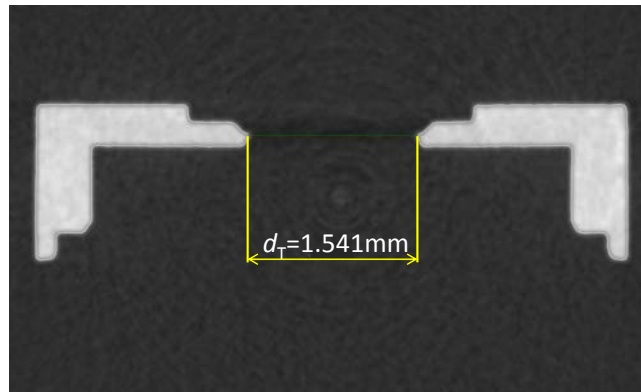


**Figure 6.26:** Measurement of inner diameter  $d_T$  in a cross-sectional view in SW2. The figure shows rather a poor quality of the manufactured edge.

It was investigated that bias was dominating uncertainty contributor for measurements on both volume and surface data.

### 6.3.6 Conclusion

The main conclusions from this case study are summarized in the following:

- Diameter measurements of cylindrical features for both aluminium and plastic parts resulted in small bias and low measurement uncertainties compared to distance and height measurements. This was due to a robust fitting of well-defined geometrical features.
- Bias as well as measurement uncertainties calculated for measurements using SW3 for the pipe connector were generally bigger compared to measurements using SW1 and SW2. This was due

to the fact that measurements carried out in SW3 were done on the surface data (STL), generally resulting in worsened quality and impression in measurement due to the polygonal mesh created on the surface. In contrast, for the toggle, bias as well as measurement uncertainties were calculated in the same range for all the three software packages, except for outer diameter measurements (these were smaller).

- It was investigated that the choice of a specific measuring strategy applied to measure different features does not play a major role in this case study and it is therefore a free choice for the operator who will not significantly influence the result of CT measurements. Small variations in the choice of measuring strategy were, however, observed.

### **6.3.7 Outlook**

This investigation presents a case study only. Greater variability of parts, i.e., parts of different materials, different geometries and sizes should be considered to generalize the influence of measuring strategies on measurement uncertainty. The same concerns dimensional and geometrical tolerances, i.e., not only those tolerances used in our case should be considered to quantify effects connected with CT measurements, but other should be taken into account.

In the case of a presence of image noise on the CT data set, one can filter these data before applying the surface (STL). One should however be careful since this may lead to degradation of the original data set and therefore significantly change shape of a part and therefore obtain different measurement result. Another possibility how to avoid noise is to change the scanning parameters (e.g. integration time, current), which is in many cases rather difficult task.

A special care shall be taken for the alignment of the CT volume model. Only the features of the volumetric model which are not significantly influenced by noise or any other image artifacts should be considered for the alignment, which might further lead to measurement inaccuracies.

## 6.4 Tolerance verification of industrial parts

Due to the fact that many types of CT systems are being manufactured, it can be expected that each of them yields different performance characteristics. Different CT scanners are suitable for different applications, i.e., some CT systems are preferable for small parts rather than big ones, some of them are more suitable for scanning of low-density materials and thus do not require high-power X-ray sources compared to high-density materials, and so on. It is, therefore, the objective of this work to investigate the influence of the CT systems employed in the present case study on various performance parameters.

Moreover, after the part is scanned and a 3D model reconstructed, the question about which software to use for data evaluation arises. Again, different software packages offer different approaches for fitting geometrical primitives, and, therefore, an assessment of measuring strategy plays a role [131]. Another consideration is whether the measurement should be performed on a voxel model or a surface model (also called STL). The latter generally yields poorer quality and therefore results in measuring impressions [129], however, data saved in STL format can be easily handled by many software packages for point cloud and surface model inspection.

Due to these influencing factors in terms of machine, software, and data, the specific aims of the present investigation are assessed as follows:

- Comparison of voxel models from two CT systems (→ CT system performance comparison)
- Comparison of voxel model and STL model from each of the scanners (→ data format comparison)
- Comparison of voxel model from one CT system evaluated in two different software packages (→ software comparison)

### 6.4.1 Case description

#### Test object

The test object under investigation is a housing of an insulin pen (see figure 6.27) manufactured by Novo Nordisk A/S. As the name indicates, it houses other parts that are needed for complete function of the insulin pen as a whole. The housing was produced by injection moulding and is made of polypropylene (PP). It is a medium-sized object made of material highly suitable for micro CT due to its low density and, therefore, high penetrability rate (=low attenuation) can be achieved. Five measurands (three dimensional and two geometrical) were defined and are indicated in figure 6.28. These are: outer diameter of the housing ( $D$ ) defined on the external surface of the part, inner diameter of the flange ( $d$ ), distance ( $L$ ) between the flange and the end of the housing, coaxiality ( $C$ ) between the circular part of the flange and a cylindrical surface on the inner thread, and parallelism ( $P$ ) of the flat surface on the window and a datum plane defined on the inner grooves. Nominal dimensions and related tolerances are as follows:  $D=15.35\pm0.05$  mm,  $d=6.4\pm0.05$  mm,  $L=52.5\pm0.05$  mm,  $C=0.1$  mm and  $P=0.2$  mm. Due to a confidentiality agreement with the company, all presented tolerances are virtual and do not reflect the real tolerances of the part.

#### Variables

Two cone beam CT systems at Novo Nordisk A/S, Nanotom CT scanner from GE Phoenix|x-ray



**Figure 6.27:** Insulin pen ma Nordisk A/S. The housing is indicated.

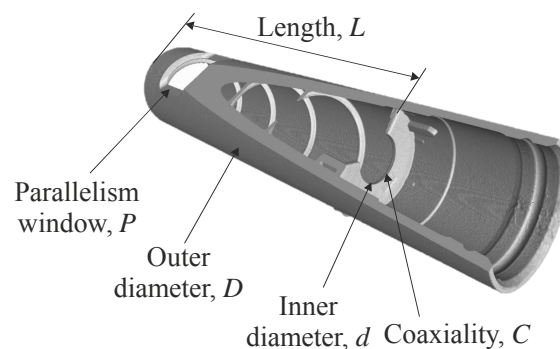


**Figure 6.28:** Definition of measurands.

and Metrotom 1500 CT scanner from Zeiss, were used for tolerance verification of the housing. Two commercial software packages, VG Studio Max from Volume Graphics and Calypso CT from Zeiss, were used for data evaluation. Measurements in Calypso CT were performed on a voxel model, whereas measurements in VG Studio Max were performed on both voxel and STL models. An overview of software packages and CT systems along with the acronyms used in the present investigation is provided in table 6.12.

**Table 6.12:** An overview of CT systems and software packages used in the present investigation.

|          | CT system        |               | Software name and version |                 |
|----------|------------------|---------------|---------------------------|-----------------|
|          | Nanotom          | Metrotom 1500 | VG Studio Max 2.1         | Calypso CT 4.10 |
| Producer | GE Phoenix x-ray | Zeiss         | Volume Graphics           | Zeiss           |
| Acronym  | CT1              | CT2           | SW1                       | SW2             |

## 6.4.2 Measurement setup

The part under investigation was first measured using a tactile CMM, and then CT scanned using two commercial CT scanners.

### Tactile reference measurements

The tactile measurements of the housing were performed using a Zeiss OMC 850 CMM with stated  $MPE=(3+L/250) \mu m$  ( $L$  in mm). Measurements performed on the CMM were considered as reference measurements. Measurements were performed in a temperature-controlled laboratory at a temperature of  $20\pm0.5^\circ C$ . A specially built probe configuration was used, consisting of eight styli with a corresponding number of probes, including cylindrical probes, with nominal dimensions in the range 0.6 to 6.0 mm. Such a probe configuration enables measurements of difficult-to-reach features without repositioning the part. A probe of suitable size and shape was carefully assigned to a specific feature depending on the part's material, surface roughness, Young's modulus, desired resolution, and uncertainty. Three specimens from the production batch were measured, each specimen only once. Batch, in our case, is a mould which consists of 32 cavities. The three specimens measured by the CMM were those belonging to one cavity, into which a total of three injection "shots" were done. This was done to check variation due to the manufacturing process (reproducibility of

producing the same part in one mould and a specific cavity with more injection shots). Thus, in this investigation, industrial procedure is followed. The data evaluation was accomplished using the Calypso 4.8 software from Zeiss.

### CT measurements

Three CT measurements were realised using CT1 and CT2 on only one randomly chosen part from different shots belonging to one cavity. The part was freely placed on polystyrene (PS), which is often used as a fixture. This is because the material's low density enables easy penetration of X-rays and does not influence the attenuation of the scanned part. Scanning parameters which were carefully chosen by two different operators for the two CT systems are shown in table 6.13. It can be seen from the table that both systems yield different performances. Different setting parameters are also chosen due to the scanners' distinctive designs. In particular, due to the large size of the sample, in CT1, a detector feature called "Shifting Detector" was used to enlarge the measuring area. The detector was moved in a horizontal direction to acquire two images and combine them into one, which enabled the sample to fit in the central detector area.

**Table 6.13:** An overview of scanning parameters.

| Parameter              | Unit          | Nanotom     | Metrotom 1500 |
|------------------------|---------------|-------------|---------------|
| Voltage                | kV            | 100         | 150           |
| Current                | $\mu\text{A}$ | 100         | 200           |
| Focal spot size        | $\mu\text{m}$ | 9.3         | 32.5          |
| Detector matrix        | pixel         | 1152 x 1152 | 1024 x 1024   |
| Detector pixel size    | $\mu\text{m}$ | 100         | 400           |
| Integration time       | ms            | 500         | 1000          |
| No. of views           |               | 720         | 800           |
| Magnification          |               | 2           | 3             |
| Uncorrected voxel size | $\mu\text{m}$ | 50          | 134           |

Due to anisotropies in the measuring volume of the scanner, errors occur on the reconstructed model. In particular, geometrical errors from the manipulator, focus spot drift, and scaling errors of the 3D image lead to errors in voxel size and systematic length measurement. Such errors can be corrected using calibrated ball bars with known distances between sphere centres (this procedure was in details discussed in section 3.3.1 and section 3.5). In this case, the ball bar was scanned after each scan of the housing using the same setting parameters. The correction method using the ball bar was only carried out in connection with CT1. CT2 performs the correction of voxel size automatically.

### 6.4.3 Process chain for data evaluation and definition of measuring strategies

A schematic representation of the process chain for measurement of the part on voxel and STL models is shown in figure 6.29. Geometrical primitives (features) were defined by least square method.

After the part is scanned and reconstruction of projection images completed, a 3D voxel model is visualised using specific software. Using SW1, the surface is extracted on the part using a local adaptive threshold method. After this, measurements on the voxel and surface models are performed

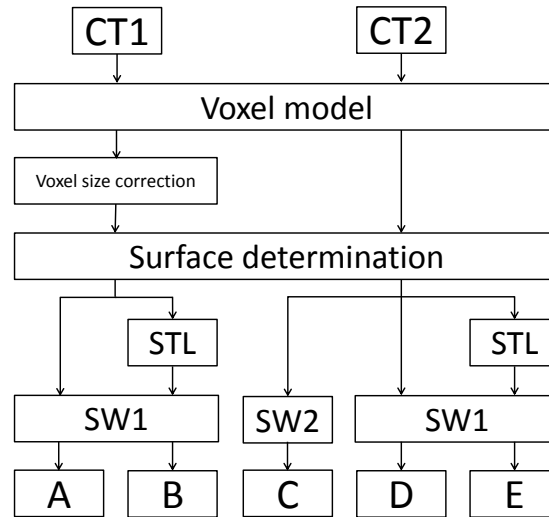


**Figure 6.29:** Measurement procedure for data evaluation.

by defining measurands directly on the 3D models. An STL obtained from CT1 yields approximately 2 million triangles, whereas from CT2 approximately 800.000 triangles were generated using the same STL extraction method. In SW2, a CAD model with already defined measuring strategies for selected measurands is imported and aligned with the voxel model using a best fit method. The alignment is run several times to achieve a good fit. Then, the program is run in a CMM mode and results are obtained. The reconstructed voxel model from CT1 is corrected for scale errors by scanning a ball bar. Since CT2 corrects the measuring errors automatically, no scanning of the ball bar is necessary. Symbols A-E in figure 6.29 represent combinations of variables (CT system, data set, and software), which are compared among each other according to the specific objectives.

Due to the use of different approaches for fitting geometrical primitives on the 3D features of the part, the two software packages offer different measuring strategies. Measuring strategy is an important factor, since knowledge of number of points, measured positions, measurand definition, and fitting element is needed for a more precise interpretation of results. The influence of measuring strategies is pointed out in [131]. Table 6.14 presents an overview of measuring strategies used for assessing selected measurands.

**Table 6.14:** An overview of fitting elements for measurand assessment. Fitting elements in the brackets are datum features with respect to which the geometrical tolerances were verified.

| Measurand | Fitting element   |                     |                   |
|-----------|-------------------|---------------------|-------------------|
|           | CMM/Calypso       | SW1                 | SW2               |
| <i>P</i>  | Plane (Plane)     | Plane (Plane)       | Plane (Plane)     |
| <i>C</i>  | Circle (Cylinder) | Cylinder (Cylinder) | Circle (Cylinder) |
| <i>L</i>  | Plane - Plane     | Plane - Plane       | Plane - Plane     |
| <i>d</i>  | Circle            | Cylinder            | Circle            |
| <i>D</i>  | Circle (2x)       | Cylinder            | Circle (2x)       |



#### 6.4.4 Uncertainty assessment

Results of uncertainty calculations from the reference measurements were taken into account when calculating the uncertainty from CT measurements, which provides the necessary traceability link. Tolerance verification, i.e., a conformity check, of the part was carried out for both tactile and CT measurements according to ISO 14253-1 [33].

##### Uncertainty estimation for tactile measurements

Measurement uncertainties for tactile measurements  $U_{\text{cal}}$  for the housing were estimated according to a simplified uncertainty budget - PUMA method (ISO 14253-2) [74], as described in equation 6.5.

$$U_{\text{cal}} = k \sqrt{u_i^2 + u_p^2 + u_w^2} \quad (6.5)$$

where  $k$  is coverage factor ( $k=2$  for a confidence level of 95%),  $u_i$  is standard calibration uncertainty of the measuring instrument, taking into account the MPE of the machine, calculated as  $u_i = \text{MPE}/2$ ,  $u_p$  is standard uncertainty of the measurement procedure, calculated as  $u_p = h \cdot (s / \sqrt{n})$ , where  $h$  is safety factor ( $h=2.3$  for three measurements),  $s$  is standard deviation from measurements of three specimens produced in one cavity within a mould by three subsequent injection shots and  $n$  is number of parts measured ( $n=3$ ),  $u_w$  is temperature-related standard uncertainty calculated for a deviation of  $\pm 0.5^\circ\text{C}$  and using a coefficient of linear expansion for PP of  $(90 - 100) \cdot 10^{-6}(\text{C})^{-1}$ .

The author is aware of the fact that uncertainty estimation using MPE specification is unreliable, especially for form measurements, however, an industrial approach is applied to this task, where no real calibration of the master piece was done (i.e., calibration with no repetition carried out on one part, or a task-specific calibration).

Uncertainty budget for tactile measurements of selected geometrical and dimensional tolerances is shown in table 6.15. The tree uncertainty sources from equation 6.5 are listed.

**Table 6.15:** Uncertainty budget for CMM measurements of the housing. All values are in  $\mu\text{m}$ .

| Uncertainty component | Symbol                | Standard uncertainty |      |      |      |      |
|-----------------------|-----------------------|----------------------|------|------|------|------|
|                       |                       | $P$                  | $C$  | $L$  | $d$  | $D$  |
| Instrument            | $u_i$                 | 1.50                 | 1.50 | 1.57 | 1.51 | 1.52 |
| Procedure             | $u_p$                 | 2.24                 | 2.95 | 3.22 | 1.19 | 0.74 |
| Temperature           | $u_w$                 | 0.00                 | 0.00 | 3.15 | 0.38 | 0.92 |
| Expanded uncertainty  | $U_{\text{cal}}(k=2)$ | 5.4                  | 6.6  | 9.5  | 3.9  | 3.8  |

##### Uncertainty estimation for CT measurements

Measurement uncertainties for CT measurements  $U_{\text{CT}}$  of the housing were estimated according to PUMA method (ISO 14253-2) [74] too, as described in equation 6.6.

$$U_{\text{CT}} = k \sqrt{u_{\text{cal}}^2 + u_p^2 + u_w^2} \quad (6.6)$$

where  $k$  is coverage factor ( $k=2$  for a confidence interval of 95%),  $u_{\text{cal}}$  is standard uncertainty as previously calculated for tactile and optical measurements ( $u_{\text{cal}} = U_{\text{cal}}/k$ ),  $u_p$  is standard uncertainty

of the measurement procedure for each measurand, calculated as  $u_p = h \cdot (s / \sqrt{n})$ , where  $h$  is safety factor ( $h=2.3$  for three CT measurements),  $s$  is standard deviation from the reproduced measurements and  $n$  is number of measurements ( $n=3$ ),  $u_w$  is temperature-related standard uncertainty calculated for a deviation of  $\pm 0.5^\circ\text{C}$  and using a coefficient of linear expansion for PP of  $(90 - 100) \cdot 10^{-6}(\text{C})^{-1}$  (calculated according to equation 6.11).

### 6.4.5 Results and discussion

Results from measurements of the housing using CT are presented in this section. The conformity check of selected tolerances was realised by measuring individual features using selected software. Results of geometrical and dimensional tolerances of the housing are plotted in figure 6.30. Each column in the figure represents an average value of three CT measurements of the part. The error bars represent expanded uncertainty estimated according to equation 6.6. The designation of symbols A-E is explained in figure 6.29 and refers to a combination of variables employed in this investigation. The red full lines are average values measured by the CMM on three parts from one cavity, and the red dashed lines show the range of expanded uncertainties calculated according to equation 6.5.

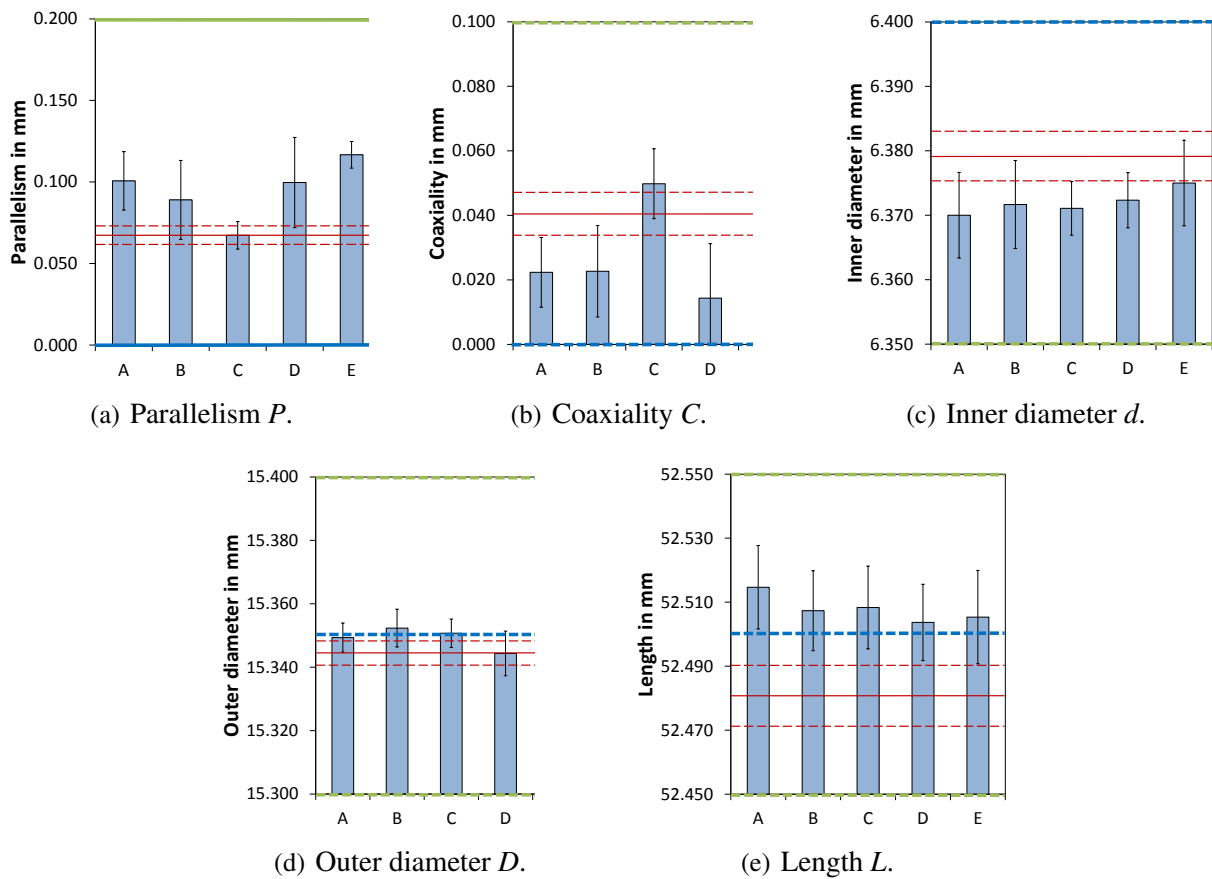


**Figure 6.30:** Results of geometrical and dimensional tolerance analysis. Each column represents an average value of three CT measurements. The error bars represent expanded uncertainty for CT measurements at 95% confidence interval, calculated according to equation 6.6. The designation of symbols A-E is explained in figure 6.29 and refers to a combination of variables employed. The red full lines are average values measured by the CMM, and the red dashed lines show the range of expanded uncertainties at 95% confidence interval.

As can be seen in figure 6.30, variation of results is evident and is dependent on the chosen combination of CT system, data set, and software. The three specific objectives of this investigation mentioned at the beginning of this section are presented in the following. Before that, it shall be noted that the results presented here show absolute values which were not corrected for systematic errors (bias).

- Considering the performance of both CT scanners (columns A and D in figure 6.30), i.e., quantitative comparison of measurements performed on the voxel models and evaluated in SW1, slightly higher values of all measurands were obtained from CT1 (column A), except for inner diameter. However, the difference was not significant, a maximum deviation of average measured values of  $11\mu\text{m}$  was observed for length measurement.
- Considering the comparison of the two data sets, voxel model and STL model, analysed separately for each of the CT scanners (columns A and B, and D and E in figure 6.30), and all evaluated in SW1, variations in the mean values can be observed for both geometrical and dimensional tolerances. However, no concrete evidence about that, e.g., measurements performed on the STL data yield poorer quality as discussed in section 2.3.4 due to the triangulated surface, were not confirmed. There is a fairly good agreement between the two data sets in this case, also considering the calculated uncertainties.
- A quantitative comparison of the data set from CT2 evaluated in SW1 and SW2 (columns C and D in figure 6.30) resulted in significant deviations for geometrical measurements and rather small deviations for dimensional measurements. Maximum deviations of  $6.4\mu\text{m}$  were found for the latter (i.e., diameters and length), resulting in a good agreement between the two software packages. One has to be aware of the fact that both SW1 and SW2 use different approaches for fitting geometrical primitives, and so individual measurands are defined differently: SW1 takes full advantage of the CT scanner capabilities, i.e., geometrical elements like cylinders, spheres, planes, and so on are fit on the whole model surface. On the other hand, SW2 uses an approach applied to CMM, for example, a cylinder can be fit by use of a number of circles or spirals. *Moreover, the same (number of) measuring points are used in SW2 as they are used in the software for the calibration of the part.* That is why results of parallelism and coaxiality measurement are, for example, opposite for measurements on the voxel data processed in SW2 (column C) compared to measurements in SW1 (the remaining four columns). Parallelism tolerance is found to be smaller in SW2, whereas coaxiality is much higher. Parallelism tolerance was defined by only a few points taken on a flat surface in the housing window and a datum plane defined on the flat surfaces of two grooves. In contrast, coaxiality tolerance was defined by tactilely taking hundreds of points on the inner surface of the flange and a cylindrical datum surface of the inner thread using a scanning probe. It is, however, difficult to explain why measurement of coaxiality is so much different for all the variable combinations A-E. On the other side, results of the geometrical tolerances (parallelism and coaxiality) are in a range of calibrated values. It is known, that measurement of geometrical features is considered more difficult compared to dimensional measurements [40].

It can be observed from the plots that both CMM and CT measurements of the housing satisfied the manufacturer's specifications. Geometrical tolerances were found below the specified tolerance limits, and dimensional tolerances were in the tolerance range, both taking into account the estimated expanded uncertainties.

Looking at the CMM and CT results of inner and outer diameter and length measurement, it can be noticed that values from CMM measurements of inner diameter are greater than CT measurements, and an opposite behaviour is for outer diameter and length measurement. If the housing was, e.g., metallic, influence of beam hardening could be a reasonable explanation. Since the housing is a plastic component, beam hardening shall be neglected, and the only explanation for such an opposite behaviour can be the determination of the surface.

Measurement uncertainties were calculated generally in a range that is acceptable for CT measurements. Namely, outer diameter  $D$  and inner diameter  $d$  yielded average expanded uncertainty of  $6\text{ }\mu\text{m}$ , taking into account measurements using the two CT scanners, measurements performed on two data sets, and evaluation in two different software packages. Length  $L$  and coaxiality  $C$  yielded expanded uncertainty of  $13\text{ }\mu\text{m}$ , and parallelism  $P$   $17\text{ }\mu\text{m}$ . In metrology a tool for decision making about a suitability of a measuring equipment (measuring system) for a given measuring task exists. This is called "golden rule" of metrology, and states that the measurement uncertainty shall be less than 10% of the tolerance to be verified, i.e.,  $U/T < 10\%$ , or at least less than 20% [132]. This ratio then influences the conformance zone [33]. It can be observed in table 6.16 that the dimensional tolerances ( $d$  and  $D$ ) satisfy the golden rule of 10%, and all are smaller than 20%. It shall be noted that the tolerance limits are, in this case study, virtual and do not reflect the real tolerance limits (due to confidentiality reasons as outlined at the beginning of this section). At least, the author found it useful to present how to evaluate the performance of the CT system. Considering that measurement uncertainties from reference measurements are smaller for all measurands while the tolerance limits are the same, the golden rule is fulfilled for all of them.

**Table 6.16:** Maximum calculated expanded uncertainty, tolerance limit, uncertainty to tolerance ratio and available conformance zone for the housing.

| Measurand | $U_{CT}(k=2)$ in mm | $T$ in mm | $U_{CT}/T$ in % | Conformance zone in % |
|-----------|---------------------|-----------|-----------------|-----------------------|
| $P$       | 0.028               | 0.2       | 13.8            | 72.3                  |
| $C$       | 0.017               | 0.1       | 16.9            | 66.2                  |
| $L$       | 0.015               | 0.1       | 14.6            | 70.8                  |
| $d$       | 0.007               | 0.1       | 6.8             | 86.3                  |
| $D$       | 0.007               | 0.1       | 7.0             | 85.9                  |

Measurement uncertainties estimated for measurements on the volume and surface models did not result in any significant differences, as it was for example investigated in section 6.3.

#### 6.4.6 Conclusion

This case study discusses results of tolerance verification of a plastic housing for an insulin pen manufactured by Novo Nordisk A/S. Estimation of measurement uncertainties was taken into account for decision making regarding the specified tolerance limits. It was found that measurements from CMM, including three samples from one cavity of the same mould, each measured only once, and CT measurements, including three reproducible measurements on the same part, fulfilled the tolerance specifications for all selected geometrical and dimensional tolerances for a number of variables

applied in this work. It should also be mentioned, that the tolerances shown were only virtual tolerances (due to confidentiality reasons). The notion that measurement of geometrical features is more difficult and yields bigger variations was also investigated.

#### **6.4.7 Outlook**

In this case, i.e., in mass production where thousands of parts are produced from a single mould, calibration should be performed on a specially developed master piece, where measurements of individual features are the same as, or similar to, a real product. This approach is in accordance with procedures described in ISO 15530-3 [75], where a number of repeated measurements are performed on the calibrated workpiece, enabling the manufactured parts to be traceably verified using a CMM integrated within the production. For example, such a calibrated part was used in [82] for a number of metrological investigations. This piece is dismountable and its segments can be registered by means of regular geometries. In [61], a procedure using a calibrated aluminium test part was applied to document the effects of several system parameters, which can be influenced by the operator.

It is also an intention of the author to focus on this approach for uncertainty estimation, in order to investigate CT-related uncertainty contributions directly, which is presented in the following section 6.5.

## 6.5 Application of the substitution method using calibrated workpieces for uncertainty estimation of dimensional and geometrical measurements

The general concept of ISO 15530-3, substitution method, was described in section 3.4. We found it useful to document the applicability of this approach for uncertainty estimation of CT measurements. Since the ISO standard suggests carrying out at least 20 measurements, in case of CT, this would be too much time consuming, as well as costly, thus we decided to perform only nine CT measurements. It is also stated in the ISO standard, that the position and orientation of the calibrated workpiece shall be systematically varied. However, this is a critical aspect for CT measurements, as it is generally known that positioning and orientation of the workpiece for CT acquisition has a great influence on dimensional measurements [2, 99, 117]. Therefore, the calibrated workpiece was in our case scanned under unchanged conditions.

The GUM suggests correcting measurement results for systematic effects. During the substitution measurement, the working standard and the object are measured alternately on the CMM. First, the working standard is measured, providing geometrical information about the measurand. The result of this measurement is compared to the calibration certificate, and the difference  $\Delta X_{iCMM}$  is used to correct the measurement results of an object (master piece in case of CMM) under investigation  $X_{iCMM}$ , resulting in the corrected value  $Y_{iCMM}$ . This principle is schematically shown in figure 6.31 in blue (full line). Mathematically, the correction of the measurement result is expressed in equation 6.7. As discussed in section 3.4, the method of uncertainty estimation using the substitution method is the only valid approach for CT. Thus, the general approach shown in figure 6.31 in blue can be extended to CT measurements, where the master piece for CT will work as the working standard for CMM measurements. Measurement traceability will be ensured by the CMM measurement. Then, the whole procedure for CMM will be applied to CT measurements (see figure 6.31 in red, dashed line). Difference between CMM and repeated CT measurements carried out on the master piece (already corrected for CT-related errors like scale errors, threshold, etc.)  $\Delta X_{iCT}$  will be used to correct a measurement result of any CT measurement of uncalibrated workpiece  $X_{iCT}$  (also corrected for CT-related errors), resulting in the corrected value  $Y_{iCT}$ . This procedure for calculation of corrected value of CT measurements is presented in equation 6.8.

$$Y_{iCMM} = X_{iCMM} + \Delta X_{iCMM} \quad (6.7)$$

$$Y_{iCT} = X_{iCT} + \Delta X_{iCT} \quad (6.8)$$

### 6.5.1 Measurement setup

Measurement setup for calibration of the component of a dose engine is in details described in section 4.3.1. In the following, measurement setup for CT scanning is described.

#### Measurement setup for CT measurements

Nanotom cone beam CT system at Novo Nordisk A/S from GE Phoenix|x-ray was used in this study. The object, introduced in section 4.3, was placed in the scanner in nearly vertical orientation, freely placed on a polystyrene (PS) (see figure 6.32(a)). Figure 6.32(b) presents a setup for acquisition

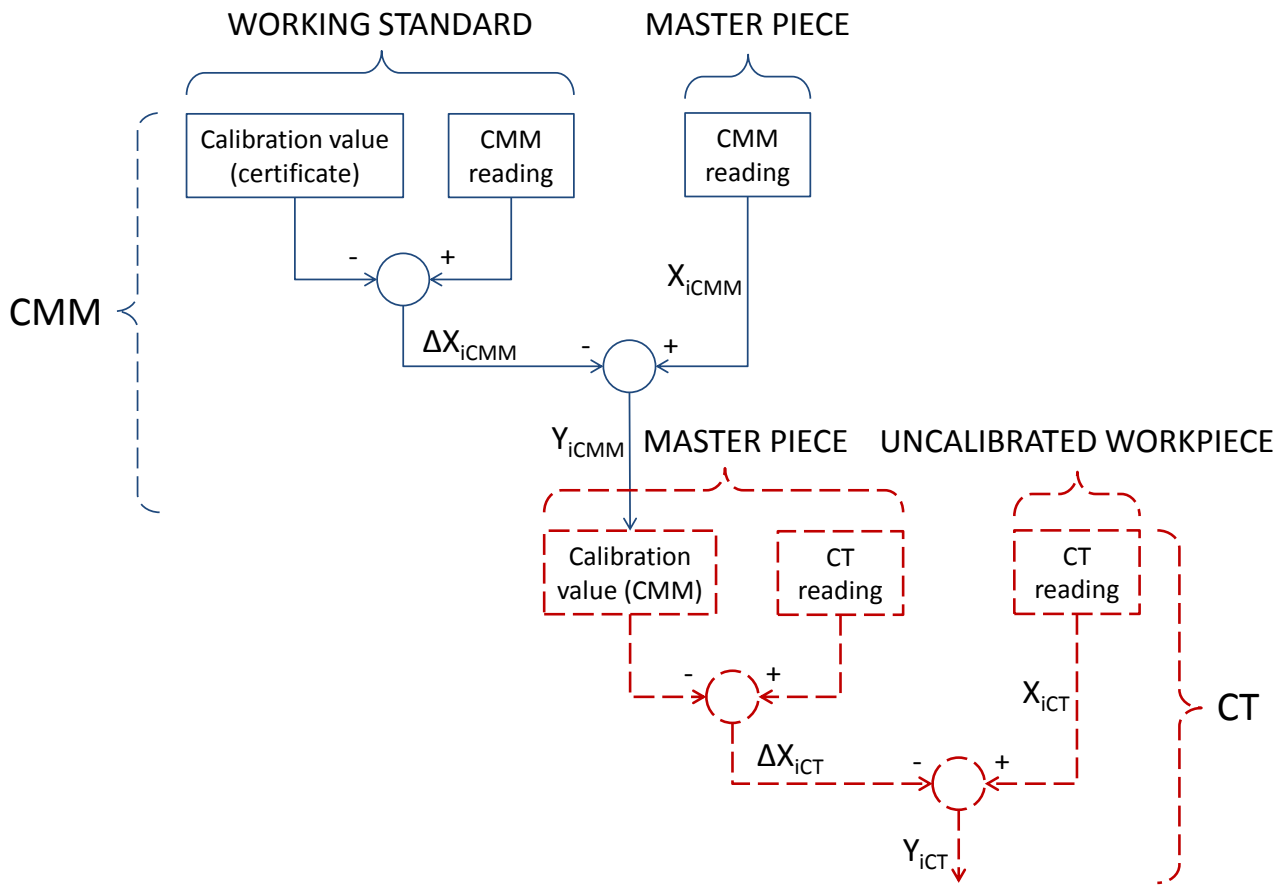
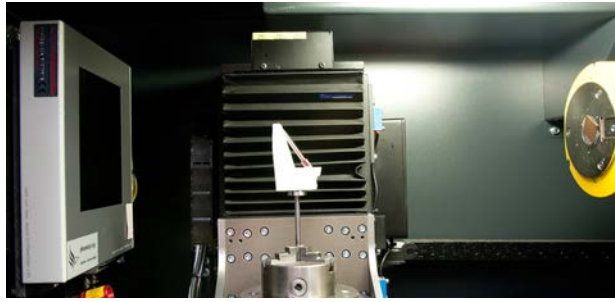


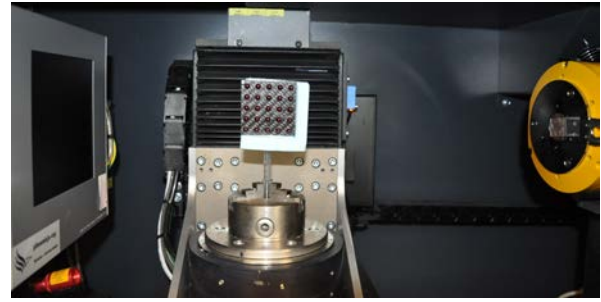
**Figure 6.31:** Adapted principle [133] for calculation of corrected value of measurement using the substitution method.

of the CT ball plate, which is used in this case study for scale error correction. The reference object is scanned in vertical orientation because in this way it covers (especially in the vertical direction) a similar measuring volume as the object under study. Other object for this purpose, ball bar, is not shown. Scanning parameters presented in table 6.17 are the same for all the objects in this investigation (one master piece, two reference objects for scale error correction and three uncalibrated workpieces). As will be explained in section 6.5.3, two operators scanned the master piece independently.

Reconstruction of the CT data set (projection images) was done in software *datos|x* from GE Phoenix|x-ray. Before the reconstruction, a preset value for beam hardening correction (BHC) shall be chosen. This value strongly depends on a material being scanned, and in many cases on operator's experience. For a brass component, such as our master piece, occurrence of beam hardening artifacts is expected, so a preset value of 9 (on a scale from 1 to 10) was selected as a first estimate. Then, the same data set was reconstructed using other similar preset values and the result is shown in figure 6.33. Measurements of inner and outer diameters on the master piece were carried out for all selected preset values and were compared to calibrated measures (the diameter was assessed by probing a circle with high point density approximately in the middle height of the part). The preset value for which the CT measurements are closest to the calibrated values shall be applied to all the reconstructions of all the CT scans. It can be observed that by changing the preset values does not change measurements



(a) Setup of the master piece in the CT scanner.



(b) Setup of the CT ball plate in the CT scanner.

**Figure 6.32:** Setup of the items for CT scanning.

**Table 6.17:** An overview of scanning parameters.

| Parameter              | Unit          | Operator 1  | Operator 2  |
|------------------------|---------------|-------------|-------------|
| Voltage                | kV            | 150         | 140         |
| Current                | $\mu\text{A}$ | 50          | 130         |
| X-ray pre-filter       |               | Cu 0.63 mm  | Cu 0.5 mm   |
| Detector matrix        | pixel         | 1152 x 1152 | 1152 x 1152 |
| Detector pixel size    | $\mu\text{m}$ | 100         | 100         |
| Integration time       | ms            | 1250        | 1000        |
| No. of views           |               | 720         | 720         |
| No. of image averaging |               | 3           | 3           |
| No. of skipped images  |               | 1           | 1           |
| Magnification factor   |               | 1.7         | 2.0         |
| Uncorrected voxel size | $\mu\text{m}$ | 60          | 50          |

of inner diameter, but on the contrary significantly changes measurements of outer diameter. Finally, preset value 9 was selected. The right way to do this, i.e., the method for finding the correct preset BHC value, would be to use a calibrated workpiece, similar (in shape) to the real part and made of the same material, e.g. a hollow cylinder.

## 6.5.2 Data evaluation

### Surface determination

The surface for all the objects in this study was determined using an inspection software VG Studio Max 2.2. Automatic (global) threshold method was used for the master piece as a first estimate for surface determination followed by adaptive (local) threshold method for a better estimation of the surface. Description of the surface determination on the CT ball plate was discussed in section 4.1.4. In case of the ball bar, and due to the fact that the ball bar is a multi-material object (ruby spheres and carbon fibre rod and shank), the segmentation of the material (ruby spheres) from the background (air) was done by manually selecting the ruby spheres on the reconstruction images from different views. Afterwards, advanced surface threshold method was applied.



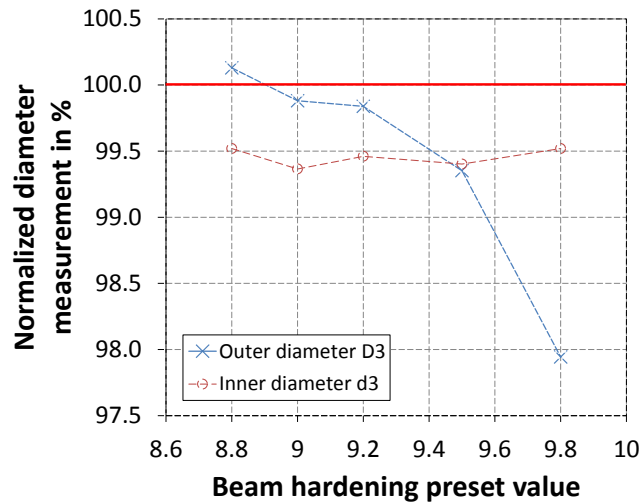


**Figure 6.33:** Diameter measurements for different beam hardening correction preset values. Values are normalized with respect to the calibration values of inner  $d_3$  and outer  $D_3$  diameter (horizontal red line). Definition of sampling strategy for  $d_3$  and  $D_3$  is explained in the following section 6.5.2.

### Definition of measurands

All the dimensional measurements carried out on the CT data were done in software VG Studio Max 2.2. Alignment of the voxel volumes was identical with the alignment defined for the calibration of the part (see figure 4.23). Measurands indicated in figure 4.24 for the calibration of the part are obviously the same also for CT measurements. However, their definition is slightly different, since, generally, CT works with point clouds and CMM with single points. The description of the measurands is given in the following:

- 3 x Diameter  $\varnothing 3.4$  mm ( $d_{1,2,3}$ ) and 2 x Roundness ( $R_{1,2}$ ): Diameters and roundness measurands are defined by creating Circle features and fitting approximately 1000 points, equally distributed around the hole circumference. Diameters are measured at height 2 mm, 5 mm and 15 mm, respectively, in the negative direction of the  $w$ -axis and roundness at height 2 mm and 5 mm, respectively.
- 2 x Diameter  $\varnothing 1.9$  mm ( $D_{1,2}$ ): Diameters are defined by creating a Cylinder feature and fitting approximately 1000 points approximately in the middle of the pins, i.e., in the area not affected by other surfaces or edges.
- Diameter  $\varnothing 4.12$  mm ( $D_3$ ): Diameter is defined by creating Circle feature and fitting approximately 1000 points, equally distributed around the circumference of the outer surface of the object at height 15 mm in the negative direction of the  $w$ -axis.
- Length 6.3 mm ( $L_F$ ): Length is defined as a distance between two parallel planes created on the flat surfaces by fitting approximately 1000 points, in a reasonable distance from edges. The length is measured in the direction of  $u$ -axis.
- Length 46.4 mm ( $L_T$ ): The total length of the object is defined as a distance between two parallel planes created on both sides of the object, by fitting approximately 1000 points equally distributed on flat surfaces at both ends. Length is measured in the direction of  $u$ -axis, defined in the same way as for the calibration of the object.

- 2 x Symmetry (S): Symmetry of the two pins of diameter  $\varnothing 1.9$  mm is measured with respect to the symmetry plane defined between the two parallel surfaces identified for measurements of  $L_F$ .

*Note:* All the features are defined following Least Square Method.

### Scale error correction

Discussion about why it is important to correct the original volume data set (correction of the voxel size) was held in section 3.3.1. In this case study, the reconstructed data sets were corrected using the following four methods: (i) using the CT ball plate, (ii) using a "data base" of 50 CT scans of a ball bar, (iii) using calibrated features of the object's geometry measured by CMM and (iv) using another ball bar (by Operator 2 as it is explained in section 6.5.3). The individual methods are described in the following:

- The method for scale correction using the CT ball plate was described in section 4.1.6. In our case, scanning of the reference object was done before and after scanning of the real part, and an average correction factor was calculated and applied for the correction.
- An attempt in this investigation was to use information from CT scans of a ball bar (calibrated distance between sphere centres 14.7437 mm and nom. diameter of spheres  $\varnothing 2$  mm) scanned under different conditions: 50 independent CT measurements of the ball bar were carried out using Nanotom CT scanner under different scanning settings (scanning parameters) by a number of operators in a period of approximately two years. Figure 6.34 presents the results of correction factor ( $s_{\text{vox}}$ ), calculated according to equation 3.5, plotted as a function of geometrical magnification. Very good fit of values ( $R^2=0.81817$ ) can be observed considering that 50 independent CT measurements of the ball bar were carried out by different operators under different operating conditions. Using the equation of the fit ( $y = -0.00054x + 1.00261$ ) and applying magnification factor of 1.67 (magnification level at which the part under study was scanned), it is possible, in the intersection with a mean correction factor  $\overline{s_{\text{vox}}}$ , to read corresponding  $s_{\text{vox}}$  on y-axis ( $s_{\text{vox}}=1.00171$ ). This  $s_{\text{vox}}$  is then used to correct the voxel size for all nine CT measurements of the master piece (see test plan in section 6.5.3). The selection of the mean  $\overline{s_{\text{vox}}}$  has, however, an attributed uncertainty (standard deviation  $s_{\overline{s_{\text{vox}}}}$ ) which should be taken into account when correcting the voxel size.
- As discussed in section 3.3.1, as well as applied in section 6.2, in case that reference objects for scale error correction are not available, the correction can be done through measurements of calibrated features. In our case, this correction approach is also considered, to investigate the applicability of this method. The features used for scale error correction are outer diameter ( $\varnothing 4.12$  mm) and inner diameter ( $\varnothing 3.4$  mm) measured at the same level, defined at a distance of 15 mm in the negative direction of the  $w$ -axis (for orientation see figure 4.24). A correction factor can be calculated according to equation 6.9.

$$s_{\text{vox}} = \frac{\left(\frac{D+d}{2}\right)_{\text{CMM}}}{\left(\frac{D+d}{2}\right)_{\text{CT}}} \quad (6.9)$$

where  $D$  and  $d$  are outer and inner diameters, respectively, measured by CMM (reference values) and CT at the same height. Average diameter values for the two measurements are considered. In this way, elimination of the threshold determination can be partially achieved.

- A ball bar (calibrated distance between sphere centres 59.8295 mm and nom. diameter of spheres  $\varnothing 6$  mm) was also scanned before and after scanning of the real part (three CT scans carried out by Operator 2), and an average correction factor was calculated.

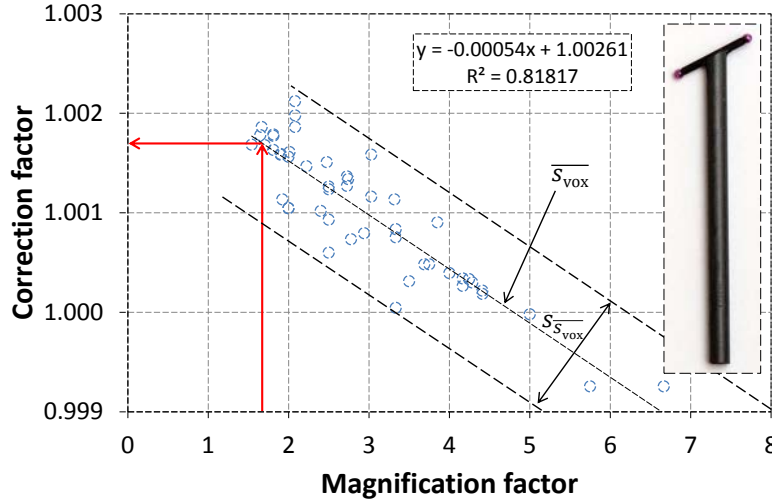


**Figure 6.34:** Correction factor calculated for 50 independent CT measurements of a ball bar (shown in the figure) with calibrated length of 14.7437 mm. Using relatively big amount of measurements carried out using Nanotom CT scanner under different conditions (scanning settings), a reasonably good fit is used for the application of the correction factor which is calculated based on magnification level under which the master piece is scanned. The selection of the mean  $\overline{s_{vox}}$  has an attributed uncertainty (standard deviation  $s_{\overline{s_{vox}}}$  in the figure).

### 6.5.3 Test plan

Experimental test plan is schematically shown in figure 6.35. It can be noticed from the figure that the experiment was carried out in a sequence, corresponding to different days of CT scanning. Reference objects (CT ball plate and ball bar) were scanned before and after scanning of the object (master piece or additional uncalibrated workpieces). Even though it was investigated in section 6.2 that there is no need for scanning of the reference object before and after, but only after scanning of the real part is appropriate, we decided to carry out two CT scans of the reference object due to the fact that the CT scanner has been used for the whole day, during which the X-ray source may drift a lot or other anisotropies of the CT system may occur. Correction factor ( $s_{vox}$ ) used for correcting the voxel size is then calculated as an average value for scanning before and after (basically, at the beginning and at the end of the day). Two operators were involved in performing all the scanings. Operator 1 carried out nine repeated CT measurements of the master piece in two days, Operator 2 carried out three repeated measurements of the master piece. Each operator applied scanning settings of his best choice (for orientation see table 6.17). Additionally, Operator 1 performed CT scans of three uncalibrated workpieces taken from the same production batch as the master piece, each workpiece was scanned once.

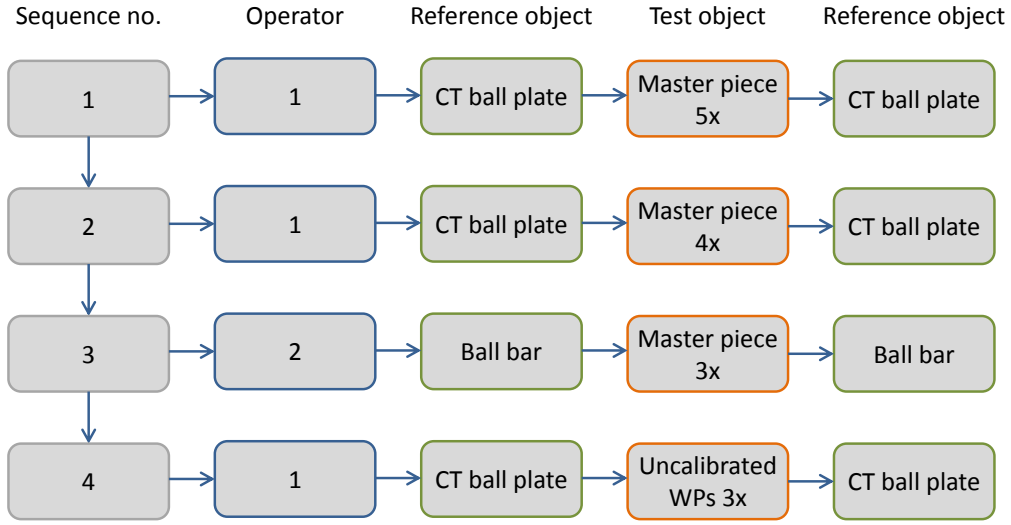


**Figure 6.35:** Experimental test plan.

### 6.5.4 Uncertainty estimation

Measurement uncertainties related to the calibration of the master piece and its individual features (measurands) have been discussed in section 4.3.1.

#### Uncertainty estimation for CT measurements

Measurement uncertainties  $U_{CT}$  for CT measurements were estimated following ISO 15530-3 [75], a substitution method discussed in section 3.4 and at the beginning of this section, according to equation 6.10.

$$U_{CT} = k \sqrt{u_{cal}^2 + u_p^2 + u_w^2 + u_b^2} \quad (6.10)$$

where

- $k$  is coverage factor ( $k=2$  for a confidence interval of 95%)
- $u_{cal}$  is standard uncertainty as previously calculated for tactile reference measurements ( $u_{cal}=U_{cal}/k$ )
- $u_p$  is standard uncertainty of the measurement procedure for each measurand, calculated as  $u_p = h \cdot s$ , where  $h$  is safety factor ( $h=1.2$  for nine measurements), and  $s$  is standard deviation of nine repeated measurements
- $u_w$  is standard uncertainty from the manufacturing process, taking into account temperature-related standard uncertainty calculated for estimated deviation of 4°C from reference temperature and using a range of expansion coefficient of the uncalibrated workpiece ( $(18.7-21.4) \cdot 10^{-6} (°C)^{-1}$ ) delivered by material suppliers, expressed in equation 6.11
- $u_b$  is standard uncertainty of the residual bias contribution, taking into account two contributors, (i) residual bias  $u_{bR}$  (difference between measurements performed using CT scanner and tactile CMM (reference measurements)) and (ii) effect of the uncertainty in the CTE value for the calibrated workpiece  $u_{bT}$ , expressed in equation 6.12

$$u_w = u_{w_T} = (T - 20) \cdot \left( \frac{\alpha_1 - \alpha_2}{2\sqrt{3}} \right) \cdot l_{avg} \quad (6.11)$$

where  $T$  is average measured temperature during CT measurements,  $\alpha_1$  and  $\alpha_2$  correspond to a range (upper and lower) of CTEs of the material of the uncalibrated workpiece stated by different manufactures and considering a rectangular distribution ( $1/2\sqrt{3}$ ) [134] and  $l_{avg}$  is average measured dimension.

$$u_b = \sqrt{u_{b_R}^2 + u_{b_T}^2} = \sqrt{\left( \frac{s}{\sqrt{n}} \right)^2 + \left( (T - 20) \cdot \left( \frac{\alpha_3 - \alpha_4}{2\sqrt{3}} \right) \cdot l_{avg} \right)^2} \quad (6.12)$$

where  $s$  is standard deviation of the difference between CT measurements and calibrated values,  $n$  is number of measurements ( $n=9$ ),  $T$  is average measured temperature during CT measurements,  $\alpha_3$  and  $\alpha_4$  correspond to a range (upper and lower) of CTEs of the material of the calibrated workpiece stated by different manufactures and considering a rectangular distribution ( $1/2\sqrt{3}$ ), and  $l_{avg}$  is average measured dimension. In our specific case, when the uncalibrated workpieces are identical with the calibrated workpiece,  $\alpha_1$  and  $\alpha_2$  are the same as  $\alpha_3$  and  $\alpha_4$ .

Every measurement result  $l_m$  was first corrected for a temperature change  $\Delta T$  from the reference temperature of 20°C. The change in dimension  $\Delta l$  due to the change of temperature can be expressed as follows:

$$\Delta l = \alpha_{avg} \cdot \Delta T \cdot l_m \quad (6.13)$$

where  $\alpha_{avg}$  is average coefficient of linear expansion for brass alloy,  $\Delta T$  is change of temperature from 20°C and  $l_m$  is measurement result.

The corrected measurement result due to the temperature changes  $l_{cor}$  is then expressed as follows:

$$l_{cor} = l_m + \Delta l \quad (6.14)$$

Moreover, measurement result is accompanied by a statement about a bias (see equation 3.9). This is mainly due to the fact that CT and CMM technologies are still so different, so that the absolute difference of measurements between the two instruments is of a big interest.

For the purposes of this investigation, assessment of several uncertainty contributors, specified below, has been modified, in order to estimate its impact on the estimated measurement uncertainty  $U_{CT}$ , expressed in equation 6.10.

(a) **Influence of scanning procedure  $u_p$ :** Operator 1 is compared with Operator 2

The assessment method of the following uncertainty contributors for Operator 2 is as follows:

- $u_p$ :  $h=2.3$  for  $n=3$  measurements performed by Operator 2
- $u_{w_T}$  and  $u_{b_T}$ :  $l_{avg}$  is average measured dimension by Operator 2
- $u_{b_R}$ :  $s$  is standard deviation of the difference between CT measurements performed by Operator 2 and calibrated values,  $n$  is number of measurements ( $n=3$ )

(b) **Influence of scanning procedure  $u_p$ :** Operator 1 and Operator 2 are considered together

The assessment method of the following uncertainty contributors for considering both operators simultaneously is as follows:

- $u_p$ :  $u_p = s$  ( $h$  is not involved since number of measurements  $n$  is greater than 10 ( $n=12$ )),  $s$  is calculated as a standard deviation from 12 CT measurements performed by Operator 1 and Operator 2 (Operator 1 performed nine measurements and Operator 2 three measurements)
- $u_{w_T}$  and  $u_{b_T}$ :  $l_{avg}$  is average measured dimension by Operator 1 and 2
- $u_{b_R}$ : is calculated as  $u_{b_R} = s / \sqrt{n}$ , where  $s$  is standard deviation of 12 measurements performed by Operator 1 and Operator 2 and  $n$  is number of measurements ( $n=12$ )

Operator 2 will not only influence the estimation of the measurement uncertainty but will also have an impact on bias measurements.

(c) **Influence from uncalibrated workpieces  $u_w$ :** Scanning of additional three uncalibrated workpieces

The assessment method of the following uncertainty contributor when scanning additional three uncalibrated workpieces from the same production batch is as follows:

- $u_{w_U}$ : this term is part of  $u_w$  expressed as follows:

$$u_w = \sqrt{u_{w_T}^2 + u_{w_U}^2} \quad (6.15)$$

where  $u_{w_U}$  is experimental standard deviation from measurements of three uncalibrated workpieces, scanned under the same conditions as the master piece.

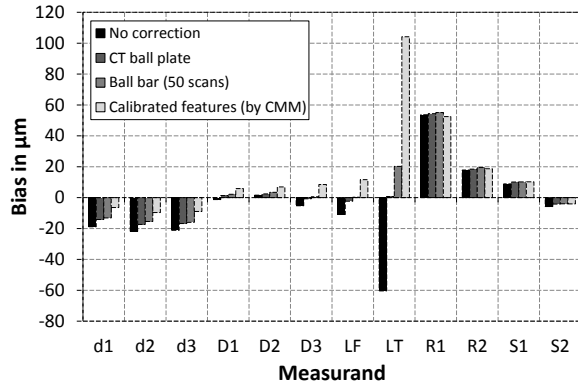
(d) **Influence of scale error correction method:** Reconstructed data sets corrected by different methods

There are no changes in the original equation 6.10, as the only variable influenced here is the bias.

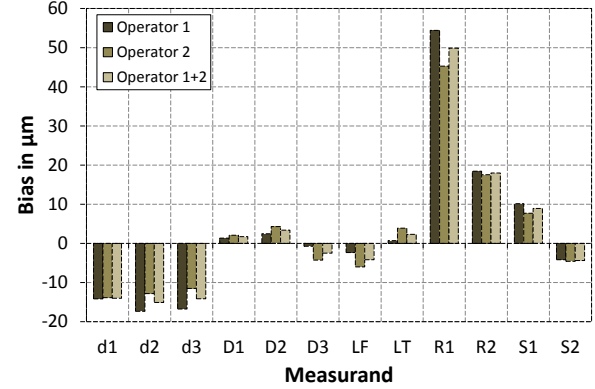
## 6.5.5 Results and discussion

The main results of this investigation are summarized in figure 6.36. The figure is divided into four graphs. Two graphs show the influence of scale error correction method and operator on bias, two other graphs show the influence of operator and scanning of uncalibrated workpieces on the estimation of the measurement uncertainty.

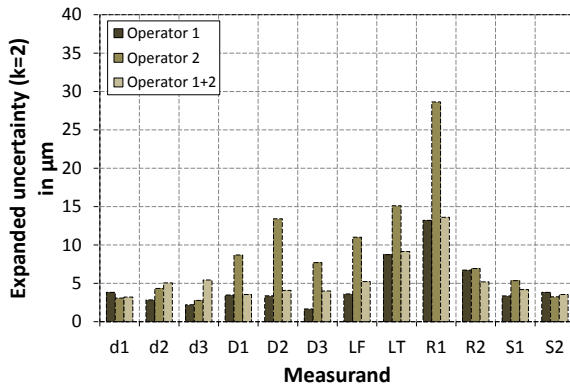
Results of different methods for scale error correction are shown in figure 6.36(a). Results in the uncorrected (for scale errors) state are also presented, only to point out the magnitude of errors with respect to the corrected data. As explained earlier, three correction methods were applied on nine repeated CT measurements of the master piece: (i) using the CT ball plate, (ii) using the "data base" of 50 independent CT measurements of a ball bar and (iii) correction through the calibrated features measured by CMM. Uncorrected voxel sizes as well as calculated correction factors ( $s_{vox}$ ) and resulting voxel sizes corrected applying the three correction methods are presented in table 6.18. The table also provides information about voxel sizes from Operator 2 using the bigger ball bar



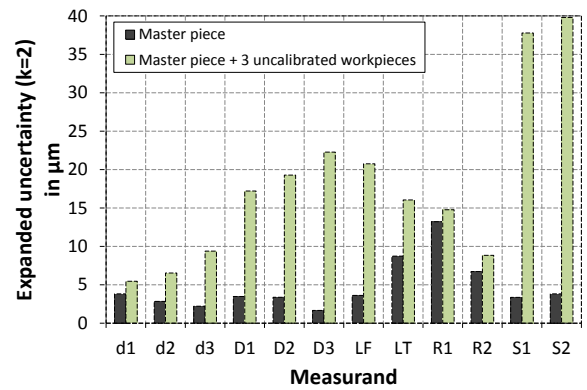
(a) Influence of scale error correction method: bias.



(b) Operator influence: bias.



(c) Operator influence: uncertainty.



(d) Influence of uncalibrated workpieces: uncertainty.

**Figure 6.36:** Results of the influence of bias and measurement uncertainty on dimensional and geometrical measurements of the component under different scanning conditions. Nominal values for measurands indicated in the figure are as follows:  $d_1=d_2=d_3=3.4$  mm,  $D_1=D_2=1.9$  mm,  $D_3=4.12$  mm,  $L_F=6.3$  mm,  $L_T=46.4$  mm.

(nom. length of 60 mm) for the correction. The  $s_{\text{vox}}$  in the table for the CT ball plate is calculated as an average value from two corrections performed in two days (for orientation see test plan in section 6.5.3). The  $s_{\text{vox}}$  for 50 CT scans of the ball bar is calculated using the fitted linear regression line in figure 6.34. The  $s_{\text{vox}}$  for calibrated features measured by CMM is calculated as an average  $s_{\text{vox}}$  for all nine CT measurements of the master piece. It can be observed from the figure that the greatest bias was obtained for measurements of inner diameters and roundness. The two measurands ( $d$  and  $R$ ) are measured inside of the tube in the area with increased wall thickness and greater complexity of the part's geometry causing elevated effects of the beam hardening and noise. This can be seen, for example, in figure 6.37 showing two reconstruction images taken at two distinctive heights, at  $w=-2$  mm and  $w=-30$  mm (for orientation see figure 4.23). Here, it is clear that measurements inside of the tube are significantly influenced by inhomogeneous distribution of gray values belonging to air, which are different from gray values outside of the object. Variation of gray values inside of the part at height  $w=-2$  mm is greater than at  $w=-30$  mm which is due to enhanced wall thickness in this part of the object. Contrast in this area is lower, too. Dimensional measurements in this area are influenced not only by beam hardening but also by scatter radiation, and both then cause problems in threshold determination. In case of roundness measurement, we know that in general, geometrical

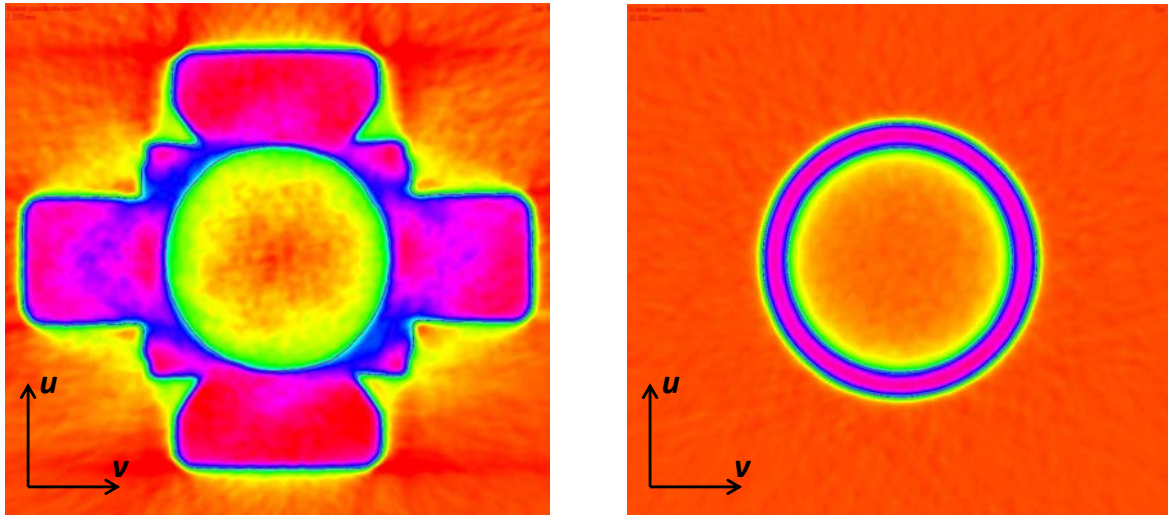
tolerances are very sensitive to CT data [40, 131], as it was discussed in several parts in the thesis. Moreover, very low roundness of  $3\ \mu\text{m}$  was measured by CMM, and so resulting in a significant difference between the two instruments. The magnitude of bias for measurements of all diameters inside the hole ( $d_1$ ,  $d_2$  and  $d_3$ ) is the same, as well as for measurements of all outer diameters ( $D_1$ ,  $D_2$  and  $D_3$ ). Outer diameters and lengths yield reasonably low bias values. Bias values for symmetry tolerance are measured also small, but in this case, it is because the calibrated symmetry tolerance values were quite big, comparable with CT measures. In general, results of inner and outer diameter measurements as well as bi-directional length measurements behave in opposite way, i.e., by applying the correction, the bias for inner diameter measurements decreases while bias for measurements of outer dimensions (both diameter and length) increases. The correction from the calibrated features measured by CMM provides a symmetrically (around zero) displayed bias for measurements of inner and outer dimensions. This could be due to the fact that the correction method is the most related to the actual object's geometry, it is not influenced by any CT-related effects and basically eliminates these effects, and it is therefore more robust for threshold estimation. Measurement of the total length  $L_T$  behaves unexpectedly and it is difficult to draw any meaningful explanations: bias of  $-60\ \mu\text{m}$  of uncorrected data set and  $+103\ \mu\text{m}$  for corrected data set with the calibrated features are obtained. In contrast to the correction done with the calibrated features, the CT ball plate or the ball bar can only correct effects related to manipulator system and focus drift. Moreover, by correcting the voxel data using the two reference objects set the threshold on the outer surface (bias for measurements of outer geometries is nearly zero) and far from the inner surface (bias values of approximately  $-20\ \mu\text{m}$ ). From the graph it can be seen that correction method has no effect on measurements of geometrical tolerances (roundness and symmetry). Looking at the bias obtained after the correction of the data set using the "data base" of 50 CT measurements done using the ball bar, it can be noticed that results of any measurand are comparable with those when using, e.g., the CT ball plate. This is a very good result as it indicates that if measuring errors of a specific CT system are monitored for a longer period using a reference object (in this case - ball bar), providing a good relationship between  $s_{\text{vox}}$  and magnification level, one can use this information and correct the measurement result accordingly, as it is shown in figure 6.34. It shall be noted that the ball bar was scanned under a big variety of scanning settings, always in the central beam (i.e., there where the measuring errors of the system are minimized).

**Table 6.18:** Uncorrected voxel size, calculated correction factors and corrected (re-scaled) voxel sizes for the application of different methods for scale error correction.

| Correction method            | Uncorrected voxel size              | Calculated correction factor | Corrected (re-scaled) voxel size  |
|------------------------------|-------------------------------------|------------------------------|-----------------------------------|
|                              | $s_{\text{uncor}}$ in $\mu\text{m}$ | $s_{\text{vox}}$             | $s_{\text{cor}}$ in $\mu\text{m}$ |
| CT ball plate                | 59.99982                            | 1.00129                      | 60.07711                          |
| Ball bar (50 scans)          | 59.99982                            | 1.00171                      | 60.10242                          |
| Calibrated features (by CMM) | 59.99982                            | 1.00353                      | 60.21138                          |
| Ball bar (60 mm)             | 49.99981                            | 1.00131                      | 50.06529                          |

It can be observed in figure 6.36(b) that the operator has nearly no influence on the bias. However, it has to be noted that Operator 1 carried out nine CT scans and Operator 2 only three. Considering the fact that both operators used different scanning settings for acquisition of the master piece (see





(b) Reconstruction image at  $w=-30$  mm.

**Figure 6.37:** Reconstruction images taken in the  $uv$  plane of the workpiece coordinate system at height  $w=-2$  mm and  $w=-30$  mm. The figure shows inhomogeneous distribution of gray values of air outside and inside of the object.

table 6.17), and that Operator 2 scanned the object at different magnification level ( $m=2$ ) resulting in smaller voxel size of  $50\text{ }\mu\text{m}$  and used the bigger ball bar (nom. length 60 mm) for correction of voxel size, does not yield any significant differences.

Uncertainties estimated for repeated CT measurements of the master pieces are found to be relatively small for all considered measurands (less than  $15\text{ }\mu\text{m}$ ), see figure 6.36(c). A detailed uncertainty budget for repeated CT measurements carried out on the master piece is presented in table 6.19. The table also includes calculation of bias contribution. Generally speaking, very high repeatability of CT scanning of the master piece was achieved, which can be noticed from standard uncertainty  $u_p$ , being less than  $2\text{ }\mu\text{m}$  for most of the measurands. Furthermore, it can be observed in the table that even though relatively big bias was attributed to measurements of inner diameter (approximately  $-17\text{ }\mu\text{m}$ ) compared to outer diameter (approximately  $2\text{ }\mu\text{m}$ ), uncertainties for both (inner and outer diameters) are in the same range (from  $1.7\text{ }\mu\text{m}$  to  $3.8\text{ }\mu\text{m}$ ). Moreover, the uncertainty decreases in the direction of reduced occurrence of beam hardening effect. Uncertainties in case of Operator 2 are bigger compared to Operator 1. This is most likely due to the few number of CT measurements carried out by Operator 2, as with greater number of CT scans the uncertainty decreases (this is demonstrated in the third column in the figure - Operator 1+2). Moreover, as explained earlier, a safety factor  $h$  is used in connection with number of measurements ( $h$  increases with fewer measurements). Measurement uncertainties for roundness measurement are greatest since even one outlier in the data set significantly influences the result. It shall also be noted that the data was not filtered in our case.

By scanning additional three uncalibrated workpieces from the same production batch as the master piece, and considering and adding their contribution to the uncertainty budget yields results presented in figure 6.36(d). Measurement uncertainty is significantly increased for some measurands, which is expected and which is obviously caused by the variation in the manufacturing process. By scanning more uncalibrated workpieces from the production batch could lead to reduction of the uncertainty, as

**Table 6.19:** Uncertainty budget for repeated CT measurements performed on the master piece. Contribution from bias is also presented. All values are in  $\mu\text{m}$ .

| Measurand      | $b$   | $u_{\text{cal}}$ | $u_{\text{p}}$ | $u_{\text{w}}$ | $u_{\text{b}}$ | $U_{\text{CT}}(k=2)$ |
|----------------|-------|------------------|----------------|----------------|----------------|----------------------|
| $d_1$          | -14.2 | 0.90             | 1.60           | 0.27           | 0.44           | <b>3.8</b>           |
| $d_2$          | -17.4 | 0.86             | 1.05           | 0.27           | 0.29           | <b>2.8</b>           |
| $d_3$          | -16.8 | 0.87             | 0.60           | 0.27           | 0.17           | <b>2.2</b>           |
| $D_1$          | 1.4   | 1.13             | 1.26           | 0.15           | 0.35           | <b>3.5</b>           |
| $D_2$          | 2.5   | 0.50             | 1.54           | 0.15           | 0.43           | <b>3.4</b>           |
| $D_3$          | -0.7  | 0.42             | 0.61           | 0.33           | 0.17           | <b>1.7</b>           |
| $L_{\text{F}}$ | -2.4  | 1.34             | 1.06           | 0.50           | 0.29           | <b>3.6</b>           |
| $L_{\text{T}}$ | 0.7   | 0.91             | 2.01           | 3.72           | 0.58           | <b>8.7</b>           |
| $R_1$          | 54.4  | 0.63             | 6.33           | 0.00           | 1.76           | <b>13.2</b>          |
| $R_2$          | 18.4  | 0.61             | 3.19           | 0.00           | 0.89           | <b>6.7</b>           |
| $S_1$          | 10.2  | 1.58             | 0.56           | 0.00           | 0.15           | <b>3.4</b>           |
| $S_2$          | -4.2  | 1.46             | 1.18           | 0.00           | 0.33           | <b>3.8</b>           |

bigger population of samples would be taken into account for variation distribution (of course under the consideration that the parts are manufactured with high precision). Nevertheless, uncertainties estimated for our case (except of symmetry tolerance) are 20  $\mu\text{m}$  and smaller, which is a reasonable range for CT measurements.

Applying the approach presented in figure 6.31 yields results highlighted in table 6.20. As an example, results of diameter measurements  $d_1$  are presented (see a graphical presentation in figure 6.38). In particular, results of data sets uncorrected for scale errors, data sets corrected for scale errors (using CT ball plate) and data set corrected for scale errors and applying the substitution method are shown, along with associated expanded uncertainties. It can be seen from the results, that all the three uncalibrated workpieces are measured in the same range, also considering the estimated uncertainties. Furthermore, this is a sign of a very repeatable manufacture of the workpieces from the same production batch. The correct statement about the final result is important from the point of view of decision making with regards to tolerance limits. We can only see from the figure that the measurement results are very close to the nominal value of the diameter ( $d_1=3.4$  mm), which can indicate the correct application of the substitution method. The corrected value from CT measurements of individual uncalibrated workpiece is strongly influenced by repeated CT measurements of the master piece, which is, in our case, dependent on the method for correction of the voxel size (this corresponds to row "CT reading" in the table).

As discussed earlier in this section, the method for scale error correction using calibrated features measured by CMM seems to work well in our case. For all the nine repeated CT measurements carried out on the master piece, and by comparing CT and CMM measurement results of inner  $d_3$  and outer  $D_3$  diameters according to equation 6.9, an average correction factor  $s_{\text{vox,avg}}$  can be calculated. This value basically characterizes the behaviour of the CT system when measuring a specific object under investigation. Thus, this method for scale error correction using calibrated features was further tested, the  $s_{\text{vox,avg}}$  was applied to eight uncalibrated workpieces, additionally scanned under the same conditions as the master piece. The result is shown in figure 6.39. An example is shown for diameter

**Table 6.20:** A procedure for calculation of a corrected value for diameter  $d_1$  measurements using CT, following the adapted approach from figure 6.31. All values in mm.

|     |                        |                              | 1             | 2             | 3             |
|-----|------------------------|------------------------------|---------------|---------------|---------------|
| CMM | Workpiece standard     | Cal. value (certificate)     | 7.9999        | 7.9999        | 7.9999        |
|     |                        | CMM reading                  | 8.0001        | 8.0001        | 8.0001        |
|     |                        | Difference $\Delta X_{iCMM}$ | -0.0002       | -0.0002       | -0.0002       |
|     | Master piece           | CMM reading $X_{iCMM}$       | 3.3993        | 3.3993        | 3.3993        |
|     | Corrected CMM result   | $Y_{iCMM}$                   | 3.3991        | 3.3991        | 3.3991        |
| CT  | Master piece           | Cal. value (CMM)             | 3.3991        | 3.3991        | 3.3991        |
|     |                        | CT reading                   | 3.3850        | 3.3850        | 3.3850        |
|     |                        | Difference $\Delta X_{iCT}$  | 0.0142        | 0.0142        | 0.0142        |
|     | Uncalibrated workpiece | CT reading $X_{iCT}$         | 3.3816        | 3.3791        | 3.3829        |
|     | Corrected CT result    | $Y_{iCT}$                    | <b>3.3958</b> | <b>3.3932</b> | <b>3.3970</b> |

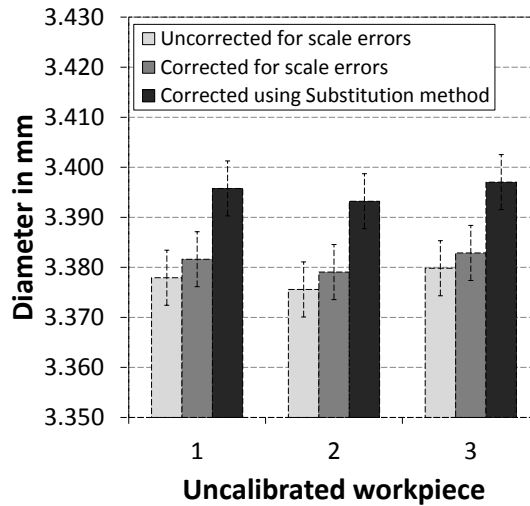


**Figure 6.38:** Results of diameter measurements  $d_1$  of three uncalibrated workpieces. Results of data sets uncorrected for scale errors, data sets corrected for scale errors and data set corrected for scale errors after the application of the substitution method are presented. Data sets were corrected for scale errors using the CT ball plate. Error bars represent expanded uncertainties ( $k=2$ ) estimated according to equation 6.10 and equation 6.15.

$d_1$  measurements. One can observe, again, that after the application of the substitution method, the results of all the eight uncalibrated workpieces are within the estimated uncertainties.

## 6.5.6 Conclusion

In this work, a method for estimation of measurement uncertainty using calibrated workpieces (ISO 15530-3) was presented. We have shown that this method, well accepted method for uncertainty estimation using CMM technique, can also be applied to CT measurements. The method is based on repeated measurements carried out on a calibrated master piece, which in our case was an object - component of a dose engine of an insulin pen - from production. By performing repeated

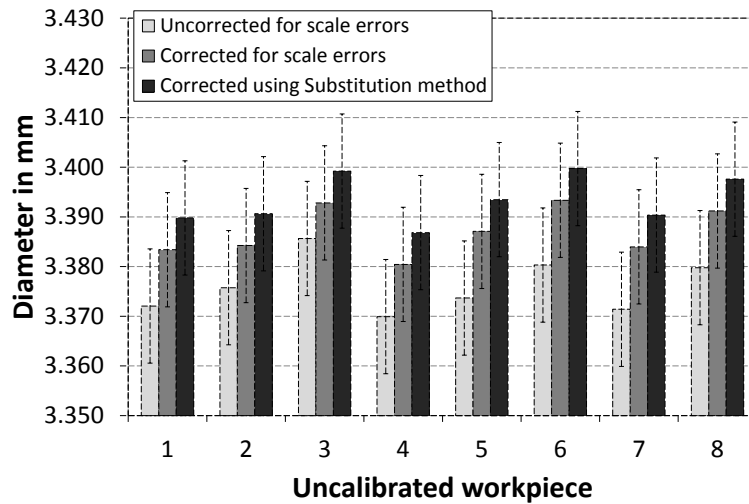


**Figure 6.39:** Results of diameter measurements  $d_1$  of additional eight uncalibrated workpieces. Results of data sets uncorrected for scale errors, data sets corrected for scale errors and data set corrected for scale errors after the application of the substitution method are presented. Data sets were corrected for scale errors using the calibrated features measured by CMM. Error bars represent expanded uncertainties ( $k=2$ ) estimated according to equation 6.10 and equation 6.15 including eight CT measurements.

measurements using a CT system under investigation, it is possible to characterize properties of the CT system and to transfer uncertainty from repeated measurements on to other uncalibrated workpieces, which are CT scanned under similar conditions as the master piece. Based on the results obtained, several conclusions can be drawn:

- Several methods for scale error correction (correction of a voxel size) were applied for correcting the reconstructed CT volume data sets. It was investigated that individual methods have bigger or smaller influence on bias, which than influences the result of each of the uncalibrated workpieces after the application of the substitution method. It turned out that all three methods for scale error correction (i.e., using the CT ball plate, using the "data base" of 50 CT measurements of the ball bar and using calibrated features measured by CMM) yield comparable results, which is, generally speaking, a very good result. Especially, the method using the "data base" appeared to work well, indicating, that if the properties of a CT system under investigation are monitored using a reference object (ball bar in our case), a correction factor which characterizes such a CT system can be applied for scale error correction of any object. The method using the calibrated features worked well, too. In this case, bias obtained for measurements of inner and outer diameters was approximately equally displayed around zero, compared to other correction methods, which can be explained by the fact that the correction method is not influenced by any CT-related effects, as it is form example in case of the CT ball plate or the ball bar. Furthermore, it was investigated that selection of the correction method does not influence bias measurements for geometrical tolerances (roundness and symmetry).
- Dimensional measurements performed inside the tube were strongly influenced by beam hardening. This was observed on reconstructed images taken at different heights along the tube. Inhomogeneous distribution of gray values belonging to air inside the tube lead to uncertainty in threshold determination which was further connected with enhanced bias contribution as well as uncertainties for measurements of inner diameters and roundness.

- No significant differences in bias contribution as well as in estimated measurement uncertainties between measurements performed by the two operators were realized, taking into account variation of the selected scanning settings, number of repeated measurements, and scale correction method applied.
- Very high measurement repeatability was achieved by CT scanning of the master piece. Standard uncertainty from the measurement procedure was calculated to be less than  $2\text{ }\mu\text{m}$  for most of the measurands. Moreover, expanded uncertainties estimated for Operator 1 did not exceed  $15\text{ }\mu\text{m}$  for any considered measurands, which is a range acceptable for CT measurements.
- Measurement uncertainty obviously increased when scanning additional uncalibrated workpieces from the same production batch as the master piece. This was mainly caused by the manufacturing inaccuracies of all the samples. Uncertainties up to  $22\text{ }\mu\text{m}$  were obtained for all measurands but symmetry tolerance, for which uncertainties raised up to  $40\text{ }\mu\text{m}$ .
- Results obtained for measurements of uncalibrated workpieces corrected using the substitution method were found, in our case, to be in the range of estimated uncertainties. This was presented for inner diameter measurements only, performed on three uncalibrated workpieces scale corrected using the CT ball plate and for additional eight uncalibrated workpieces scale corrected using the calibrated features.
- Results obtained for measurements of uncalibrated workpieces corrected using the substitution method were found very close to the nominal values for diameter measurements, also taking into account the estimated uncertainties. We can consider this result as very promising which can indicate the correct application of the substitution method.
- By estimating the task-specific measurement uncertainty following the method using calibrated workpieces, we can say at the end, that the results of measurements obtained in this work are traceable. Measurement uncertainties estimated for the repeated measurements carried out on the master piece were transferred on to the uncalibrated workpieces, which is the general idea of this approach.

### 6.5.7 Outlook

The application of the substitution method seems to be well applicable also for CT measurements. We found this method for uncertainty estimation to be easily implemented in the production environment. As it was said, the method basically requires (i) a calibrated workpiece (e.g., a sample from a production as it was in our case) on which individual features were assessed by a traceable measuring machine and (ii) repeated CT measurements of the master piece, which might be time consuming, but efficient at the end, and is therefore recommended.

The method for scale error correction using the "data set" of 50 CT measurements shall be validated and applied on other objects of different sizes, materials and geometries. It would be interesting to consider and calculate the  $s_{\text{vox}}$  for a smaller range of the magnification level at which the actual part is scanned. This means that if, in our case, the part scanned at a magnification of 1.67, we should only consider points in the graph in the magnification range of, e.g., 1.5 to 2.1. This is schematically

shown in figure 6.40. Based on the equation of the fit, the  $s_{\text{vox}}$  was calculated to be 1.00176 resulting in the voxel size of  $s_{\text{cor}}=60.10522 \mu\text{m}$ , which is not much different from the original estimation.

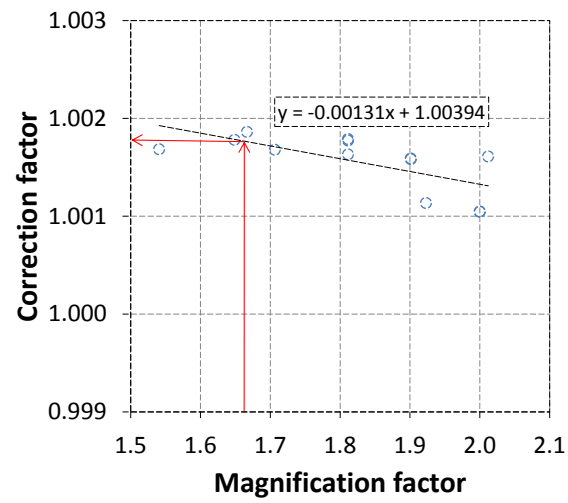


**Figure 6.40:** Correction factor calculated in a smaller magnification range from 1.5 to 2.1, in which the real part is scanned.



# Chapter 7

## Conclusion

### 7.1 Summary

This thesis is divided in three parts: In the first part of the thesis (chapter 1-3) a general introduction to computed tomography (CT), considered to be the third generation of measuring techniques in coordinate metrology, was given, followed by a principle of CT, including description of individual steps of the CT process chain, and issues concerning measurement traceability, including discussions on available standards and guidelines, identification and description of influence factors and the use of reference objects. In the second part of the thesis (chapters 4 and 5), use, manufacture and calibration of reference objects developed by the author at DTU were discussed, and their applications for characterization of CT systems and measurement errors presented. In the third part (chapter 6), an experimental study with focus on identification, quantification and correction of error sources (influence factors) in CT was presented. In the following, the overall conclusions of this work are drawn.

- Due to the fact that in CT many error sources influence the whole process chain for dimensional measurement and because standards and guidelines for CT applications are still under development, traceability cannot be fully ensured. The general idea is to use knowledge from classical coordinate metrology. In particular, application of ISO 10360-2 shall be adapted to CT to define performance characteristics, and ISO 15530-3 for uncertainty estimation. The following methods for uncertainty estimation were discussed in the thesis:
  - GUM - requires a model equation where individual influence factors and their contribution to the uncertainty shall be known. Up to now the application of the method is a challenge for most of the researchers.
  - ISO 14253-2 - the so called PUMA method is a simplified version of the GUM. This standard requires a model equation too, along with a statement about the target uncertainty.
  - ISO 15530-3 - experimental method using calibrated workpieces (master pieces) on which repeated measurements are performed, allowing characterization of error sources in a given CT system for a specific task, and for which the estimation of measurement uncertainty is assessed and is then transferred to other uncalibrated workpieces, pieces from the same production batch as the master piece. This method was applied in this thesis and appeared to be a suitable method for uncertainty estimation in dimensional CT metrology, where calibration of the master piece using an accurate and traceable CMM provided the link to achieve traceability of CT measurements.



- ISO/DTS 15530-2 - use of multiple measurements based on measurements with different positions and orientations of the object in the measuring (CT) volume. This method is not ideal for CT measurements, as it is in case of, e.g., CMM, because the properties of X-ray absorption change in different positions and orientations.
- Simulation methods (e.g. Monte Carlo simulation) were discussed only briefly.

It was also discussed that measurement traceability can be achieved through the use of reference objects, as it is done in classical coordinate metrology. A state of the art of reference objects for CT is given in chapter 3. Here, reference objects of different shapes and materials are used for specific purposes, e.g., for analysis of material-specific absorption, for threshold value determination, for correction of scaling errors and for identification and characterization of anisotropies in the measuring volume.

- In the scope of this thesis, two reference objects, *CT ball plate* and *CT tree*, were developed. Both objects consist of ruby spheres which are supported by or connected to a carbon fibre material which can be CT scanned without causing image artifacts. The evaluation of sphere centres is in case of spheres very precise. Test procedures including surface determination, data evaluation and scale error correction, were developed. The CT ball plate was used in connection with performance characterization of three industrial CT systems and for quantification of influence quantities related to image quality. It appeared that the object could be used for assessment of CT system's MPE value and for optimization of scanning settings respectively. The CT tree was used for characterization of measurement errors and in particular, for investigation of the effect of a tilt of the rotary table axis and Feldkamp effect. Following the proposed procedures helped to identify and quantify these two influences.
- Investigation on the influence of a total scanning time, determined through a combination of scanning parameters, on dimensional and geometrical measurements was carried out. The object under study was an industrial part - component of a dose engine from an insulin pen. A  $2^3$  design of experiment (DOE) was carried out, considering the following three factors: integration time, number of image averaging and number of projection views. Each of the factors notably influences noise in the CT data. However, it appeared that the selection of parameters does not have any significant effect on selected evaluation parameters (length, diameter, symmetry, etc.). A maximum difference of  $20\text{ }\mu\text{m}$  for geometrical and a maximum difference of  $8.6\text{ }\mu\text{m}$  for dimensional measurements was obtained for CT scanning of the object ranging from 9 min to 213 min. CT scans at low levels resulted in reconstructed volumes with "rough" surfaces caused by high noise, and measurement of flatness tolerance indicated that smaller flatness was obtained at higher scanning times. However, in conclusion, this means that there is no need for making long scans yielding small "roughness" of the voxel model as the dimensional (geometrical) measurements do not change significantly.
- Several methods for scale error correction of the CT data were applied throughout the thesis: (i) using reference objects featuring spheres like CT ball plate, CT tree, CT tetrahedron, ball bar, (ii) using calibrated features measured by CMM and (iii) using "data base" of 50 independent CT measurements of a ball bar scanned under different conditions in one CT system.

CT tetrahedron and CT tree were used to correct measurement results of a Lego brick. It turned out that the use of the CT tree in this case was, first, more repeatable (scanning repeatability for measurements of the knob diameters was better than  $0.5\text{ }\mu\text{m}$ ) and second, more applicable

with regards to measurements of knob diameters and distance between knob centres. The latter was based on a hypothesis that the CT tree basically covered a measuring area more similar to the Lego brick and can compensate errors caused by the Feldkamp effect. Another aim in this case study was to find out whether scanning of the reference object is necessary to be performed before & after or only after scanning of the real part. Scanning of the reference object before & after is generally done to eliminate influence of, e.g., the focus drift. It turned out that difference for measurements of diameter of the knobs after the application of scale error correction using these two approaches (i.e., before & after and after) is smaller than 1  $\mu\text{m}$ . Thus, it was concluded that scanning of the reference object only after scanning of the real part is appropriate in our case, which also saves time and costs.

The use of the calibrated features measured by (traceable) CMM worked well as well. This method was applied in connection with measurements carried out on the Lego brick and on the component of a dose engine. In both cases, information from calibration of inner and outer diameters was considered for the correction. In this way, errors connected to, e.g., threshold value determination were minimized. Applying this method led to elimination of other CT-related influences, as it could not be achieved in case of, e.g., reference objects featuring spheres. This correction method seemed to be a good alternative to common correction method using, e.g., ball bar (which is based on measurements of distance between sphere centres and comparison with calibrated measures), especially in case when high power settings are applied. In that case, the reconstructed voxel model of such a ball bar with ruby spheres (of diameter e.g.  $\varnothing 2\text{ mm}$ ) would yield "rough" surfaces on the spheres on which the estimation of the center would be uncertain.

A very interesting and valuable observation was achieved by correcting the CT data sets using the "data base" approach. This approach was based on scanning of a ball bar (calibrated distance between sphere centres 14.7437 mm and nom. diameter of spheres  $\varnothing 2\text{ mm}$ ) under different conditions. Fitting a linear regression line through a data set of 50 calculated correction factors (based on measurements of  $SD$  parameter) yielded a fit of  $R^2=0.818$ . The calculated correction factor was plotted as a function of geometrical magnification. By scanning of an object at a certain magnification level, a corresponding correction factor can be read and applied for correcting the uncorrected reconstructed volume model. Dimensional measurements performed after the application of this method yielded results similar and in some cases even better (i.e., closer to calibrated values) than after the correction using other methods. This was, however, investigated only for one case and should be experimented further.

It was observed that the scale error correction basically does not influence measurements of geometrical tolerances (e.g., roundness, symmetry).

- Measurement uncertainties estimated in this thesis were based on ISO 14253-2 (section 6.4), ISO/TS 15530-3:2009 (section 6.3) and ISO 15530-3:2011 (section 6.5). As discussed in the thesis, the GUM suggests to correct a measurement result for any systematic effects (bias). It was experienced in this work that bias was in most of the cases a dominant uncertainty component, and as such should always be written together with the result and associated uncertainty as follows:

$$Y = y - b \pm U \quad (7.1)$$

In general, bias associated with measurements of outer diameter was smaller compared to

measurements of inner diameter and length. Measurements performed inside holes were influenced by beam hardening and scattered radiation (in case of metals) and thus in threshold value determination. This was, however, not the case when scanning plastic parts. The same as for inner diameter applied to bidirectional distance measurements. Bias for geometrical tolerances was much bigger compared to dimensional measures. Therefore, measurement uncertainty estimated following ISO/TS 15530-3:2009 was obviously influenced by this contribution. In some cases bias represented up to 50% of the calculated expanded uncertainties. Measurement uncertainties could, in principle, be reduced following approach presented in ISO 15530-3:2011, where the bias is assessed separately, only a residual bias contribution is involved in the assessment of the uncertainty.

Furthermore, it was investigated that dimensional CT measurements and associated estimated uncertainties are influenced by the reconstructed 3D model (voxel/surface), i.e., whether measurements are carried out on the original voxel data or the surface (STL) data. Measurement uncertainties obtained for measurements on the STL data were in case of a metal object (pipe connector) considerably bigger compared to measurements of a plastic part (toggle). This was attributed to the occurrence of image artifacts (noise) which appeared in the reconstructed model in the areas with increased thickness and in the area where the object was close to the detector borders.

Uncertainty estimation using the substitution method proved to be applicable for dimensional CT. The method is based on repeated measurements carried out on a calibrated master piece, which in our case was a component from the production (component of a dose engine). Scanning the object repeatedly with a CT system under investigation, it was possible to characterize the CT system and to transfer uncertainty from repeated measurements to other uncalibrated workpieces, which are CT scanned under similar conditions as the master piece. The final corrected results for selected measurands of additionally scanned uncalibrated workpieces considering the estimated measurement uncertainties were very to the nominal values (real tolerances of the part were confidential). It was investigated that the measurement result is influenced by a method for scale error correction used to correct voxel size of reconstructed models obtained from the repeated measurements.

- It appeared that CT is a suitable technique for tolerance quality control and verification of industrial parts. For the case study presented (housing of the insulin pen scanned using two commercial CT scanners), the ratio  $U_{CT}/T$  was smaller than 17% for all considered measurands, taking into account maximum measurement uncertainties estimated for a combination of different variables considered (CT system, data set, and software). The presented tolerance limits were in that case virtual.

## 7.2 Outlook

Based on the results obtained throughout in this Ph.D. work and the experience of the author in the field of dimensional CT metrology in the last three years, the following points for further research work are suggested:

- The design of the CT ball plate could be further improved enabling a full DKD calibration [102], i.e., measurement in four positions defined by flipping the plate. This would allow elimination of CMM errors which cannot be achieved by measuring only in two positions, even though

repeated measurements are carried out. The design of the new version of the CT ball plate should be more similar to the design of the conventional ball plate used for calibration of the CMMs [135].

- Due to the lack of standardized procedures for testing of industrial CT systems and their comparison with other traceable coordinate measuring systems (CMS), also because of a big number of factors influencing the whole CT process chain, traceability in CT cannot be ensured. Therefore, to make CT a traceable CMS, there is great need for development of such procedures. This further encompasses assessment of procedures for comparison of CT with well accepted coordinate measuring machines (CMMs), including procedures for correct alignment strategies between the CT data and CMM data.
- In principle, there is no reference object capable to correct all the errors of a given CT system. This is one of the reasons why the estimation of measurement uncertainty in CT is rather a difficult task and which is why CT is still not yet recognized and traceable measuring system. Development of an object for correcting of all the influence factors, during scanning or during the post-processing phase, is nearly impossible. For this reason, the use of calibrated workpieces for task-specific uncertainty estimation of dimensional measurements seems to be the only valid approach.
- To make a high resolution CT scan of an object, while at the same time trying to avoid any image artifacts in the reconstructed voxel model, is still a challenging task, due to a great variety of scanning settings which have to be selected prior the scanning, even for an experienced operator. Thus, it is required to eliminate the operator influence by, e.g., simulating the optimal positioning of the object in the measuring volume [136] or by suggesting optimized setting parameters [137–139], so that the final measurement result will yield the best possible accuracy and measurement traceability will be achieved. Therefore, the direction of the research should be in the development of methodologies supporting the selection of optimized setting parameters.
- A special care shall be taken when defining an alignment of the measured objects through features which might be exposed to image artifacts (beam hardening or scattered radiation), as it was experienced in case of the pipe connector. This problem mainly concerns scanning of metal objects consisting of features with increased wall thickness and complex geometries. A more precise definition of measurands with respect to the coordinate system, and so more accurate dimensional measurements, can be achieved if the alignment is created on features with reduced occurrence of image artifacts.
- Throughout the thesis it was experienced that image artifacts, and mainly those caused by beam hardening effect, influence the measurement result. Even though some pre-processing steps for reducing image artifacts (or noise) are done, e.g., in the reconstruction software, they still appear in the voxel model. Artifacts, in general, make it difficult to accurately determine regions of different materials and are a cause to measurement impression. Provided that the demands on the accuracy of dimensional CT metrology are increasing, there is a need for development of new procedures and segmentation algorithms (while reducing the necessary computational times).
- It was investigated in the thesis that scanning of the reference object (for correction of measurement errors) only after scanning of the real part is sufficient. It was also suggested

that scanning of the reference object and the real part can be done simultaneously in one setup, reducing the necessary scanning time and related costs. Care must be taken so that the two objects do not overlap during the acquisition, which might have a negative influence on the accuracy of dimensional measurements.

- The approach for scale error correction using the so called "data base" method shall be further studied and tested on objects with complex geometries and objects of different materials. It appeared that the application of this method for correcting (re-scaling) the voxel size works ok. In this case, once the CT system under study is characterized for errors occurring in the measuring volume, a correction factor corresponding to a magnification level at which an object under study is scanned, can be used for correction of the voxel size. Several points for improvement are suggested: (i) In order to fully characterize the CT system, it is necessary to CT scan the reference object not only at different magnification levels and applying a big variety of scanning settings, but also include scanning of the object at different positions in the measuring volume, for example, at the borders with the detector, where other errors from errors occurring in the central plane, are expected. The correction will than be more robust. (ii) Use of a reference object consisting of ball bars of different lengths, e.g. the CT tree, can be beneficial, which enables to cover bigger measuring range (i.e., most of the size of the scanned part). (iii) It is also suggested to use only a smaller range of magnification levels in which the actual part is scanned. However, once all the suggested points are taken into account and the method is validated, there would be no further need for use of reference objects for scale error correction. Additional uncertainty contribution will, however, have to be added for the correction of the voxel size, characterizing the spread of values of the fit for which the correction factor is estimated.
- Future trends in CT lead into in-line CT and related fast CT. The scan itself is performed in a very short time, typically smaller than 2 minutes. As the names suggest, the CT acquisition and further post-processing phase shall be fast, but on the other side accurate, resulting in a reconstructed model which will satisfy the tolerance limits of the part under study. Thus, it is of a great effort to speed-up the CT process chain, but still there is a high demand on the accuracy of the dimensional measurements and especially on 100% quality control. Both in-line CT and fast CT can work in connection with a robot arm, which places and removes the parts from the measuring volume. Once set, these systems work fully automated and data analysis and evaluation are done online. Both in-line CT and fast CT are, in principle, determined by scanning parameters like, e.g., integration time, number of image averaging and number of projection images per revolution. This was in fact experienced, into some extent, in this thesis, where CT scans of a metal object yielded scanning times of 9 min and 213 min respectively. The voxel models appeared "rough" for the short time CT scan (in this case we can say a "fast CT") and still the differences in dimensional (geometrical) measurement from the long CT scan were smaller than 20  $\mu\text{m}$ .
- Today, the tendency is to scan objects with features smaller than 1 mm (i.e., micro parts), having complex 3D geometries, with high aspect ratio features and complex internal structures. These parts are generally produced by  $\mu\text{EDM}$  machining or  $\mu$ -injection moulding processes. Great demands are placed on tight tolerance ranges connected with the micro components. Scanning of such small parts requires to position the parts close to the X-ray source to obtain high voxel resolution. As it was discussed throughout the thesis, objects scanned at high resolution are

subjected to greater demands on accuracy. Thus, individual components of the CT system have to fulfil the highest expectations in terms of stable X-ray sources, high precision manipulator systems and high resolution X-ray detectors. This will be achieved through development of new procedures for calibration of CT systems. In this case, influences due to X-ray focus drift and rotary axis positional errors will be minimized or eliminated. There will be no further need for objects like ball bars, CT ball plate, CT tree and other objects specially designed for correction of scaling errors. Focus should be also in development of procedures and reference objects for elimination of these error sources at micrometer range.



# References

- [1] M. Bartscher, U. Hilpert, J. Goebbels, G. Weidemann, Enhancement and proof of accuracy of industrial computed tomography (CT) measurements, *CIRP Annals - Manufacturing Technology* **56** (1) (2007) pp. 495–498, doi:10.1016/j.cirp.2007.05.118.
- [2] J.-P. Kruth, M. Bartscher, S. Carmignato, R. Schmitt, L. De Chiffre, A. Weckenmann, Computed tomography for dimensional metrology, *CIRP Annals - Manufacturing Technology* **60** (2) (2011) pp. 821–842, doi:10.1016/j.cirp.2011.05.006.
- [3] J.-P. Kruth, Industrial application of ct scanning in engineering and manufacture, *14th CMM Danish users' club conference on 'Application of CT scanning in industry'* (2010) Presentation slides.
- [4] M. Bartscher, U. Neuschaefer-Rube, F. Wäldele, Computed tomography - A highly potential tool for industrial quality control and production near measurements, *NUMB* 1860 (2004) pp. 477–482.
- [5] [http://pdf.directindustry.com/pdf/rx-solutions/products-and-services/Show/54468-74540-\\_2.html](http://pdf.directindustry.com/pdf/rx-solutions/products-and-services/Show/54468-74540-_2.html) (Online; accessed 13-November-2012).
- [6] A. Staude, M. Bartscher, K. Ehrig, J. Goebbels, M. Koch, U. Neuschaefer-Rube, J. Nötel, Quantification of the capability of micro-CT to detect defects in castings using a new test piece and a voxel-based comparison method, *NDT&E International* **44** (2011) pp. 531–536, doi:10.1016/j.ndteint.2011.05.006.
- [7] P. Müller, A. Cantatore, J. L. Andreasen, J. Hiller, L. De Chiffre, Computed tomography as a tool for tolerance verification of industrial part, *CIRP Conference on Computer Aided Tolerancing (CIRP CAT)* (2012) 10 pp.
- [8] J. L. Andreasen, Industrial application of ct scanning in engineering and manufacture, *14th CMM Danish users' club conference on 'Application of CT scanning in industry'* (2010) Presentation slides.
- [9] M. Franz, Ch. Funk, J. Hiller, S. Kasperl, M. Krumm, S. Schröpfer, Reliability of dimensional measurements by computed tomography for industrial applications, *4th European-American Workshop on Reliability of NDE* (2009) 8 pp.
- [10] L. A. Feldkamp, L. C. Davis, J. W. Kress, Practical cone-beam algorithm, *Journal of the Optical Society of America A* **1** (6) (1984) pp. 612–619.



- [11] T. M. Buzug, Computed Tomography: From Photon Statistics to Modern Cone-Beam CT, Springer-Verlag Berlin Heidelberg (2008), doi: 10.1007/978-3-540-39408-2, ISBN 978-540-39407-5.
- [12] A. Sasov, Comparison of fan-beam, cone-beam and spiral scan reconstruction in X-ray micro-CT, *Proceedings of SPIE* **4503** (2002) pp. 124–131.
- [13] R. A. Ketcham, W. D. Carlson, Acquisition, optimization and interpretation of X-ray computed tomographic imagery: Applications to the geosciences, *Computers & Geosciences* **27** (2001) pp. 381–400.
- [14] R. J. Jennings, A method for comparing beam-hardening filter materials for diagnostic radiology, *Medical Physics* **15** (4) (1988) pp. 588–599.
- [15] ASTM E 1441-11 - Standard Guide for Computed Tomography (CT) Imaging, ASTM International, United States.
- [16] <http://www.ndt-ed.org> (Online; accessed 30-November-2012).
- [17] E. Van de Casteele, Model-based approach for beam hardening correction and resolution measurements in microtomography, Ph.D. thesis, Universiteit Antwerpen, Antwerpen (2004).
- [18] R. Christoph, H. J. Neumann, X-ray Tomography in Industrial Metrology - Precise, Economical and Universal, Süddeutscher verlag onpact GmbH (2011), ISBN 978-3-86236-020-8.
- [19] T. Paul, Z. He, Advanced NDT with high resolution computed tomography, *Proceedings of the 17th World Conference on Nondestructive Testing (WCNDT)* (2008) 9 pp.
- [20] S. Carmignato, Traceability of dimensional measurements in computed tomography, *Proceedings of 8th A.I.Te.M. conference* (2007) 11 pp., ISBN/ISSN 88–7957–264–4.
- [21] N. Otsu, A threshold selection method from grey level histograms, *IEEE Transactions on Systems, Man, and Cybernetics* **9** (1) (1979) pp. 62–66.
- [22] Ch. Reinhart, Industrial computer tomography - A universal inspection tool, *Proceedings of the 17th World Conference on Nondestructive Testing (WCNDT)* (2008) 10 pp.
- [23] P. Müller, J. Hiller, A. Cantatore, L. De Chiffre, Investigation of measuring strategies in computed tomography, *New technologies in manufacturing (NEWTECH)* (2011) pp. 31–42, ISBN 978–80–214–4267–2.
- [24] S. Kasperl, J. Hiller, M. Krumm, Computed tomography metrology in industrial research and development, *MP Materials Testing* **51** (6) (2009) pp. 405–411.
- [25] A. Weckenmann, J. Hoffmann, Probing systems for coordinate measuring machines, in: P.H. Pereira, R.J. Hocken (Eds.), *Coordinate Measuring Machines and Systems*, CRC Press (2011), ISBN 978-1-57444-652-4.
- [26] P. H. Pereira, R. J. Hocken, Measurement uncertainty for coordinate measuring systems, in: P.H. Pereira, R.J. Hocken (Eds.), *Coordinate Measuring Machines and Systems*, CRC Press (2011), ISBN 978-1-57444-652-4.

- [27] J. Hiller, L. Reindl, A computer simulation platform for the estimation of measurement uncertainties in dimensional X-ray computed tomography, *Measurement* **45** (2012) pp. 2166–2183.
- [28] H. Schwenke, F. Wäldele, C. Weiskirch, H. Kunzmann, Opto-tactile sensor for 2D and 3D measurement of small structures on coordinate measuring machines, *CIRP Annals - Manufacturing Technology* **50** (1) (2001) pp. 361–364, [http://dx.doi.org/10.1016/S0007-8506\(07\)62140-4](http://dx.doi.org/10.1016/S0007-8506(07)62140-4).
- [29] L. De Chiffre, H. N. Hansen, Metrological limitations of optical probing techniques for dimensional measurements, *CIRP Annals - Manufacturing Technology* **44** (1) (1995) pp. 501–504, [http://dx.doi.org.globalproxy.cvt.dk/10.1016/S0007-8506\(07\)62372-5](http://dx.doi.org.globalproxy.cvt.dk/10.1016/S0007-8506(07)62372-5).
- [30] M. Krumm, S. Karlson, M. Franz, Reducing non-linear artifacts of multi-material objects in industrial 3D computed tomography, *NDT&E International* **41** (2008) pp. 242–251.
- [31] ISO 9001 - Quality Management Systems - Requirements, International Organization for Standardization, Geneva (2008).
- [32] ISO/IEC 17025 - General requirements for the competence of testing and calibration laboratories, International Organization for Standardization, Geneva (2005).
- [33] ISO 14253-1 - Geometrical Product Specifications (GPS) – Inspection by measurement of workpieces and measuring equipment – Part 1: Decision rules for proving conformance or non-conformance with specifications, International Organization for Standardization, Geneva (1998).
- [34] International vocabulary of metrology - basic and general concepts and associated terms VIM, ISO/IEC Guide 99 (2007).
- [35] R. G. Wilhelm, R. Hocken, H. Schwenke, Task specific uncertainty in coordinate measurement, *CIRP Annals - Manufacturing Technology* **50** (2) (2001) pp. 553–563, doi:[http://dx.doi.org/10.1016/S0007-8506\(07\)62995-3](http://dx.doi.org/10.1016/S0007-8506(07)62995-3).
- [36] VDI/VDE 2617-13 - Accuracy of coordinate measuring machines - Characteristics and their testing - Guideline for the application of DIN EN ISO 10360 for coordinate measuring machines with CT-sensors, VDI/VDE 2630-1.3 - Computed tomography in dimensional measurement - Guideline for the application of DIN EN ISO 10360 for coordinate measuring machines with CT-sensors, VDI/VDE Society for Metrology and Automation Engineering (GMA), Duesseldorf (2011).
- [37] ISO/IEC Guide 98-3 - Uncertainty of measurement – Part 3: Guide to the expression of uncertainty in measurement (GUM:1995), International Organization for Standardization, Geneva (2008).
- [38] VDI/VDE 2630-1.2 - Computed tomography in dimensional measurement - Influencing variables on measurement results and recommendations for computed tomography dimensional measurements, VDI/VDE Society for Metrology and Automation Engineering (GMA), Duesseldorf (2010).

- [39] H. Lettenbauer, B. Georgi, B. Weiss, Means to verify the accuracy of CT systems for metrology applications (In the absence of established international standards), *International Symposium on Digital industrial Radiology and Computed Tomography* (2007) 6 pp.
- [40] S. Carmignato, Accuracy of industrial computed tomography measurements: experimental results from an international comparison, *CIRP Annals - Manufacturing Technology* **61** (1) (2012) pp. 491–494, doi:<http://dx.doi.org/10.1016/j.cirp.2012.03.021>.
- [41] ISO 10360-2 - Geometrical product specifications (GPS) – Acceptance and reverification tests for coordinate measuring machines (CMM) – Part 2: CMMs used for measuring linear dimensions, International Organization for Standardization, Geneva (2009).
- [42] S. Carmignato, D. Dreossi, L. Mancini, F. Marinello, G. Tromba, E. Savio, Testing of x-ray microtomography systems using a traceable geometrical standard, *Measurement Science and Technology* **20** (8) (2009) 084021, 7 pp.
- [43] VDI/VDE 2634-2 - Optical 3-D measuring systems - Optical systems based on area scanning, VDI/VDE Society for Metrology and Automation Engineering (GMA), Duesseldorf (2012).
- [44] VDI/VDE 2630-1.1 - Computed tomography in dimensional measurement - Basics and definitions, VDI/VDE Society for Metrology and Automation Engineering (GMA), Duesseldorf (2009).
- [45] VDI/VDE 2630-1.4 - Computed tomography in dimensional metrology - Measurement procedure and comparability, VDI/VDE Society for Metrology and Automation Engineering (GMA), Duesseldorf (2008).
- [46] ISO 15708-1 - Non-destructive testing - Radiation methods - Computed tomography: Part 1: Principles, International Organization for Standardization, Geneva (2002).
- [47] ISO 15708-2 - Non-destructive testing - Radiation methods - Computed tomography: Part 2: Examination practices, International Organization for Standardization, Geneva (2002).
- [48] EN 16016-1 - Non Destructive Testing - Radiation method - Computed tomography - Part 1: Terminology (2011).
- [49] EN 16016-2 - Non Destructive Testing - Radiation method - Computed tomography - Part 2: Principle, equipment and samples (2011).
- [50] EN 16016-3 - Non Destructive Testing - Radiation method - Computed tomography - Part 3: Operation and interpretation (2011).
- [51] EN 16016-4 - Non Destructive Testing - Radiation method - Computed tomography - Part 4: Qualification (2011).
- [52] ISO/WD 10360-11 (Draft) - Geometrical product specifications (GPS) – Acceptance and reverification tests for coordinate measuring machines (CMM) – Part 11: Computed tomography, International Organization for Standardization, Geneva (2011).
- [53] ASTM E 1695-95e1 - Standard test method for measurement of computed tomography (CT) system performance, ASTM International, United States (2006).

- [54] ASTM E 1570-11 - Standard practice for computed tomographic (CT) examination, ASTM International, United States.
- [55] ASTM E 1672-12 - Standard guide for computed tomographic (CT) system selection, ASTM International, United States.
- [56] VDI/VDE 2617-6.1 - Accuracy of coordinate measuring machines - Characteristics and their testing, Coordinate measuring machines with optical probing - Code of practice for the application of DIN EN ISO 10360 to coordinate measuring machines with optical sensors for lateral structures, VDI/VDE Society for Metrology and Automation Engineering (GMA), Duesseldorf (2007).
- [57] VDI/VDE 2617-6.2 - Accuracy of coordinate measuring machines - Characteristics and their testing, Guideline for the application of DIN EN ISO 10360 to coordinate measuring machines with optical distance sensors, VDI/VDE Society for Metrology and Automation Engineering (GMA), Duesseldorf (2005).
- [58] M. Bartscher, H. Bremer, T. Birth, A. Staude, K. Ehrig, The resolution of dimensional CT - an edge-based analysis, *Proceedings of the Conference on Industrial Computed Tomography (ICT)* (2012) pp. 191–200, ISBN 978–3–8440–1281–1.
- [59] S. Carmignato, A. Pierobon, P. Rampazzo, M. Parisatto, E. Savio, CT for industrial metrology - Accuracy and structural resolution of CT dimensional measurements, *Proceedings of the Conference on Industrial Computed Tomography (ICT)* (2012) pp. 161–172, ISBN 978–3–8440–1281–1.
- [60] A. Weckenmann, Ph. Krämer, Predetermination of measurement uncertainty in the application of computed tomography, *11th CIRP International Conference on Computer Aided Tolerancing* (2009) 5 pp.
- [61] R. Schmitt, Ch. Niggemann, Uncertainty in measurement for X-ray-computed tomography using calibrated workpieces, *Measuring Science and Technology* **21** (2010) pp. 1–9.
- [62] F. Welkenhuyzen, K. Kiekens, M. Pierlet, W. Dewulf, P. Bleys, J.-P. Kruth, A. Voet, Industrial computer tomography for dimensional metrology: Overview of influence factors and improvement strategies, *4th International Conference on Optical Measurement Techniques for Structures and Systems (OPTIMESS)* (2009) 9 pp.
- [63] M. Bartscher, M. Neukamm, U. Hilpert, U. Neuschaefer-Rube, F. Härtig, K. Kniel, K. Ehrig, A. Staude, J. Goebbels, Achieving traceability of industrial computed tomography, *Key Engineering Materials* **437** (2010) pp. 79–83, doi:10.4028/www.scientific.net/KEM.437.79.
- [64] U. Bonse, F. Busch, X-ray computed microtomography ( $\mu$ CT) using synchrotron radiation (SR)., *Progress in Biophysics and Molecular Biology* **65** (1-2) (1996) pp. 133–169.
- [65] O. Brunke, K. Brockdorf, S. Drews, B. Müller, T. Donath, J. Herzen, F. Beckmann, Comparison between X-ray tube based and synchrotron radiation based  $\mu$ CT, *Proceedings of SPIE* 7078 (2008) 12 pp.

- [66] M. Simon, I. Tiseanu, Ch. Sauerwein, S.-M. Yoo, I.-S. Cho, Development of multi sensor and multi source computed tomography systems, *International Symposium on Digital industrial Radiology and Computed Tomography* (2009) 9 pp.
- [67] Ch. Heinzl, J. Kastner, T. Müller, , M. E. Gröller, Statistical analysis of multi-material components using dual energy ct, *Vision, Modeling and Visualization (VMV)* (2008) pp. 179–188.
- [68] J. Kastner, D. Heim, D. Salaberger, Ch. Sauerwein, M. Simon, H. Wälischmiller, Advanced applications of computed tomography by combining of different methods, *Proceedings of 9th European Conference on Nondestructive Testing (ECNDT)* (2006) 8 pp.
- [69] S. Kasperl, J. Hiller, Artefact correction at coordinate measuring with industrial X-ray computed tomography (in German), *Technisches Messen* **76** (9) (2009) pp. 401–409, doi:10.1524/teme.2009.0918.
- [70] G. T. Herman, Correction for beam hardening in computed tomography, *Physics in Medicine and Biology* **21** (1) (1979) pp. 81–106.
- [71] G. T. Herman, Image Reconstruction from Projections: the Fundamentals of Computerized Tomography, 2nd Edition, Academic Press, Inc, New York (1980), ISBN 978-1-85233-617-2.
- [72] R. A. Brooks, G. Di Chiro, Beam hardening in X-ray reconstructive tomography, *Physics in Medicine and Biology* **21** (3) (1976) pp. 390–398.
- [73] A. Cantatore, Graphical User Interface (GUI) for correction of beam hardening effects in X-ray computed tomography, User guide, Technical University of Denmark (2012).
- [74] ISO 14253-2 - Geometrical product specifications (GPS) – Inspection by measurement of workpieces and measuring equipment – Part 2: Guide to the estimation of uncertainty in GPS measurement, in calibration of measuring equipment and in product verification, International Organization for Standardization, Geneva (2011).
- [75] ISO 15530-3 - Geometrical product specifications (GPS) – Coordinate measuring machines (CMM): Technique for determining the uncertainty of measurement – Part 3: Use of calibrated workpieces or measurement standards, International Organization for Standardization, Geneva (2011).
- [76] ISO/DTS 15530-2 - Geometrical product specifications (GPS) – Coordinate measuring machines (CMM): Technique for determining the uncertainty of measurement – Part 2: Use of multiple measurements strategies, International Organization for Standardization, Geneva (2002).
- [77] ISO/IEC Guide 98-3/Suppl 1 - Propagation of distributions using a Monte Carlo method, International Organization for Standardization, Geneva (2008).
- [78] VDI/VDE 2617-7 - Accuracy of coordinate measuring machines - Parameters and their checking - Estimation of measurement uncertainty of coordinate measuring machines by means of simulation, VDI/VDE Society for Metrology and Automation Engineering (GMA), Duesseldorf (2006).

- [79] ISO/TS 15530-4 - Geometrical product specifications (GPS) – Coordinate measuring machines (CMM): Technique for determining the uncertainty of measurement – Part 4: Evaluating task-specific measurement uncertainty using simulation, International Organization for Standardization, Geneva (2008).
- [80] M. Bartscher, K. Ehrig, A. Staude, J. Goebbels, U. Neuschaefer-Rube, Application of an industrial CT reference standard for cast freeform shaped workpieces, *International Symposium on Digital Industrial Radiology and Computed Tomography* (2011) 12 pp.
- [81] P. Wenig, S. Kasperl, Examination of the measurement uncertainty on dimensional measurements by X-ray computed tomography, *Proceedings of 9th European Conference on Nondestructive Testing (ECNDT)* (2006) 10 pp.
- [82] M. Bartscher, M. Neukamm, M. Koch, U. Neuschaefer-Rube, A. Staude, J. Goebbels, K. Ehrig, Ch. Kuhn, A. Deffner, A. Knoch, Performance assessment of geometry measurements with micro-CT using a dismountable work-piece-near reference standard, *Proceedings of the 10th European Conference on Nondestructive Testing (ECNDT)* (2010) 10 pp.
- [83] P. Müller, R. A. Pacurar, L. De Chiffre, A. Cantatore, P. Berce, Geometrical metrology on silicone rubber by computed tomography, *Proceedings of the 11th International Conference of the European Society for Precision Engineering and Nanotechnology (euspen)* **1** (2011) pp. 243–246, ISBN13 978–0–9553082–9–1.
- [84] P. Müller, J. Hiller, YY. Dai, J. L. Andreasen, H. N. Hansen, L. De Chiffre, Industrial application of uncertainty estimation using calibrated workpieces for dimensional measurements in X-ray computed tomography, Submitted to *Measurement Science and Technology*.
- [85] ISO/TS 15530-3 - Geometrical product specifications (GPS) – Coordinate measuring machines (CMM): Technique for determining the uncertainty of measurement – Part 3: Use of calibrated workpieces or standards, International Organization for Standardization, Geneva (2009).
- [86] J. Hiller, Estimation of uncertainties at dimensional measuring with industrial X-ray computed tomography by simulation (in German), Ph.D. thesis, University of Freiburg i. Br. (2011).
- [87] S. Carmignato, A. Pierobon, Preliminary results of the 'CT Audit' project: First international intercomparison of computed tomography systems for dimensional metrology, *International Symposium on Digital industrial Radiology and Computed Tomography* (2012) 8 pp.
- [88] S. Carmignato, A. Pierobon, E. Savio, First international intercomparison of computed tomography systems for dimensional metrology, *Proceedings of the 11th International Conference of the European Society for Precision Engineering and Nanotechnology (euspen)* **1** (2011) pp. 84–87, ISBN13 978–0–9553082–9–1.
- [89] S. Carmignato, A. Pierobon, E. Savio, CT audit interlaboratory comparison of CT systems for dimensional metrology, University of Padova, Project report (2011) 323 pp.
- [90] P. Müller, Use of reference objects for correction of measuring errors in X-ray computed tomography, Technical University of Denmark, Report (2010) 34 pp.

- [91] M. Schulze, M. Neugebauer, R. Meess, J. Brzoska, A. Jung, A. Staude, K. Ehrig, Der Einfluss unterschiedlicher Materialzusammensetzungen auf das dimensionelle Messen von Mikroobjekten mittels Mikro-Computertomographie (in German), *DGZfP-Jahrestagung* (2010) pp. 1–9.
- [92] U. Neuschaefer-Rube, M. Bartscher, M. Neukamm, F. Härtig, K. Ehrig, A. Staude, J. Goebbels, Dimensional measurements with micro-CT - Test procedures and applications, *Microparts Interest Group Workshop* (2009) Presentation slides.
- [93] U. Neuschaefer-Rube, M. Neugebauer, W. Ehrig, M. Bartscher, U. Hilpert, Tactile and optical microsensors: Test procedures and standards, *Measurement Science and Technology* **19** (2008) 084010, 5 pp., doi:10.1088/0957-0233/19/8/084010.
- [94] M. Neugebauer, U. Hilpert, M. Bartscher, N. Gerwien, M. Krystek, C. Schwehn, M. Trenk, J. Goebbels, G. Weidemann, Investigation of the measurement of micro geometries with large tactile CMMs and application at a micro-CT artefact (in German), *Technisches Messen* **75** (3) (2008) pp. 187–198, doi:10.1524/teme.2008.0826.
- [95] J. Hiller, S. Kasperl, U. Hilpert, M. Bartscher, Coordinate measuring with industrial X-ray computed tomography (in German), *Technisches Messen* **74** (11) (2007) pp. 553–564, doi:10.1524/teme.2007.74.11.553.
- [96] K. Kiekens, F. Welkenhuyzen, Y. Tan, Ph. Bleys, A. Voet, J.-P. Kruth, W. Dewulf, A test object with parallel grooves for calibration and accuracy assessment of industrial computed tomography (CT) metrology, *Measuring Science and Technology* **22** (2011) 115502.
- [97] L. De Chiffre, S. Carmignato, A. Cantatore, J. D. Jensen, Replica calibration artefacts for optical 3D scanning of micro parts, *Proceedings of the 9th International Conference of the European Society for Precision Engineering and Nanotechnology (euspen)* **2** (2009) pp. 352–355, ISBN13 978-0-9553082-6-0.
- [98] A. Cantatore, L. De Chiffre, S. Carmignato, Investigation on a replica step gauge for optical 3D scanning of micro parts, *Proceedings of the 10th International Conference of the European Society for Precision Engineering and Nanotechnology (euspen)* **1** (2010) pp. 200–203, ISBN13 978-0-9553082-8-4.
- [99] A. Cantatore, J. L. Andreasen, S. Carmignato, P. Müller, L. De Chiffre, Verification of a CT scanner using a miniature step gauge, *Proceedings of the 11th International Conference of the European Society for Precision Engineering and Nanotechnology (euspen)* **1** (2011) pp. 46–49, ISBN13 978-0-9553082-9-1.
- [100] A. Cantatore, J. Angel, L. De Chiffre, Material investigation for manufacturing of reference step gauges for CT scanning verification, *Proceedings of the 12th International Conference of the European Society for Precision Engineering and Nanotechnology (euspen)* **1** (2012) pp. 129–132, ISBN13 978-0-9566790-0-0.
- [101] P. Müller, J. Hiller, A. Cantatore, G. Tosello, L. De Chiffre, New reference object for metrological performance testing of industrial CT systems, *Proceedings of the 12th International Conference of the European Society for Precision Engineering and Nanotechnology (euspen)* **1** (2012) pp. 72–75, ISBN13 978-0-9566790-0-0.

- [102] H. Kunzmann, E. Trapet, F. Wäldele, Results of the international comparison of ball plate measurements in CIRP and WECC, *CIRP Annals - Manufacturing Technology* **44** (1) (1995) pp. 479–482, doi:[http://dx.doi.org/10.1016/S0007-8506\(07\)62367-1](http://dx.doi.org/10.1016/S0007-8506(07)62367-1).
- [103] H. N. Hansen, L. De Chiffre, A combined optical and mechanical reference artefact for coordinate measuring machines, *CIRP Annals - Manufacturing Technology* **46** (1) (1997) pp. 467–470, [http://dx.doi.org/10.1016/S0007-8506\(07\)60867-1](http://dx.doi.org/10.1016/S0007-8506(07)60867-1).
- [104] L. De Chiffre, H. N. Hansen, R. E. Morace, Comparison of coordinate measuring machines using an optomechanical hole plate, *CIRP Annals - Manufacturing Technology* **54** (1) (2005) pp. 479–482, [http://dx.doi.org/10.1016/S0007-8506\(07\)60149-8](http://dx.doi.org/10.1016/S0007-8506(07)60149-8).
- [105] EA-10/05 - Coordinate Measuring Machine Calibration, European cooperation for Accreditation (1995).
- [106] Kalibrering af kugleplader (in Danish), Nr.: KO-401, CGM, Kgs. Lyngby (1997).
- [107] ISO/IEC 17043 - Conformity assessment - General requirements for proficiency testing, International Organization for Standardization, Geneva (2010).
- [108] H. Lettenbauer, METROTOM - Measure in a new dimension, *Inovation SPECIAL Metrology* **9** (2007) pp. 12–13.
- [109] V. Andreu, B. Georgi, H. Lettenbauer, J. A. Yagüe, Analysis of the error sources of a computer tomography machine, *9th International Conference and Exhibition on Laser Metrology, Machine Tool, CMM and Robotic Performance* (2009) pp. 462–471.
- [110] W. A. Kalender, Computed Tomography: Fundamentals, System Technology, Image Quality, Applications, 2nd Edition, Wiley-VCH (2006), ISBN13 978-3895782169.
- [111] J. Hiller, T. O. J. Fuchs, L. M. Reindl, Influence of the quality of X-ray computed tomography image on coordinate measurements: Principles, measurements and simulations (in German), *Technisches Messen* **78** (7-8) (2011) pp. 334–347.
- [112] J. Hiller, M. Maisl, L. M. Reindl, Physical characterization and performance evaluation of an X-ray micro-computed tomography system for dimensional metrology applications, *Measurement Science and Technology* **23** (085404, 18 pp.) (2012) 18 pp., doi:[10.1088/0957-0233/23/8/085404](https://doi.org/10.1088/0957-0233/23/8/085404).
- [113] M. J. Flynn, S. M. Hames, D. A. Reimann, S. J. Wilderman, Microfocus X-ray sources for 3D microtomography, *Nuclear Instruments and Methods in Physics Research A* **353** (1994) pp. 312–315.
- [114] X. Yang, Y. Meng, Q. Luo, H. Gong, High resolution in vivo micro-CT with flat panel detector based on amorphous silicon, *Journal of X-Ray Science and Technology* **18** (4) (2010) pp. 381–392.
- [115] M. Hilts, C. Duzenli, Image noise in X-ray CT polymer gel dosimetry, *Journal of Physics: Conference Series* **3** (2004) pp. 252–256, doi:[10.1088/1742-6596/3/1/040](https://doi.org/10.1088/1742-6596/3/1/040).



- [116] D. Weiss, A. Deffner, Ch. Kuhn, Einfluss der Quellbewegung auf Reproduzierbarkeit und Antastabweichung im Röntgen-Computertomographen (in German), *Proceedings Fachtagung Industrielle Computertomographie (CTC)* (2010) pp. 227–234.
- [117] J. Kumar, A. Attridge, P. K. C. Wood, M. A. Williams, Analysis of the effect of cone-beam geometry and test object configuration on the measurement accuracy of a computed tomography scanner used for dimensional measurement, *Measurement Science and Technology* **22** (2011) 035105, 14 pp.
- [118] J. Hsieh, *Computed Tomography: Principles, Design, Artifacts, and Recent Advances*, 2nd Edition, Vol. PM188, SPIE Press Book (2003), ISBN13 978-0819444257.
- [119] P. Müller, J. Hiller, A. Cantatore, M. Bartscher, L. De Chiffre, Investigation on the influence of image quality in X-ray CT metrology, *Proceedings of the Conference on Industrial Computed Tomography (ICT)* (2012) pp. 229–238, ISBN 978–3–8440–1281–1.
- [120] D. Weiss, R. Lonardoni, A. Deffner, Ch. Kuhn, Geometric image distortion in flat-panel X-ray detectors and its influence on the accuracy of CT-based dimensional measurements, *Proceedings of the Conference on Industrial Computed Tomography (ICT)* (2012) pp. 175–181, ISBN 978–3–8440–1281–1.
- [121] A. Weckenmann, Ph. Krämer, Assessment of measurement uncertainty caused in the preparation of measurements using computed tomography, *XIX IMEKO World Congress of Fundamental and Applied Metrology* (2009) pp. 1888–1892, ISBN 978–963–88410–0–1.
- [122] W. Dewulf, Y. Tan, K. Kiekens, Sense and non-sense of beam hardening correction in CT metrology, *CIRP Annals - Manufacturing Technology* **61** (1) (2012) pp. 495–498, doi:<http://dx.doi.org/10.1016/j.cirp.2012.03.013>.
- [123] F. Vogeler, W. Verheecke, A. Voet, J.-P. Kruth, W. Dewulf, Positional stability of 2D X-ray images for computed tomography, *International Symposium on Digital Industrial Radiology and Computed Tomography* (2011) 9 pp.
- [124] J. P. Steffen, T. Fröba, Reducing the focal spot shift of microfocus X-ray tubes to increase the accuracy of CT-based dimensional measurement, *International Symposium on Digital Industrial Radiology and Computed Tomography*.
- [125] S. Gasparin, G. Tosello, H. N. Hansen, M. B. Jørgensen, Quality control of injection moulded micro mechanical parts, *Proceedings of the 5th International Conference on Multi-Material Micro Manufacture (4M/ICOMM)* (2009) pp. 175–178, doi:10.1243/17547164C0012009031.
- [126] G. Tosello, H. N. Hansen, S. Gasparin, Applications of dimensional micro metrology to the product and process quality control in manufacturing of precision polymer micro components, *CIRP Annals - Manufacturing Technology* **58** (1) (2009) pp. 467–472, doi:10.1016/j.cirp.2009.03.027, ISSN 0007–8506.
- [127] ISO/TS 15530-3 - Geometrical product specifications (GPS) – Coordinate measuring machines (CMM): Technique for determining the uncertainty of measurement – Part 3: Use of calibrated workpieces or standards, International Organization for Standardization, Geneva (2004).

- [128] F. Härtig, M. Krystek, Correct treatment of systematic errors for the evaluation of measurement uncertainty, *Proceedings of 9th International Symposium on Measurement Technology and Intelligent Instruments (ISMTII)* **1** (2009) pp. 1–016–1–019.
- [129] Ch. Reinhart, Ch. Poliwoda, T. Guenther, W. Roemer, S. Maas, Ch. Gosch, Modern voxel based data and geometry analysis software tools for industrial CT, *Proceedings of the 16th World Conference on Nondestructive Testing (WCNDT)* (2004) 8 pp.
- [130] S. Ontiveros, J. A. Yagüe-Fabra, R. Jiménez, G. Tosello, S. Gasparin, A. Pierobon, S. Carmignato, H. N. Hansen, Dimensional measurement of micro-moulded parts by computed tomography, *Measurement Science and Technology* **23** (2012) 125401, 9 pp., doi:10.1088/0957-0233/23/12/125401.
- [131] P. Müller, J. Hiller, A. Cantatore, L. De Chiffre, A study on evaluation strategies in dimensional X-ray computed tomography by estimation of measurement uncertainties, *International Journal of Metrology and Quality Engineering* **3** (2) (2012) pp. 107–115, doi:10.1051/ijmqe/2012011.
- [132] W. Knapp, Tolerance and uncertainty, *Proceedings of the 5th International Conference on Laser Metrology, Machine Tool, CMM and Robot Performance (LAM DAMAP)* (2001) pp. 357–366.
- [133] H. N. Hansen, Verification and calibration of coordinate measuring machines, Ph.D. thesis, Technical University of Denmark, Kgs. Lyngby (1997).
- [134] ISO/TS 23165 - Geometrical product specifications (GPS) – Guidelines for the evaluation of coordinate measuring machine (CMM) test uncertainty, International Organization for Standardization, Geneva (2006).
- [135] H. Kunzmann and E. Trapet and F. Wäldele, Report on the EAL interlaboratory comparison M 16 "Ball plate calibration", Physikalisch Technische Bundesanstalt, Final report (1995) 50 pp.
- [136] Ch. Heinzl, J. Kastner, A. Amirkhanov, E. Gröller, M. Reiter, Fast estimation of optimal specimen placements in 3D X-ray computed tomography, *International Symposium on Digital Industrial Radiology and Computed Tomography* (2011) 8 pp.
- [137] R. Schmitt, Ch. Niggemann, Method for efficient identification of similar work pieces for X-ray computed tomography, *International Symposium on Digital Industrial Radiology and Computed Tomography* (2011) 9 pp.
- [138] S. Reisinger, S. Kasperl, M. Franz, J. Hiller, U. Schmid, Simulation-based planning of optimal conditions for industrial computed tomography, *International Symposium on Digital Industrial Radiology and Computed Tomography* (2011) 8 pp.
- [139] R. Schmitt, Ch. Isenberg, Ch. Niggemann, Knowledge-based system to improve dimensional CT measurements, *Proceedings of the Conference on Industrial Computed Tomography (ICT)* (2012) pp. 363–372, ISBN 978-3-8440-1281-1.



# Own references

- [1] P. Müller, Use of reference objects for correction of measuring errors in X-ray computed tomography, Technical University of Denmark, Kgs. Lyngby, Report (2010) 34 pp.
- [2] A. Cantatore, P. Müller, Introduction to computed tomography, Technical University of Denmark, Kgs. Lyngby, Report (2011) 71 pp.
- [3] P. Müller, R. A. Pacurar, L. De Chiffre, Geometrical metrology on silicone rubber by computed tomography, Technical University of Denmark, Kgs. Lyngby, Report (2011) 61 pp.
- [4] P. Müller, R. A. Pacurar, L. De Chiffre, A. Cantatore, P. Berce, Geometrical metrology on silicone rubber by computed tomography, *Proceedings of the 11th International Conference of the European Society for Precision Engineering and Nanotechnology (euspen)* 1 (2011) pp. 243-246, ISBN13 978-0-9553082-9-1.
- [5] A. Cantatore, J. L. Andreasen, S. Carmignato, P. Müller, L. De De Chiffre, Verification of a CT scanner using a miniature step gauge, *Proceedings of the 11th International Conference of the European Society for Precision Engineering and Nanotechnology (euspen)* 1 (2011) pp. 46-49, ISBN13 978-0-9553082-9-1.
- [6] P. Müller, J. Hiller, A. Cantatore, L. De Chiffre, Investigation of measuring strategies in computed tomography, *New technologies in manufacturing (NEWTECH)* (2011) pp. 31-42, ISBN 978-80-214-4267-2.
- [7] P. Müller, A. Cantatore, J. L. Andreasen, J. Hiller, L. De Chiffre, Computed tomography as a tool for tolerance verification of industrial part, *CIRP Conference on Computer Aided Tolerancing (CIRP CAT)* (2012) 10 pp.
- [8] P. Müller, J. Hiller, A. Cantatore, G. Tosello, L. De De Chiffre, New reference object for metrological performance testing of industrial CT systems, *Proceedings of the 12th International Conference of the European Society for Precision Engineering and Nanotechnology (euspen)* 1 (2012) pp. 72-75, ISBN13 978-0-9566790-0-0.
- [9] P. Müller, J. Hiller, A. Cantatore, M. Bartscher, L. De De Chiffre, Investigation on the influence of image quality in X-ray CT metrology, *Proceedings of the Conference on Industrial Computed Tomography (ICT)* (2012) pp. 229-238, ISBN 978-3-8440-1281-1.

- [10] P. Müller, J. Hiller, A. Cantatore, L. De Chiffre, A study on evaluation strategies in dimensional X-ray computed tomography by estimation of measurement uncertainties, *International Journal of Metrology and Quality Engineering* **3** (2) (2012) pp. 107-115, doi:10.1051/ijmqe/2012011.
- [11] P. Müller, Report on research activities in the field of dimensional X-ray computed tomography carried out at the PTB, Physikalisch Technische Bundesanstalt, Confidential report (2012) 59 pp.
- [12] P. Müller, J. Hiller, YY. Dai, J. L. Andreasen, H. N. Hansen, L. De Chiffre, Industrial application of uncertainty estimation using calibrated workpieces for dimensional measurements in X-ray computed tomography (submitted to *Measurement Science and Technology*).
- [13] P. Müller, J. Hiller, YY. Dai, J. L. Andreasen, H. N. Hansen, L. De Chiffre, Quantitative analysis on the influence of scaling errors in dimensional CT metrology (under preparation for submission to *Precision Engineering*).

# Appendix

This Appendix contains calibration certificates of two reference objects:

- **CT ball plate**

Calibrated at the DTU laboratory in Kgs. Lyngby using a Zeiss UPMC CARAT CMM

- **CT tree**

Calibrated at the ISM3D laboratory in Gijon using a Zeiss Prismo Navigator CMM

## CALIBRATION CERTIFICATE

|                           |   |
|---------------------------|---|
| Calibrated object         | CT ball plate   |
| Manufacturer              | DTU Mekanik   |
| Calibration date          | 18.6.2012   |
| Operator                  | Erik Larsen   |
| Instrument                | Coordinate measuring machine (CMM) Zeiss UPMC 850<br>CARAT, $MPE_E = (0.4 + L/900) \mu m$ ( $L$ in mm)                            |
| Probe configuration       | Diameter 2 mm and 55 mm long conical stylus   |
| Measuring force           | 0.05 N  |
| Length standard           | Ball plate RP05 400-90.05 ( $U = 0.6 \mu m + 0.9 \cdot 10^{-6} L$ ), traceable to Zeiss, cert. no. 13782, calibrated on 15.5.2008 |
| Environmental temperature | $20 \pm 0.5 \text{ } ^\circ C$  |

### 1. Calibrated object

The calibrated object features a regular 5 x 5 array of ruby spheres, which are glued on a 2 mm thick carbon fibre plate. Nominal diameter of spheres is 5 mm with sphericity of 0.0006 mm. The nominal pitch between sphere centers is 10 mm. Material characteristics are summarized in table 1.

**Table 1.** Material characteristics of the CT ball plate.

| Part name | Material                                 | Density<br>$\rho$ [ $g \cdot cm^{-3}$ ] | Thermal expansion coefficient<br>CTE [ $K^{-1}$ ] |
|-----------|--|---|---|
| Spheres   | Synthetic ruby monocrystal ( $Al_2O_3$ ) | 3.99                                    | $(5.4 \pm 0.5) \cdot 10^{-6}$                     |
| Plate     | Carbon fibre                             | 1.50                                    | $(0.0 \pm 0.5) \cdot 10^{-6}$                     |

### 2. Calibration procedure

The object was measured in two orientations in the measuring volume of the CMM (figure 1), D0 and D180, defined by turning the object by  $180^\circ$ . Measurement in D0 position was repeated five times, measurement in D180 position three times. In both positions two measurements were performed: (1) measurement in counter-clockwise (spiral-in) and (2) measurement in clockwise (spiral-out) spiral sequence. The first mentioned started by probing sphere no. 1 and finished in sphere no. 13 and the second mentioned started from sphere no. 13 and finished in sphere no. 1. Measurements in X and Y direction were corrected for scaling errors by measuring a length standard (ball plate). Each sphere was measured by probing five points – four at the equator and one at the pole.

### 3. Coordinate system and alignment

Coordinate system and numbering of the balls are defined in figure 2. Coordinate system was defined through spheres no. 1, 5 and 21.

### 4. Calibration uncertainty

Calibration uncertainty resulted from three contributors: (1) calibration certificate of the ball plate, (2) measurement during traceability transfer and (3) measurement repeatability assessed through repetitive measurements and measurements in different orientations. The model equation for calibration uncertainty is shown below. Calibration uncertainties were assessed at a confidence interval of 95%, corresponding to  $k=2$ . Table 2 presents results of uncertainty estimation for four measurands: diameter and form error of spheres and X-, Y- and Z-coordinates of sphere centers.

$$U = k \cdot \sqrt{u_{cert}^2 + u_{tran}^2 + u_{repeat}^2} \quad (1)$$

**Table 2.** Uncertainty budget. All values are in  $\mu\text{m}$ .

| Uncertainty contributor | Description   | Measurand  |            |            |            |            |
|-------------------------|---|------------|------------|------------|------------|------------|
|                         |   | Diameter   | Form       | X-coord.   | Y-coord.   | Z-coord.   |
| $u_{cert}$              | Standard uncertainty from the calibration certificate of the ball plate |            |            | 0.3        | 0.3        | 0.3        |
| $u_{tran}$              | Standard uncertainty during the traceability transfer                   |            |            | 0.0        | 0.0        |            |
| $u_{repeat}$            | Standard uncertainty from measurement repeatability                     | 1.2        | 0.7        | 0.7        | 0.6        | 1.5        |
| $U(k=2)$                | Expanded calibration uncertainty  | <b>2.5</b> | <b>1.4</b> | <b>1.6</b> | <b>1.4</b> | <b>3.1</b> |

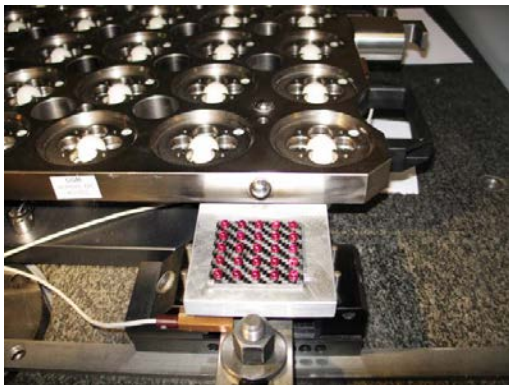


**Figure 1.** Calibration setup for measurements of the CT ball plate using the UPMC 850 CARAT tactile CMM.

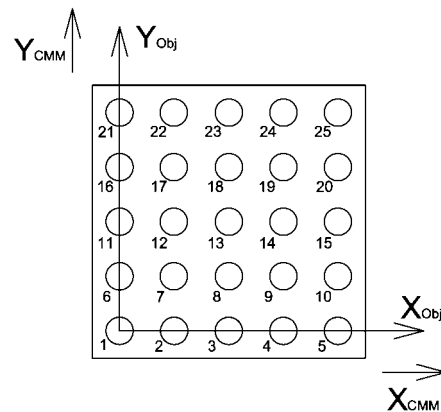


**Figure 2.** Position of the reference coordinate system and numbering of spheres.



**Table 3.** Measurement results.

| Sphere no. | Diameter [mm] | Form [mm] | X-coord. [mm] | Y-coord. [mm] | Z-coord. [mm] |
|------------|---------------|-----------|---------------|---------------|---------------|
| 1          | 5.0002        | 0.0001    | 0.0000        | 0.0000        | 0.0000        |
| 2          | 5.0002        | 0.0001    | 10.0030       | -0.0054       | -0.0009       |
| 3          | 5.0002        | 0.0002    | 19.9935       | 0.0095        | -0.0004       |
| 4          | 5.0001        | 0.0002    | 30.0030       | -0.0004       | -0.0022       |
| 5          | 5.0002        | 0.0001    | 39.9964       | 0.0000        | 0.0000        |
| 6          | 5.0002        | 0.0002    | 0.0008        | 9.9979        | -0.0004       |
| 7          | 5.0002        | 0.0002    | 10.0013       | 9.9915        | 0.0003        |
| 8          | 5.0002        | 0.0002    | 20.0038       | 9.9989        | -0.0022       |
| 9          | 5.0001        | 0.0002    | 30.0032       | 9.9949        | -0.0048       |
| 10         | 5.0002        | 0.0002    | 39.9987       | 9.9938        | -0.0032       |
| 11         | 5.0003        | 0.0001    | 0.0026        | 19.9954       | -0.0018       |
| 12         | 5.0001        | 0.0001    | 9.9963        | 19.9916       | 0.0030        |
| 13         | 5.0003        | 0.0001    | 20.0048       | 19.9976       | -0.0035       |
| 14         | 5.0001        | 0.0001    | 29.9981       | 19.9954       | -0.0019       |
| 15         | 5.0002        | 0.0002    | 40.0030       | 19.9962       | -0.0040       |
| 16         | 5.0001        | 0.0001    | -0.0069       | 29.9877       | -0.0037       |
| 17         | 5.0003        | 0.0002    | 10.0014       | 29.9907       | 0.0066        |
| 18         | 5.0003        | 0.0002    | 20.0039       | 29.9984       | 0.0030        |
| 19         | 5.0003        | 0.0002    | 30.0054       | 29.9952       | -0.0022       |
| 20         | 5.0002        | 0.0001    | 40.0016       | 29.9920       | -0.0028       |
| 21         | 5.0001        | 0.0001    | -0.0026       | 39.9920       | 0.0000        |
| 22         | 5.0002        | 0.0002    | 10.0061       | 39.9968       | 0.0071        |
| 23         | 5.0002        | 0.0002    | 20.0050       | 39.9965       | 0.0062        |
| 24         | 5.0002        | 0.0002    | 30.0074       | 39.9977       | 0.0013        |
| 25         | 5.0002        | 0.0002    | 40.0046       | 39.9998       | -0.0074       |

## Calibration Certificate

|                               |                               |
|-------------------------------|-------------------------------|
| Certificate No                | ISM 01-24.01.2012             |
| Item                          | Ball Array                    |
| Manufacturer                  | DTU, Denmark                  |
| Model                         |                               |
| Serial No                     |                               |
| Manufacturing date            | Jan 2012                      |
| Range                         | 100 mm                        |
| Thermal Expansion Coefficient | 0.0000005 (+/- 0.0000003) 1/K |
| Applicant                     | DTU                           |

The above described item was calibrated in the ISM3D laboratory in Gijón on a coordinate measuring machine. The results, the method and the reference standards used in this calibration are described in the following. All reference standards used in the calibration are traceable to national and international standards.  
The results are valid for the conditions and at the time of the calibration in ISM3D.

Date of the calibration Gijón (Asturias/Spain), 13.1.2012

Responsible for the calibration:



Clemente García, Dipl. Ing. (FH)

### **Method**

The ball array (in form of a "ball tree") was measured according to the procedure T2-04 "Calibration de of 3D Ball Artefacts" of ISM3D in an area on a coordinate measuring machine (CMM) which had been calibrated for the linear scale factors in X, Y and Z - and consequently corrected for these factors - by a reference standard in the volume where the artefact was measured. The artefact was calibrated by measuring ball coordinates in the object coordinate system as defined below. A total of 12 measurements of all balls were taken. Each ball was measured by scanning more than 1000 points, distributed in 2 circular trajectories. All measurements were averaged. As results of the calibration, the coordinates of all ball centers, the distances of pairs of balls belonging to one rod, and the form errors of all balls are reported.

### **Coordinate system and alignment**

The coordinate system and the numbering of the balls are defined in the attached sketch. Note that Y points to the drawing plane.

### **Environmental conditions**

The reference temperature is 20°C. All measured coordinates are referred to 20°C. The temperature of the environment was kept at 20°C +/- 0.3 K during the calibration. According to experience with similar materials (1D and 2D carbon fibre composites), the following thermal expansion coefficients are assumed: In X-direction 0.0000003 1/K, in Y-direction 0.0000038 1/K; these values have an uncertainty of 0.0000005 1/K (k=2).

### **Uncertainty of the results**

The uncertainty  $U$  (for  $k=2$ ) of all calibrated coordinates X, Y, Z is **1.2  $\mu\text{m}$**  (k=2). This uncertainty results from the calibration of the CMM, the uncertainty resulting from the repeatability of the measurements, taking into account the number of repetitions, and from the probing process which includes deflections of the object. The uncertainty for the lengths in X-direction is **1.0  $\mu\text{m}$**  (k=2) . The uncertainty of the results of the form errors is **0.8  $\mu\text{m}$**  (k=2), being the form error as obtained from a measurement of a reference sphere with very small form error, using a similar strategy as applied for the calibration of the object.

### Results

The calibrated distances of the ball centres ( $k=2$ ) are:

| <b>Distances<br/>between balls No.</b> | <b>Distances in mm</b> |
|--|------------------------|
| 1 and 2                                | 40.12126               |
| 3 and 4                                | 34.35474               |
| 5 and 6                                | 28.48553               |
| 7 and 8                                | 22.23953               |
| 9 and 10                               | 16.40100               |

The ball centre coordinates are:

| <b>Ball No.</b> | <b>Coordinates (in mm): X</b> | <b>Y</b> | <b>Z</b> |
|-----------------|-------------------------------|----------|----------|
| 1               | 0.00000                       | 0.00000  | 0.00000  |
| 2               | 40.12126                      | 0.00000  | 0.00000  |
| 3               | 2.71785                       | 10.05045 | -0.00609 |
| 4               | 37.07213                      | 9.87672  | -0.03721 |
| 5               | 5.02006                       | 19.90878 | 0.06273  |
| 6               | 33.50512                      | 20.03653 | -0.03959 |
| 7               | 8.55192                       | 29.87876 | 0.03060  |
| 8               | 30.78826                      | 30.25493 | 0.00965  |
| 9               | 10.94820                      | 40.09010 | 0.00000  |
| 10              | 27.34898                      | 40.03706 | -0.06601 |
| D5              | 19.64293                      | 49.01467 | 0.25762  |

The diameters are as follows:

| <b>Ball No.</b> | <b>Diameter</b> |
|-----------------|-----------------|
| 1               | 3.00004         |
| 2               | 3.00047         |
| 3               | 2.99980         |
| 4               | 2.99989         |
| 5               | 2.99987         |
| 6               | 2.99998         |
| 7               | 2.99997         |
| 8               | 2.99981         |
| 9               | 2.99936         |
| 10              | 2.99999         |
| D5              | 5.00002         |

The form errors are as follows:

(note that the form errors are measured with a CMM. Actual form errors may be smaller and these results should only be regarded as an upper limit):

| <b>Ball No.</b> | <b>Form Error</b> |
|-----------------|-------------------|
| 1               | 0.00058           |
| 2               | 0.00040           |
| 3               | 0.00064           |
| 4               | 0.00056           |
| 5               | 0.00051           |
| 6               | 0.00061           |
| 7               | 0.00060           |
| 8               | 0.00066           |
| 9               | 0.00065           |
| 10              | 0.00085           |
| D5              | 0.00044           |

#### **Standards used:**

##### **CMM**

Type: ZEISS Prismo Navigator  
 Serial Number: 149583  
 Calibrated range (linear factor): X/Y/Z<sub>CMM</sub> in mm: from 0/-1480/-580 to 780/-20/-20  
 Procedure for calibration: T01-02, Calibration of the linear correction of CMMs  
 Date of calibration: 26.10.2011  
 Used length standards: Gage Blocks KOBA, 1000 mm, 500 mm  
 Cal.Cert.No.: 6849, DKD-K-01301, 2011-03 (KOBA)  
 U= 0.00005 mm + 0.0000005 L  
 Therm.exp. of CMM scales 0 (+/- 0.0000003) K<sup>-1</sup>

##### **Thermometer for the object temperature**

Type: CMM-own sensors  
 Calibrated: 15.6.2011 by ISM3D according to procedure  
 ISM3D T-05-01  
 Calibration uncertainty,  $U$  ( $k=2$ )) 0.05 K



